Design of stimuli-responsive polymer capsules by interfacial complexation

Lucas Sixdenier

Sorbonne Université

École doctorale 388

Chimie Physique et Chimie Analytique de Paris Centre

École Normale Supérieure – Département de Chimie

Laboratoire PASTEUR – Pôle de Chimie Physique et Biologique de la Matière Vivante

Design of stimuli-responsive polymer capsules by interfacial complexation

Par Lucas SIXDENIER

Thèse de doctorat de Chimie Physique

Dirigée par Emmanuelle MARIE

Présentée et soutenue publiquement le 28 janvier 2022 devant un jury composé de :

M. LECOMMANDOUX Sébastien	Professeur	Examinateur
Mme MARIE Emmanuelle	Directrice de recherche	Directrice de thèse
Mme RAVAINE Valérie	Professeure	Rapportrice
Mme RIEGER Jutta	Directrice de recherche	Examinatrice
M. TRIBET Christophe	Directeur de recherche	Membre invité
M. TSAPIS Nicolas	Directeur de recherche	Rapporteur
M. ZHAO Yue	Professeur	Membre invité

Table of Content

List of abbreviations and symbols

Abbreviations

ANS: 8-anilinonaphthalene-1-sulfonic acid

AuNP(s): gold nanoparticle(s)

CarboxyNP(s): carboxylate-modified polystyrene nanoparticle(s)

CMC: Critical micellar concentration

Coum: Coumarin

DLS: Dynamic light scattering

eGFP: enhanced Green Fluorescent Protein

FRAP: Fluorescence recovery after photobleaching

GSPM: Grating-shadow phase microscopy

GUV(s): Giant unilamellar vesicle(s)

LbL: Layer-by-layer

LCST: Lower critical solution temperature

NeutravNP(s): NeutrAvidin-modified polystyrene nanoparticle(s)

NHS: N-hydroxysuccinimide

NP(s): Nanoparticle(s)

OPD: Optical path difference

PAAMAN: Poly(acrylamide-co-acrylonitrile)

PEG: Poly(ethylene glycol)

PFO: Perfluorinated oil

PISA: Polymerization-induced self-assembly

PLL: Poly(L-lysine)

PNIPAM: Poly(N-isopropylacrylamide)

PVP: Poly(vinylpyrrolidone)

QPM: Quantitative phase microscopy

RAFT: Reversible addition-fragmentation chain-transfer

Rho: Rhodamine

SEM: Scanning electron microscopy

UCST: Upper critical solution temperature

W/O: water-in-oil (emulsion)

W/W: water-in-water (emulsion)

Symbols

$\boldsymbol{C}$: concentration

$\boldsymbol{d}$: droplet diameter

$\boldsymbol{e}$: droplet flattening thickness

$\boldsymbol{I}$: fluorescence intensity

$\boldsymbol{M_f}$: polymer mobile fraction

$\boldsymbol{n}$: refractive index

$\boldsymbol{Q}$: heat power

$\boldsymbol{P}$: light power

$\boldsymbol{R}$: droplet radius

$\boldsymbol{T}$: temperature

$\boldsymbol{\delta}$: optical path difference

$\boldsymbol{\kappa}$: thermal conductivity

Chapter 1

General introduction

In everyday life, packing objects in containers, moving them, and unpacking them wherever and whenever we want is a common thing. Transposing this process at the micro- and nanoscale has been a crucial, albeit challenging, issue in many application fields, the most important one being probably the vectorization of drugs or bioactive substances for pharmacological and medical purposes. Mastering the steps of encapsulation and release of molecules or nanomaterials is much more difficult to achieve at these small scales since a direct manipulation of such tiny objects is out of the reach of human hands. As a consequence, alternative levers have been sought to remotely control the packing and unpacking of molecular payloads in micro- and nanocarriers.[*] For the last 20 years, the scientific research relative to the encapsulation of materials at microscales has skyrocketed due to the versatility of the approach and the diversification of the potential applications (see **Figure 1.1**).

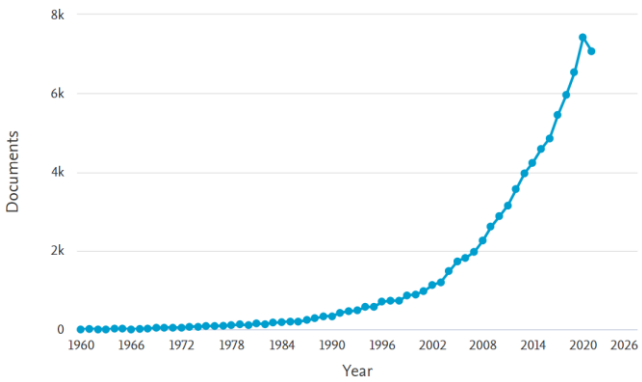

Figure 1.1. Annual number of publications (articles, reviews, and book chapters) referring to "encapsulation" in the fields of Chemistry, Materials and Life Science from 1960 to current 2021 (Source: Scopus, Nov. 2021).

The recent large-scale development of mRNA vaccines to fight against COVID-19 has been an illustrative example of recent achievements made in the field of microencapsulation. The effective encapsulation of negatively-charged mRNA in lipid-based nanoparticles was enabled by a precise

[*] In this thesis, the discussion will be restricted to the physico-chemistry relative to the design and characterization of colloidal systems (with typical sizes between 10 nm and 100 µm). As a consequence, the terms relative to "encapsulation" (including "capsules", "containers", "compartments", "carriers") may be used without specifying the prefixes "micro" or "nano".

optimization of the composition of the nanocontainers.[1] This example illustrates the general issue of multiscale optimization of the formulation to enhance the efficiency of both steps of encapsulation and delivery. It's all a matter of (i) chemical design at the molecular scale, (ii) colloidal stability at the mesoscopic scale and (iii) spatiotemporal control of the delivery at the scale of the target, while overall preserving the activity of interest of the encapsulated payload.

mRNA vaccines are only one example among the tremendous variety of encapsulation systems that have been explored so far for potential medical and biotechnological applications such as bioimaging (e.g. via the encapsulation of fluorescent reporters[2–4] or MRI contrast agents[5–8]), in-situ release or production of therapeutic agents[9–11] (with a particular attention focused on cancer therapy,[12–14] see **Figure 1.2**), tissue engineering and repairing,[15–17] or multimodal approaches such as theranostics that combines in-situ diagnostics and therapy.[18–21] Besides the biomedical field, encapsulation processes have also been extensively developed for various applications in agriculture (e.g. for soil fertilization or for safer pesticide release),[22,23] in food science (e.g. for food preservation or additive delivery),[24,25] in cosmetics (e.g. for fragrance encapsulation or for cosmeceutical applications),[26,27] or in material science (e.g. for self-healing properties[28,29] or for thermal energy storage[30]).

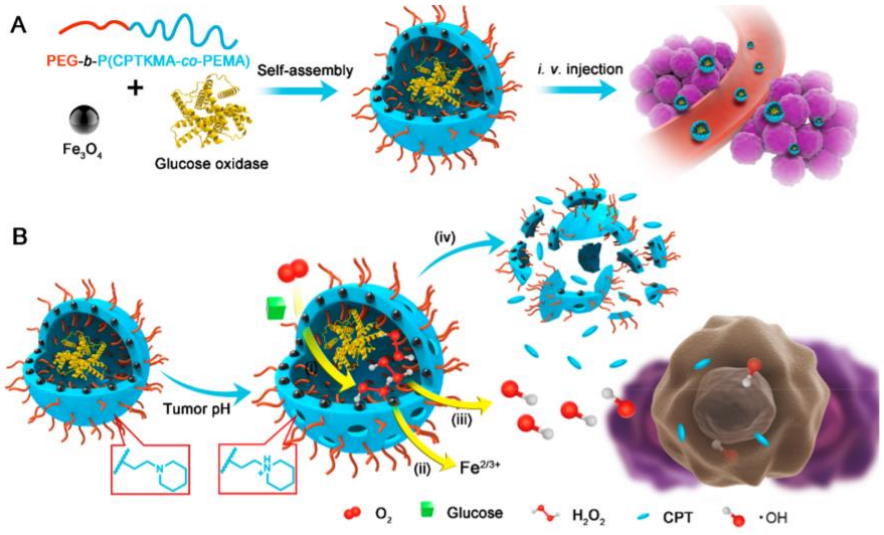

Figure 1.2. Example of in-situ production of therapeutic agents from engineered hybrid vesicles for cancer therapy. A polymeric vesicle entrapping a glucose-sensitive enzyme and iron nanoparticles are injected in the blood circulation. At the contact with tumor pH, the permeability of the vesicle dramatically increases and subsequent reactions between diffusing glucose and oxygen and the vesicle content yield hydroxyl radicals that are able to kill tumor cells.[14]

Beyond delivery applications, the design of micro- and nanocompartments has been extensively investigated in emergent topics related to fundamental research. For instance, nanoreactors have been designed for the study of confinement effects on chemical reaction rates,[31,32] for the study of reactivity at the single-molecule level,[33,34] for the production of nanomaterials,[35,36] for energy production, storage and conversion,[37] or for the development of catalysis for "greener" chemistry.[38]

At the interface between chemistry and biology, the topic of "artificial cells" (or "protocells") has also recently drawn increasing attention. Because of the intrinsic complexity of living matter, the precise role of biological processes can be difficult to decipher *in vivo*. To simplify the approach and better understand the general principles underlying life, chemists have proposed to design artificial microcompartments that could in a sense mimic cellular structures and functions but with a limited number of components and a better control on the physico-chemistry of the system. As a first step towards the imitation of cellular structures, multi-compartmentalized and multi-components artificial structures have been successfully designed since the end of the 2000s (see **Figure 1.3**).[39–41] Elegant works have evidenced the implementation of life-inspired functions in such protocells, including self-replication,[42] differentiation,[43] photosynthesis[44], phagocytosis,[45] or intracellular signalization.[46] The issue of cell-cell communications and interactions has also been explored within protocell communities,[47–49] and the formation of prototissues by controlled aggregation of artificial cells has also been recently demonstrated.[50] As living cells are highly out-of-equilibrium machineries, recent efforts have been made to design active artificial cells that integrate out-of-equilibrium chemical reactions to mimic for instance biological self-sustained motion,[51] or chemical exchanges with the extracellular environment.[52]

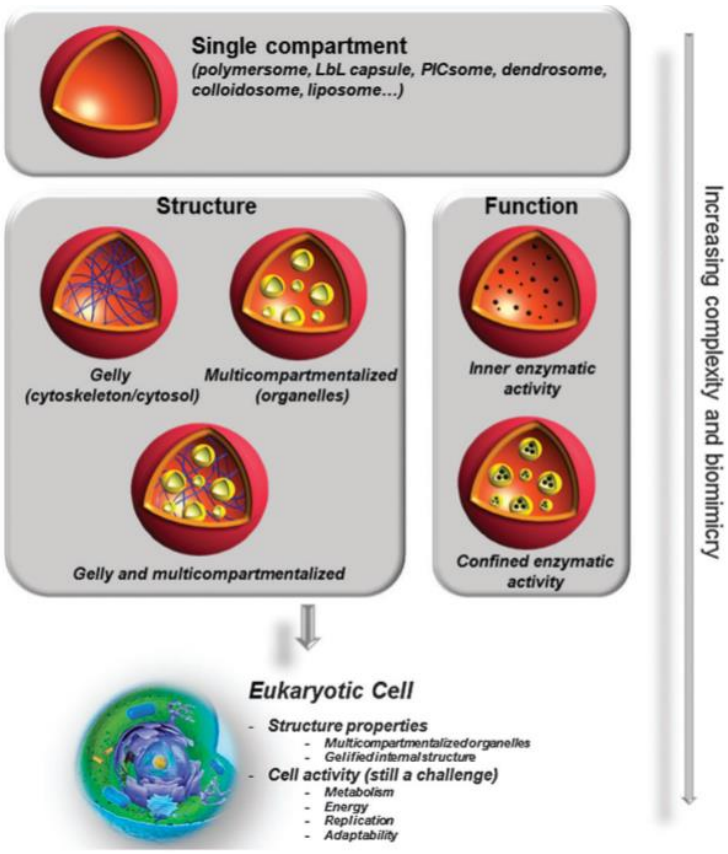

Figure 1.3. Synthetic multicompartmentalized nanocontainers have been developed to mimic the structures and functions of living cells with a lower level of complexity and a better control on the physico-chemistry of the systems.[39]

In this context of bio-delivery and bio-mimicking, biomacromolecules such as proteins, peptides, or DNA can play a crucial role, but their encapsulation in increasingly complex containers can be limited by their intrinsic fragility. The objective of the present work was to develop a versatile approach for the design of stimuli-responsive polymer capsules, in conditions which are compatible with the presence of potentially fragile biomacromolecules.

For that purpose, we used the phenomenon of interfacial complexation in water-in-oil emulsions to achieve the formation of capsules composed of an aqueous core and a thermo-responsive polymer shell. Thermally-induced changes of the physico-chemical properties of the capsules were essentially assessed with *in situ* fluorescence imaging. We also evaluated the compatibility of the interfacial complexation process with the presence of a model protein for potential applications as biomacromolecules delivery system. In addition, we demonstrated that the thermal properties of the polymers used in formulation enables the straightforward

incorporation of nanoparticles in the polymer shells, extending the functionalities that can be imparted to the capsules. This was in particular applied to gold nanoparticles that exhibit optical properties that make them efficient light-to-heat converters at the nanoscale, paving the way for photo-thermal stimulation of the capsules.

This manuscript has been organized in the following way: Chapter 2 presents a selective state of the art on the field of encapsulation at small scales, with a special focus on methods compatible with the encapsulation of fragile biomolecules such as proteins, before introducing the interfacial complexation approach that has been specifically developed in this work. Chapter 3 illustrates the formation of polymer shells by interfacial complexation with a first thermo-responsive polymer based on the well-known LCST-type poly(N-isopropylacrylamide), and details the imaging protocols that have been used to characterize *in situ* the physico-chemical properties of the so-formed polymer shells. Chapter 4 focuses on the incorporation of nanoparticles in the polymer capsules and details the thermometry protocol that has been developed to characterize photothermal effects in presence of gold nanoparticles. Chapter 5 presents the results obtained with a second thermo-responsive polymer, based on poly(acrylamide-co-acrylonitrile) that exhibits UCST properties which seem more promising for the encapsulation and on-demand release of payloads upon thermal and light stimulation.

Chapter 2

State of the art and positioning of the present work

2.1 The specific challenge of protein encapsulation and release

The highly specific bioactivity of proteins and peptides, optimized by billions of years of evolution, makes them ideal candidates for advanced therapeutic applications. The rise of protein-based medical treatments has been associated to the development of two techniques, the DNA recombinant technology and the solid phase peptide synthesis, which have enabled the production and purification of tailor-made synthetic proteins and peptides at large scale. As a non-exhaustive list of proteins of interest for biomedical or biotechnological applications, we can mention protein drugs for the treatment of chronical disease (such as insulin for diabetes),[53] growth factors for tissue repairing or engineering,[54] antibodies for bio-diagnostics or immunotherapy,[55] or neuropeptides for the treatment of neurological disorder or the investigation of neuronal signaling pathways.[56]

The specific activity of a protein is correlated to its well-defined structural organization which is dictated by (i) the chemical composition of the amino-acid sequence (primary structure), (ii) the local conformations of the chain backbone (secondary structure) and (iii) the tridimensional folding of the entire structure resulting from intrachain interactions and reorganization of the solvation sphere (tertiary structure). Any small alteration of this optimized structure may induce a complete loss of the protein bioactivity and may be prejudicial for therapeutic goals, making these biomacromolecules highly sensitive to their environment. As an illustration, the first formulations that have been developed for protein delivery were made of aqueous solutions of "raw" proteins (i.e. unprotected or unmodified). Upon injection *in vivo*, these proteins were readily exposed to (i) the recognition and elimination by the immune system and/or (ii) multiple pathways of chemical degradation (hydrolysis or β-elimination along the backbone, deamidation of asparagine or glutamine residues, oxidation of methionine residues, cleavage or interchange or cysteine disulfide bonds).[57] Chemical degradation induced denaturation of the protein, i.e. misfolding or unfolding of the tridimensional structure, resulting in the loss of its biological activity and the formation of potentially harmful side-products.[58] In addition, due to their high molecular weight and high hydrophilicity, non-modified proteins are less able to cross the amphiphile cellular membrane (compared to conventional small molecular drugs) and thus exhibit low levels of cellular

internalization. At the end, liquid formulations of raw proteins showed poor therapeutic efficiency, and significant side-effects for the patients.

To circumvent these pitfalls, the microencapsulation of proteins appeared as a relevant strategy to protect them from environmental degradation, maximize their stability, decrease their immunogenicity, prolong their lifetime in biological conditions, increase their cellular uptake and eventually optimize their therapeutic effect. However, the issue of protein denaturation can also be faced during the formulation of the encapsulation system, since it may involve physical of chemical treatments that may be harmful for proteins, such as high temperatures, mechanical stress, chemical reactions, or presence of incompatible solvents. Thus, achieving an efficient encapsulation of such fragile biomacromolecules while maintaining their stability and bioactivity is still a challenge in the field of drug delivery.

Different encapsulation systems have been explored for the stabilization and vectorization of proteins. Only organic systems will be discussed in this thesis and some of them are represented in **Figure 2.1**. The encapsulation systems can be classified according to their structure (matrix-like *vs* reservoir-like) and their nature (hydrophobic *vs* hydrophilic). In matrix-like systems, such as colloidal hydrogels, complex coacervates, polymer microspheres, or polymer micelles, the protein is embedded in a solid-like environment usually made of entangled polymer chains. In reservoir-like systems, like emulsion droplets, vesicles such as liposomes and polymersomes, or polymer capsules, the protein is entrapped in a liquid core surrounded by a protective layer. Depending on the nature of the polymer matrix or of the liquid reservoir, the systems may be more appropriate for the encapsulation of either hydrophobic or hydrophilic payloads. Polymer microspheres, polymer micelles, oil droplets and oil-core polymer capsules are usually suitable for the encapsulation of hydrophobic compounds. Liposomes, polymersomes, colloidal hydrogels and aqueous-core polymer capsules are usually appropriate for the encapsulation of hydrophilic species. As most of therapeutic proteins are hydrophilic, the discussion will only focus on hydrophilic encapsulation systems throughout this Chapter.

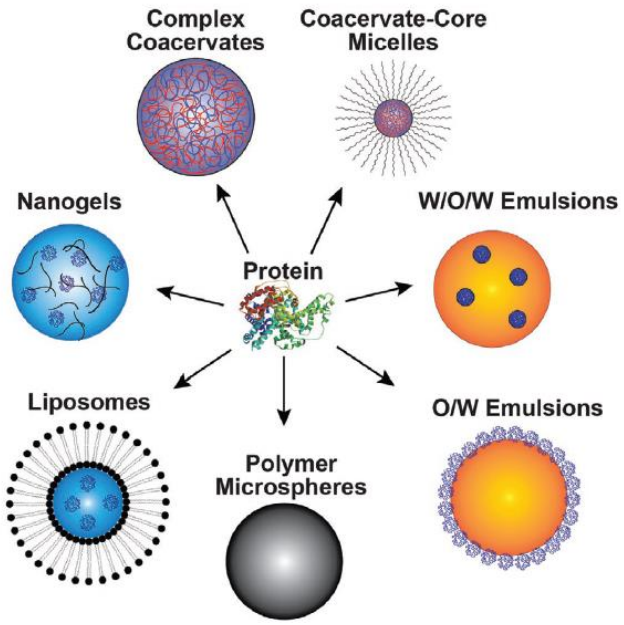

Figure 2.1. Various nano- and microcontainers that have been proposed for the encapsulation and delivery of proteins.[59]

Three crucial issues must be considered for the design of protein encapsulation systems: the efficiency of protein loading during the encapsulation process, the preservation of the stability/activity of the protein within the container, and the control of the release kinetics for delivery applications.

Therapeutic applications do not always require high amounts of delivered proteins to be effective. However, the effects of dilution upon release *in vivo* may decrease the local concentration of delivered protein and thus reduce the efficiency of its biological action. As a consequence, high encapsulation efficiencies (typically > 50 %) of proteins are usually targeted upon formulation. In any case, the waste of product related to poor encapsulation may be regrettable (especially for proteins that are difficult and expensive to produce) and motivates the optimization of encapsulation efficiencies. The second major issue is the preservation of the protein integrity upon encapsulation. As previously mentioned, proteins are highly sensitive to their environment and can be impaired in presence of mechanical stress or chemical reactions. The encapsulation of proteins may thus require mild conditions of formulation.

In the next section, we will describe the most common encapsulation systems that have been developed in the literature for the vectorization of hydrophilic payloads, and concomitantly discuss

their relevance regarding protein encapsulation. Then, we will address the issue of controlled delivery in relation to these encapsulation systems. At the light of this state of the art, we will eventually settle upon a system that seems promising for the encapsulation of proteins in mild conditions and their controlled release upon stimulation.

2.2 Micro- and nanocontainers developed for the encapsulation of hydrophilic payloads

2.2.1 Vesicles: liposomes and polymersomes

Vesicles are core-shell systems composed of an aqueous core protected by a molecular bilayer (also termed "membrane") formed by the self-assembly of amphiphilic molecules. Two main types of vesicles have been extensively studied for encapsulation applications: liposomes in which the membrane is made of a lipid bilayer, and polymersomes in which the membrane is made of a bilayer of amphiphilic copolymers (**Figure 2.2**). The self-organization of these amphiphilic molecules in a well-defined bilayer is entropically driven by the water desolvation of their hydrophobic moieties (the hydrophobic tail of lipids and the hydrophobic block of copolymers). In the resulting membrane, the hydrophobic moieties are buried in the middle of the bilayer and the hydrophilic moieties are exposed to water at the inner and outer surface of the bilayer.

To favor the formation of spherical enclosed bilayers (low-curvature objects), rather than micelles (high-curvature objects), a relatively high degree of hydrophobicity is required in the molecular building block. Typically, liposomes are formed for a lipid packing parameter comprised between 1/2 and 1, and polymersomes are formed for a mass fraction of the hydrophobic block higher than 60 %.[60] The main advantage of the vesicular structure is the possibility to encapsulate hydrophilic species in the aqueous core (or lumen) of the vesicle and also to entrap hydrophobic species inside the bilayer membrane. The typical diameter of both types of vesicles can vary between 10-20 nm (for Small Unilamellar Vesicles, or SUVs) and 100-200 µm (for Giant Unilamellar Vesicles, or GUVs), depending on the method of preparation.[61]

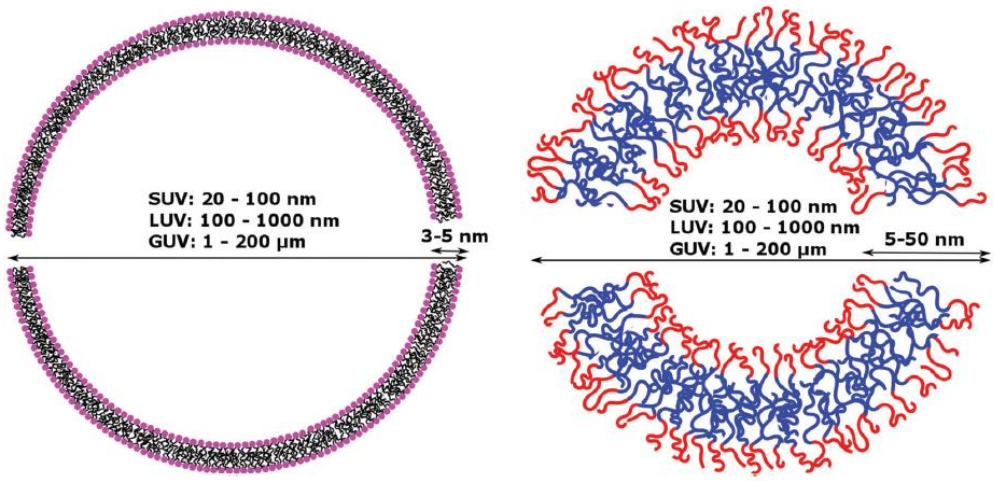

Figure 2.2. Comparison of the structures of liposomes (left) and polymersomes (right). SUV/LUV/GUV: small/large/giant unilamellar vesicles.[61]

In terms of structural and physico-chemical properties, the main differences between liposomes and polymersomes are essentially due to the intrinsic differences in size and chemical composition of their respective molecular building blocks (lipids *vs* polymer chains). As natural lipids (mostly phospholipids) have a typical molecular weight of ~ 100-1000 g/mol, the membrane thickness of liposomes is limited to 3-5 nm. As the molecular weight of amphiphilic copolymers can be tuned between ~ 1000 and 10 000 g/mol during their synthesis, polymersomes can exhibit a membrane thickness ranging from 5 to 50 nm.

Since lipids are small and highly mobile molecules, the membrane of liposomes is characterized by a high lateral fluidity and consequently a high permeability (**Figure 2.3**). This may be an advantage to mimic the biophysical properties of cell membranes or to interact with such membranes, but this may be a drawback regarding the encapsulation of molecules for on-demand delivery as they could be subject to significant and uncontrolled leakage. Lipid molecules have the major advantage to be biocompatible, but they are easily subject to chemical degradation (via hydrolysis of ester bonds and oxidation of unsaturated tails especially), making liposomes relatively fragile and unstable in biological environments over long time periods.[61]

On the other side, the membranes of polymersomes are characterized by low lateral fluidity and consequently low permeability and better mechanical properties (compared to liposomes), essentially due to the high degree of entanglement of the polymeric hydrophobic moieties within

the bilayer (**Figure 2.3**). These properties make polymersomes good candidates for encapsulation applications. In addition, the synthetic control over the composition and functionality of the polymer blocks gives more modularity and versatility to tune the physico-chemical properties of the polymersome membrane (compared to natural lipids which show lower potential for functionalization). As an example, reactive groups can be introduced along the polymer chains to cross-link the polymersome membrane for improving its retention efficiency[62,63] or for modulating its permeability.[64] As a limitation, the polydispersity inherent to the polymer synthesis can affect the structural properties of the polymersomes.[65]

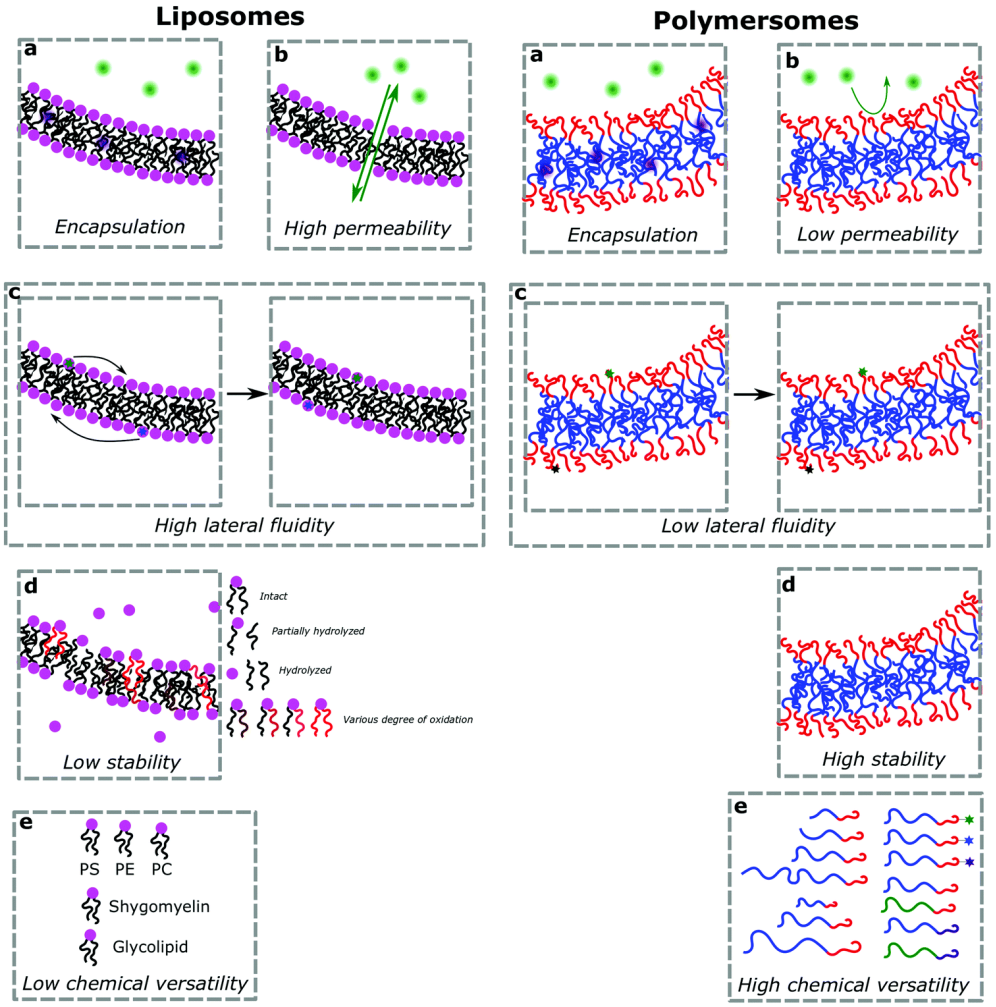

Figure 2.3. Comparison of the dynamics and chemical stability of the membranes in liposomes and polymersomes.[61]

The formation of liposomes and polymersomes can be achieved via similar methods, the most used being probably film hydration and solvent displacement methods.

Film hydration consists in dissolving the amphiphile in a suitable organic solvent and to let the solution dry on a substrate, leading to the deposition of an amphiphile multilayer film on the substrate. Then, the addition of water (that may contain hydrophilic species to encapsulate) on the film induces its progressive swelling and budding resulting in the detachment of spherical vesicles (**Figure 2.4**). Film hydration can be assisted by different external fields: sonication, intercalation of a gel interlayer between the substrate and the amphiphilic film (the swelling of this gel interlayer facilitates the detachment of vesicles upon rehydration) or application of an electric field on the substrate that supports the film (the electric field induces fluctuation in the amphiphile film and favors the formation of vesicles, especially GUVs).

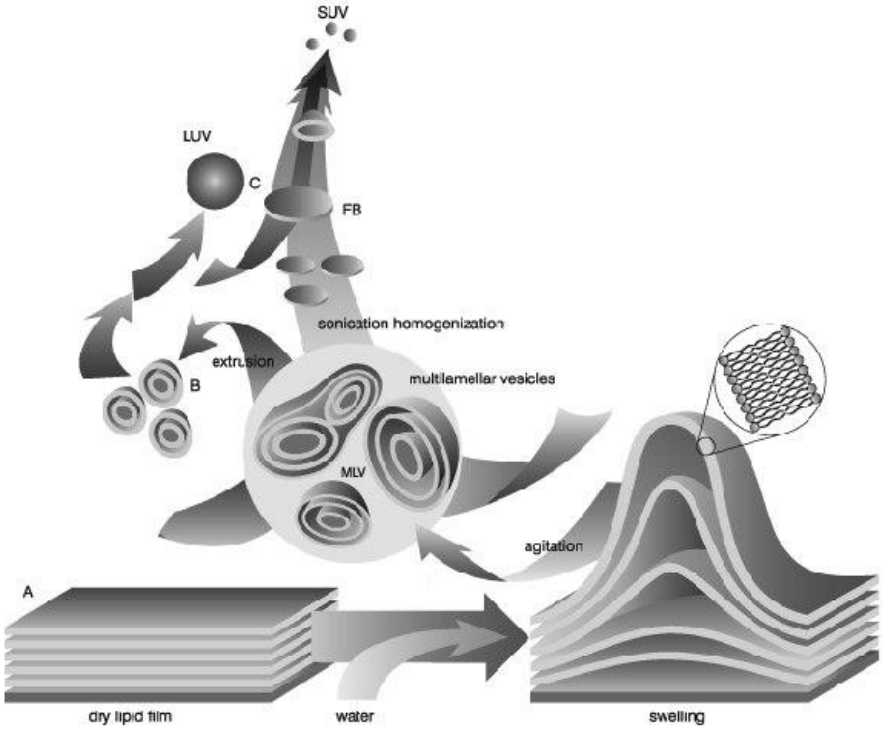

Figure 2.4. Formation of liposomes by the film hydration method.[66]

Film hydration is easy to implement but the encapsulation yield can be limited for hydrophilic molecules since they have to pervade and intercalate between the densely packed layers of the amphiphile film to be readily entrapped in the lumen of the vesicles during their detachment. This

limitation is particularly true for proteins (and other biomacromolecules) which are high molecular weight and highly charged molecules, and thus poorly disposed to be inserted in the dried film.[67–69] Some techniques have been proposed to increase the encapsulation yield of such macromolecules in particular conditions, such as in presence of polymeric crowding agents.[70] Besides, the use of physical treatments such as sonication or electric field can be harmful for fragile biomacromolecules to encapsulate.

Solvent displacement methods rely on the formation of emulsion droplets containing the amphiphiles, followed by the removal of organic solvents temporary used during the process. The simplest solvent displacement method consists in dissolving the amphiphiles in a volatile compatible solvent (e.g. ether) and to rapidly inject this solution in a water bath under vigorous stirring, resulting in the formation of organic nano- or microdroplets that contain the amphiphiles. Then, the progressive "displacement" of the organic solvent (i.e. its removal, by evaporation or dialysis for instance) induces the self-assembly of the amphiphiles in spherical membranes, eventually resulting in vesicles (usually small, multilamellar and polydisperse) suspended in aqueous solution. This method is easy to implement but is not suitable for the encapsulation of hydrophilic species since the amphiphiles are initially solubilized in an organic solvent.

As an alternative, the emulsion phase transfer method can be used. An initial water-in-oil emulsion is formed with the amphiphile decorating the water droplets (that may contain hydrophilic species). Then this emulsion is slowly injected in a water-organic biphasic solution separated by an interfacial amphiphile monolayer. As the emulsion water droplets sink towards the bottom aqueous phase, they cross the water/organic interface and collect a thin organic layer stabilized by amphiphiles on its two sides. The removal or dewetting of the organic layer eventually leads to the formation of the vesicular bilayer membrane.[71]

The recent generalization and improvement of microfluidic techniques have enabled considerable progress in the control of emulsion phase transfer for the production of vesicles, in terms of (i) optimization of size and dispersity of the objects,[72] (ii) formation of multicompartmentalized structures,[73] (iii) tunability of the membrane and lumen compositions (see **Figure 2.5**),[74] and (iv) encapsulation efficiency.[75]

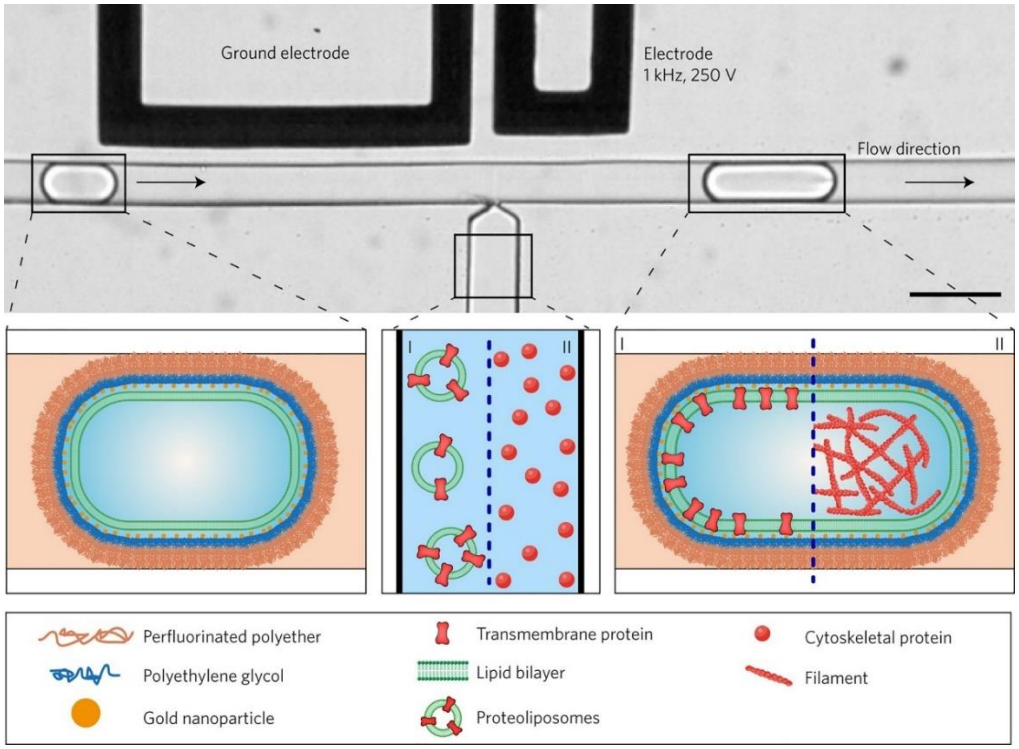

Figure 2.5. Microfluidics-generated sequential bottom-up assembly of transmembrane and cytoskeletal proteins by high throughput pico-injection into droplet-stabilized GUVs with complex membrane (scale bar = 50 mm).[74]

These approaches based on water-in-oil emulsions have usually better encapsulation yields than film hydration since the hydrophilic payloads are initially confined in water droplets that are "converted" into vesicle lumen upon formation of the membrane.

However, these approaches can be inappropriate for the encapsulation of sensitive and fragile proteins due to the presence of organic solvents that can impair their stability.[76] Indeed, in native aqueous environment, the tertiary structure of proteins is mostly maintained by intrachain hydrophobic interactions. Upon contact with an organic solvent, proteins can be subject to unfolding due to the affinity of their hydrophobic domains with the organic solvent. This denaturation process usually induces the aggregation of proteins at water/organic interfaces and the loss of their bioactivity.[77–79] This interface-induced degradation of proteins is likely to occur in any encapsulation approach that involves water-in-oil or oil-in-water emulsions. It is the case for the preparation of vesicles by phase transfer methods but also for the preparation of other encapsulation systems as it will be mentioned later.

To limit the phenomenon of interface-induced degradation, some formulation adjustments have been proposed such as the use of highly concentrated protein solutions to promote the formation of a "sacrificial" protein layer at harmful interfaces that may shield the rest of the aqueous solution ("self-protecting effect"), or the use of surfactant- or polymer-based protective coatings of proteins that may reduce their direct contact with organic solvents and enhance their stability.[80,81] However, these solutions are usually not generalizable and may be ineffective, or even prejudicial, when switching from one protein of interest to another. As a general statement, the effects of additives such as surfactants, co-solvents, sugar, polymers, salts (added for the necessity of the formulation or as additional ingredients) can have either positive or negative effects on the stability of proteins (depending on its nature) and are difficult to rationalize.[57]

As an alternative to emulsion-based approaches, the phenomenon of polymerization-induced self-assembly (PISA) has led to breakthroughs in the design of functional polymersomes and other types of self-assembled nanostructures in water.[82,83] In the PISA process, the sequential growth of amphiphilic polymer chains triggers their self-assembly *in situ* in well-defined nanostructures (spherical micelles, worm-like micelles, vesicles). The rise of this technique has been largely enabled by the optimization of reversible-deactivation radical polymerization (also termed "controlled" or "living" radical polymerization).[84,85] Briefly, after the synthesis of a "living" hydrophilic block in water, the polymerization is carried on by the addition of monomers whose corresponding homopolymer is hydrophobic and insoluble in water. Upon extension of the hydrophobic block, an amphiphilic character is progressively imprinted to the growing chains, resulting in their self-assembly in nanostructures whose morphology can be controlled via the nature of the monomers, the degrees of polymerization, or the use of additives (**Figure 2.6**).[86]

Regarding the production of vesicles, PISA has been for long restricted to the formation of nano-polymersomes (typically 10-100 nm), but the formation of 10-µm GUVs has been recently achieved with this method.[87] Recent works have also demonstrated the potential of PISA-based polymersomes for protein encapsulation, either in the lumen[88] or in the membrane of the vesicles.[89]

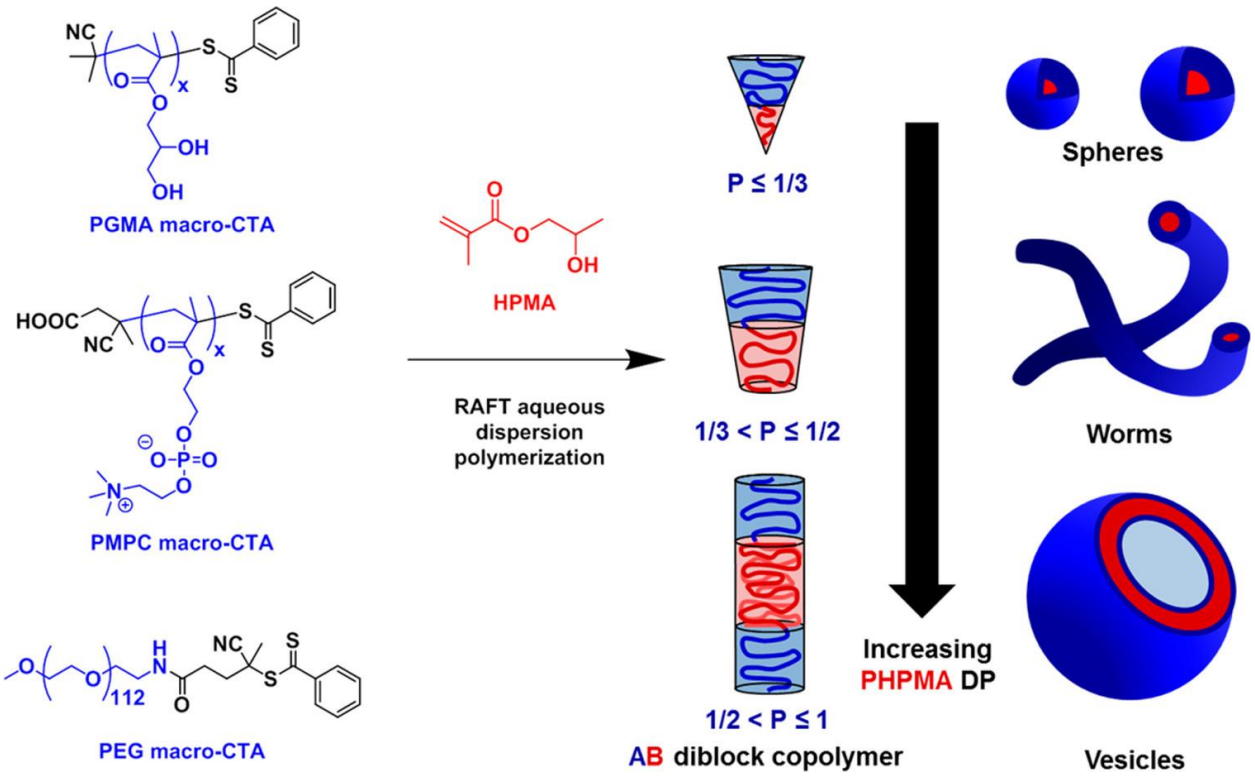

Figure 2.6. Illustration of the polymerization-induced self-assembly (PISA) process. The RAFT polymerization of a hydrophobic block of poly(2-hydroxypropyl methacrylate) from a hydrophilic macromolecular chain transfer agent (either poly(glycerol monomethacrylate), poly[2-(methacryloyloxy)ethyl phosphorylcholine], or poly(ethylene glycol)) produces amphiphilic chains that self-assemble in nanostructures. Spheres, worms, or vesicles can be produced by judicious variation of the packing parameter (P) which is determined by the relative volume fractions of the hydrophilic and hydrophobic blocks.[86]

2.2.2 Colloidal hydrogels

Colloidal hydrogels are micro- or nanospheres obtained by physical or chemical cross-linking of hydrophilic polymer chains, resulting in a colloidal network that can swell in water without falling apart. Colloidal hydrogels are usually termed microgels or nanogels according to their size.

Hydrogels are commonly prepared according to one of the three following conventional approaches: the polymerization of a colloidal network from monomer and cross-linker building

blocks, the chemical cross-linking of pre-formed reactive polymer chains, and the physical cross-linking of pre-formed interactive polymer chains (see **Figure 2.7**).[90,91]

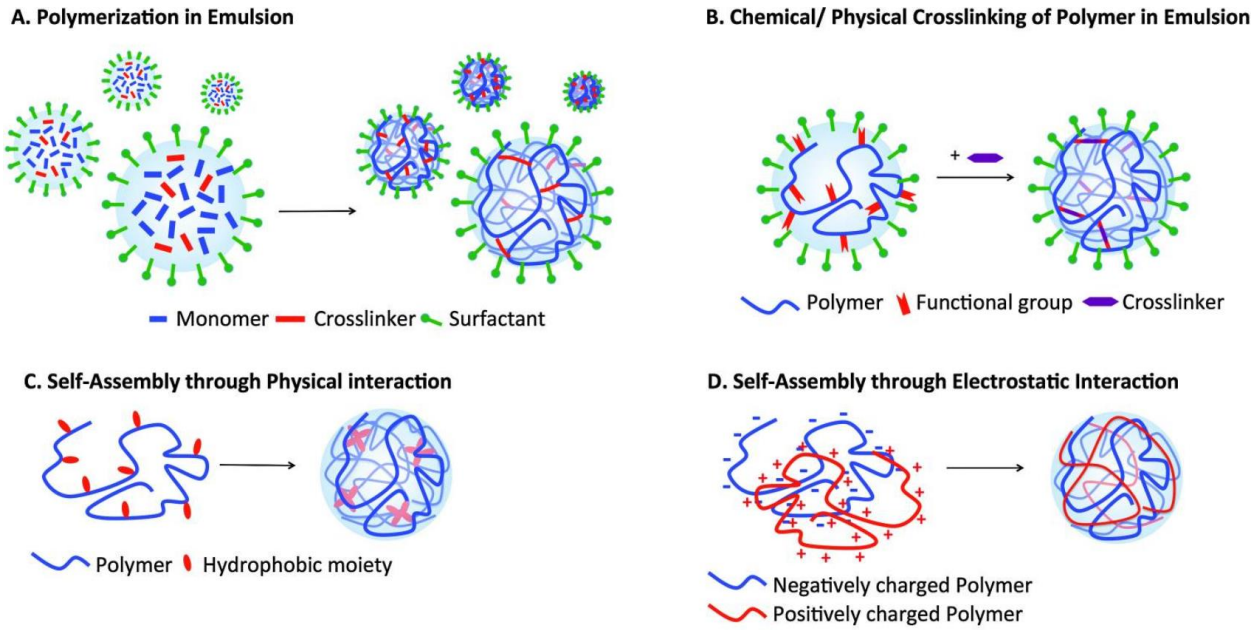

Figure 2.7. Various approaches for the formation of micro- and nanogels.[92]

The formation of hydrogels by polymerization of monomer and cross-linker units (usually hydrophilic acrylate derivatives) can take place directly in water (homogenous conditions) or in emulsion (heterogenous conditions).[93]

In homogeneous conditions, the formation of colloidal hydrogels has been markedly enhanced by the development of reversible-deactivation (or "controlled") radical polymerization that provides a better control on the propagation reactivity and favors the intrachain cross-linking over interchain cross-linking (this latter resulting in macrogelation and not in the formation of individualized colloidal gels).[93,94] An other widespread method for producing colloidal gels in homogenous conditions is the precipitation polymerization, relying on the difference of solubility between the polymer precursors (water-soluble monomers and cross-linkers) and the final network (insoluble in water after reaching a critical size).[95]

The most common method for preparing colloidal hydrogels is however the polymerization in emulsion, and especially in water-in-oil inverse emulsion. An aqueous solution containing the

polymer precursors (monomers, cross-linker, and initiator) is emulsified in an immiscible organic solvent containing a surfactant. The polymerization occurs within surfactant-stabilized water droplets that play the role of a template, yielding spherical hydrogels. After polymerization, the organic phase is removed (by evaporation or centrifugation) and the hydrogels are redispersed in water to eventually recover a colloidal suspension. This versatile approach enables a good control on the chemical composition and the cross-linking density of the final gels.

Colloidal hydrogels can also be achieved by chemical or physical cross-linking of preformed polymer chains. Chemical cross-linking relies on the presence of reactive chemical functions along the polymer backbones, that can react either together or with additional cross-linking species to form covalent networks.[96,97] This approach turned out to be favored when the reactive polymer chains were either confined in emulsion droplets, pre-self-assembled in nanostructures (such as micelles), or adsorbed on solid core templates.

As an alternative to chemical reactions, colloidal hydrogels can also be formed upon physical cross-linking of polymer chains, i.e. via non-covalent interactions (hydrophobic interactions, electrostatic interactions, hydrogen bonds, metal-ligand complexation, host-guest interactions).[98–101] They however may suffer from poorer stability compared to covalently cross-linked analogs. Despite this limitation, one particular type of physical cross-linking has recently aroused increasing attention and is called complex coacervation. The phenomenon of complex coacervation designates the liquid-liquid phase separation that can spontaneously occur between aqueous solutions of oppositely charged macromolecules. This process results in the formation of nano-condensates that are maintained by electrostatic interactions and that can be seen as physically cross-linked hydrogels. Being highly versatile, tunable and suitable for the efficient entrapment and stabilization of biomacromolecules, including proteins (**Figure 2.8**), complex coacervation has become a promising platform for the engineering of biocompatible and easily cell-internalizable nanocarriers.[59,102,103]

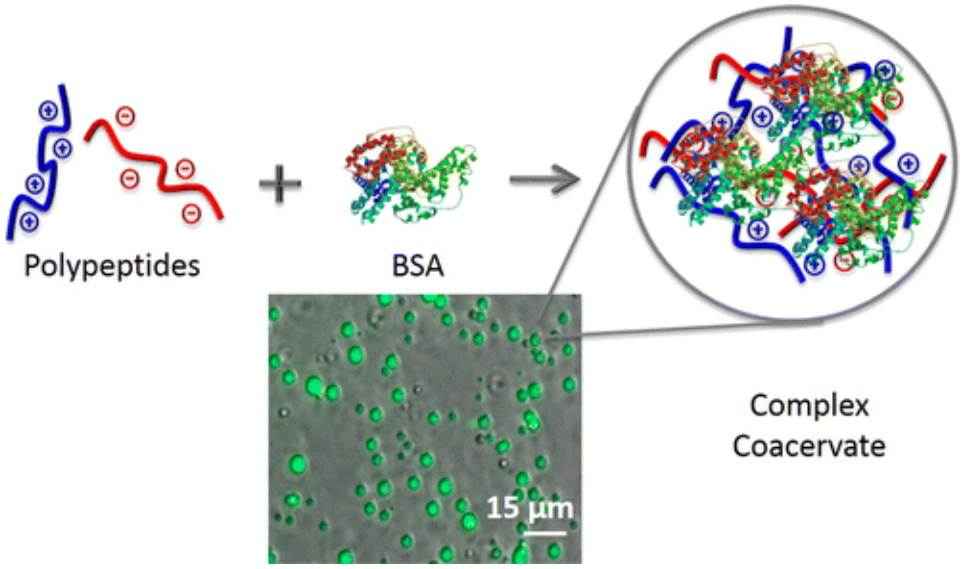

Figure 2.8. Encapsulation of a model protein (BSA) in complex coacervate microdroplets formed by liquid-liquid phase separation of an aqueous solution of oppositely charged polypeptides.[102]

To broaden the applicability of colloidal hydrogels, a progressive diversification in the choice of the monomer or polymer precursors has been proposed in the literature. The diversification of the monomer units has enabled the design of amphiphilic hydrogels to favor the incorporation of more hydrophobic drugs in matrices that are mostly hydrophilic.[104,105] The development of physically cross-linked hydrogels has included the use of biopolymers (such poly(amino acids) or polysaccharides) in the particle scaffolds to favor the accommodation of biomacromolecules (including proteins) and the biocompatibility of the carriers.[106–110]

The incorporation of proteins in colloidal gels can be achieved concomitantly with the formation of the polymer matrix by simply mixing the protein with the polymer precursors.[111] In that case, the encapsulation efficiency of the protein is markedly governed by the polymer properties (chain molecular weight or polymer concentration in solution).[112] This approach may expose the proteins to organic solvents and/or radical species that can be prejudicial for their stability. As an alternative, it has been proposed to dissociate the steps of gel formation and protein encapsulation, by loading the proteins of interest in pre-formed colloidal gels by impregnation (diffusion through the polymer matrix)[113] or by adsorption at their surface.[114] The efficiency of the impregnation process (in terms of yield and uniformity) depends on the chemical nature and the internal structure

of the gels, especially on the crosslink density which dictates the size of the voids in the polymer network.[114,115] The process of adsorption usually suffers from limited encapsulation yields and does not protect the protein of interest from the environment.

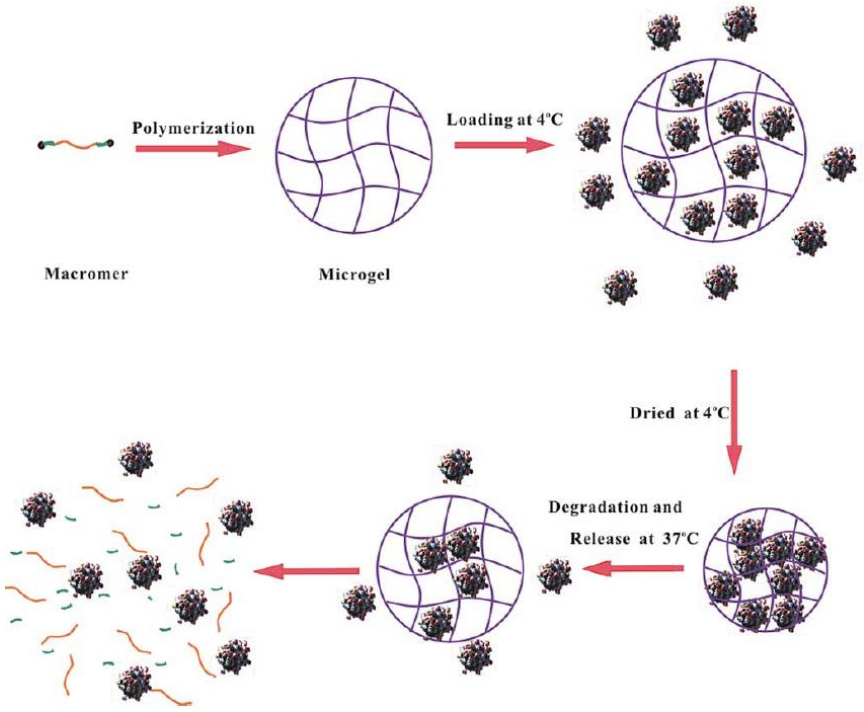

Figure 2.9. Schematic presentation of a post-fabrication encapsulation strategy of protein drugs in microgels. Microgels were obtained from cross-linking of the pre-designed macromers. After microgel preparation, drug loading was performed by soaking aqueous solution of proteins with microgels at 4 °C (below volume phase transition temperature). The gel microparticles collapsed after drying and thus entrapped proteins in the microgel network. When released in buffer at human body temperature, striking early release of protein was decreased because of the shrinkage of microgels at 37 °C with respect to at 4 °C. The drug release proceeded with hydrolysis of microgels and underlying diffusion. All of proteins were eventually released due to complete biodegradation of the polymeric network.[113]

In colloidal gels loaded with proteins, cross-talks between the protein and the polymer matrix may have a crucial influence on both the protein stability and the gel properties. Protein-polymer interactions, such as electrostatic attraction or hydrogen bonding, can be beneficial to increase the loading and retention of proteins,[115–117] to improve their thermal stability by hindering thermally-induced conformational changes, and even to enhance their bioactivity.[118] *A contrario*, the potential reactivity of the polymer network may also lead to protein deterioration. For instance, in polyester matrices – which are interesting for their biocompatibility and biodegradability – the hydrolysis of polymer ester groups into carboxylic acids induces a progressive acidification of the

microenvironment (to pH as low as 3),[119] that may eventually trigger the destabilization of encapsulated proteins. Note that if the polymer properties may influence the structure of the protein, reciprocally the presence of proteins may change the structural properties of the polymer matrix. In colloidal gels, a deswelling of the matrix is usually observed upon the loading of oppositely charged proteins, essentially due to protein-polymer electrostatic attraction that favor water expulsion from the matrix.[114,115]

2.2.3 Polymer microcapsules

Polymer microcapsules are hollow microspheres composed of an internal reservoir surrounded by a polymer envelope. They can be seen as "core-shell" systems with a core made of an organic or aqueous solution, and a shell made of polymer chains that can be chemically cross-linked or maintained by non-covalent interactions. In contrast to the precise structuration of the bilayer membrane in polymersomes, capsule shells are usually made of a more chaotic arrangement of polymer chains in intertwined mesh, network, or multiple layers. The shell thickness of polymer capsules is highly dependent on the preparation method but can range from a few tens of nm to several microns, and is usually much ticker than polymersome membrane which is restricted to 5-50 nm (as roughly given by twice the length of the polymeric building block). Polymer capsules thus associate (i) the reservoir structure of vesicles with (ii) shell physical properties that are close to hydrogels.

In absence of intrinsic amphiphilicity, polymer chains have no reason to spontaneously self-organize into hollow structures. The formation of polymer capsules thus requires a template to drive the assembly or the growth of polymer chains into shells with well-defined size and morphology. The main techniques that have been developed for that purpose use solid nanoparticles or emulsion droplets as spherical template for the design of liquid-core hollow capsules (see **Figure 2.10**).

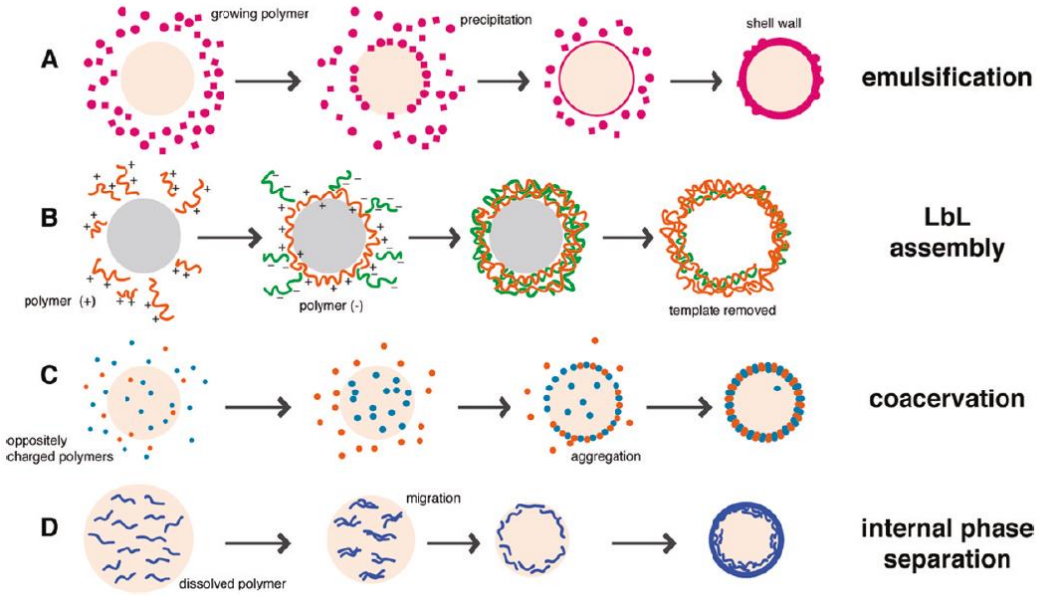

Figure 2.10. Various template-based strategies for the design of liquid-core hollow polymer capsules.[120]

Solid cores can be used as sacrificial templates for the successive deposition of oppositely charged polymers, resulting in a multi-stacked polymer shell self-maintained by electrostatic interactions after removal of the solid core. This technique, usually referred to as layer-by-layer (LbL) assembly, enables a good control on the composition and thickness of the shells but at the expense of numerous preparation steps.[121] Note that other types of interactions have also been used to drive the LbL assembly, such as hydrogen-bonding (**Figure 2.11**),[122] or host-guest supramolecular interactions,[123] but electrostatic interactions remain the most studied ones.

Despite numerous examples of bio-applications of LbL capsules,[124] this encapsulation technique is not necessarily appropriate for all payloads since (i) the encapsulation efficiency is intrinsically limited by the presence of the solid template all along the capsule formation and (ii) the removal of the solid template usually involves drastic chemical treatments (including strong acidic or alkaline conditions) that may be harmful for fragile biomacromolecules such as proteins.[125] To circumvent these issues, some examples of LbL assembly on liquid core templates have been proposed.[126,127]

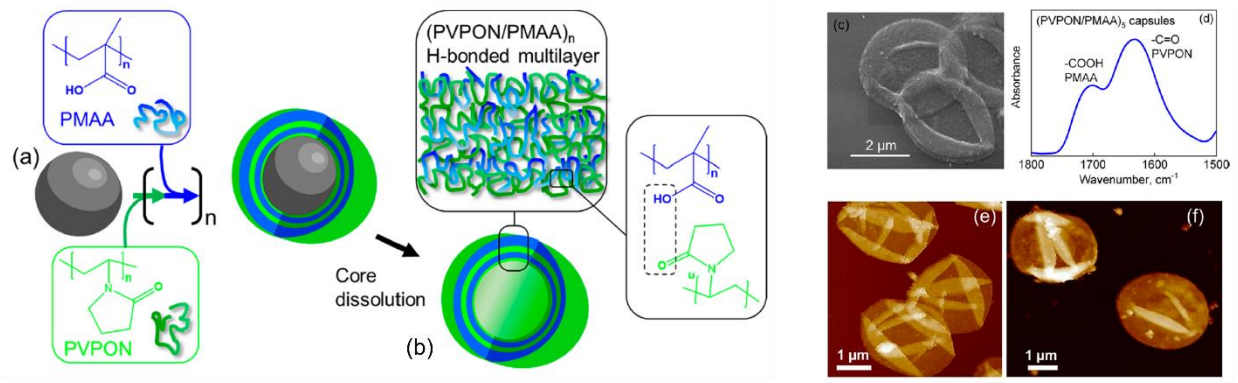

Figure 2.11. Schematics for the multilayer assembly of hydrogen-bonded (PVPON/PMAA) capsules. (a) Silica cores (a) were exposed alternately to PVPON and PMAA polymer solutions in methanol with two rinsing steps in methanol between the layers. (b) After a desired number of (PVPON/PMAA) bilayers (denoted as n) were assembled, silica cores were dissolved in hydrofluoric acid and dialyzed at pH 3, leaving behind hollow hydrogen-bonded (PVPON/PMAA)n capsules. The dashed rectangle highlights the functional groups interacting through hydrogen bonding. (c) SEM image and (d) infrared spectrum of $(PVPON/PMAA)_5$ capsules assembled in methanol. Atomic force microscopy topography images of (e) 5 bilayer and (f) 10 bilayer (PVPON/PMAA) capsules dried on silica wafer surfaces from methanol.[122]

Most of techniques of capsule formulation rely on emulsion droplets as the template for the formation or the self-assembly of polymer shells. It is the case for internal phase separation, which consists in progressively triggering the precipitation of polymer chains confined in emulsion droplets by changing its affinity with the droplet solvent. Initially the polymer is dissolved in a mixture of good and poor solvent, which is then emulsified in an immiscible continuous phase. The good solvent is progressively removed from the droplets by evaporation, leading to the phase separation of the polymer from the poor solvent remaining in the droplets. This process eventually results in polymer segregation at the droplet surface, forming liquid-core rigid capsules dispersed in the continuous phase. This approach has been used to produce aqueous-core poly(methyl methacrylate) capsules in oil (with acetone/water as good/poor polymer solvent).[128]

Internal phase separation can also be triggered in droplets containing only a good solvent for the polymer, the poor solvent coming from the continuous phase. This process was observed in an aqueous dispersion of chloroform droplets containing polyester chains and a surfactant.[129] The presence of the surfactant in the chloroform droplets triggers the self-emulsification of water (coming from the continuous phase) within the droplets. Water being a poor solvent for the

polymer chains, the growth of the water droplets in the chloroform droplet, concomitant with the evaporation of the chloroform, progressively leads to the formation of polyester shells (**Figure 2.12**).

In these approaches based on internal phase separation, the structural features of the polymer microcapsules (capsule size, shell thickness and porosity) can be tuned by varying the size of the templating emulsion droplets, the mass of the polymer initially dissolved in the dispersed phase and the evaporation rate of the good solvent. However, these approaches require the use of organic solvents in the dispersed phase, which is barely compatible with the presence of proteins.

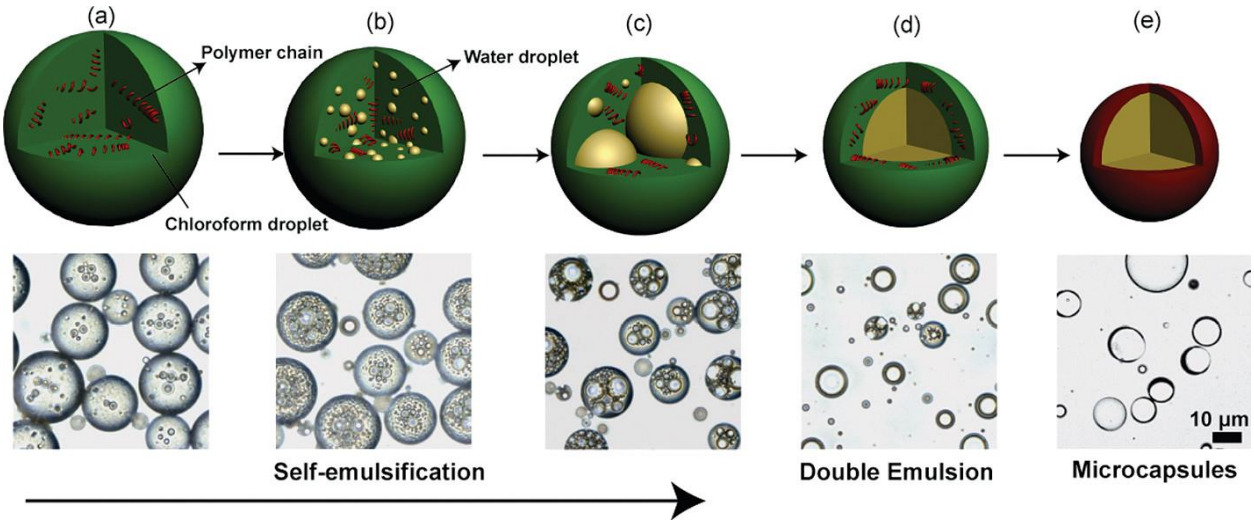

Figure 2.12. Illustration of microcapsules formation by internal phase separation induced. (a) Chloroform droplets containing polylactide chains and bis(2-ethylhexyl) sulfosuccinate surfactant were formed upon emulsification in an aqueous phase. Rapidly, water diffused in the chloroform droplets and formed aqueous inclusions upon internal self-emulsification. (b) Count and size of the internal water droplets increase with the increase of time; (c) Internal tiny droplets coalesce into bigger ones; (d) Double emulsion droplets were formed via coalescence of the internal water droplets; (e) Polylactide microcapsules were obtained after complete evaporation of chloroform.[129]

Another approach for emulsion-templated capsule formation consists in directly growing or cross-linking polymer chains *in situ*, i.e. at the surface of emulsion droplets. This general strategy is usually referred to as interfacial polymerization.[†]

Polyaddition reactions offer a broad choice of monomer or polymer building blocks for the design of capsules by interfacial polymerization. Polymer capsules can be achieved by coupling reactive species that are initially soluble in their own phase but that can meet and react at the water/oil interface after emulsification. Common click or metathesis reactions between difunctional complementary monomers or macromonomers have been used in that sense, such as azide-alkyne cycloaddition with or without Cu catalyst,[130,131] thiol-ene coupling,[132] or olefin cross-metathesis.[133]

Radical interfacial polymerization has also been proposed to build polymer shells *in situ*. In this approach, the main challenge was to confine the chain propagation at the interface while limiting its extension to the bulk phases of the emulsions. For that goal, the polymerization must be mediated by reactants that are surface active, i.e. that have a high affinity with the water/oil interface. Effective interfacial radical polyaddition have been demonstrated using amphiphilic or surface-active monomers,[134] radical initiators,[135] initial radical species,[136] or RAFT agents[137] (**Figure 2.13**). The interfacial sequestration of polymer can also be achieved if the growing chains have no affinity neither for water nor for oil, resulting in the formation of a polymer shell at the water/oil interface.[138]

Polycondensation reactions can also be used to form polymer capsules at the surface of emulsion droplets. These reactions usually involve addition-elimination reactions between water-soluble diamines or diols and oil-soluble diacyl chloride or diisocyanates, yielding polyester, polyamide, polyurea (and other derivatives) capsule shells.[139] This approach can be extended to the formation of cross-linked polymer shells by starting from (at least) tri-functional reactive species, such as lignin.[140] As for click polyaddition, these polycondensation reactions involve complementary but immiscible reactive species, naturally restricting the polymerization at the

[†] In this document, interfacial polymerization will only refer to reactions that produce *covalent bonds* between monomers or polymer chains at the interface between two immiscible media. Some authors may also include non-covalent cross-linking (e.g. via hydrophobic or host-guest supramolecular interactions) or metal-ligand coordination among the list of interfacial polymerization reactions.

water/oil interface. Note that this interfacial condensation strategy has also been implemented in sol-gel processes to readily form aqueous-core silica hollow nanocapsules.[141] Interfacial polymerization techniques usually lead to the formation of robust polymer shells despite their low thickness (typically below 100 nm because the diffusion of reactive species towards the interface is quickly hindered by the presence of the growing shell). However, since these strategies of capsule formation are based on *in situ* chemical reactions, they may be inappropriate for the encapsulation of fragile payloads, especially for proteins that may be degraded in presence of radicals, thiol groups, carboxylic acid derivatives or organic solvents that are commonly encountered in interfacial polymerization.

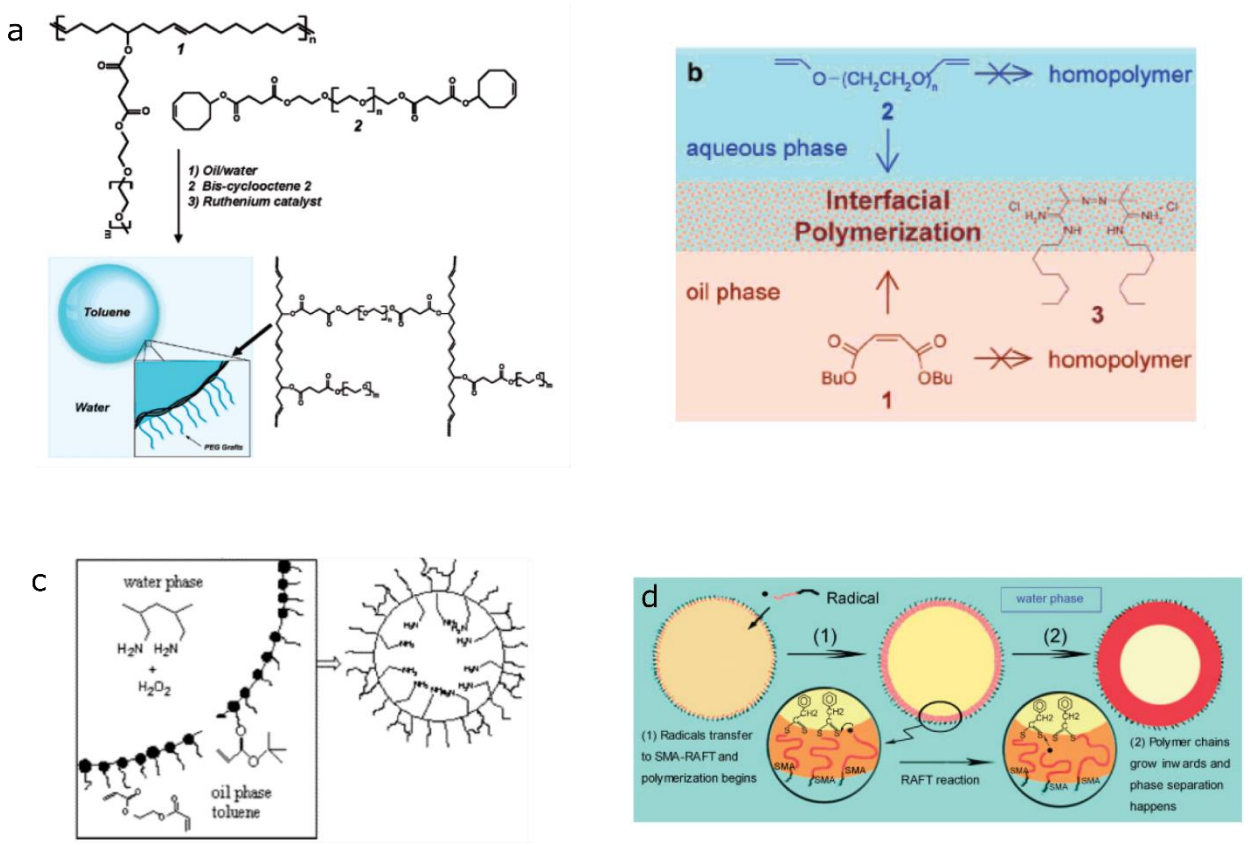

Figure 2.13. Interfacial polyaddition based on the confinement of reactive species at the water/oil interface of emulsion droplets. The reaction was confined thanks to the surface-active properties of a) monomers,[134] b) radical initiators,[135] c) initial radical species,[136] or d) RAFT agent.[137]

An alternative method to the interfacial polymerization may be to assemble pre-formed polymer chains at the surface of emulsion droplets to readily produce polymer shells without resorting to *in situ* chemical reactions. The formation of polymer capsules may be thus induced by non-covalent (weak) interactions between complementary interactive chains that are present on the two sides of the water/oil interface. This approach, termed interfacial self-assembly, includes multiple variants such as interfacial complexation, coordination, supramolecular polymerization, depending on the interactions which are involved in the shell structuration. The most studied ones are probably electrostatic interactions that are implicated in interfacial complexation: when two oppositely charged species are solubilized in each phase of an emulsion, they spontaneously accumulate at the surface of the emulsion droplets, driven by coulombic attraction across the liquid-liquid interface. The formation of aqueous-core polymer capsules by interfacial complexation has already been reported in water-in-oil (W/O) (**Figure 2.14**),[142,143] and in water-in-water (W/W) emulsions.[144–147]

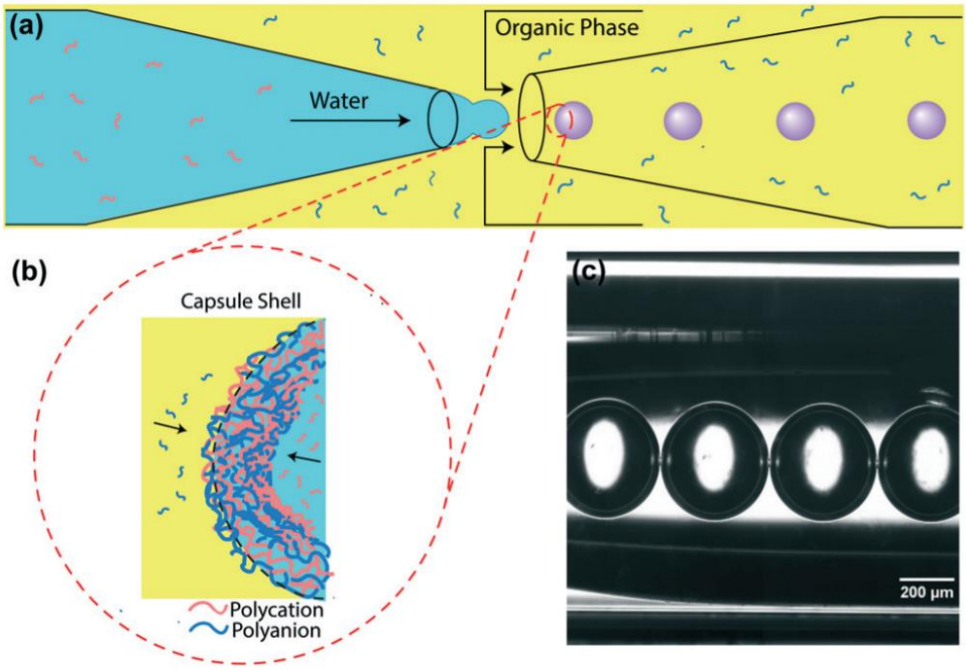

Figure 2.14. Schematic of the capsule fabrication method in a microfluidic device. (a) Aqueous phase (turquoise) containing a water soluble polyelectrolyte and an oil phase (yellow) containing oil soluble polyelectrolyte are brought into contact to fabricate aqueous-core microcapsules with a polymeric shell. (b) Electrostatic interaction of the polycation (red) and polyanion (blue) across the droplet interface generates a robust shell with thickness in the range of 1–2 µm. (c) Optical image of monodisperse stable capsules (diameter ~200 µm) in the exit flow capillary.[143]

W/W emulsions (also termed all-aqueous emulsions or aqueous two-phase systems) can be generated by spontaneous demixing of solutions of hydrophilic polymers that are incompatible above a critical concentration (typically occurring with poly(ethylene glycol) and dextran aqueous solutions).[148] The introduction of oppositely charged polymers in the two immiscible aqueous phases enables the production of aqueous-core polymer capsules by interfacial complexation in absence of organic solvents, which is major advantage for the design of biocompatible nanocarriers and which enabled the encapsulate of proteins and cells with success.[149,150] However, controlling the partitioning of water-soluble species between the inner and outer aqueous phases, and thus the encapsulation efficiency, remains a crucial challenge in all-aqueous systems.[150]

Beyond simple emulsions, polymer capsules have also been achieved by interfacial complexation in multiple emulsions such as W/O/W[151,152] or W/W/W.[149,153] For the first case, the formation of a polymer shell by complexation at the inner O/W interface can trigger the spontaneous dewetting of the oil intermediary layer, resulting in the production aqueous-core capsules dispersed in water.[151,152]

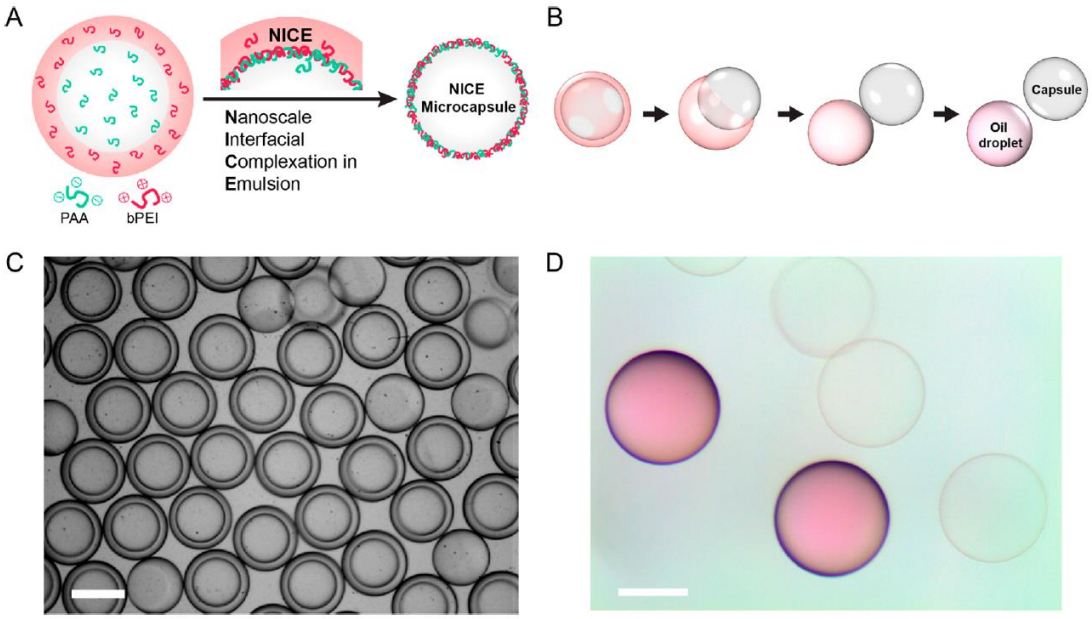

Figure 2.15. A) Schematic illustration for the formation of microcapsules by Nanoscale Interfacial Complexation in Emulsion (NICE) from a water-in-oil-in-water (W/O/W) double emulsion. B) Schematic illustration showing complete dewetting of a NICE microcapsule from an oil droplet. C) Optical microscopy image of W/O/W double emulsions generated using a glass capillary microfluidic device. D) Optical microscopy image of NICE microcapsules completely separated from oil droplets (pink). The oil droplets contain 0.1 wt % Nile red.[151]

The phenomenon of interfacial complexation has been extensively described through the formation of electrostatic interactions but other interactions have also been used to produce rigid microcapsules such as interfacial metal-ligand coordination[154] or interfacial hydrogen bonding[155]. The formation of multiple interpolymer hydrogen bonds have also been used to drive the generation of hollow polymer capsules from compact nanoparticles by spontaneous maturation at an appropriate pH.[156] This self-structuration phenomenon has the advantage to produce polymer capsules without the use of an external template.

2.3 Remote control of payload release from microcontainers

Any encapsulation system is subject to payload release via a "natural" mechanism of passive diffusion out of the container scaffold. The kinetics of this mechanism is intrinsically related to the size of the payload and to the internal structure of the container. For instance, considering polymer scaffolds of the same nature, the delivery of proteins is faster from hollow containers than from dense ones, because the thickness of the polymer matrix to cross is lower in the first systems than in the second.[157] In colloidal gels, the release rate is essentially governed by the swelling capacities of the polymer network, and can be lowered for example by increasing the cross-link density or by introducing more hydrophobic polymer moieties.[158] For any polymer-based encapsulation systems, the protein-polymer interactions play also in important role on the kinetics and efficiency of the release. Specific attractive interactions as well as non-specific adsorption of proteins in the polymer matrix may reduce the release fraction and lower the delivery kinetics.[159]

Delivery systems based on passive diffusion suffer from a poor spatio-temporal control of the release since the kinetics is "pre-recorded" in the structure of the encapsulation system and cannot be modulated *in situ*. The possibility to trigger and modulate the release *on demand* has been a hot topic in the field of molecular delivery for the last 20 years. Major progresses have been made thanks to the design of stimuli-responsive nanocontainers, i.e. structures that can be modified or destabilized upon specific chemical or physical stimulation. The on demand release can proceed via two types of response of the encapsulation system upon stimulation: either *via* a change in

porosity/permeability of the scaffold (leading to the enhancement of the diffusion kinetics) or via a partial or total disruption/disassembly of the scaffold.

2.3.1 Internal and external stimuli

Two categories of stimuli have guided the design of responsive nanocontainers: internal stimuli which are intrinsically present in the delivery area, leading to environmentally-controlled release, and external stimuli which are triggered by an operator out of the delivery area, leading to remotely-controlled release.[10]

Common internal stimuli for *in vivo* applications are the temperature of the living organism (usually higher than the ambient temperature) and the chemical environment (acidic pH, redox conditions, presence of reactive biomolecules such as sugars or enzymes). External stimuli include light irradiation, magnetic field, and ultrasounds. These stimuli are said "non-invasive" as long as they can be effective remotely, i.e. without physical intrusion of the stimulation source in the biological target. For that, the penetration length scale of these stimuli should be high enough. High magnetic fields or light with a wavelength which is not absorbed by the tissue are thus required.

The challenge for chemists and material scientists has been to design nanocontainers that can be sensitive to these stimuli, and to be able to tune the rate and the efficiency of the release. In the following, the discussion will focus on temperature and light as they turned out to be promising levers for on-demand delivery.

2.3.2 Temperature as an internal trigger

The internal temperature of the biological target can be used as a trigger for the destabilization of encapsulation systems. Temperature-sensitive containers rely on changes in physical properties of their scaffold upon heating to trigger the release of their payloads. For that thermo-responsive polymers are ideal tools are as they are characterized by a drastic change of their physico-chemical properties in solution, concomitant with a transition of the chain conformation, at a critical

temperature.[11] This critical temperature can be a Lower Critical Solution Temperature (LCST), associated to a transition of the polymer chains from hydrophilic soluble coils below the LCST to hydrophobic collapsed globules above the LCST. This transition is due to an entropically-driven desolvation of the polymer chains upon heating resulting in their association via hydrophobic interactions (**Figure 2.16**.a). At the macroscale, this transition manifests through the formation of polymer aggregates that precipitate in the solvent upon heating. Polymers exhibiting this type of behavior are called "LCST polymers" by misuse of language.[160]

Conversely, the critical temperature can be an Upper Critical Solution Temperature (UCST) associated to the reverse transition: polymer chains are insoluble below the UCST and soluble above the UCST, and the precipitation of the polymer occurs upon cooling. Polymers exhibiting this type of behavior are called "UCST polymers". Below the UCST, the insolubility of the polymer is due to multiple inter-chains weak interactions (mostly electrostatic interactions and hydrogen bonds) that maintain the polymer chains in an aggregative state. Upon heating, this network of interactions is progressively broken, resulting in the solubilization of the polymer chains.[161]

The critical temperature of transition depends on the concentration of the thermo-responsive polymer in solution. The curve giving the evolution of the critical temperature as a function of the polymer concentration is called the binodal curve. This curve separates the experimental domain where the polymer is soluble from the domain where it phase-separates from the solvent. To be rigorous, the notions of LCST and UCST correspond to the extrema of the binodal curve (the minimum for the LCST and the maximum for the UCST) and is thus valid for one polymer concentration (**Figure 2.16**.b). The generalization of this notion of critical temperature at any polymer concentration is called the "cloud point" since it separates the temperature domain where the polymer is soluble in the solvent (transparent solution) from the temperature domain where the polymer precipitates in the solvent (turbid solution) (**Figure 2.16**.c).

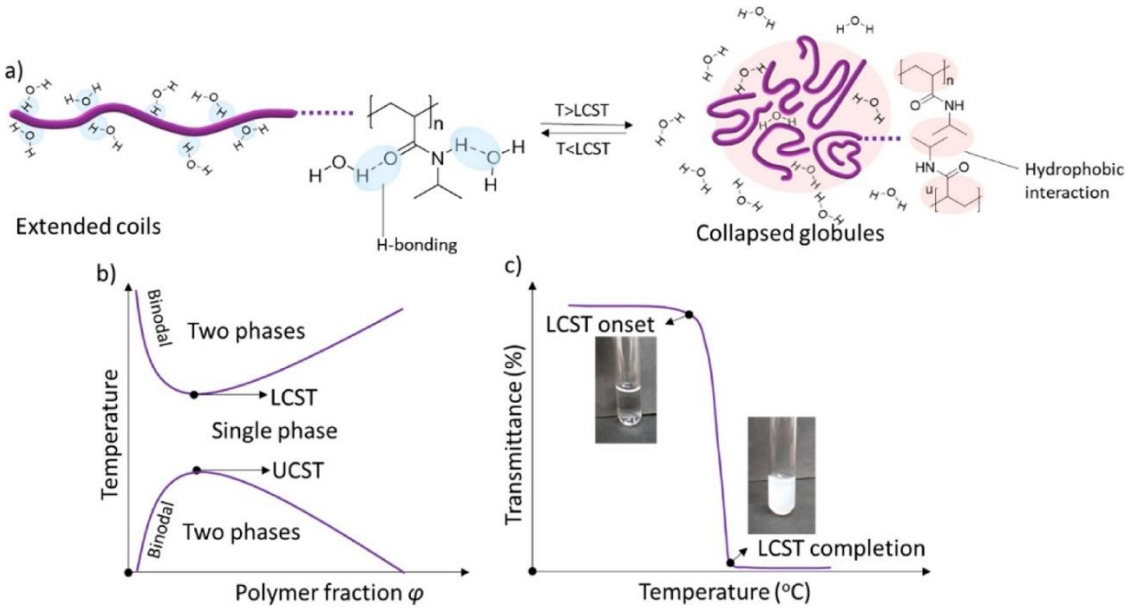

Figure 2.16. Illustration of a LCST behavior in the case of poly(N-isopropylacrylamide) (PNIPAM) a) Coil-to-globule transition of PNIPAM, corresponding to a switch from a hydrophilic state with solvated chains below the LCST to a hydrophobic state dominated by inter-chains interactions above the LCST. b) Binodal diagrams for UCST and LCST polymers depending on polymer fraction. c) Typical turbidity heating curve of a PNIPAM solution. The solution is transparent (maximum transmittance) below the cloud point and turbid (zero transmittance) above the cloud point.[160]

In aqueous environment, LCST polymers have been studied since decades. The most popular one has been undoubtedly the poly(N-isopropylacrylamide) (PNIPAM),[162] but increasing attention has been recently paid to other families of LCST polymers such as oligo(ethylene glycol)s,[163] poly(oxazoline)s[164] or poly(N-vinylcaprolactam)s.[165] Their implementation in delivery systems essentially relies on the deswelling or rigidification of materials at 37 °C (above the cloud point) resulting from the hydrophilic-to-hydrophobic transition of the polymer. Typically, a "squishing" release mechanism was observed during deswelling of PNIPAM microgels upon heating.[166] This thermal behavior usually leads to passive, slow an incomplete release.

For reservoir-like systems, a heat-induced on-demand delivery via LCST polymers added in the membrane/shell seems counterintuitive since the increase of temperature makes the chains more hydrophobic, i.e. less permeable to hydrophilic payloads. Accordingly, polymersomes or polymer capsules based on LCST polymers usually exhibit a delivery upon cooling rather than upon heating.[167,168] However, some aqueous-core systems have been successfully designed for a release at high temperature, such as polymersomes destabilized by heat-induced collapse of LCST

polymer chains[169,170] or polymer capsules including PNIPAM colloidal hydrogels as thermo-responsive gates in their shells (**Figure 2.17**.).[171]

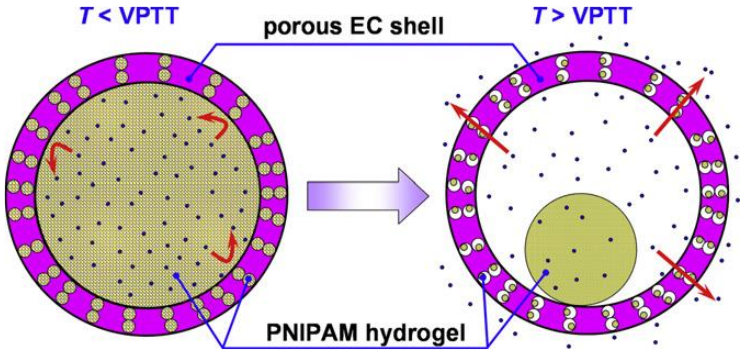

Figure 2.17. Thermo-responsive polymer capsules made of a PNIPAM hydrogel core and a porous ethylcellulose (EC) core embedded with PNIPAM microgels. The collapse of the PNIPAM microgels above a critical transition (called Volume Phase Transition Temperature or VPTT here) acts as gate opening in the polymer shell and triggers the release of content encapsulated in the capsule core.[171]

In contrast, UCST polymers are obviously more suitable for heat-triggered permeabilization, because they form insoluble materials at low temperature (below UCST), that can be dissolved upon remote heating. Yet, only a handful of UCST-based delivery systems has been proposed. Although UCST is most likely observed in non-aqueous and hydro-organic solvents, polymers with UCST behavior in pure water are not rare.[172,173] Several ones exhibit a thermal transition in temperature windows relevant for most practical application (typically 10-50°C) and/or in physiological conditions.[174,175] Their main drawback to date has been their sensitivity to environmental and structural features: the transition temperature depends on the polymer structure (composition, chain length, end-groups) and on minor chemical degradation or changes in the environment (e.g. effect of pH, presence of salts).[176] For instance, acidic or salt impurities may shift the working temperature by > 10°C.[172] In this line, the UCST of poly(N-acryloyl glycinamide), one of the earliest non-ionic copolymers with chemically adjustable properties, can be dramatically shifted upon monomer degradation (e.g. via hydrolysis) or in presence of poorly controlled chain ends.[177] In addition, the UCST transition shows a high hysteresis upon heating/cooling cycles. Polyzwitterionic chains are more robust alternatives, and the permanent hydration of ionic comonomers makes them particularly convenient for the design of hydrophilic materials, such as temperature-responsive colloidal hydrogels,[178,179] but the high density of ionic

groups may be prejudicial for the stability of encapsulated proteins. One class of non-ionic copolymers, the poly(acrylamide-co-acrylonitrile) (PAAMAN), combines the desirable properties of (i) becoming hydrophobic at low temperature, (ii) having a tunable UCST via simple balance of monomer composition, and (iii) exhibiting a robust UCST transition in water (minimal hysteresis and minimal shift upon temperature cycling).[180] However, the UCST of PAAMAN remains sensitive to the presence of additives such as salts or drug loading.[181,182]

To date, most of the microcontainers exhibiting a UCST behavior have been prepared under the form of colloidal gels,[173,179,183,184] and only a few examples of aqueous-core systems, essentially polymersomes, have been reported.[174,185,186] To the best of our knowledge, aqueous-core polymer capsules with UCST behavior has never been reported.

2.3.3 Light as an external trigger

Using light as an external trigger is interesting since it allows a precise spatial and temporal control of the stimulation. Indeed, the irradiation is instantaneous (contrary to the temperature triggers that may suffer from heating inertia) and the spatial resolution is essentially dictated by the size of the light source spot (that can reach the microscale for focalized laser beam). For biological applications, the high tunability offered by light excitation (in terms of wavelength and power) can be limited by two factors: the high absorption of biological tissues in the visible range and the potential phototoxicity of energetic irradiation such as UV light. These issues usually restrain the use of light-induced delivery to the study of transparent or poorly absorbent model organism (such as zebrafish larva) or to the design of near-infrared-sensitive systems (as the near infrared region is a transparent window for biological tissues).

Intrinsically light-controllable release systems are essentially based on two families of light-sensitive molecular building blocks: photo-isomerizable groups and photo-cleavable groups.[187]

Photo-isomerizable groups can undergo a reversible conformational change upon light irradiation, inducing a drastic switch of shape and polarity. The most common photo-isomerizable groups are derivatives of azobenzene that are characterized by a cis-trans isomerization, or of spiropyran, dithienylethene, or donor-acceptor Stenhouse adducts (DASA) that are characterized

by an open-closed isomerization. The incorporation of photo-isomerizable groups in the structure of polymeric building blocks may enable to form light-responsive structures that can undergo drastic changes in structural organization and/or polarity/hydrophilicity upon light irradiation, providing a simple way to control the release of pre-encapsulated content.

The permeability of polymer capsules or colloidal gels can be photo-regulated by using azobenzene groups as supramolecular or physical cross-links that can be disrupted when azobenzene are in their cis form (**Figure 2.18**).[188,189] The modulation of permeability has also been demonstrated in polymersomes bearing spiropyran or DASA groups (the permeability being higher when these groups are in their hydrophilic open form).[190,191] The release of pre-encapsulated content can also be triggered by more drastic phenomena such as the partial or total destabilization of self-assembled polymeric compartments as it was demonstrated for polymersomes containing azobenzene groups (dramatic change in the membrane curvature upon isomerization)[192,193].

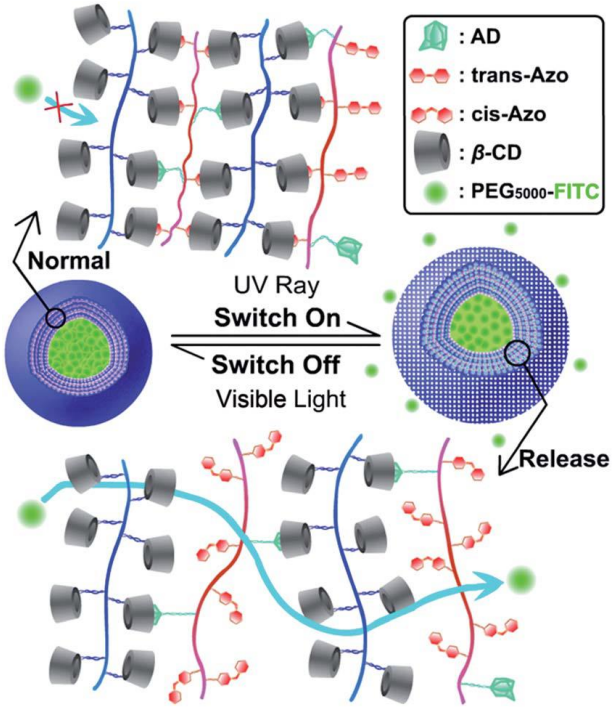

Figure 2.18. Light-responsive microcapsules made by layer-by-layer supramolecular assembly of poly(acrylic acid-g-azobenzene-g-adamantane) (PAA-g-AD-g-Azo) and poly(aspartic acid-g-β-cyclodextrin) (PASP-g-β-CD). Upon UV irradiation, the *trans*-to-*cis* isomerization of azobenzene moieties triggers the dissociation of the host-guest cross-links formed with β-CD, leading to an increase of the permeability of the capsule shell and the release of the pre-encapsulated content (here fluorescent PEG).[189]

Photo-cleavable groups can undergo irreversible splitting in (at least) two residues upon light irradiation. The most common photo-cleavable groups are *o*-nitrobenzyl esters, polyaromatic hydrocarbon methyl esters (pyrene, perylene, …) or *p*-methoxyphenacyl esters.[187] Introducing photo-cleavable groups in encapsulation/release polymeric systems allows the partial or total degradation of the structure of the container, resulting in the release of the pre-encapsulated content.

Polymer chains containing *o*-nitrobenzyl ester units along their backbone thus been used to form polymer micelles[194], polymersomes[195] or polymer microspheres[196] that can be rapidly dismantled upon light irradiation. Photo-cleavable cross-links based on *o*-nitrobenzyl ester units have also been used in colloidal gels[111] or polymer capsules,[197] enabling the light-induced release of pre-encapsulated payloads including proteins. Photo-cleavable groups can also be used as "capping" agents that can be removed on-demand to change the properties of polymer chains, such as the hydrophilicity, or to trigger chain reactions. For instance, Sun et al. showed that the photo-cleavage of *o*-nitrobenzyl ester groups in polymersome membranes could trigger the hydrophobic-to-hydrophilic transition of the bilayer concomitantly to *in situ* cross-linking that prevented any denaturation. This photo-activation eventually resulted in an increase of the membrane permeability and a subsequent release of the pre-encapsulated payload.[198]

Photo-cleavable groups have also been used as triggers for the depolymerization of "self-immolative" polymers. These polymers are designed to be crumbled by a succession of intramolecular reactions, provided an initial fragmentation trigger. Photo-cleavable units have been introduced for this purpose, as side-groups or end-groups on the polymer backbone, to promote the self-immolative degradation of polymer microspheres[199] or polymersomes[200] upon light irradiation (**Figure 2.19**).

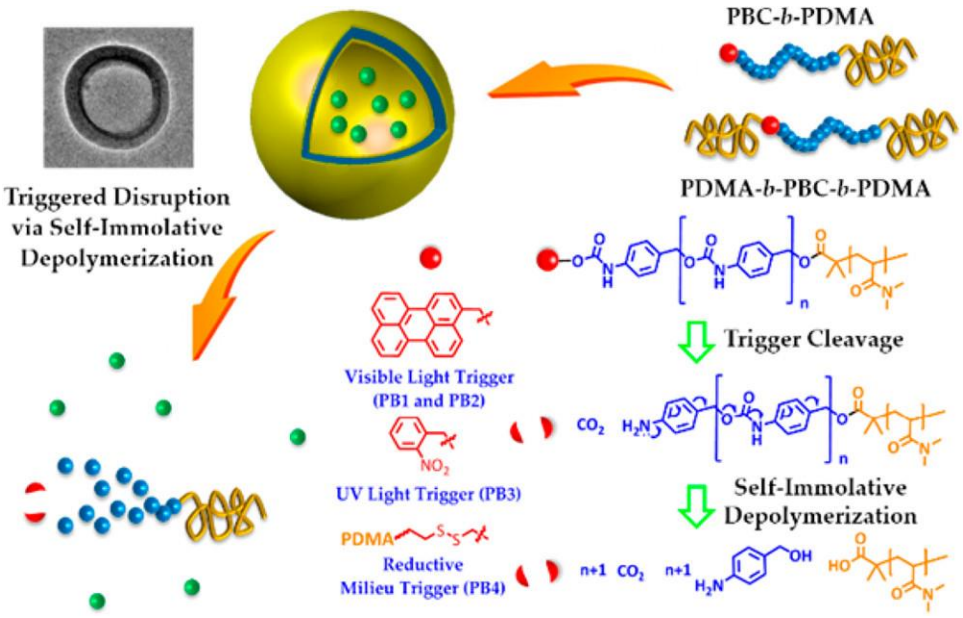

Figure 2.20. Schematic illustration of self-immolative polymersomes self-assembled from poly(benzyl carbamate)-b-poly(N,N-dimethylacrylamide) amphiphilic block copolymers containing hydrophobic poly(benzyl carbamate) blocks, which are subjected to self-immolative depolymerization into small molecules upon cleavage of "capping" moieties (i.e., perylen-3-yl, 2-nitrobenzyl or disulfide for stimuli of visible light, UV light, and reductive milieu, respectively).[200]

Photo-cleavable groups have also been used in a diverted way to induce the burst of liquid-core polymer compartments. Instead of being incorporated in the polymer scaffold, photo-cleavable molecules can be directly loaded or dispersed in the lumen upon encapsulation. The photo-degradation of these molecules may produce a high concentration of side-products that may increase the osmotic pressure in the core of the compartment. At some point, the stress exerted by this internal pressure on the polymer envelope may lead to its burst. This approach has been successfully implemented on polymersomes[201] and polymer capsules.[202] In the latter case, the photo-cleavable molecules were designed to release CO_2 upon fragmentation. The pressure-induced rupture of the polymer shell wall was thus attributed to the rapid expansion of gas bubbles in the core of the capsules.

2.3.4 Combining photo- and thermo-sensitivity with plasmonic nanoparticles

The design of polymers that are intrinsically light-responsive can be complicated as it may require complex synthesis and complete isolation from parasitic light to avoid sample degradation. In comparison, thermo-responsive polymers are easier to manipulate and can even be commercially available. Being able to stimulate a thermo-responsive scaffold with light as a primary trigger may enable to combine the high spatio-temporal control offered by light with the versatility offered by thermo-responsive polymers. For that purpose, plasmonic nanoparticles are interesting candidates as they can convert light excitation in heat generation.

At the nanoscale, noble metal particles (essentially silver and gold) exhibit a very specific resonance phenomenon called localized surface plasmon resonance. Upon light excitation at an appropriate wavelength, collective electron oscillations are produced at the surface of the nanoparticles. The damping of these oscillations by Joule effect generates heat in the vicinity of the nanoparticles with a typical time scale of 10 ns,[203] i.e. quasi instantaneously. Noble metal nanoparticles can thus be seen as efficient light-to-heat converters at the nano- and microscales and have paved the way for the development of a new field called "thermoplasmonics".[204]

Gold nanoparticles (AuNPs) are particularly interesting plasmonic structures since their plasmon resonance occurs in the visible range. More interestingly, the spectral location of this resonance can be tuned by changing the size and morphology of the particles.[205] For instance, the excitation wavelength for gold nanospheres is typically around 530 nm (in the green), whereas it is red-shifted towards near infrared for gold nanorods (the shifting amplitude being roughly proportional to the aspect ratio of the nanoparticles).[206] Gold nanorods are thus good candidates for biological applications of thermoplasmonics since the near infrared region is a "transparent" window for biological tissues (compared to the rest of the visible range).[207]

For the last 15 years, many efforts have been made to design photo-responsive encapsulation systems based on thermoplasmonic properties. A first strategy has been focused on the photothermal destabilization of microcompartments doped with AuNPs. Upon thermoplasmonic

excitation, sufficiently high temperatures can be reached to trigger the rupture (or at least the poration) of the compartment membrane/shell as it has been demonstrated in liposomes[208], polymersomes,[209] or multi-layer polymer capsules.[210,211] Another approach has been based on the change of permeability of the container induced by gold nano-heaters. For instance, the rise of temperature induced by irradiated AuNPs has been used to trigger glassy-to-rubbery transition in polyester microcapsules,[212] therefore leading to a higher diffusion of the payload across the capsule shell.

AuNPs have also been coupled with intrinsically thermo-responsive polymers in hybrid compartments. The first systems were based on LCST polymers, essentially on PNIPAM. Amstad et al. have designed a polymersome containing PNIPAM-based copolymers and AuNPs embedded in the membrane.[170] Upon light irradiation, the heat generated by AuNPs triggers the hydrophilic-to-hydrophobic thermal transition of PNIPAM blocks, resulting in destabilization and eventually rupture of the vesicle within a few minutes (**Figure 2.21**). Hybrid PNIPAM-AuNPs colloidal gels have also been designed, either by incorporation of AuNPs in preformed gels[213] or by formation of the polymer network around AuNPs used as a template.[214] In both cases, light irradiation was able to trigger the thermal collapse of the PNIPAM matrix and the subsequent release of molecules that were entrapped in the gel network (via a "sponge squishing" mechanism). PNIPAM-AuNPs hybrid nanogels were also used as photo-responsive gates in amorphous shells to modulate the permeability of polymer capsules upon light irradiation.[215] In contrast, only a few examples of light-responsive nano-carriers combining UCST polymers and AuNPs have been proposed. Two examples of hybrid nano-assemblies have been published quite recently.[216,217] In these systems, the delivery of pre-encapsulated content upon light irradiation was associated to the solubilization of the UCST polymer upon AuNPs heat generation.

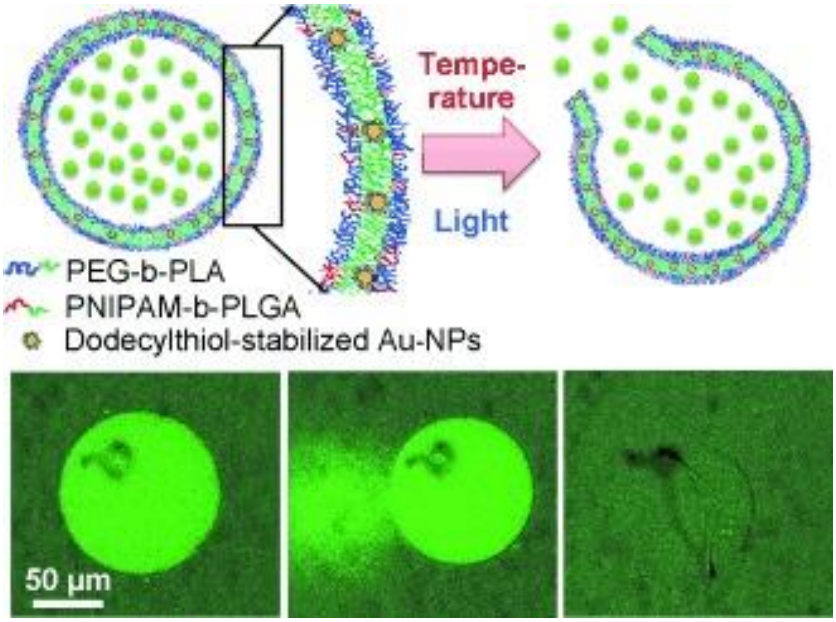

Figure 2.21. Photo-responsive polymersomes based on thermo-plasmonic effects of gold nanoparticles (AuNPs). The membrane of the polymersomes is composed of a bilayer of PEG-b-PLA and PNIPAM-b-PLGA diblock copolymers, embedded with dodecylthiol-stabilized AuNPs. Upon light irradiation, AuNPs generate heat that trigger the thermal transition of PNIPAM blocks from hydrophilic to hydrophobic, leading to the destabilization of the polymersome membrane and the release of the pre-encapsulated content.[170]

2.3.5 The issue of release in the second or sub-second range

For some specific applications, the release of a high dose of bioactive molecules can be required to circumvent dilution effects that may occur upon delivery. It may be the case for the local activation of cell receptors or the local stimulation of neuron networks. For such applications, being able to deliver high amounts of molecules in a few ms can be advantageous to actuate biological targets with a high spatial resolution. Unfortunately, only a few systems have been designed to undergo on-demand *burst* release of their contents. This is essentially due to the fact that sudden structural changes in soft nano-containers are usually hindered by long relaxation times and/or multiple local reorganizations of the system.

Note that the term of "burst release" should be used cautiously since, in the jargon of drug delivery, the "burst release effect" corresponds to a sudden and early release of a fraction of the

payload immediately after the introduction of the carriers *in vivo*, and by extension in any biological conditions.[218] This "burst release effect" is not controlled and occurs accidentally at relatively short time scales and, most of the time, far from the biological targets. In addition, it leads to a loss of the payload and a shortening of the controlled release period. That is why many efforts have been made to reduce this undesired effect, mostly by tuning the structure and permeability of the encapsulating scaffold. In the following the notion of burst release will only refer to the *on demand* sudden release of pre-encapsulated content, i.e. voluntarily triggered upon precise stimulation

Most of the effective burst-release systems have been based on the increase of the internal pressure of hollow containers until sudden rupture of their rigid membrane/shell. This mechanical effect can be mediated by the formation of gas bubbles in liquid cores, either by ultrasound-induced evaporation of a volatile solvent (such as perfluoroalkanes),[219] or by light-induced production of CO_2 from photo-degradable molecules.[202] Another approach consists in increasing the internal osmotic pressure by generating high concentrations of solutes in the core, as previously mentioned in section 2.3.3. For instance photo-degradable molecules have been loaded in the core of liposomes[220] or polymersomes[201] to induce the rupture of the membrane upon light irradiation in less than 1 s (**Figure 2.22**). As an alternative to photo-stimulation, Zhang et al. showed that asymmetric polymer capsules can undergo rapid shell fracturing when placed in hypotonic conditions, as a consequence of water infiltration through the thinnest part of the shell wall.[221]

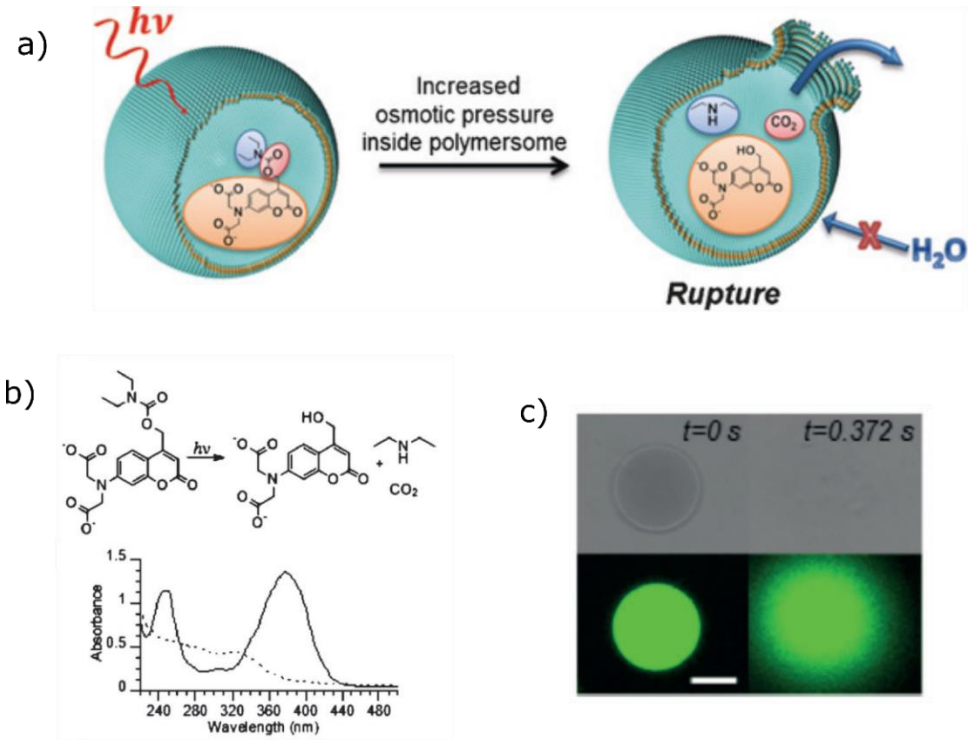

Figure 2.22. a) Light-induced rupture of polymersome membrane by sudden increase of internal osmotic pressure triggered by photo-degradation of encapsulation light-sensitive molecules. b) Photocleavage of coumarin derivative under irradiation and corresponding absorption spectrum in aqueous solution before (solid line) and after (dashed line) 30 min of irradiation at 365 nm. c) Confocal observation of a coumarin-loaded GUV (green channel, emission range of coumarin, 485 nm). The vesicle undergoes fast (few milliseconds) rupture upon 50-mW irradiation at 405 nm (scale bar = 10 mm).[201]

On-demand burst release can also be induced by an intrinsic perturbation of the polymer structure of the container upon external stimulus. Mabrouk and al. showed that polymersomes containing azobenzene-based liquid crystal moieties can experience a burst curling of the membrane in less than 1 s upon light irradiation.[193] This process is induced by a dramatic change in the membrane curvature induced by the photo-isomerization of the azobenzene moieties. Hybrid polymersomes combining AuNPs and thermoresponsive polymers such as PNIPAM can also undergo rapid disassembly upon plasmonic resonance of AuNPs.[170]

The previous examples highlight the fact that light is an optimal trigger for controlled burst release since the stimulation is instantaneous. The efficiency of the bursting is then only dictated by the responsiveness of the chemical components of the nanocontainer. In this context, vesicles turned

out to be the most efficient systems since a small mechanical perturbation of the membrane can lead to a dramatic disruption of the entire structure in short time scales, typically below 1 s. Alternative systems relying on temperature or pH triggering have also been proposed for rapid release but were less efficient in term of temporal response than light-sensitive systems.[222,223]

To the best of our knowledge, this issue of controlled burst release has not been extensively explored for protein delivery. However, the sudden release of high amounts of proteins may be interesting in many biological applications. For instance, the delivery of neuropeptides at specific neuronal interfaces with a high spatio-temporal control may be helpful to decipher certain neuronal pathways. This issue of controlled burst release of proteins combines two challenges that have been mentioned throughout this chapter: the encapsulation of proteins without altering their stability, and their on demand release in the sub-second range.

2.4 Objective of the PhD work

The objective of this PhD work was to develop a chemical platform to design stimuli-responsive and functional polymer capsules suitable for the versatile encapsulation and on demand (including burst) release of proteins or other fragile biomacromolecules. Regarding the state of the art presented in this work, we could imagine a promising formulation approach.

To limit potentially undesired interactions between the proteins and the container scaffold, reservoir-like structures with an aqueous core should be favored. Along this line, we decided to focus on aqueous-core polymer capsules. The use of chemical reactions should be limited during the formation of the capsule shell to avoid potential degradation of the payloads. For that purpose, the self-assembly of preformed polymer chains is an interesting approach and we decided to explore the strategy of interfacial complexation. The diversity of the polymer chains that can be used in interfacial complexation is also an advantage towards the design of functional, especially stimuli-responsive, capsules.

The formulation of aqueous-core polymer capsules by interfacial complexation requires emulsion droplets as a template. As previously mentioned, the presence of organic solvents in water-in-oil emulsions can induce interfacial aggregation of the proteins that can impair their

biological activity. The use of water-in-water emulsions is interesting but may suffer from encapsulation yield limitations due to partitioning issues between the two aqueous phases. As an alternative, the use of perfluorinated oils (PFO) as the continuous phase of water-in-oil emulsions is a promising approach for several reasons: first, as aqueous and hydrocarbon species show an extremely poor solubility in PFO,[224] the issue of phase partitioning as well as molecular cross-talks between droplets are limited in water-in-PCO emulsions,[225,226] suggesting that high yields of encapsulation may be achieved in the aqueous core of the capsules. Second, PFO are more biocompatible than their hydrocarbon analogs.[227,228] Fluorinated solvents have even been considered as promising candidates for the design of artificial blood substitutes, thanks to their high capacity to solubilize oxygen.[229] Issues of protein aggregation at water/PFO interfaces have been addressed and partially solved with the utilization of suitable fluorinated surfactants.[230–232] Finally, PFO are compatible with the microfluidic technologies, especially with poly(dimethyl siloxane) (PDMS) devices as they do not induce PDMS swelling contrary to common hydrocarbon oils. The phenomenon of interfacial complexation in water-in-PFO has not been extensively studied for the design of polymer capsules and we proposed to explore this strategy in the following chapters.

Chapter 3

Formation of stimuli-responsive polymer shells by interfacial complexation: the case of poly(N-isopropylacrylamide) shells

Note: This chapter contains results that have been published in the following peer-reviewed article:

L. Sixdenier, C. Tribet, E. Marie. Emulsion-Templated Poly(N-Isopropylacrylamide) Shells Formed by Thermo-Enhanced Interfacial Complexation. *Adv. Funct. Mater.* **2021**, 2105490. https://doi.org/10.1002/adfm.202105490

To clarify the research approach and to make the results more comprehensive for a PhD manuscript, the content of this article has been reorganized and enriched with complementary and non-published results.

3.1 Introduction

According to the specifications set at the end of Chapter 2, we will describe in this Chapter the experimental approach that we developed to design stimuli-responsive polymer microcapsules by interfacial complexation in water-in-perfluorocarbon oil (PFO) emulsions.

Interfacial complexation in water-in-PFO has not been extensively explored but has been well characterized in a representative system by DeJournette et al.[233] They evidenced the formation of a complex layer by polymer-surfactant interfacial complexation at the edge of water droplets between a water-soluble diamine (Jeffamine) and a PFO-soluble macrosurfactant (a carboxylate-terminated perfluoro-PEG called Krytox) (**Figure 3.1**). The tight interactions between Jeffamine and Krytox were evidenced at the molecular level (using FT-IR spectroscopy, mass spectrometry and NMR) and *in operando* at the water/oil interface in inverse emulsion (using fluorescence microscopy). These interfacial interactions are likely due to a combination of electrostatic and hydrogen bonding between amino groups of the polyamine and carboxylic groups of Krytox, as previously described by O'Neal and al. on analogous systems.[234,235]

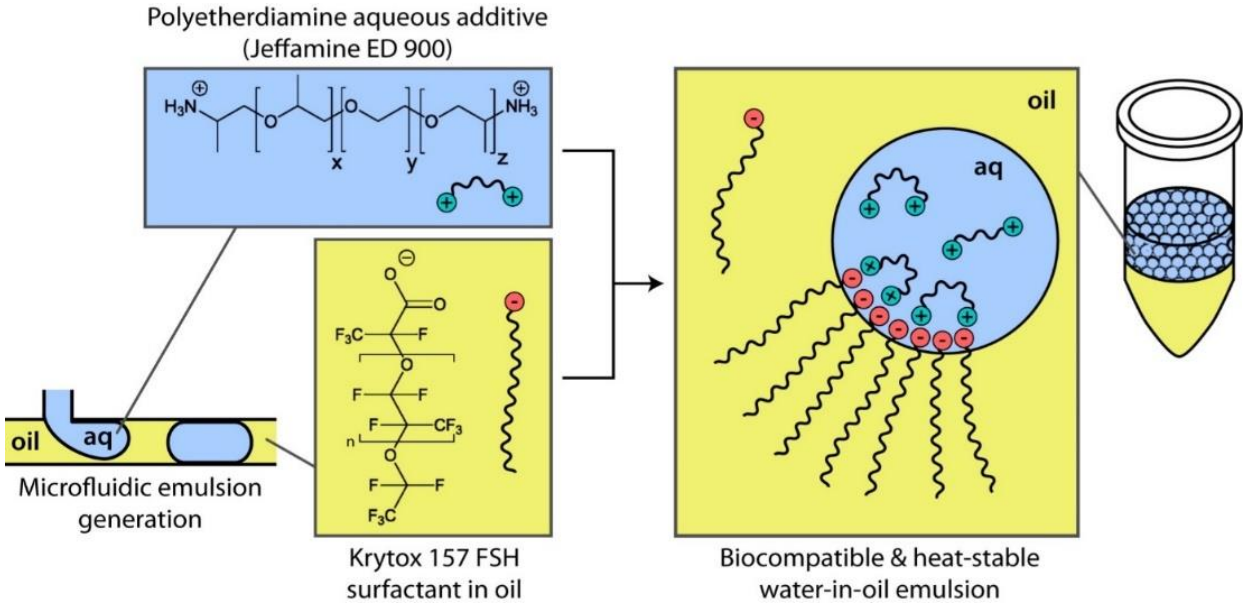

Figure 3.1. Interfacial complexation in water-in-perfluorocarbon oil emulsion between a cationic diamine (Jeffamine ED 900) present in water droplets an anionic surfactant (Krytox 157 FSH) present in the continuous oil phase.[233]

More recently, Abell and co-workers used a similar polymer-surfactant interfacial complexation between a cationic polymer and Krytox to favor the formation of supramolecular microcapsules. They showed that interfacial complexation enables to increase the concentration of the polycation at the water/PFO interface and subsequently to favor supramolecular cross-linking of adjacent chains by cucurbituril units to form thin hydrogel shells (**Figure 3.2**).[236,237]

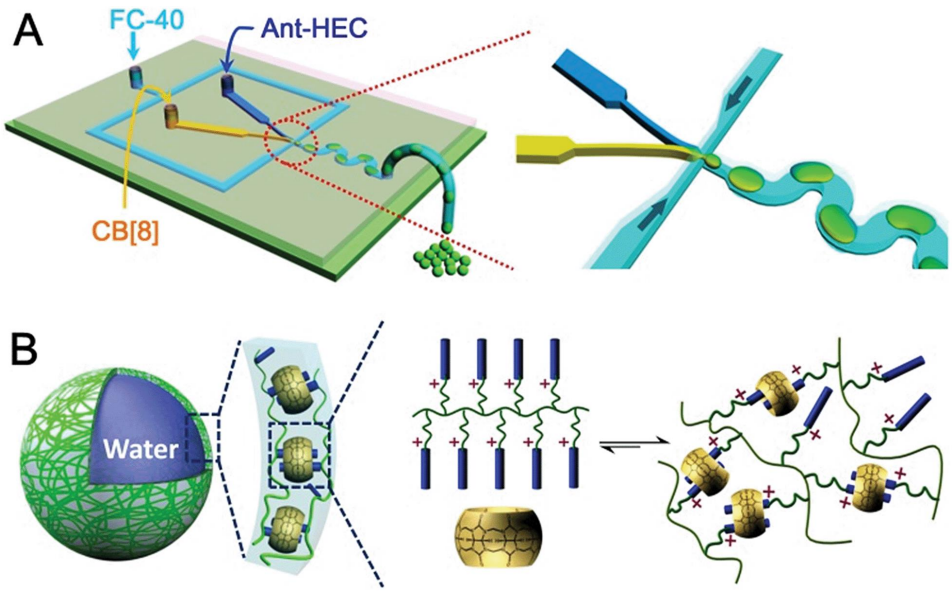

Figure 3.2. Formation of supramolecular hydrogel microcapsules by host-guest cross-linking between anthracene-functionalized hydroxyethyl cellulose (Ant-HEC) and cucurbit[8]uril (CB[8]) units. The cross-linking is enabled by an increase of the Ant-HEC concentration at the interface of a water-in-PFO emulsions via interfacial complexation between cationic Ant-HEC in water and anionic Krytox in FC-40 PFO.[237]

Inspired by these examples, we decided to implement polymer-surfactant interfacial complexation in water-in-PFO emulsions between cationic poly(L-lysine) (PLL) – which is nothing else than a polyamine – and anionic Krytox. PLL has the advantage to be bio-compatible and to be easily functionalizable by reactions involving its side amino groups, giving access to a wide library of PLL-based functional polymers.[238] In a first approach, we prepared a LCST derivative of this polymer by grafting PNIPAM strands onto PLL backbone. We demonstrated that the resulting PLL-g-PNIPAM leads to the formation of thermo-responsive shells at the surface of water droplet in water-in-PFO emulsions

3.2 Evidence for interfacial complexation of PLL comb-like derivatives in water-in-fluorocarbon oil emulsions

3.2.1 Measurement of water/oil interfacial tension by the rising drop method

As a complement of the experimental evidence of polyamine-Krytox interactions reported by DeJournette and O'Neal, we proposed to specifically reveal the PLL/Krytox complexation by interfacial tension measurements. To be close to the experimental conditions of an inverse emulsion, a water droplet containing PLL was grown in a bath of fluorocarbon oil containing Krytox and the water/oil interfacial tension was deduced from the shape of the droplet. Since the aqueous phase is less dense than the oil phase (density 1.0 vs 1.9), the experiments were performed using the rising droplet configuration (**Figure 3.3**.A).

The complexation between cationic amino groups of PLL and anionic carboxylate groups of Krytox is expected to occur at the surface of the droplet as the Krytox molecules may deprotonate at the contact with water. Note that in bulk fluorocarbon oil, Krytox molecules are likely under the form of dimers connected via hydrogen bonds between carboxylic acid groups, as it has been previously reported for other perfluoro-carboxylic acids in fluorinated solvents.[239] This is likely due to the commonly low solubility of H^+ in fluorinated solvents and to the low basicity of fluorinated amines such as the constituents of the FC-40 oil.[240] Having that in mind and in order to limit the complexity of the schematics, Krytox molecules will always be represented under its deprotonated form – even in bulk oil – in the schematics of this manuscript, as in **Figure 3.3**.A.

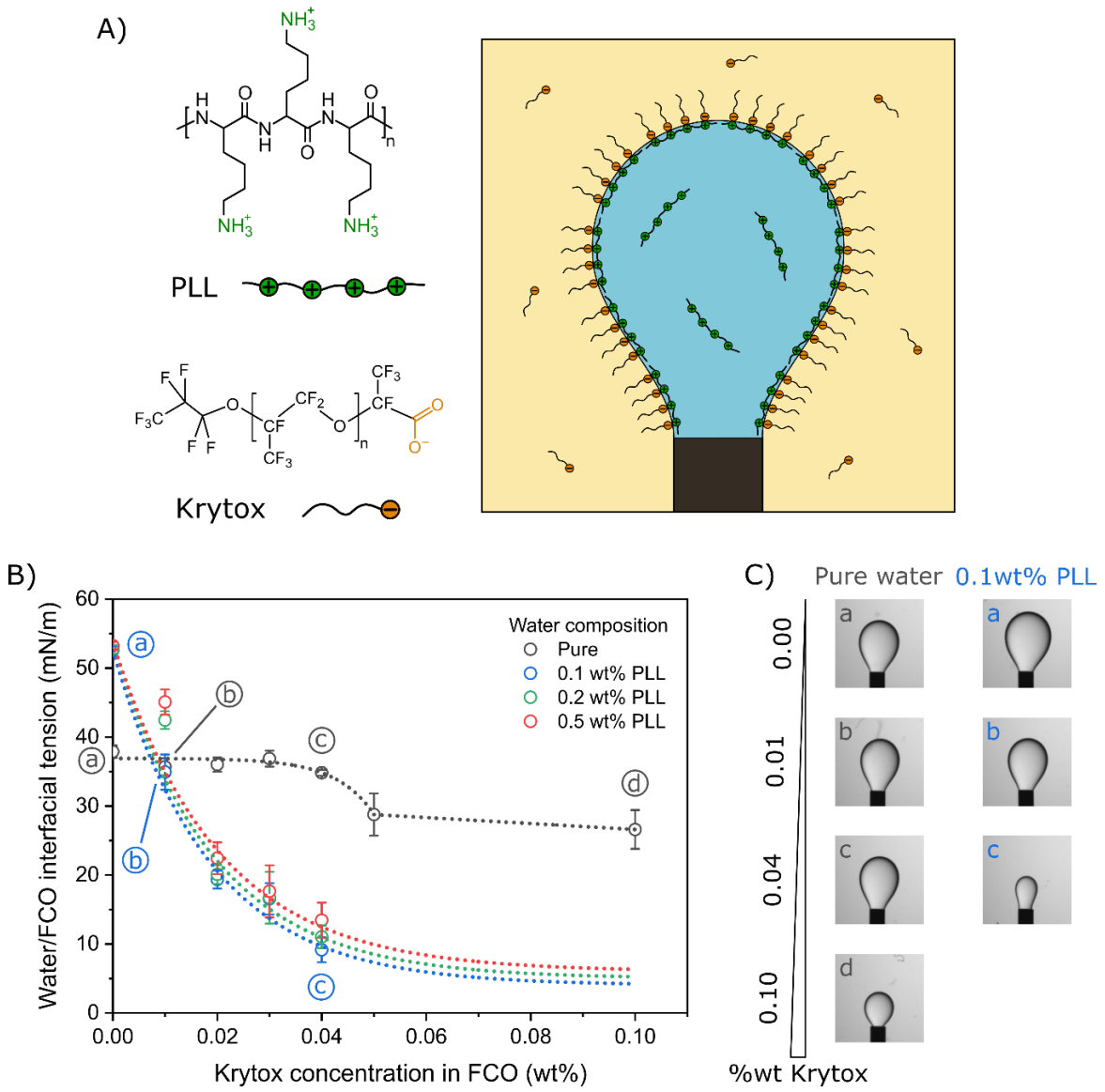

Figure 3.3. Water/oil interfacial tension measurements using the rising drop method. A) Schematics of the rising drop configuration in the case of interfacial complexation between PLL present in the water droplet and Krytox surfactant molecules present in the continuous oil phase. B) Evolution of the water/oil interfacial tension as a function of the Krytox concentration in the oil for different PLL concentrations in water (error bars = standard errors on 6 droplets per condition). The dashed lines are guides for the eyes. C) Representative images of rising droplets for the conditions indicated with a letter in the graph.

Figure 3.3.B shows the evolution of the water/oil interfacial tension as a function of the Krytox concentration in oil for a given PLL concentration in water. The dashed lines are arbitrary guides for the eyes and are not fitting curves taken from any theoretical models.

For droplets containing pure water, the water/oil interfacial tension was constant around 37 mN/m for Krytox concentrations below 0.04 wt% in the oil phase, and showed a slight decrease to ~ 30 mN/m for Krytox concentrations higher than 0.05 wt%. Considering these raw data, a critical micellar concentration (CMC) of 0.05 wt% for Krytox in FC-40 may be deduced, i.e. 200 µM considering a molar mass of 2.5 kDa for Krytox 157 FSL. However, considering the experimental limitations for the measurement of the interfacial tension (see **Appendix A**), this value of CMC should be taken with caution.

In her PhD manuscript, Birte Riechers reported the same experimental issues concerning the reliability of water/fluorocarbon oil interfacial tension measurements using the pendant drop method.[241] As an alternative, she used the Wilhelmy plate method to measure more precisely the CMC of Krytox and eventually found a value of 4 µM,[242] i.e. 0.001 wt% considering a molar mass of 2.5 kDa for 157 FSL Krytox. This value is 50 times lower than the approximate value we obtained with the rising drop method. Note that Riecher used a different fluorinated oil (Novec^{TM} 7500 instead of Fluorinert^{TM} FC-40), what could partially explain the discrepancy in the CMC ranges.

As a complement, Wagner et al. measured the CMC of Krytox derivatives for which the polar head was functionalized with different linear polyglycerol moieties[232]. The pendant drop method gave CMC values between 0.01 and 0.05 wt%, what is more consistent with our result. Nevertheless, the experimental conditions in Wagner's work were different from ours as (i) the measurements were performed using the pendant (and not rising) drop method for which the phases are inverted (an oil droplet is suspended in a water bath), and (ii) the fluorinated oil was different (Novec 7500 instead of FC-40) and (iii) the chemical modification of Krytox polar head can drastically change the adsorption properties of the surfactant.

Considering all the variations in the experimental approaches, the comparison between all the CMC values must be taken cautiously and we will conclude this discussion saying that the Krytox CMC is probably below 0.05 wt% in FC-40 and analogous fluorinated oil (such as FC-70).

When PLL was added in the aqueous phase, the evolution of the interfacial tension with the Krytox concentration was significantly different from pure water. The interfacial tension fell quickly from 50 mN/m in pure oil to 10 mN/m in oil containing 0.04 wt% Krytox, and that for all

the PLL concentrations tested (in the 0.1-0.5 wt% range). The first remarkable observation is that the interfacial tension in pure oil is higher for PLL solutions compared to pure water (53 vs 37 mN/m), likely because PLL participates to the hydrogen-bond network within the aqueous phase, thus contributing to increase the energetic cost of creating water/oil interface.

As soon as Krytox is present in the oil phase, the interfacial tension drastically decreases, suggesting that a strong PLL/Krytox interaction developed across the water/oil interface. From a Krytox concentration of 0.02 wt% and above, the stabilization of the droplets (before release) was particularly arduous due to the low interfacial tension (see droplet (c) in **Figure 3.3**.B). At concentration higher than 0.04 wt% the formation of well-defined droplets was even impossible as the oil phase was forming a quasi-continuous flow out of the needle upon injection. This qualitative observation confirms the significant decrease of interfacial tension when more than 0.05 wt% of Krytox was added in the oil phase. The dashed lines used in the graph of **Figure 3.3**.A do not correspond to any theoretical fit but arbitrarily indicates the drastic diminution of the interfacial tension, probably plateauing around 5 mN/m at higher Krytox concentration. This observation qualitatively supports the idea of a tight interfacial complexation between PLL and Krytox in emulsion-like configuration, as previously described in the introduction of the section.

By taking advantage of the PLL/Krytox complexation across water/oil interfaces, we proposed to form polymer shells at the surface of water droplets by modifying the PLL backbone with polymer chains of interest. The synthesis of PLL derivatives is the subject of the next section.

3.2.2 Synthesis of PLL comb-like derivatives: PLL-g-PNIPAM and PLL-g-PEG

Given the propensity of PLL to adsorb at the water/oil interface when combined with Krytox, we decided to implement interfacial complexation with PLL derivatives in order to create functional polymer layers at the surface of water droplets dispersed in the oil. We were particularly interested in developing thermo-responsive polymer shells in this inverse emulsion configuration as they can be seen as precursors of aqueous-core polymer capsules for controlled delivery upon temperature

changes. In a first approach, the strategy was tested and optimized with the LCST-type PNIPAM. The idea was to graft PNIPAM chains onto PLL and to accumulate the so-formed copolymer at the surface of water droplets by interfacial complexation of the PLL backbone with Krytox. The expected result was the formation of droplet-templated PNIPAM shells that can change of physicochemical properties upon heating.

We took advantage of the presence of side amine groups on PLL to easily design comb-like copolymers by the "grafting to" strategy. As amine groups can be involved in nucleophilic addition on activated ester groups, we used PNIPAM chains terminated with a highly reactive N-hydroxysuccinimide (NHS) ester to promote the formation of amide bonds between PLL and PNIPAM. The resulting comb-like copolymer comprising a PLL backbone and PNIPAM macrografts was denoted PLL-g-PNIPAM. Its architecture is represented in **Figure 3.4**. The same strategy was adopted to graft PEG chains on PLL, resulting in a PLL-g-PEG comb-like copolymer. As PEG chains are hydrophilic and non-thermoresponsive, PLL-g-PEG was used as a "control" during the characterization of PLL-g-PNIPAM.

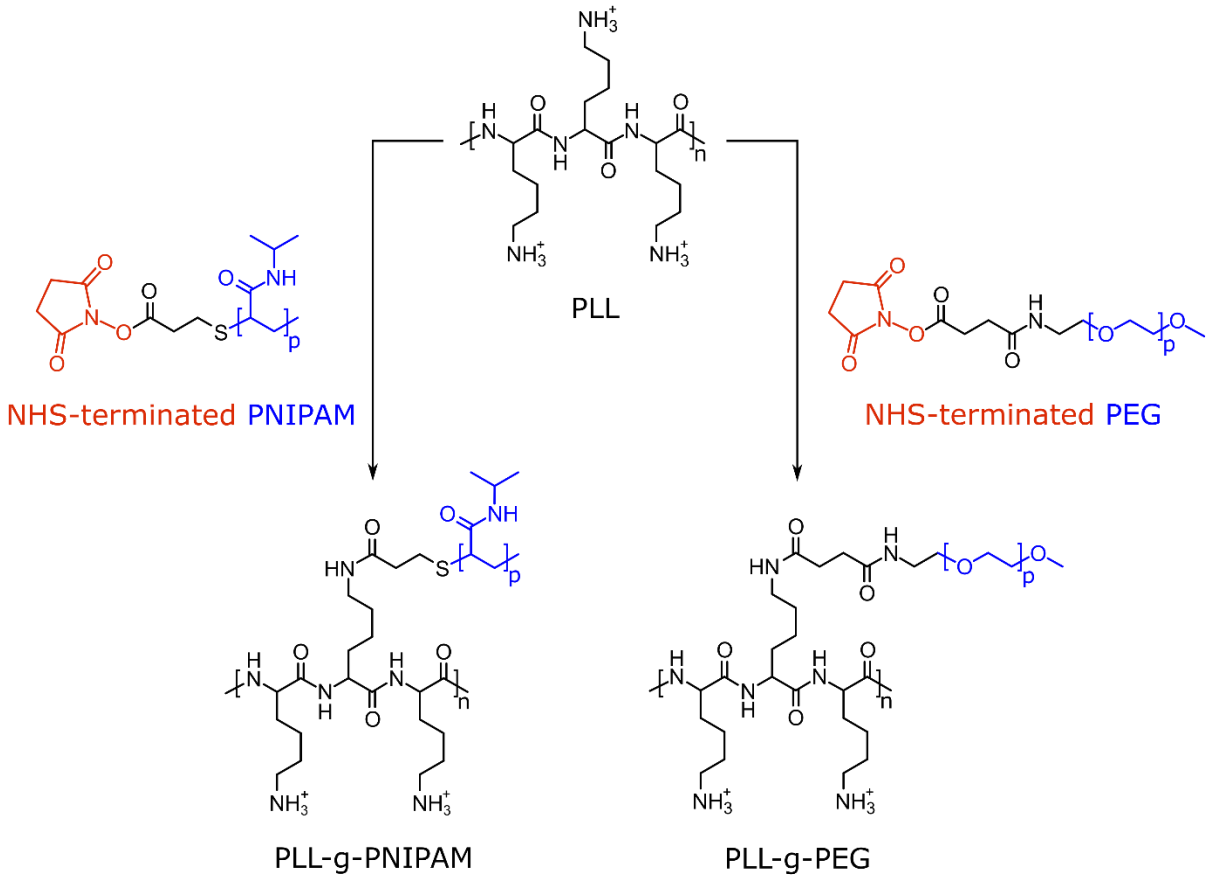

Figure 3.4. Chemical structure of the poly(L-lysine)-g-poly(N-isopropylacrylamide) (PLL-g-PNIPAM) and poly(L-lysine)-g-poly(ethylene glycol) (PLL-g-PEG) comb-like copolymers used in this chapter. The grafting approach was based on the formation of amide bonds between side amines of PLL and N-hydroxysuccinimide-activated esters (NHS) terminating the polymer strands to graft.

Note that the number of repeat units have not been specified in the polymer structures represented in **Figure 3.4**, especially because a repeat unit is not easy to define in a randomly grafted comb-like copolymer. The exact composition of the comb-like derivatives is detailed in the following: the backbone was made of a polydisperse PLL from Sigma-Aldrich with a molar mass of 15-30 kDa (72-144 lysine units/chain), the mean mass being 22 kDa (105 lysine units/chain). Both PNIPAM and PEG macrografts had a molar mass of 2 kDa (72 NIPAM units/chain for PNIPAM and 144 EG units/chain for PEG). The grafting ratio was typically of 0.20 for the two comb-like copolymers, meaning that around 1/5 of the lysine units were functionalized with a macrograft (see **Appendix A**).

During the synthesis of PLL comb-like derivatives, a fluorophore containing an NHS-ester reactive group could be added to label the PLL backbone. This dye-functionalization was used to localize the polymer in emulsion and to characterize its properties by fluorescence imaging, especially with confocal microscopy. Two different fluorophores were used (**Figure 3.5**): a carboxy-X-rhodamine (simplified to "rhodamine") and a diethylamino-coumarin (simplified to "coumarin"). The first one absorbs in the yellow range (575 nm) and emits in the orange range (600 nm), the second absorbs in the dark blue range (445 nm) and emits in the light blue range (482 nm).

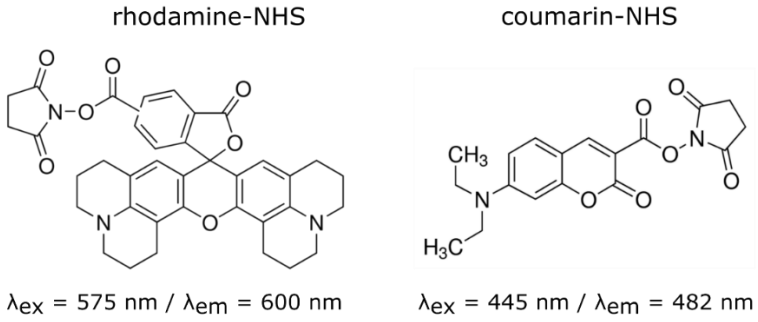

Figure 3.5. Chemical structure of the rhodamine and coumarin fluorophores covalently attached to PLL derivatives for confocal imaging. Rhodamine-NHS = 5(6)-carboxy-X-rhodamine N-succinimidyl ester, coumarin-NHS = 7-(diethylamino)coumarin-3-carboxylic acid N-succinimidyl ester.

For some control experiments, free PNIPAM chains (non-grafted on PLL) were used in the aqueous phase of the emulsions. In order to localize these chains by fluorescence microscopy, they were also functionalized with a fluorophore. This labeling was performed by strain-promoted azide–alkyne cycloaddition (a "click chemistry" technique) between azide-terminated PNIPAM chains (M_w = 5 kDa, Sigma-Aldrich) and dibenzocyclooctyne-cyanine 3 (DBCO-Cy3, Sigma-Aldrich). The Cy3 fluorophore absorbs in the green-yellow range (553 nm) and emits in the yellow range (569 nm).

Before considering the possibility to form thermo-responsive polymer capsules made of PLL-g-PNIPAM, the first step was to verify if interfacial complexation can be implemented between the PLL comb-like derivatives and Krytox in water-in-oil emulsions. This is the object of the next sections.

3.2.3 Stabilization of water-in-oil emulsions by interfacial complexation of PLL derivatives

The effectivity of interfacial complexation between PLL comb-like derivatives and Krytox was directly assessed *in operando* in water-in-oil emulsions. All these experiments have been carried out with PLL-g-PNIPAM as a representative type of PLL comb-like derivatives. We qualitatively compared the stability of emulsions with and without PLL-g-PNIPAM in the aqueous phase to evidence the formation of polymer/surfactant complexes across the water/oil interface.

In this experiment, as well as through all this Chapter, the water-in-oil emulsions were obtained as follows: 5 µL of aqueous phase were manually emulsified in 95 µL of oil phase in a 0.5 mL Eppendorf tube. If not otherwise noticed, the aqueous phase was prepared in a 7.7 mM phosphate buffer at pH = 7.3 (see **Appendix A**) and the oil phase was composed of FC-70 perfluorocarbon oil containing Krytox.

To assess the role of interfacial complexation in the stability of the emulsions, two emulsions were compared: E1 containing 1 wt% of coumarin-labeled PLL-g-PNIPAM in the aqueous phase and E2 containing no PLL-g-PNIPAM but 50 µM of free coumarin in the aqueous phase, both with 0.03 wt% of Krytox in the oil phase. The coumarin staining of both aqueous phases was used to better distinguish the two phases under UV light.

Figure 3.6 shows the aspect of both emulsions under UV light, a few seconds after emulsification. Directly after emulsification both samples became turbid, indicating the formation of an emulsion. Since the aqueous phase is less dense than the oil phase, the water droplets rapidly creamed on top of the oil phase. For E1 the homogenous turbidity was recovered upon gentle stirring of the sample. This easy redispersion of the water droplets is an indication of the stability of the emulsion. For E2, additionally to the creaming process, signs of demixing were observed a few seconds after emulsification. An aqueous supernatant rapidly appeared on top of the oil phase and could not be readily redispersed upon gentle stirring, suggesting that the water droplets were

strongly subject to coalescence. The difference in stability between E1 and E2 was highlighted under UV light thanks to the coumarin-staining of the aqueous phase (see **Figure 3.6.**B and C).

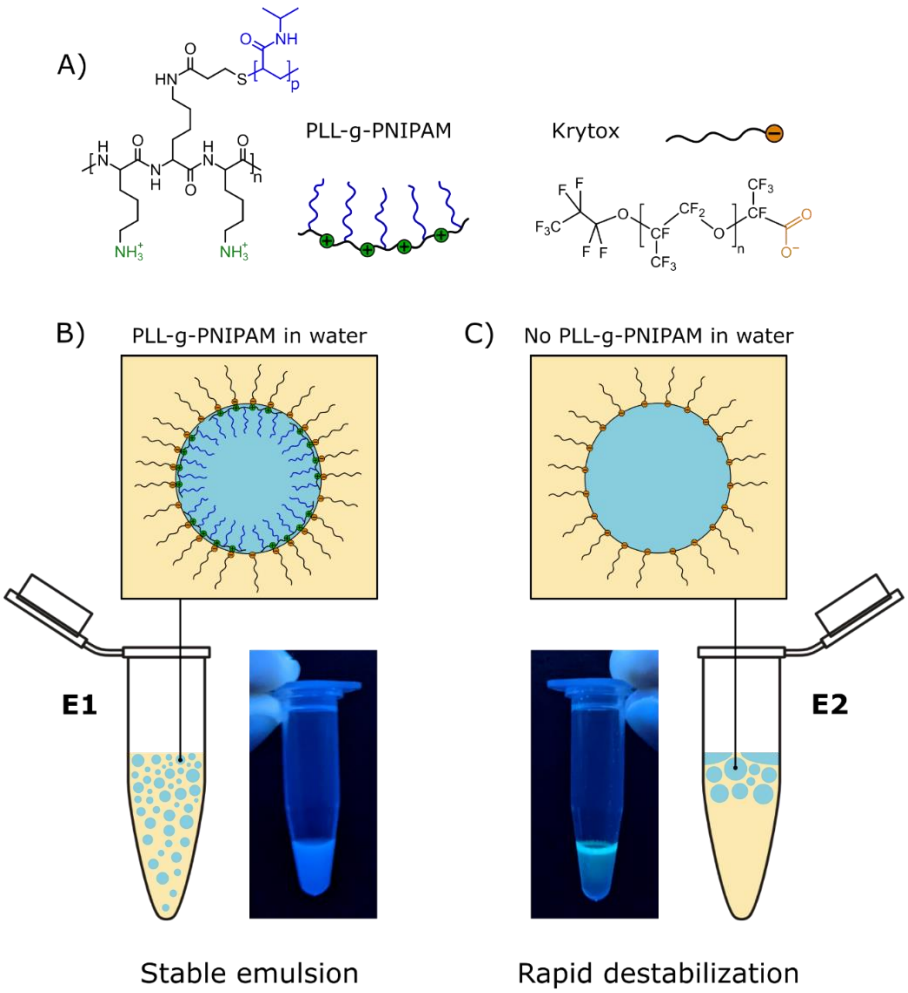

Figure 3.6. Stability of water-in-oil emulsions in the presence or absence of 1 wt% of PLL-g-PNIPAM in the aqueous phase (emulsion E1 and E2 respectively). For both emulsions, the oil phase contains 0.03 wt% of Krytox. A) Schematic representation of the PLL-g-PNIPAM copolymer and the Krytox surfactant. B) Emulsion E1: in the presence PLL-g-PNIPAM in water, a stable emulsion was formed as indicated by its uniform turbidity under UV light (the fluorescence is due to the coumarin-labeling of the polymer). C) Emulsion E2: In the absence of PLL-g-PNIPAM, the water droplets formed upon emulsification rapidly creamed and coalesced, leading to the destabilization of the emulsion as highlighted under UV light (the fluorescence is due to free coumarin added in water for staining).

The high stability observed in E1 compared to E2 can be attributed to the formation of tight interactions between PLL and Krytox across the water/oil interface. As previously described in

section 3.2.1, this interfacial complexation is responsible for a sharp decrease of the water/oil interfacial tension and thus facilitates the dispersion and stabilization of the water droplets in the fluorocarbon oil.

3.3 Microscopy imaging of emulsions

3.3.1 Stability of emulsions injected in capillary for microscopy experiments

Microscopy imaging was performed on emulsions entrapped in a rectangle glass capillary. This device has been preferred to classical slide mounting to avoid any mechanical breakage of the droplets during sample preparation or any hydrodynamic flows that could destabilize the emulsions during the observation. Since PLL derivatives are positively charged in relevant experimental conditions, they may spontaneously and strongly adsorb onto anionic surfaces including bare glass.[238,243,244] To prevent PLL derivatives present in the water droplets from adsorbing on the capillary sides, a surface treatment of the capillary was performed prior to the injection of the sample emulsion. Taking advantage of the adsorption properties of PLL, a solution of PLL-g-PEG was injected and dried in the capillary to form a “cushioning” monolayer on the internal surface of the capillary. The presence of PEG strands pointing out of the surface would thus prevent any breakage of the water droplets due to the adsorption of PLL derivatives used in emulsion.

An emulsion containing 2 wt% of PLL-g-PNIPAM in the aqueous phase and 0.05 wt% of Krytox in the oil phase was prepared as described in section 3.2.3, and injected either in a bare glass capillary or in a glass capillary previously coated with PLL-g-PEG. As the aqueous phase is less dense than the oil phase, the water droplets are expected to be in contact with the upper internal side of the capillary. **Figure 3.7** shows bright field micrographs of the emulsion in the two capillaries and a schematics representation of the situation on side view. For the bare capillary, the droplets have essentially popped and spread at the contact with the capillary side. The affinity of

PLL-g-PNIPAM present in the droplets for the bare glass surface probably favored the disruption of the water/oil interface at the contact with the capillary, leading to the destabilization of the emulsion (see **Figure 3.7.A**). In opposition, in PLL-g-PEG-coated capillary, intact spherical droplets lying onto the upper internal side of the capillary can be observed (see **Figure 3.7.B**). The PLL-g-PNIPAM monolayer previously adsorbed on the capillary surface probably acts as a "cushion" that keep the droplets out of direct contact with the glass substrate. The formation of a thin oil layer between the water droplets and the hydrophilic brush of PEG strands enhances the stability of the emulsion once injected in the capillary.

As the PLL-g-PEG coating of the capillary preserves the stability of the emulsions, this treatment was used for all the samples that were observed by microscopy.

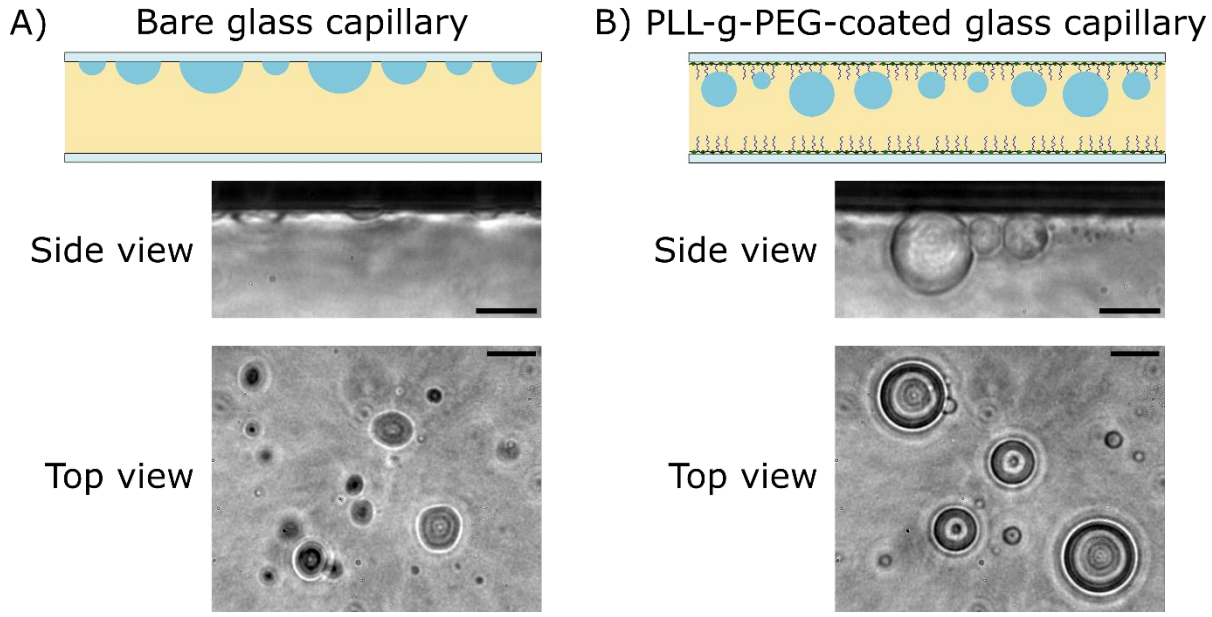

Figure 3.7. Effect of the capillary coating on the stability of an injected emulsion containing 2 wt% of PLL-g-PNIPAM in the aqueous phase and 0.05 wt% of Krytox in the oil phase. Bright field micrographs (scale bars = 30 µm) and a schematics representation of the samples are shown for the bare capillary (A) and for the capillary previously treated with PLL-g-PEG (B). The PLL-g-PEG coating is represented by the monolayer of comb-like molecules in the schematics of the treated capillary. For more readability, PLL-g-PNIPAM and Krytox molecules have not been represented in the emulsion.

To evaluate the stability of the emulsion once injected in a capillary, micrographs were taken every hour for 5h. The micrographs were taken in the phase contrast mode to highlight the edges of the

droplets (see **Figure 3.8**). No bursting or coalescence events were noticed in the sample during the 5h of incubation, suggesting that the emulsion remains intact at least at the times scale of microscopy experiments.

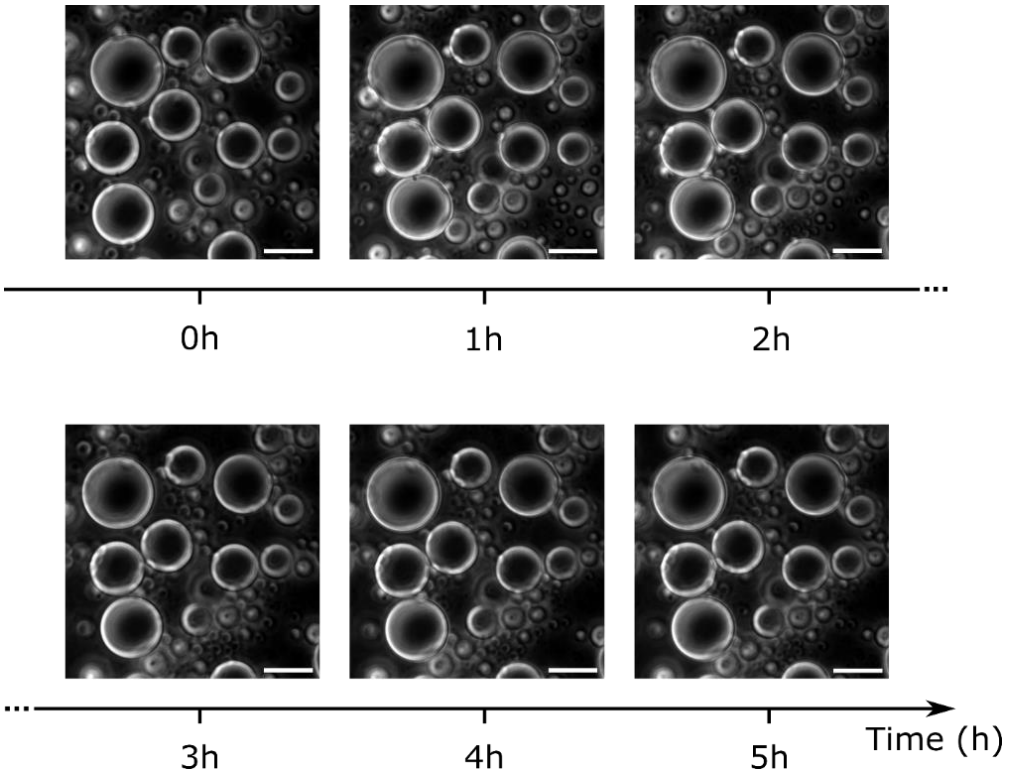

Figure 3.8. Phase contrast micrographs over time of a water-in-oil emulsion with 2 wt% of PLL-g-PNIPAM in the aqueous phase and 0.05 wt% of Krytox in the oil phase (scale bar = 30 µm). The emulsion has been injected in a PLL-g-PEG-coated glass capillary.

3.3.2 Confocal microscopy on emulsions and evidence for the formation of polymer shells by interfacial complexation

Confocal laser scanning microscopy has the great advantage to provide high spatial resolution (in the micron range) within the sample thickness that would allow to probe the equatorial plane of the water droplets and thus to image the physico-chemical processes taking place *inside* the droplets, and especially at the inner surface. First, confocal imaging was used to

evaluate the effectivity of surfactant-polymer interfacial complexation by comparing the distribution of fluorophore-labeled PLL-g-PNIPAM and free PNIPAM chains (non-grafted on PLL) in droplets.

The emulsions were prepared as described in section 3.2.3. Briefly, 5 µL of aqueous phase containing either 3 wt% of rhodamine-labeled PLL-g-PNIPAM or 2.5 wt% Cy3-labeled were emulsified manually in 95 µL of oil phase containing 0.05 wt% Krytox. Then the emulsion was injected in a glass capillary treated with PLL-g-PEG. The resulting emulsions were observed in confocal microscopy (see **Figure 3.9**).

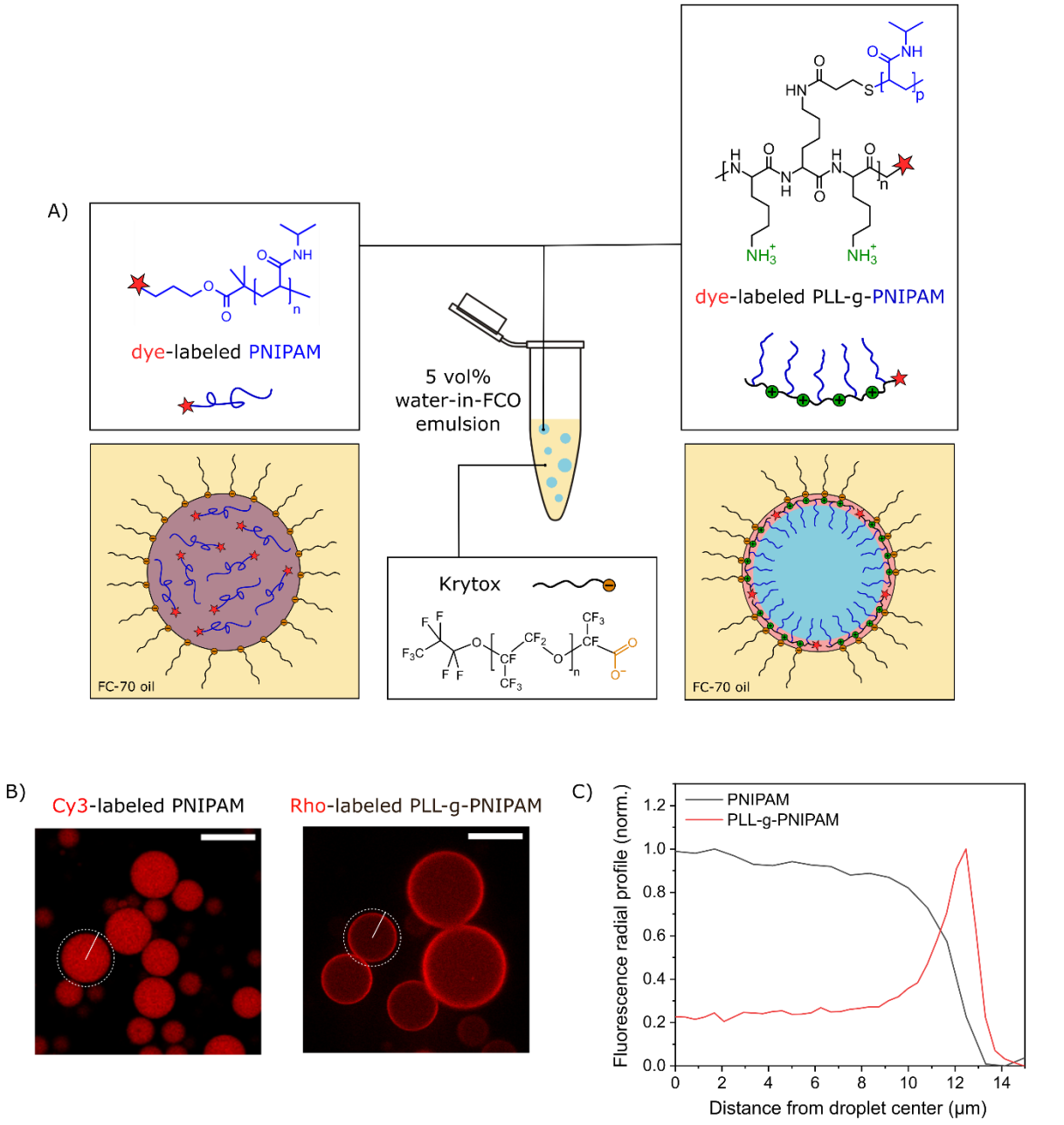

Figure 3.9. Formulation of water-in-oil emulsions with free PNIPAM chains or PLL-g-PNIPAM copolymer in the aqueous phase and Krytox surfactant in the oil phase. A) Schematics of the emulsion and the expected distribution of polymer species inside water droplets. B) Confocal micrographs of emulsions containing either 2.5 wt% of Cy3-labeled free PNIPAM chains (left) or 3 wt% of rhodamine-labeled PLL-g-PNIPAM (right) in the aqueous phase (scale = 20 μm). C) Fluorescence radial profiles of the droplets encircled in white in the micrographs.

In the emulsion containing 3 wt% of rhodamine-labeled PLL-g-PNIPAM and 0.05 wt% Krytox, the fluorescence of rhodamine was essentially localized at the edge of the water droplets, i.e. at the water/oil interface, as shown in **Figure 3.9.B**. In contrast, the fluorescence of Cy3-labeled PNIPAM free chains (in the absence of PLL) was homogenously distributed in the core of the water droplets (see **Figure 3.9.B**). The difference of distribution between free PNIPAM and PLL-g-PNIPAM is highlighted in the radial fluorescence profiles (see **Figure 3.9.C**), with a sharp peak localized at the droplet edge for PLL-g-PNIPAM and a uniform level of fluorescence within the droplet core for free PNIPAM. The higher density of PLL-g-PNIPAM at the interfaces (as compared to both the droplet cores and the continuous oil phase) is indicative of the formation of an interfacial polymer layer by complexation between cationic PLL and anionic Krytox across the interface. Conversely, free PNIPAM chains were neutral and could not be involved in interfacial electrostatic complexation. As consequence, no accumulation of free PNIPAM was observed at the inner surface of the water droplets. Thus, confocal imaging gives visual evidence of PLL/Krytox interfacial complexation in emulsion and suggests that this process can be used to accumulate PNIPAM chains at the surface of water droplets.

For our confocal experiments, we worked at relatively low magnification (x 20) to image our emulsions with a large field of view and characterize a high number of droplets at the same time. In these conditions, the imaging of small objects (typically lower than 10 µm) was limited by the optical resolution. In the case of droplets containing rhodamine-labeled PLL-g-PNIPAM, the fluorescent corona could not be distinguished at the periphery of droplets smaller than 10 µm in diameter. Instead, the fluorescence signal appeared uniform in the whole droplets because of a lack of resolution. As a consequence, the analysis of all the physico-chemical processes relying on fluorescence signal was restricted to droplets bigger than 10 µm in diameter. **Figure 3.10** shows the distribution of droplet size based on the measurement of 130 droplets from the emulsion containing 3 wt% of rhodamine-labeled PLL-g-PNIPAM showed in **Figure 3.9** and used as a representative sample of manually-prepared emulsion. Almost 2/3 of the droplets have a diameter smaller than 10 µm. Consequently, image analysis was performed on the other 1/3 of the sample.

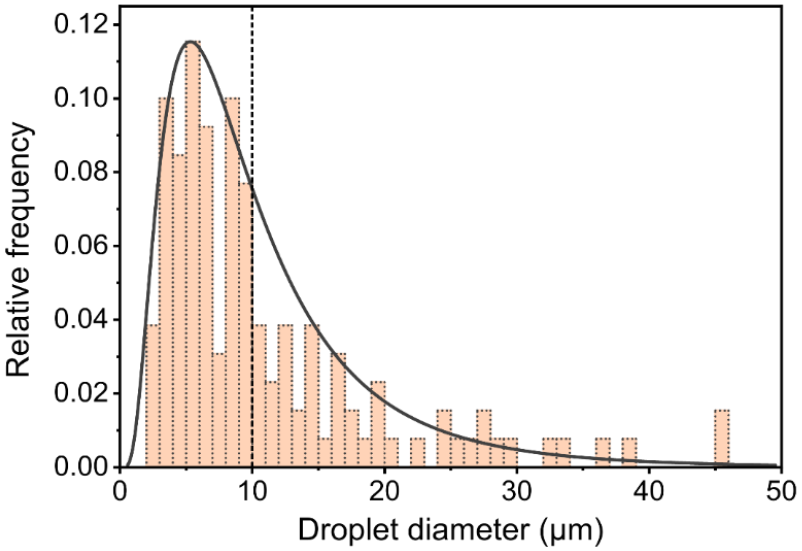

Figure 3.10. Droplet size distribution for 130 droplets of the emulsion containing 3 wt% of PLL-g-PNIPAM showed in **Figure 3.9**. The solid line corresponds to a lognormal fit.

3.4 Characterization of PLL-g-PNIPAM shells formed by interfacial complexation

3.4.1 Optimization of the formulation and observation of well-formed polymer capsules

For each batch of PLL derivatives, the Krytox/PLL-g-PNIPAM concentration ratio was adjusted to achieve an optimal deposition of PLL-g-PNIPAM at the droplet surface by interfacial complexation, evidenced by (i) the stability of the emulsion and (ii) the formation of a fluorescent layer of PLL-g-PNIPAM at the droplet periphery. This optimization is illustrated in **Figure 3.11** in the case of a coumarin-labeled PLL-g-PNIPAM.

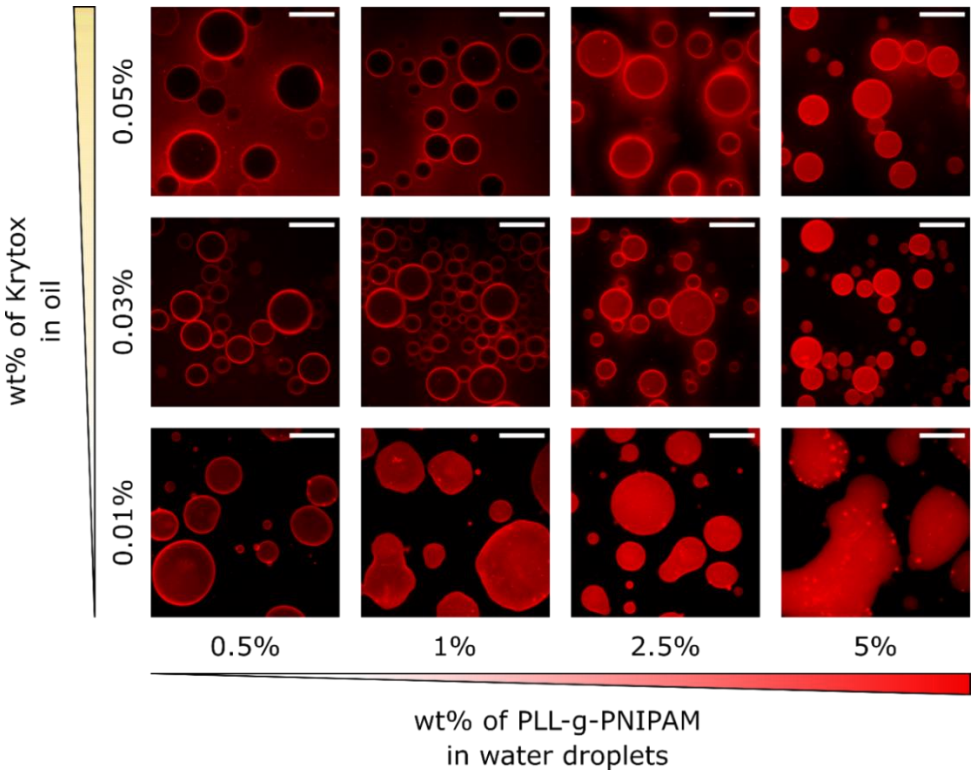

Figure 3.11. Partial formulation diagram of water-in-oil emulsions injected in a glass capillary and imaged by confocal microscopy (scale bar = 50 µm). PLL-g-PNIPAM was labeled with coumarin (in red) for fluorescence imaging.

At low Krytox concentration (typically ≤ 0.01 wt%) the coalescence of droplets onto the capillary side revealed that the surfactant concentration was insufficient to stabilize the water droplets. At high Krytox concentration (typically ≥ 0.05 wt%), the fluorescence of coumarin-labeled PLL-g-PNIPAM was essentially observed in the continuous phase, indicating a massive extraction of polymer chains in the oil phase. As pure fluorocarbon oils do not solubilize the hydrophilic hydrocarbon-based PLL derivatives, this observation suggests that the dispersion of these hydrophilic compounds in the oil was mediated by excess Krytox, likely under the form of inverse micelles.[245,246]

At intermediate Krytox concentration (typically 0.03 wt%), fluorescence micrographs showed a bright corona of PLL-g-PNIPAM localized at the droplet edges and negligible fluorescence in the oil. This observation is consistent with a process of interfacial complexation where the PLL-g-PNIPAM copolymer is attracted towards the interface upon the formation of coulombic complexes with Krytox as schematized in **Figure 3.9**. At high amount of polymer in

the aqueous phase (typically ≥ 5 wt%), the interface was saturated in PLL-g-PNIPAM, and excess polymer chains remained soluble within the droplet core, leading to a low fluorescence contrast between the edge and the core of the droplets. Because of the excessive amount of internal polymer content, this condition was not suitable for the formation of hollow polymer capsules.

In addition, Scanning Electron Microscopy (SEM) imaging was performed to visualize the interface at a higher resolution and to determine the influence of the formulation on the capsules. SEM imaging was performed on 5 µL of emulsion dried on a glass coverslip for three days at ambient air. Prior to imaging, the dried capsules were metalized by deposition of a 30-nm thin layer of Ag using an Emitech K675X Sputter Coater (Ag sputtering for 60 s at 120 mA). SEM images were recorded with a Hitachi TM3030 Tabletop Microscope at 15kV accelerating voltage.

Figure 3.12 shows SEM images of microcapsules prepared from an emulsion containing 1 wt% of either PLL-g-PNIPAM or PLL-g-PEG in the aqueous phase.

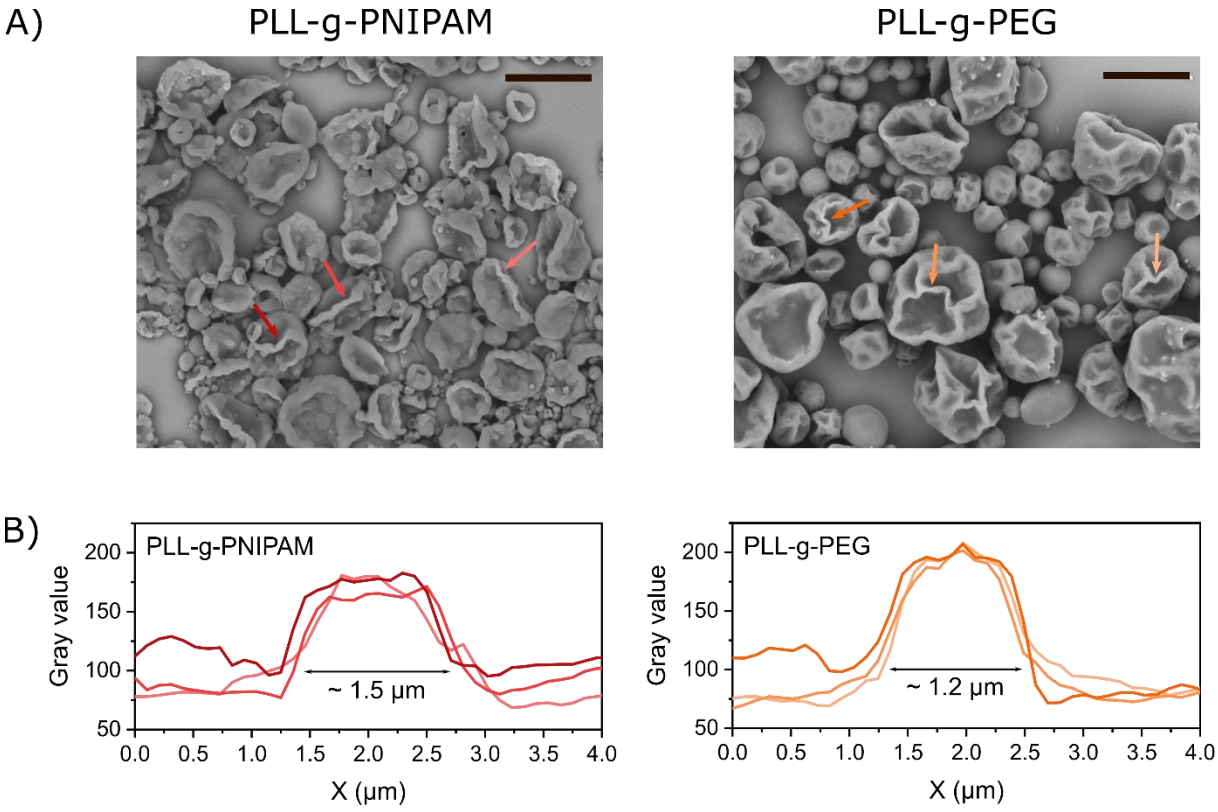

Figure 3.12. Scanning Electron Microscopy (SEM) imaging of dried emulsion showing the effective formation of polymer capsules by interfacial complexation. A) SEM micrographs of dried emulsions with 1 %wt of PLL-g-

PNIPAM or PLL-g-PEG in the aqueous phase and 0.05 wt% of Krytox in the oil phase (scale bars = 20 µm). B) Thickness profiles of the shell folds indicated by colored arrows in the micrographs and giving an estimation of twice the apparent thickness of the capsule shells (as the folds are presumably formed by the collapse of two shell layers).

SEM images on dried emulsions reveal the presence of hollow microcapsules, suggesting that drying-resistant polymer layers were initially formed at the periphery of the droplets. This result confirms that interfacial complexation is an effective technique for the formation of polymer capsules using an emulsion as a template. Their flattened aspect – presumably due to membrane collapsing during the drying step – allows for an estimate of the shell wall thickness, which is typically of 0.6 - 0.8 µm (the apparent thickness of a collapsed membrane being assumed to correspond to two stacked membrane layers, see **Figure 3.12**.B).

Figure 3.13 details the influence of the polymer and Krytox concentrations on the capsule morphologies observed by SEM in the case of PLL-g-PNIPAM.

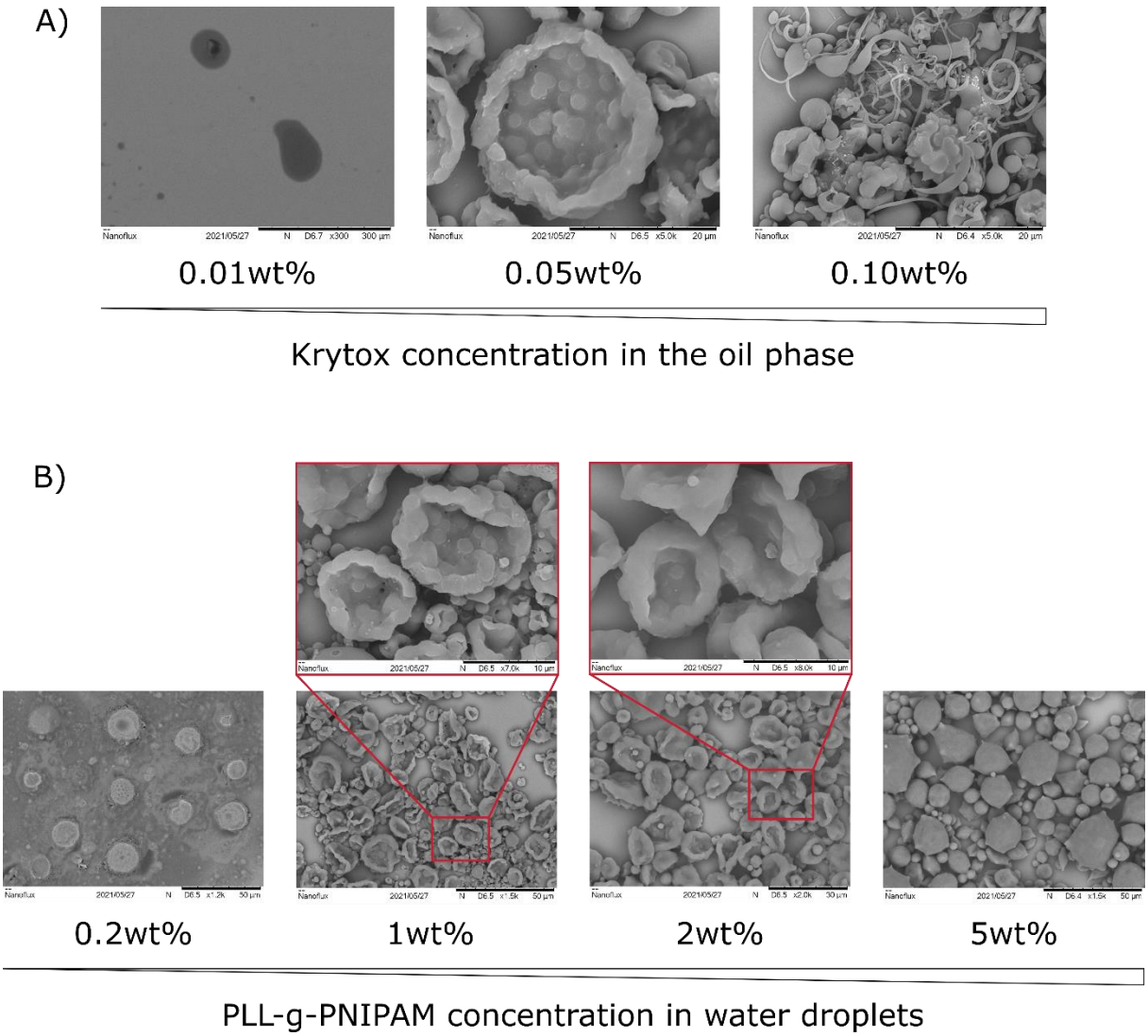

Figure 3.13. Influence of the PLL-g-PNIPAM and Krytox concentrations on the structure of PLL-g-PNIPAM capsules formed by interfacial complexation. A) SEM micrographs of dried emulsions containing 1 wt% of PLL-g-PNIPAM in the aqueous phase and an increasing concentration of Krytox in the oil phase. B) SEM micrographs of dried emulsions containing 0.05 wt% of Krytox in the oil phase and an increasing concentration of PLL-g-PNIPAM in the aqueous phase.

Figure 3.13.A shows that the concentration of Krytox has to be balanced to readily stabilize well-defined polymer capsules by interfacial complexation (at a fixed polymer concentration). At 0.05 wt% Krytox concentration, microcapsules can be observed with a typical 1 µm-thick shell wall. Their flattened aspect presumably comes from the drying step. At lower Krytox concentration (typically 0.01 wt%), no capsules were formed as not enough surfactant is present to trigger SPIC. At higher Krytox concentration (typically 0.10 wt%), a messy phase composed of intertwined

capsular structures, small aggregates and filaments was observed. The complexity of this phase and the low number of well-defined individual capsules suggests that the polymer was not distributed at the surface of the droplets in the initial emulsion but may have been extracted into the continuous oil phase by the excess of Krytox, which agrees with the high fluorescence level observed in the oil phase in the formulation diagram in **Figure 3.11**.

Figure 3.13.B shows the evolution of the capsule morphology with the concentration of PLL-g-PNIPAM in the aqueous phase, at a fixed concentration of Krytox in the oil phase. At 0.2 wt% in polymer no rigid capsules were formed, and some circular spots observed in SEM suggest that the droplets were not stable to drying. At 1 and 2 wt%, micrometer capsules were obtained with a typical shell wall thickness of ~ 1 µm. At 5 wt%, filled nanoparticles were obtained instead of hollow capsules, suggesting that the high amount of polymer chains inside the droplets leads to a bulky polymer mesh that may hinder the polymer accumulation at the interface.

3.4.2 Quantification of the polymer surface excess from fluorescence measurements

The previous results obtained by confocal imaging provided qualitative arguments in favor of the formation of a polymer shell by interfacial complexation but did not give any quantitative results concerning the fraction of polymer involved in the interfacial layer or the residual fraction of polymer that remained soluble in the core of the droplets. To access this type of information, we implemented a robust and reliable quantification method based on the measurement of the intrinsic fluorescence of dye-labeled PLL derivatives.

Taking advantage of the Beer-Lambert law relating fluorescence intensity to polymer concentration in solution, we determined the concentration in soluble polymer chains that were not involved in interfacial complexation by measuring the core fluorescence of the droplets. Once this residual polymer concentration in core was obtained, the fraction of polymer recruited in the interfacial layer was calculated as being equal to the loss of the soluble polymer amount. Finally, this fraction of interfacial polymer was converted in surface excess via the normalization by the droplet interfacial area.

Raw values of fluorescence were however biased by optical effect of droplet curvature since the water/oil interface can deviate the light beam of the microscope. To account for this optical bias, the core fluorescence of dye-labeled PLL-g-PNIPAM was normalized following a suitable calibration process which is described in the following.

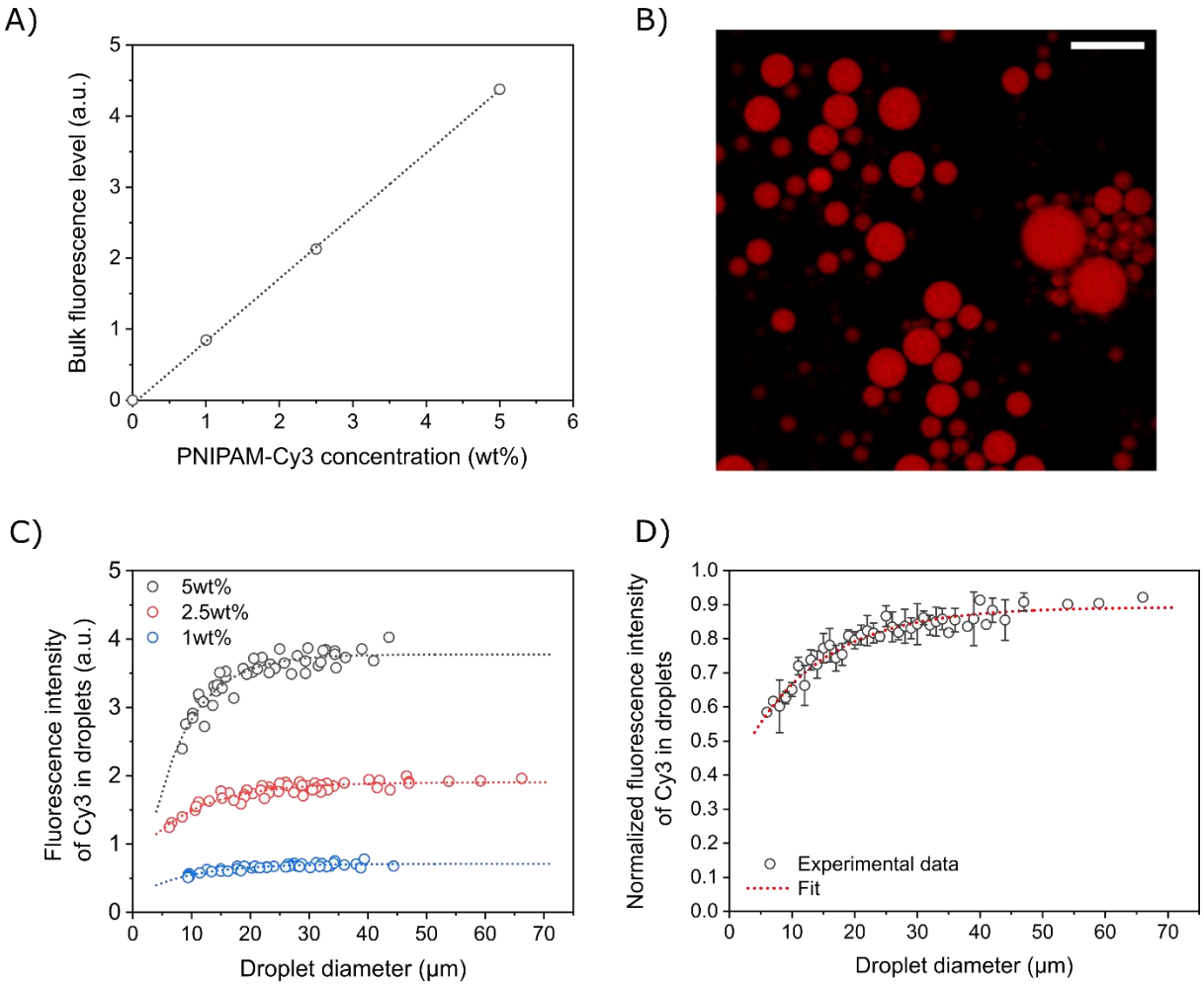

Figure 3.14. Calibration process accounting for optical bias on the measurement of fluorescence level in the droplet cores by confocal imaging. A) Beer-Lambert calibration curve of PNIPAM-Cy3 fluorescence measured in bulk solution by confocal fluorescence imaging. B) Confocal micrograph of an emulsion containing 2.5 wt% of PNIPAM-Cy3 in the aqueous phase and 0.05 wt% of Krytox in the oil phase at T = 18 °C (scale bar = 50 µm). C) Fluorescence level of PNIPAM-Cy3 measured in the core of water droplets as the function of the droplet diameter and for different concentrations of PNIPAM-Cy3. D) Normalized fluorescence level in droplets (corresponding to the ratio between core fluorescence and bulk fluorescence at the same concentration) as a function of the droplet diameter. To simplify

the distribution, each droplet diameter has been rounded down to the nearest integer (error bars = standard deviation for each integer diameter).

As Cy3-labeled PNIPAM (PNIPAM-Cy3) was homogeneously distributed within droplet cores (see section 3.3.2 and **Figure 3.9**), it was used as a reference for the calibration of core fluorescence. Based on the fluorescence of PNIPAM-Cy3 in droplets, we determined a corrective factor accounting for droplet size effects on the fluorescence signal.

First, the fluorescence intensity of aqueous solutions of PNIPAM-Cy3 at various concentrations ($I_{bulk}^{Cy3}(C)$) was measured by confocal imaging and followed a Beer-Lambert linear relation (see **Figure 3.14**.A). In the same conditions of irradiation, the fluorescence intensity of PNIPAM-Cy3 ($I_{drop}^{Cy3}(C,d)$) was measured in a polydisperse emulsion (see **Figure 3.14**.B) with water droplets (of diameter d) containing PNIPAM-Cy3 at the same concentration than the calibration curve (see **Figure 3.14**.C). The normalization of droplet intensities by the bulk intensity at the same PNIPAM-Cy3 concentration resulted in a corrective factor $I_{norm}^{Cy3}(d) = \frac{I_{drop}^{Cy3}(C,d)}{I_{bulk}^{Cy3}(C)}$ that only depends on the droplet diameter d (see **Figure 3.14**.D).

The same normalization approach was followed for the fluorescence of dye-labeled PLL-g-PNIPAM. In the following, the method is detailed for rhodamine-labeled PLL-g-PNIPAM (PLLrho-g-PNIPAM), but the same approach was followed for the coumarin-labeled PLL-g-PNIPAM.

First, the fluorescence intensity of different PLLrho-g-PNIPAM solutions was measured in bulk ($I_{bulk}^{rho}(C)$). The same solutions were emulsified in oil containing Krytox. The fluorescence intensity of PLLrho-g-PNIPAM ($I_{drop}^{rho}(C,d)$) was then measured in the droplet cores and normalized by $I_{bulk}^{rho}(C)$. The ratio between the actual PLLrho-g-PNIPAM concentration in droplet cores C_{core} and the analytical concentration C introduced in the aqueous phase before emulsification was eventually determined by the following formula:

$$\frac{C_{core}}{C} = \frac{I_{drop}^{rho}(C,d)}{I_{bulk}^{rho}(C)} \times \frac{I_{bulk}^{Cy3}(C)}{I_{drop}^{Cy3}(C,d)} = \frac{I_{norm}^{rho}(d)}{I_{norm}^{Cy3}(d)}$$

The factor $I_{norm}^{rho}(d)$ evaluates the inhomogeneity of the PLLrho-g-PNIPAM distribution in water droplets due to the massive adsorption of the polymer at the water/oil interface and the factor $I_{norm}^{Cy3}(d)$ accounts for the correction of optical bias.

The $\frac{C_{core}}{C}$ ratio will be referred as 'residual core concentration' in the main text. Physically, it corresponds to the residual fraction of polymer chains that have not been involved in the interfacial complexation with Krytox and have remained soluble in the droplet core.

Eventually, the PLLrho-g-PNIPAM surface excess Γ was defined as the excess number of polymer chains adsorbed at the interface per surface unit in conditions of interfacial complexation (compared to a hypothetic uniform distribution of the chains in the droplet volume). It is given by the following formula:

$$\Gamma = \frac{N_{excess}}{S} = \frac{(C - C_{core})V}{S} = \left(1 - \frac{C_{core}}{C}\right)\frac{d}{6}C = \left(1 - \frac{I_{norm}^{rho}(d)}{I_{norm}^{Cy3}(d)}\right)\frac{d}{6}C$$

Both the residual core concentration $\frac{C_{core}}{C}$ and the surface excess Γ were analyzed to conclude on the influence of different factors on the efficiency of the interfacial complexation process, such as the ionic strength and the pH (see section 3.4.3) or the temperature (see section 3.5.3).

3.4.3 Influence of the ionic strength and the pH on the interfacial complexation

As interfacial complexation involves coulombic interactions between carboxylate-terminated Krytox and ammonium groups of PLL, the pH as well as the ionic strength of the aqueous phase should have an important impact on the interfacial complexation equilibrium and may enable to optimize the properties of the interfacial assemblies. Beyond qualitative comparisons, a quantitative approach was required to conclude on the complexation efficiency for the different compositions of the aqueous phase.

To assess the effect of the ionic strength, we compared droplets containing either a 7.7 mM phosphate buffer (ionic strength = 17 mM, pH = 7.3), or this buffer supplemented with 100 mM or 500 mM NaCl.

To assess the effect of the pH, we used a 30 mM Britton-Robinson (BR) buffer – made of 10 mM NaH_2PO_4/10 mM NaOAc/10 mM CHES – allowing for a buffering effect on a large range of pH. Aqueous phases containing the polymer were prepared in BR buffer at either acidic or alkaline pH, namely at pH = 4.3 or pH = 9.4 (see **Appendix A**).

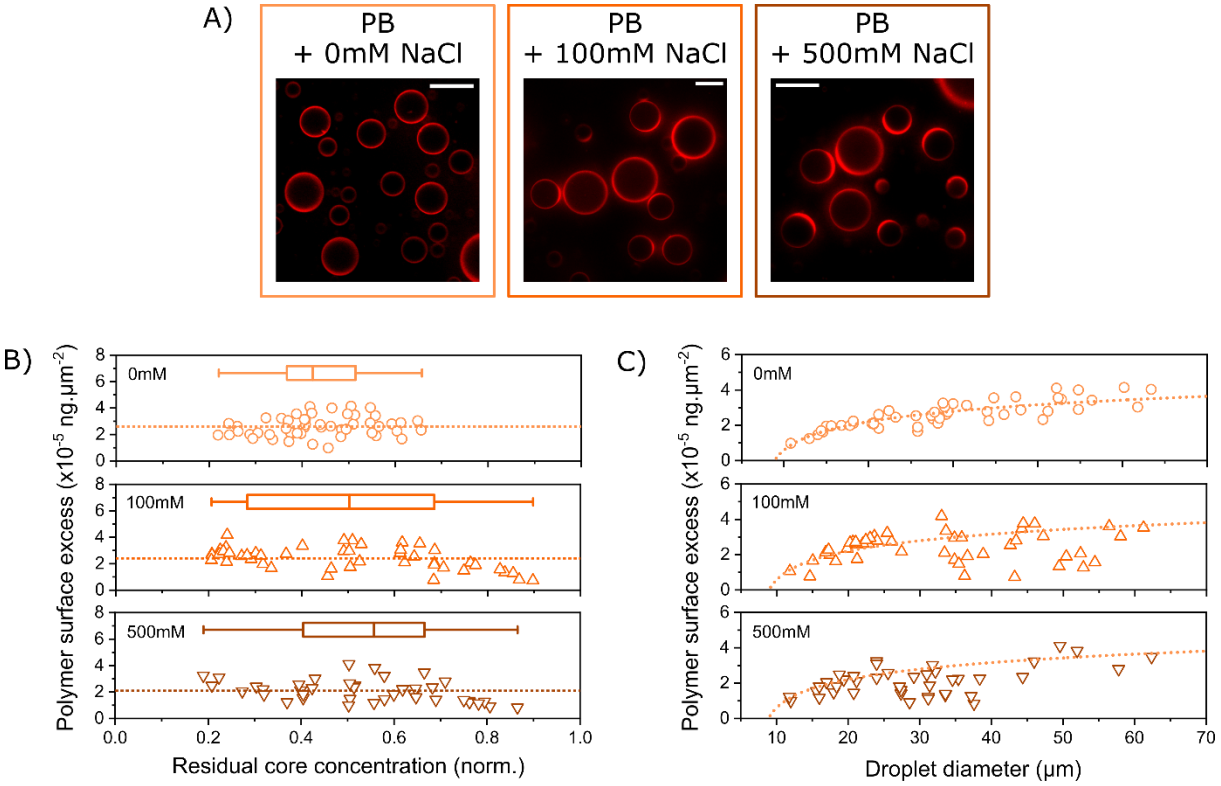

Figure 3.15. Influence of the ionic strength on the interfacial complexation between 1 wt% PLL-g-PNIPAM and 0.05 wt% Krytox at 18°C. A) Confocal micrographs of emulsions prepared with different ionic strengths in the aqueous phase (scale bars = 20 µm). PB = phosphate buffer. B) Polymer surface excess as a function of the residual core concentration (normalized by the analytical concentration of 1 wt%). Dashed lines indicate the mean level of surface excess for each condition. Box plots give the min/Q1/median/Q3/max values of the distribution of residual concentration in core for each condition. C) Polymer surface excess as a function of the droplet diameter. The light orange dashed line reported on each plot corresponds to the trend for PB without NaCl (top layer) which is used as a reference.

Irrespective of the ionic strength condition, a bright corona was visible at the edge of the droplets with a low residual fluorescence in the core (see **Figure 3.15**.A) and a non-zero surface excess was measured, suggesting that the interfacial complexation was effective even at high NaCl concentration. However, uneven distributions of fluorescence around the droplet edges were noticed in NaCl-containing emulsions, and particularly at 500 mM NaCl where “crescent moon-like” shapes of fluorescence became obvious specifically in droplets (< 20 µm). This observation suggests that the presence of salts at high concentration in the aqueous phase led to a patchy segregation of the polymer chains that significantly differ from the uniform coverage of the interface at low ionic strength. The corresponding polymer surface excesses are shown as a function of the residual core concentration and droplet diameter in **Figure 3.15**.B and C. The presence of NaCl slightly diminished the surface excess, and markedly broadened the distribution of residual core concentrations. Some droplets containing 100 mM or 500 mM NaCl had up to 80 % of residual polymer chains in their core, which suggests the weakening of interfacial binding with increasing salt. Recent articles on polycation:polyanion (PC:PA) complexes consistently report that ionic strength play a similar role as temperature in the phase diagram of complex coacervation. With increasing salt concentration solid-like PC:PA coacervates first turn to more fluid phases (gels or liquid-like) prior to become soluble.[247–249] As a tentative interpretation of "crescent-like" distribution of the polymer at interfaces, we propose that a transition to fluid phase enabled fusion and gathering of the complexes at one pole of the droplets.

To prepare capsules, a robust solid-like membrane is thus preferably obtained at low ionic strength as this offers more homogeneous interfaces and ideally a solid-like interfacial complex phase.

Regarding the influence of the pH, significant accumulation of polymer at the interface was observed in both acidic and alkaline conditions as shown by the fluorescent corona formed at the edge of the droplets (see **Figure 3.16**). The lower surface excess as well as higher residual fluorescence observed in droplet cores at pH = 9.4 as compared to pH = 4.3 clearly indicate that the PLL/Krytox complexation is less efficient in alkaline than in acidic conditions. This contrast in surface excess and the poor interfacial capture of PLL-g-PNIPAM at high pH is consistent with the decrease of the degree of ionization of PLL at higher pH: in alkaline conditions, the pH was

close to the pKa of the side amino groups of PLL (~ 10.5) and therefore a significant fraction of amine groups was deprotonated, what is expected to weaken coulombic association with Krytox. In contrast, all the side amino groups were protonated at pH = 4.3, and thus available to associate with Krytox across the water/oil interface.

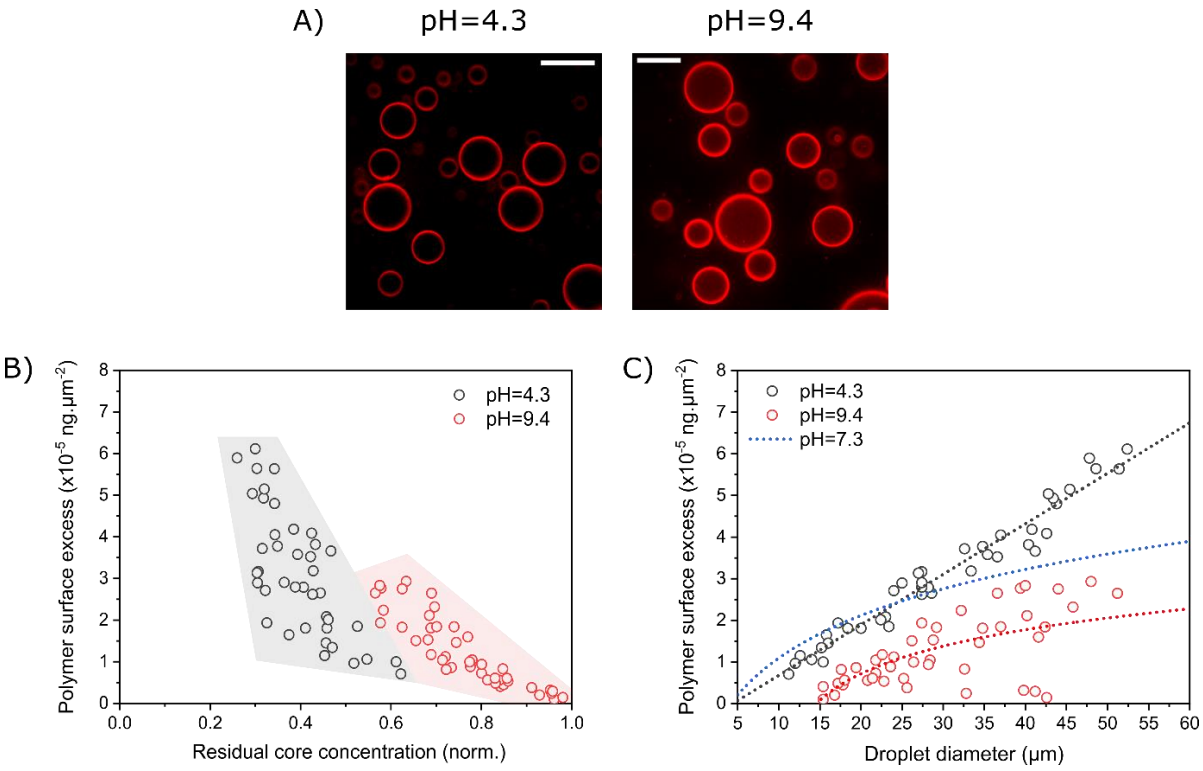

Figure 3.16. Influence of the pH on interfacial complexation between 1 wt% coumarin-labeled PLL-g-PNIPAM and 0.03 wt% Krytox at 18 °C in Britton-Robinson buffer. A) Confocal micrographs of emulsions at pH = 4.3 and 9.4 (scale bar = 30 µm). B) Correlation between polymer surface excess and residual core concentration (normalized by the analytical concentration of 1 wt%) at pH = 4.3 (black circles) and pH = 9.4 (red circles). Colored domains are guide for the eye to better visualize the scatter distributions. C) Surface excess of coumarin-labeled PLL-g-PNIPAM as a function of the droplet diameter at pH = 4.3 (black circles) and pH = 9.4 (red circles), calculated from fluorescence measurements. Dashed lines are guides for the eye. The blue dashed line is the surface excess measured at pH = 7.3 in the same conditions (raw data are not shown for more readability).

3.5 Evaluation of the thermoresponsive behavior of interfacial PLL-g-PNIPAM

3.5.1 Thermoresponsive behavior of PLL-g-PNIPAM in solution

The thermoresponsive behavior of PLL-g-PNIPAM was characterized in solution by turbidimetry and compared to free PNIPAM (see **Figure 3.17**). The transmittance profiles of either PLL-g-PNIPAM or free PNIPAM solutions decreased between 33 °C and 40 °C, indicating that PNIPAM strands – grafted or not – undergo a coil-to-globule transition in the same temperature window. A linear extrapolation of the curve around the inflexion point indicates the same cloud point 34 °C for both PNIPAM forms (coinciding with the beginning of the decrease in transmittance).

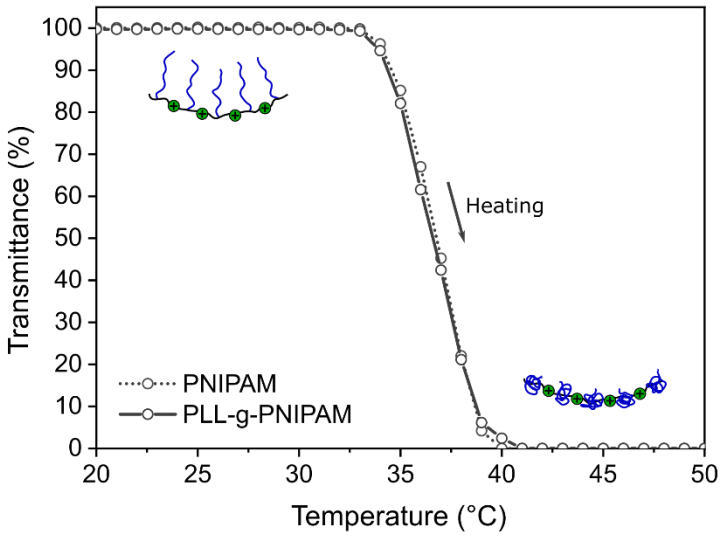

Figure 3.17. Turbidity heating curves of free PNIPAM (dashed line) and PLL-g-PNIPAM (solid line) solutions at 1 wt% in phosphate buffer.

3.5.2 Visualization of the thermal transition of PLL-g-PNIPAM in emulsion

The thermal transition of PLL-g-PNIPAM in emulsion was probed in operando using 8-anilinonaphthalene-1-sulfonic acid (ANS) as an extrinsic fluorescent reporter. The fluorescence of ANS is strongly polarity-dependent and can be used as a marker of the hydrophilic-to-hydrophobic transition of PNIPAM. In polar environments, the excited state of ANS undergoes a twisted intramolecular charge transfer (TICT) to a second and more polar excited state that rapidly relaxes to the ground state via a non-radiative decay.[250] As a consequence, the quantum yield of ANS is very low in polar solvents such as water. Conversely, the fluorescence level of ANS is enhanced when the molecule is confined in more apolar or hydrophobic environments as the radiative emission from the first excited state is favored compared to the TICT transition. These polarity-dependent fluorescence properties of ANS have been used for many characterizations of macromolecular systems, including the staining of hydrophobic protein domains,[250,251] the study of surfactant-polymer interactions,[252] or the evidence of thermal transitions in thermo-responsive polymers such as PNIPAM.[253–255]

In our system, the ANS fluorescence was used as a marker of (i) the PLL-g-PNIPAM localization in droplets since polymer-enriched regions are more hydrophobic (less polar) than the aqueous background, and (ii) the thermoresponsive properties of PNIPAM since its collapse transition to a more hydrophobic state would be evidenced by an increase in ANS fluorescence intensity.[255]

Before using ANS to characterize the thermal properties of PLL-g-PNIPAM at the water/oil interface, a first experiment was performed in emulsion with free PNIPAM chains to control the fluorescent behavior of ANS in presence of thermo-responsive chains. For this experiment, two emulsions were independently prepared and then mixed together: one containing only ANS in phosphate buffer (denoted E1), the other containing ANS and free PNIPAM chains in phosphate buffer (denoted E2). Both emulsions were prepared in an oil phase containing 0.05 wt% of Krytox. The mixed emulsion was observed in confocal microscopy at 20 °C (below the cloud point) and at

45 °C (above the cloud point) to monitor the evolution of ANS fluorescence in the two types of droplets (E1 and E2).

Figure 3.18 shows confocal micrographs of the mixed emulsion at 20 °C and 45 °C, with the E1 droplets (absence of PNIPAM) encircled in green and the E2 droplets (presence of PNIPAM) encircled in red. At 20 °C, a low fluorescence signal due to ANS could be detected in the core of both droplet types, with no high contrast between E1 and E2. At 45°C, the ANS fluorescence remained low in E1 droplets but was drastically enhanced in E2 droplets, revealing the hydrophilic-to-hydrophobic transition of the PNIPAM chains present in these droplets. The difference in ANS behavior between E1 and E2 environments is highlighted in the fluorescence radial profiles drawn for a representative droplet of each nature in **Figure 3.18**.B.

To confirm the identification of the thermal transition of PNIPAM by the fluorescence enhancement of ANS, the potential effect of the aqueous background was suppressed by calculating the E2/E1 fluorescence ratio for droplets of similar size. This ratio was plotted as a function of the temperature upon heating (**Figure 3.18**.C). The ratio increases with the temperature until reaching a maximum at 35 °C, corresponding to the cloud point of PNIPAM. Beyond this temperature, the ratio decreases but remains significantly higher than at 20 °C. This fall seems contradictory with the fact that the hydrophobicity of PNIPAM increases with temperature so that the ANS fluorescence signal should be even higher at 45 °C compared to 35 °C. This discrepancy is probably not due to the intrinsic photophysical properties of ANS or to an anomaly in the PNIPAM thermal behavior but is rather due to a combination of three other factors. The first one is the photobleaching underwent by ANS molecules along the experiments that may explain a progressive decrease of the emission intensity in highly fluorescent droplets upon heating. The second factor is the destabilization of the mixed emulsion which was evidenced by multiple coalescence events (droplets encircled in both green and red at 45 °C in **Figure 3.18**.A) and that may have led to the dilution of ANS molecules. This loss of stability can be explained by the absence of interfacial complexation in this sample (no cationic species were loaded in the aqueous phase to interact with Krytox). The third factor, which is probably the most important, was the progressive sedimentation of PNIPAM aggregates formed upon the collapse transition at high temperature (evidenced by the granular aspect of the E2 droplets at 45 °C). Due to the accumulation of polymer at the bottom of the droplets, the apparent fluorescence intensity in the

equatorial plane was lower than expected in the case of a uniform distribution of the polymer in the droplets.

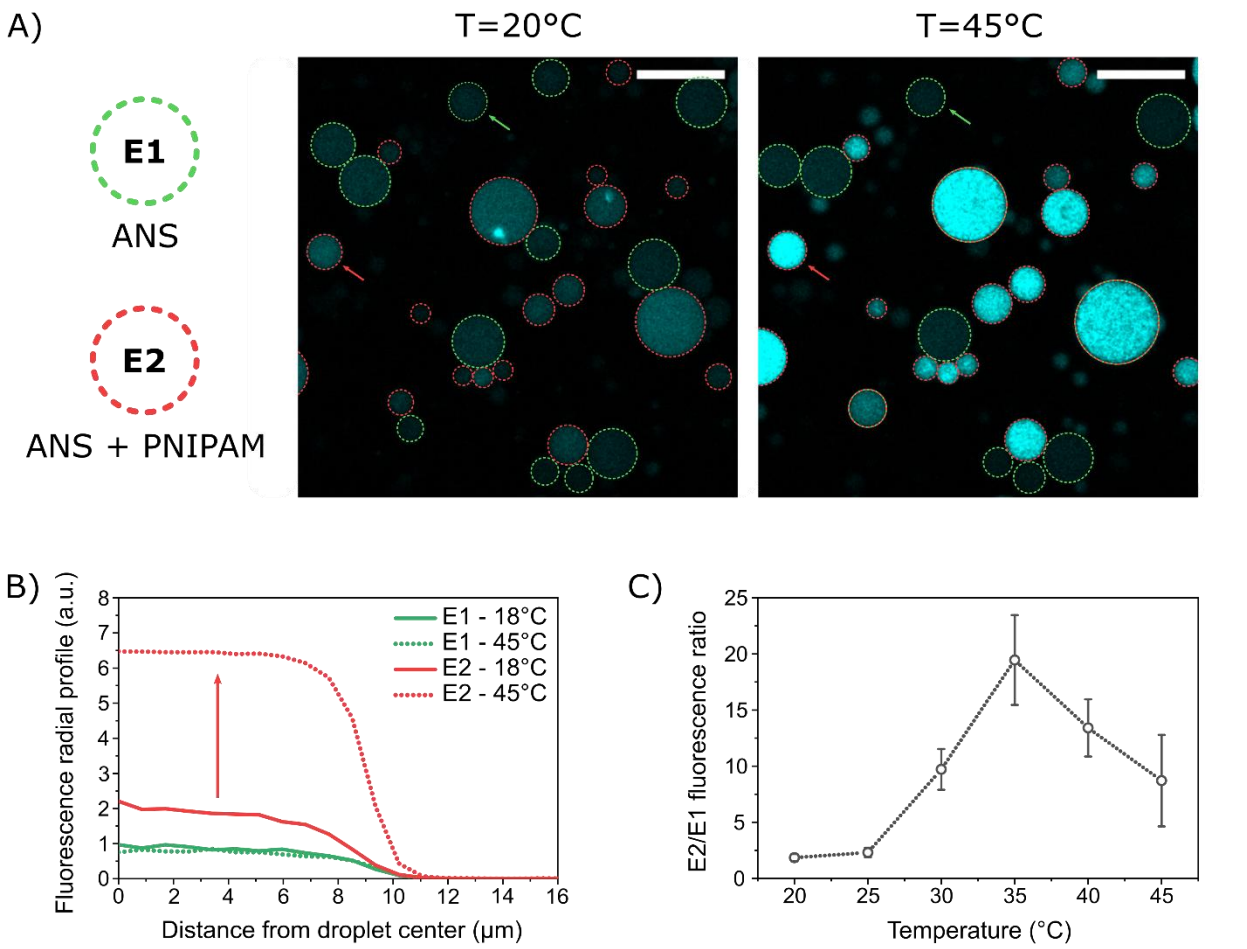

Figure 3.18. ANS fluorescence contrast upon hydrophilic-to-hydrophobic transition of PNIPAM in emulsion. A) Confocal micrographs at 20 °C and 45 °C of a mixture of two emulsions: E1 containing 500 µM ANS in phosphate buffer (droplets encircled in green) and E2 containing 100 µM ANS and 2 wt% PNIPAM in phosphate buffer (droplets encircled in red), both with 0.05 wt% Krytox in the oil phase (scale bars = 50 µm). B) Fluorescence radial profiles of a representative droplet of E1 and E2 (indicated with colored arrows in the top micrographs) at 18 °C and 45 °C. C) Evolution of the fluorescence ratio between E1 and E2 droplets of comparable size with temperature (error bars = standard error on 8 couples of droplets).

The previous results confirmed that the hydrophilic-to-hydrophobic transition of PNIPAM chains can be evidenced in aqueous droplets by an increase in the fluorescence intensity of ANS added in the aqueous phase. To probe the thermal transition of PNIPAM strands grafted on PLL

and in condition of interfacial complexation with Krytox, ANS was added in the aqueous solution of PLL-g-PNIPAM and its fluorescence was monitored upon heating. **Figure 3.19**.A shows confocal micrographs of an emulsion containing 2 wt% of PLL-g-PNIPAM and 500 µM of ANS in the aqueous phase at 20 °C and 45 °C, respectively below and above the cloud point.

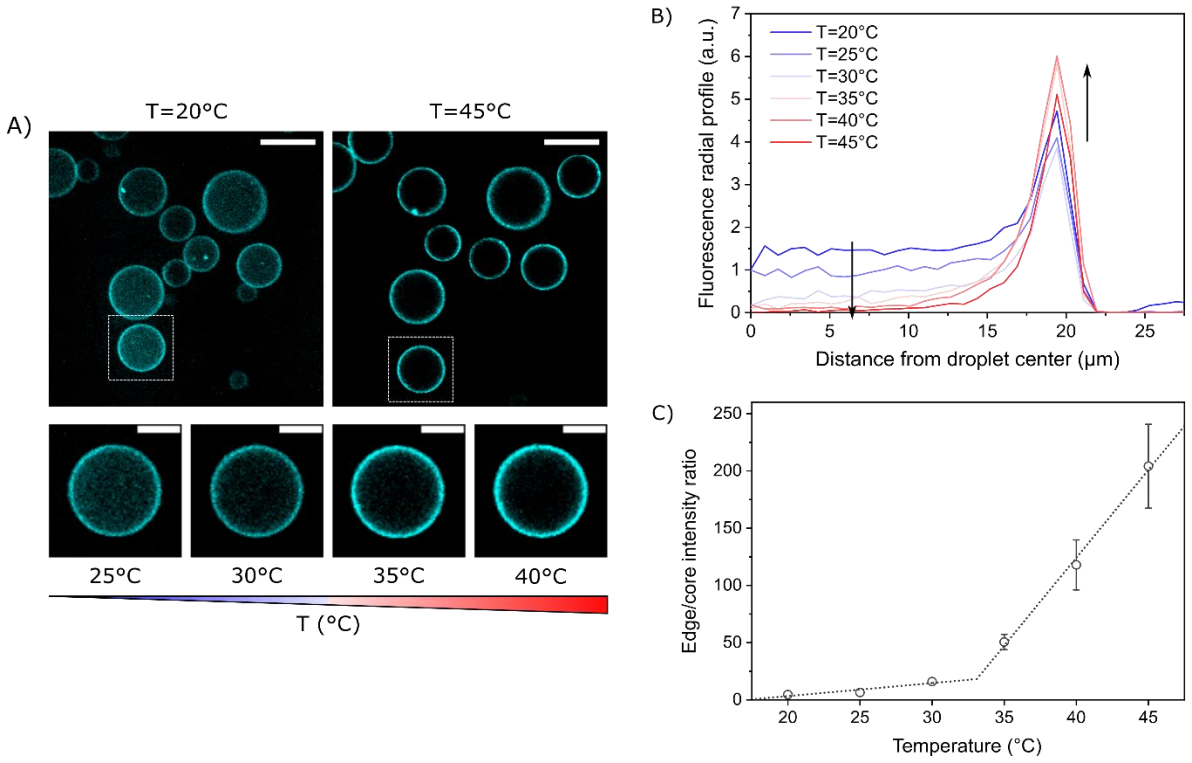

Figure 3.19. Evidence for the thermal collapse transition of PLL-g-PNIPAM in conditions of interfacial complexation. A) Top: Confocal micrographs at 20°C and 45°C of an emulsion containing 2 wt% of PLL-g-PNIPAM and 500 µM of ANS in the aqueous phase and 0.05 wt% of Krytox in the oil phase (scale bars = 50 µm). Bottom: Zoom on the droplet framed in white in the top micrographs, at intermediary temperatures (scale bars = 10 µm). B) Fluorescence radial profiles of the droplet shown in B at increasing temperature. C) Plot of the droplet edge/core intensity ratio – extracted from the fluorescence radial profiles – as a function of the temperature (error bars = standard error on 8 droplets).

At 20 °C the fluorescence signal of ANS in polymer-loaded droplets was non uniform: the intensity was higher at the droplet edge, as highlighted by the sharp peak of fluorescence (~ 3-fold higher than the core level) observed in the radial profile (see **Figure 3.19.**B). This observation, suggesting that the droplet edges are more hydrophobic than the droplet cores, is consistent with

an initial deposition of PLL-g-PNIPAM at the water/oil interface as shown in Figure 3.***9***. As temperature was increased from 20 °C to 45 °C, we observed an increase in fluorescence contrast between the edge and the core of the droplets (see **Figure 3.19**.A), due to a concomitant decrease of intensity in the core and increase of intensity of the peak at the edge (see **Figure 3.19**.B). The ratio between edge and core fluorescence intensities plotted in **Figure 3.19**.C shows a continuous increase with temperature, with a significant change of slope at 34 °C corresponding to the cloud point. The significant values of the edge/core ratio at high temperature (T > 34 °C) confirm the occurrence of the collapse thermal transition of PNIPAM at the water/oil interface at 34 °C. Moreover, the fluorescence level of ANS fell down to almost zero in droplet cores at T > 34 °C, suggesting that PLL-g-PNIPAM chains that were initially soluble in the droplet cores have enriched the interface upon heating.

The reversibility of this process was assessed by submitting an emulsion to temperature cycles while recording the edge/core ratio of ANS fluorescence (see **Figure 3.20**).

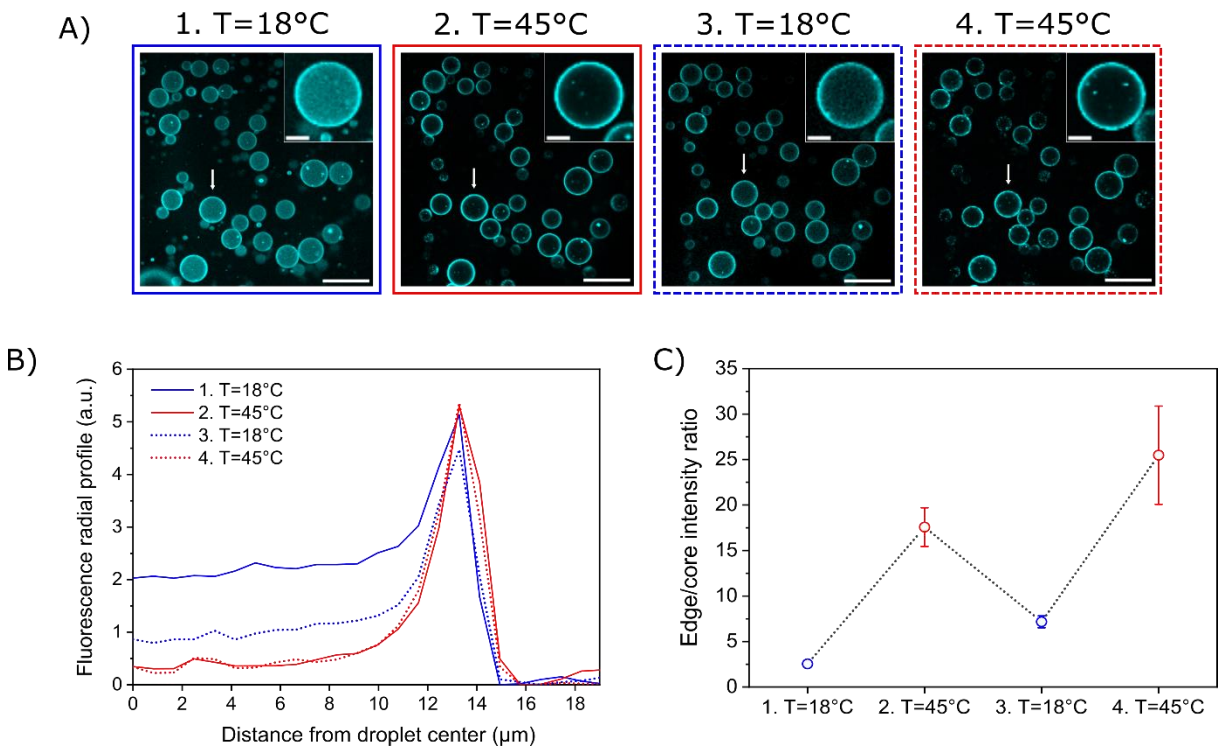

Figure 3.20. Assessment of reversibility of ANS fluorescence in presence of PLL-g-PNIPAM. A) Confocal micrographs of an emulsion with 2 wt% of PLL-g-PNIPAM and 500 µM of ANS in the aqueous phase and 0.05 wt% of Krytox in the oil phase (scale bars = 50 µm). The emulsion was alternatively thermalized at 18 °C (steps 1 and 3, blue frames) and 45 °C (steps 2 and 4, red frames). Inserts: Zoom on the droplet indicated with a white arrow in the micrograph (scale bars = 10 µm). B) Fluorescence radial profiles of the droplet shown in inserts in A (same color code). C) Edge/core fluorescence ratio calculated from the curves in B (same color code, error bars = standard error on 8 droplets).

Initially set at 18 °C, the emulsion was heated up to 45 °C, then cooled back to 18 °C and heated again to 45 °C. In samples brought back to 18 °C, the fluorescence level in the droplet cores slightly increased compared to 45 °C but did not come back to the initial value measured before heating. After the second heating step the fluorescence profile was identical to the one after the first heating step. These observations point out that after a first collapse transition in the interfacial layer, PLL-g-PNIPAM that had accumulated at the droplet edge remained stuck in the interfacial layer and did not significantly redissolve when the sample was brought back below the transition temperature (at least on experimental time scale of ~ 1 hour).

As a control experiment, the same imaging process was performed with a non-thermoresponsive poly(L-lysine)-g-poly(ethylene glycol) (PLL-g-PEG) copolymer with the same 0.20 grafting ratio than PLL-g-PNIPAM. A solution of 2 wt% of PLL-g-PEG and 500 µM of ANS was emulsified in oil phase and the emulsion was observed in confocal microscopy at 18°C and 45 °C (see **Figure 3.21**).

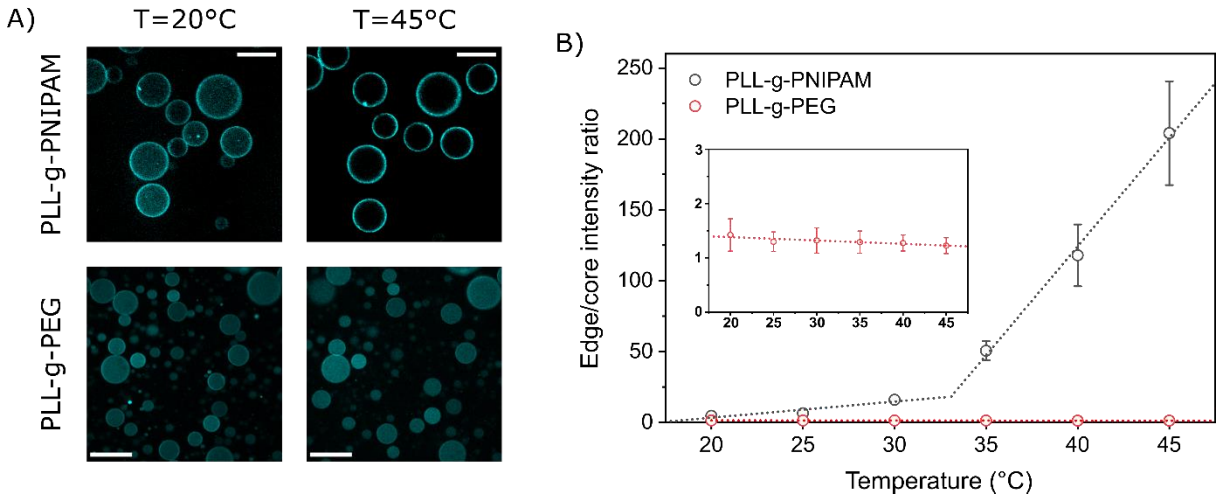

Figure 3.21. Comparison of PLL-g-PNIPAM and PLL-g-PEG regarding ANS fluorescence. A) Confocal micrographs of an emulsion containing 2 wt% of either PLL-g-PNIPAM or PLL-g-PEG and 500 µM of ANS in the aqueous phase, and 0.05 wt% of Krytox in the oil phase, at 20 °C and 45 °C (scale bars = 50 µm for PLL-g-PNIPAM and 30 µm for PLL-g-PEG). B) Edge/core intensity ratio calculated from the radial fluorescence profile of 8 droplets (error bars = standard error) plotted as a function of the temperature for PLL-g-PNIPAM (black) and PLL-g-PEG (red).

After formulation at 18 °C, the droplet edge/core ratio of ANS fluorescence was greater than 1, indicating that PLL-g-PEG has been adsorbed at the water/oil interface by complexation with Krytox, but significantly lower than for PLL-g-PNIPAM, probably because both PLL and PEG moieties are highly hydrophilic. When observed by SEM, the capsules made of PLL-g-PEG at 18 °C looked very similar both in size and effective membrane thickness (see **Figure 3.12** above). Moreover, no significant change of the edge/core ratio in droplets containing PLL-g-PEG was observed between 18 °C and 45 °C, indicating that temperature had no effect on the hydrophobicity of the interfacial polymer layer. These results confirm that the thermo-

responsiveness of PLL-g-PNIPAM highlighted by ANS fluorescence at the droplet edges is intrinsically related to the collapse transition of PNIPAM strands.

The thermo-responsiveness of the PNIPAM strands being preserved once adsorbed at the water/oil interface, we presume that these results illustrate a generic approach for imparting various chemical properties to interfacial polymer layers via the use of the PLL-based comb-like architecture. Other functional polymer strands (such as light- or redox responsive ones) could thus be grafted on PLL to design new functional polymer shells by interfacial complexation.

3.5.3 Effect of droplet radius and temperature on characteristic features of the polymer interfacial layer

To characterize the effect of the temperature on the interfacial polymer layer, we implemented the quantitative fluorescence analysis presented in section 3.4.2 to measure the polymer surface excess in the droplets at low and high temperature. As the fluorescence of carboxy-X-rhodamine (referred to as rho) is neither subject to bleaching[256] nor sensitive to temperature (see **Figure 3.22**), it was used to evaluate the concentration of rho-labeled PLL-g-PNIPAM (PLLrho-g-PNIPAM) in emulsion over temperature changes.

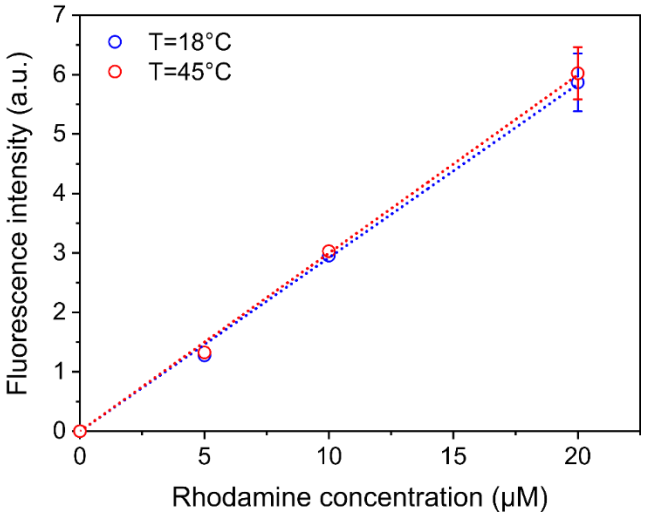

Figure 3.22. Fluorescence intensity of carboxy-X-rhodamine solutions measured with a confocal microscope in the same irradiation conditions at 18 °C and 45 °C.

Figure 3.23.A shows confocal micrographs of a water-in-oil emulsion with water droplets containing 3 wt% of PLLrho-g-PNIPAM at 18 °C and 45 °C. As previously showed in Figure 1, the fluorescence of rho was brighter at the droplet edge, indicating that PLLrho-g-PNIPAM had accumulated at the water/oil interface by conventional SPIC upon the emulsification process. At 45 °C (above the cloud point), the interface was still highly fluorescent, but the fluorescence signal had almost disappeared in the droplet core. This sharp decrease in core intensity upon heating is highlighted in the radial profiles drawn in **Figure 3.23**.A. This observation supports the idea of a thermo-induced transfer of core-soluble PLLrho-g-PNIPAM chains towards the interface, probably related to the progressive immobilization of diffusive chains onto the excess interfacial PLLrho-g-PNIPAM layer via hydrophobic interactions. This hypothesized process is depicted in **Figure 3.23**.B.

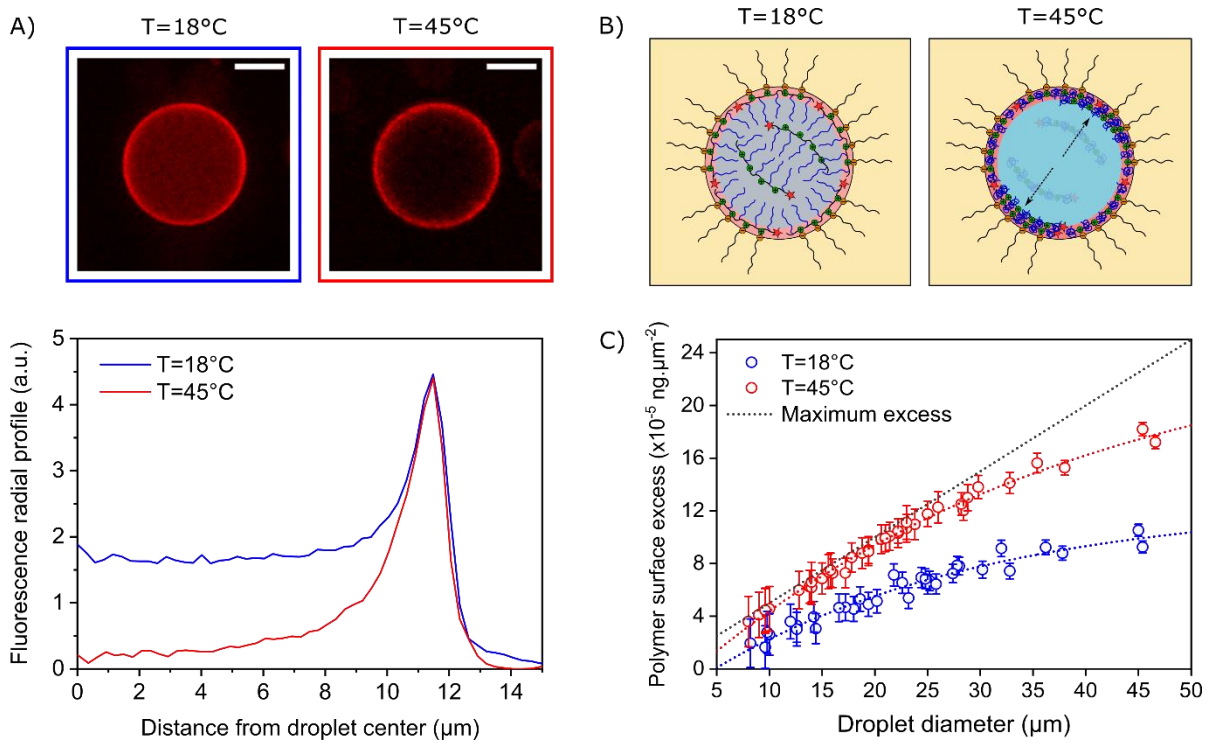

Figure 3.23. Effect of temperature on the amount of interfacial PLLrho-g-PNIPAM. A) Top: Confocal micrographs of a representative water droplet containing 3 wt% of PLLrho-g-PNIPAM dispersed in oil containing 0.05 wt% of Krytox at 18 °C and 45 °C (scale bar = 10 µm). Bottom: Fluorescence radial profiles of the top droplets. B) Schematic illustration of the accumulation of core-soluble PLLrho-g-PNIPAM chains at the droplet surface upon collapse transition in emulsion (occurring at 34 °C). C) Evolution of the surface excess of PLLrho-g-PNIPAM as a function of the droplet diameter at 18 °C and 45 °C, calculated from fluorescence measurements. The maximum surface excess (black dashed line) corresponds to the ideal case of interfacial adsorption of all the PLL-g-PNIPAM chains initially present in the droplet.

From the fluorescence radial profiles of the droplets (as shown in **Figure 3.23**.C), we could define an "apparent" thickness of the interfacial polymer layer as the width at half height of the fluorescence peak at the droplet edge. A mean value of ~ 1.5 µm was measured independently of the polymer concentrations (in the 2-5 wt% range) and at both low and high temperatures (see **Figure 3.24**). Taking into consideration the lack of resolution of fluorescence microscopy, the width of fluorescence peak measured on the confocal micrographs is rather consistent with the thickness observed by SEM (see **Figure 3.12** in section 3.4.1).

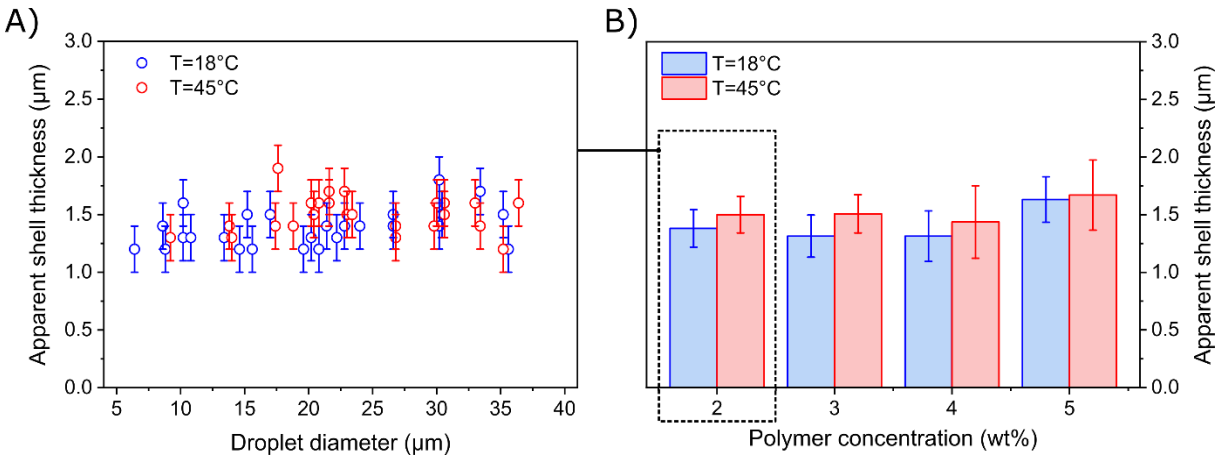

Figure 3.24. Apparent shell thickness measured from fluorescence imaging. A) Fluorescent shell thickness measured on an emulsion containing 2 wt% of PLLrho-g-PNIPAM in the aqueous phase and 0.05 wt% of Krytox in the oil phase at 18 °C and 45 °C. B) Mean shell thickness measured on emulsions with PLLrho-PNIPAM concentration in the range 2-5 wt% (error bars = standard deviation).

The evolution of the polymer surface excess with the droplet diameter at 18 °C and 45 °C is shown in **Figure 3.23**.D. Experimental data were compared to the maximum reachable surface excess, corresponding to the adsorption at the interface of all the polymer chains contained in the droplets. This maximum excess increases linearly with the droplet diameter as it is proportional to the droplet volume/surface ratio. At 18 °C, the experimental surface excess is significantly below the maximum curve and increases with droplet diameter until reaching a plateau for big droplets (> 30 µm). These observations suggest that a significant fraction of the polymer was not involved in interfacial complexation and that a saturation equilibrium between core-soluble and edge-adsorbed chains was presumably achieved at high volume/surface ratios. Interestingly, when switching temperature from 18 °C to 45 °C the surface excess almost doubled at a given droplet diameter. For small droplets (< 30 µm), the surface excess coincides with the maximum excess curve, indicating that all the polymer chains contained in the droplet have been segregated at the water/oil interface. This observation is in agreement with an enrichment of the polymer interfacial layer above the cloud point, confirming the hypothesis of a core draining and an accumulation of polymer chains at the interface via hydrophobic interactions. For big droplets (> 30 µm), the experimental surface excess deviates from the maximum excess curve, suggesting

that a saturation level has been reached in the interfacial complexation process and that a fraction of soluble polymer chains could not be recruited in the interfacial complex layer.

The evolution of surface excess as a function of the residual concentration in droplet cores is shown in **Figure 3.25**. From 18 °C to 45 °C, the fraction of core-soluble polymer chains decreased from 0.4-0.6 to less than 0.1 concomitantly to an increase in the mean surface excess, confirming that (i) a high proportion of polymer chains were not involved in interfacial complexation in conditions of conventional SPIC (at T < 34 °C) and (ii) a massive accumulation of polymer chains at the interface was observed beyond the collapse transition (at T > 34 °C).

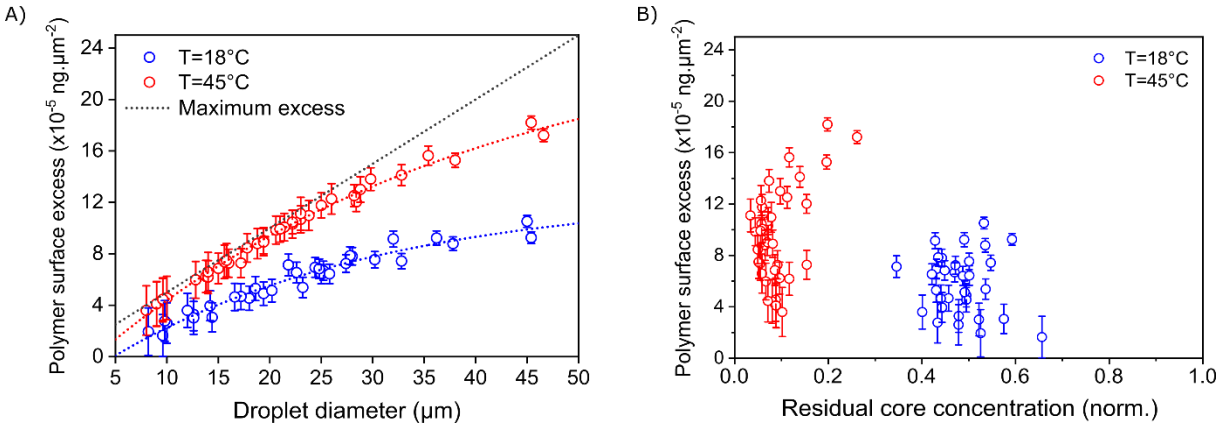

Figure 3.25. Evolution of PLLrho-g-PNIPAM surface excess with droplet diameter (A) and residual core concentration (B) at 18 °C and 45 °C. The emulsion was made of 3 wt% of PLLrho-g-PNIPAM in the water phase and 0.05 wt% of Krytox in the oil phase.

In addition, this process seems to be mainly irreversible as the surface excess remained at the same high level when a sample was cooled back at 18 °C after a first heating step at 45 °C (**Figure 3.26**). This suggests that the enrichment of the interfacial polymer layer is not subject to significant redispersion as PNIPAM chains are brought back below the cloud point.

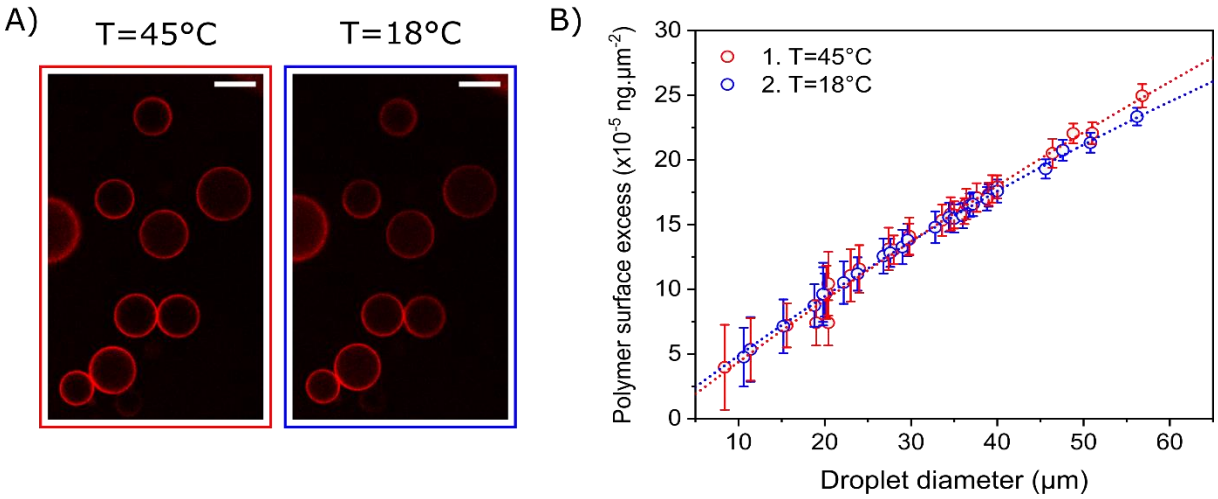

Figure 3.26. Assessment of the reversibility of PLL-g-PNIPAM adsorption at the water/oil interface upon collapse transition. A) Confocal micrographs of an emulsion containing 3 wt% of PLLrho-g-PNIPAM in the aqueous phase and 0.05 wt% of Krytox in the oil phase, heated up at 45 °C and cooled back to 18 °C (scale bars = 20 µm). Thermalization was ensured for 5 min before measurement. B) PLLrho-g-PNIPAM surface excess calculated from the measurement of rhodamine fluorescence in the droplet cores at 45 °C and 18 °C (error bars = propagation of uncertainty).

As a complement, **Figure 3.27** shows the results of polymer surface excess for emulsions containing 2 wt% or 5 wt% of PLLrho-g-PNIPAM in the aqueous phase.

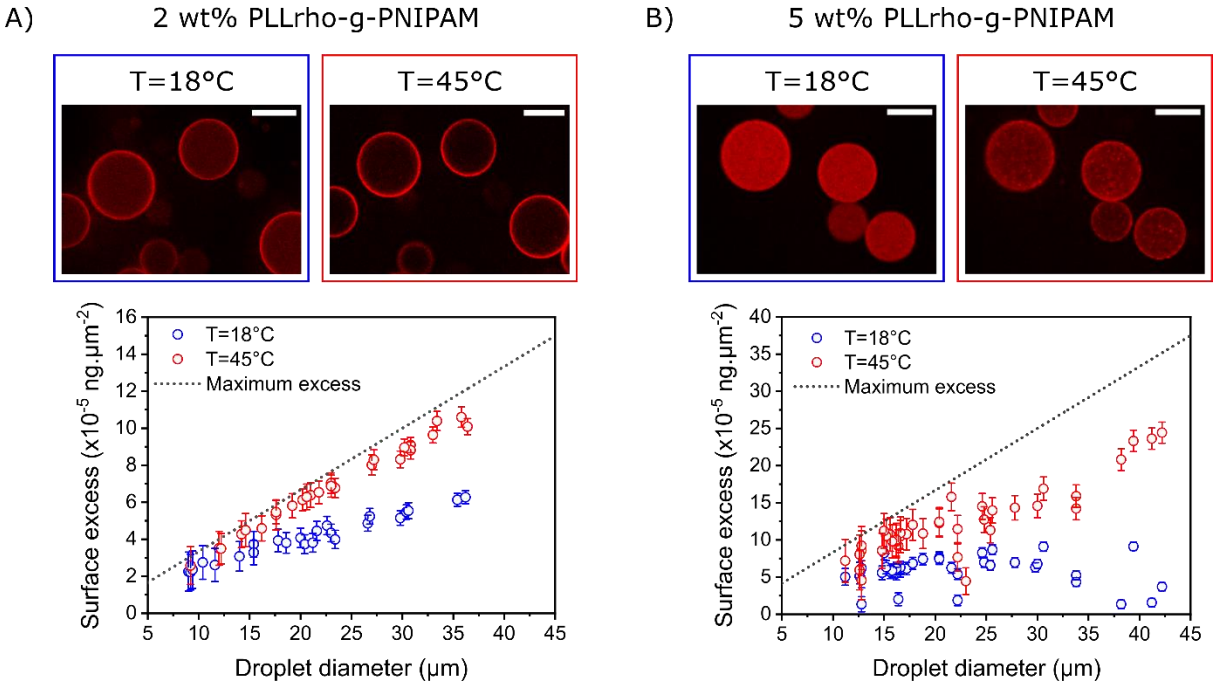

Figure 3.27. Influence of the polymer concentration on the surface excess. Confocal micrographs and evolution of the polymer surface excess as a function of the droplet diameter at 18°C and 45°C for emulsions containing either 2 wt% or 5 wt% of PLLrho-g-PNIPAM in the aqueous phase (A and B respectively).

The results of the emulsion with 2 wt% of polymer are similar to the one of the 3 wt% one presented above: a massive thermo-induced clustering of soluble polymer chains was observed at the droplet periphery upon heating, resulting in an increase of the polymer surface excess at higher temperature (**Figure 3.27**.A). For the emulsion with 5 wt% of polymer, the results are slightly different. First, the fluorescence contrast between the core and the edge of the droplets was hardly detectible at 18 °C, suggesting that the droplets were overloaded with PLLrho-g-PNIPAM to the point where the SPIC-induced deposition at the interface was hidden (the interface was oversaturated). As a consequence, the polymer surface excess deduced from the core fluorescence was well below the maximum reachable surface excess (**Figure 3.27**.B). An increase of the surface excess was observed at 45 °C but was likely due to a polymer sedimentation at the bottom of the droplets than a progressive and uniform accumulation at the surface of the droplets. Indeed, the confocal micrographs at 45 °C revealed the formation of a large amount of polymer aggregates that probably sedimented before reaching the interface by diffusion, causing a decrease of the

fluorescence in the equatorial place of the droplets. This effect was misinterpreted as an increase of the surface excess in the fluorescence quantification process.

Considering only the surface excess below the LCST, the quantitative results are consistent with the qualitative observations made in section 3.4.1 on the influence on the polymer concentration on the morphology of the polymer capsules. At polymer concentrations < 3 wt%, high surface excesses (compared to the reachable maximum) are consistent with the formation of hollow capsules. At polymer concentration > 3 wt%, poor surface excesses (due to the droplet saturation in polymer) is consistent with the formation of filled microparticles (see SEM images in **Figure 3.13**).

As a control of the PNIPAM behavior, the same quantification of the polymer surface excess was performed on a non-thermoresponsive PLL-g-PEG labeled with carboxy-X-rhodamine (PLLrho-g-PEG) and the results are shown in **Figure 3.28**.

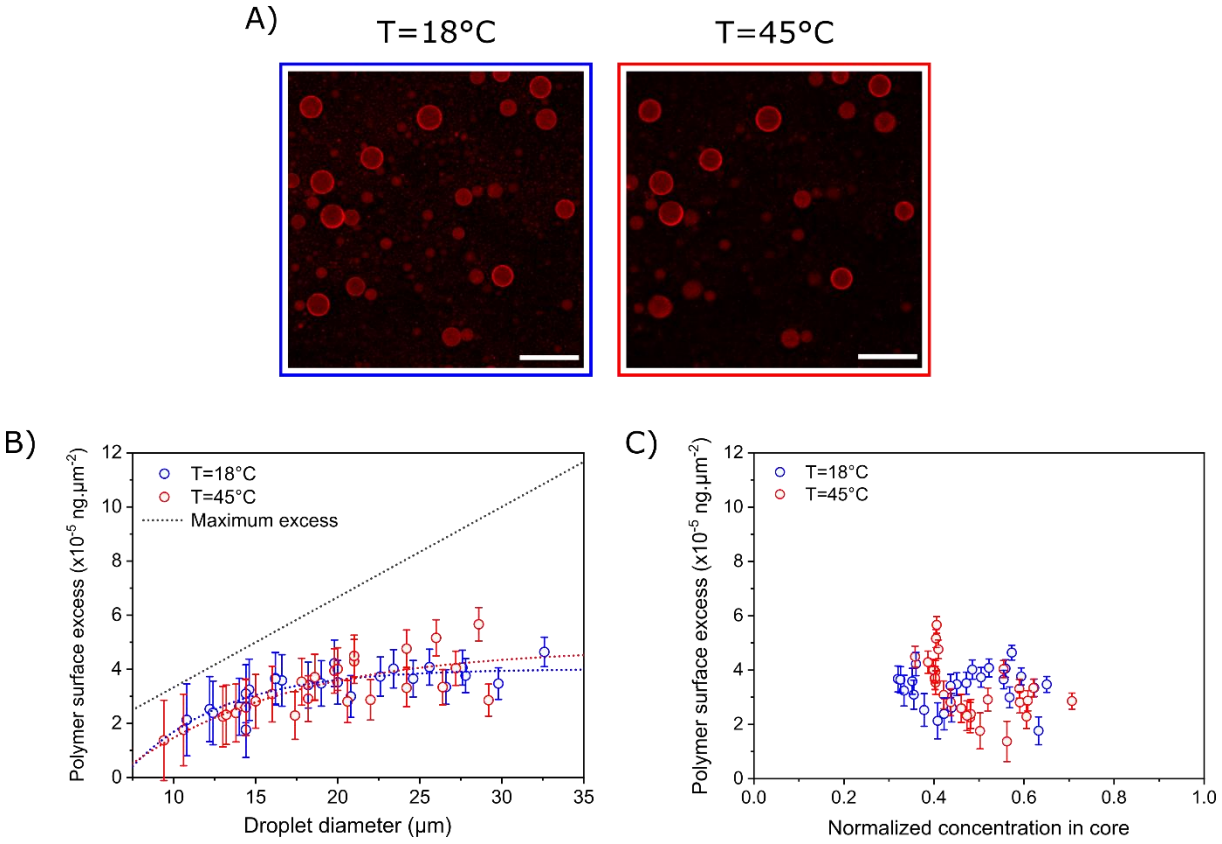

Figure 3.28. Effect of temperature on a non-thermoresponsive PLLrho-g-PEG layer. A) Confocal micrographs of an emulsion containing 2 wt% of PLLrho-g-PEG in the aqueous phase and 0.05 wt% of Krytox in the oil phase, at 18 °C and 45 °C (scale bars = 20 µm). B) PLLrho-g-PEG surface excess calculated from the measurement of rho fluorescence in the droplet cores as a function of the droplet diameter at 18 °C and 45 °C (error bars = propagation of uncertainty). C) PLLrho-g-PEG surface excess as a function of the concentration fraction in the droplet cores at 18 °C and 45 °C.

The curves of surface excess superimpose at 18 °C and 45 °C and plateau at a saturation level which is twice lower than PLL-g-PNIPAM at 18 °C (and 4 times lower at 45 °C) indicating that (i) PLL-g-PNIPAM has a higher affinity with the interface than PLL-g-PEG presumably because PNIPAM strands are shorter than PEG ones (18 vs 44 repeat units/chain respectively) and (ii) there is no effect of the temperature on the distribution of PLL-g-PEG in droplets, confirming that the process observed for PLL-g-PNIPAM is intrinsic to the thermoresponsive nature of PNIPAM strands.

3.5.4 Evidence for thermo-induced enrichment of the polymer shell with extra PNIPAM chains

The results presented in the two last sections suggested that PLL-g-PNIPAM chains can be accumulated at the interface beyond the initial deposition by interfacial complexation. This phenomenon, that we called "thermo-enhanced interfacial complexation" was likely due to the progressive accretion of soluble PLL-g-PNIPAM chains after having reached the hydrophobic state upon heating. To evaluate this hypothesis of thermo-induced accumulation of matter at the interface, we studied the behavior of free PNIPAM chains (non-grafted on PLL) in droplets that also contain PLL-g-PNIPAM. Below the LCST, PLL-g-PNIPAM was expected to form a polymer shell by interfacial complexation, but free PNIPAM chains may have no reason to be involved in this interfacial phenomenon since they were uncharged.

An emulsion was prepared with 1 wt% of coumarin-labeled PLL-g-PNIPAM and 0.5 wt% of Cy3-labeled PNIPAM in the aqueous phase (and 0.03 wt% of Krytox in the oil phase). **Figure 3.29**.A shows the distribution of these two polymer species in a representative droplet at 18 °C and at 45 °C.

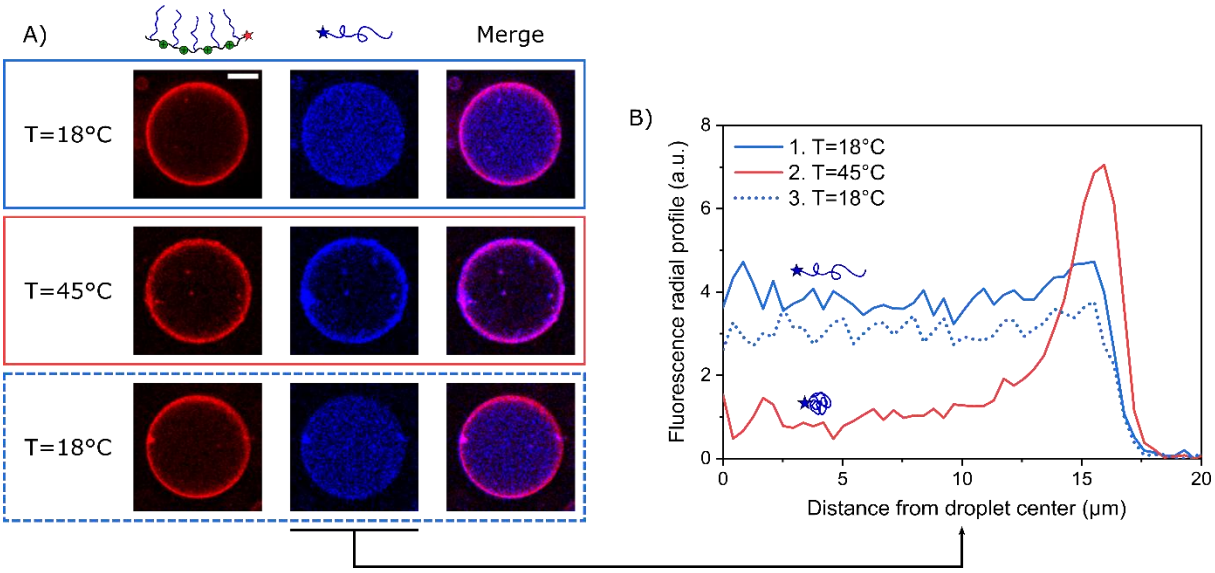

Figure 3.29. Thermo-induced accumulation of free PNIPAM chains into the PLL-g-PNIPAM shell. A) Confocal micrographs of a representative droplet containing 1 wt% coumarin-labeled PLL-g-PNIPAM (red) and 0.5 wt% Cy3-

labeled PLL-g-PNIPAM (blue) at 18 °C, 45 °C and 18 °C successively (scale bar = 10 µm). B) Fluorescence radial profiles indicating the distribution of free PNIPAM chains (Cy3 channel) at the different temperatures.

At 18 °C, PLL-g-PNIPAM (in red) was located at the droplet periphery and free PNIPAM (in blue) was uniformly distributed in the droplet core, what is consistent with the fact that interfacial complexation can occur for cationic PLL-g-PNIPAM and not for neutral PNIPAM. At 45 °C, the fluorescence of free PNIPAM has almost disappeared from the droplet core and has accumulated at the droplet periphery as indicated by the formation of a bright corona. This result is highlighted in the fluorescence profiles shown in **Figure 3.29**.B and suggests the thermo-induced accumulation of hydrophobic chains at the water/oil interface works also for free PNIPAM chains. Upon the collapse transition of the PNIPAM strands, the interfacial layer of PLL-g-PNIAPM became hydrophobic and "sticky". Free PNIPAM chains turned also to their hydrophobic and aggregative state. Upon diffusion from the droplet core to the droplet edge, free PNIPAM chains remained trapped in the interfacial layer by hydrophobic interactions, leading to a progressive accumulation of polymer at the interface.

As a control, an emulsion containing only Cy3-labeled free PNIPAM chains (an no PLL-g-PNIPAM) in the aqueous phase was observed in confocal microscopy at 18 °C and 45 °C (see **Figure 3.30**). At 18 °C the uniform distribution of polymer chains in the droplet cores was observed as expected. At 45 °C, no evidence of polymer accumulation at the edge of the droplets was noticed but the formation of hydrophobic polymer aggregates was clearly visible in the core of the droplets. The progressive sedimentation of these micrometric aggregates at the bottom of the droplets could explain the decrease of the core fluorescence detected upon heating, as highlighted in the fluorescence radial profiles in **Figure 3.30**.B.

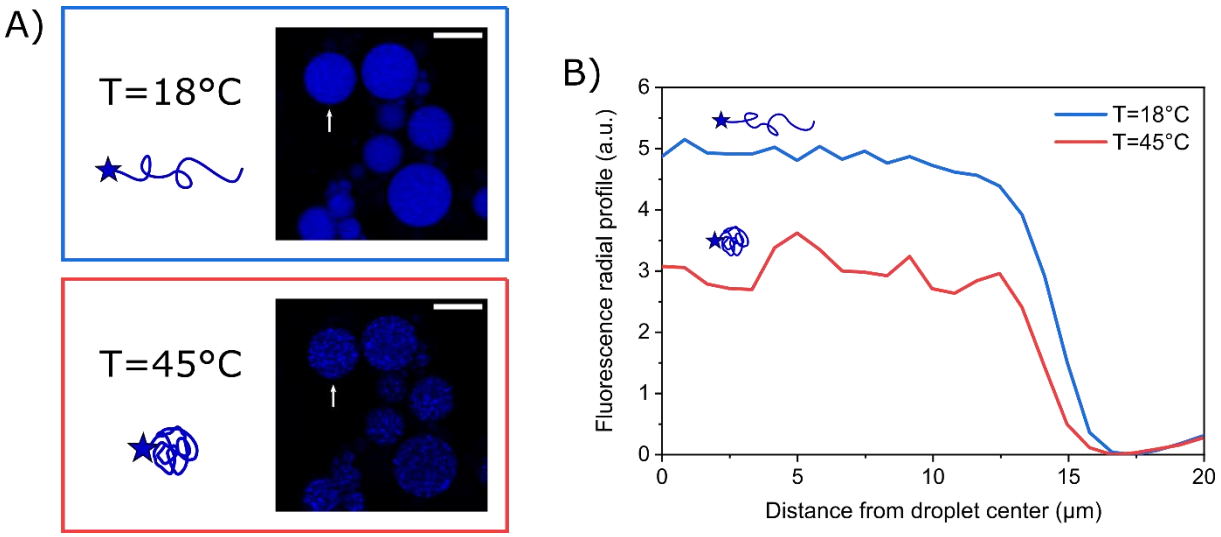

Figure 3.30. Thermal behavior of free PNIPAM chains in droplets. A) Confocal micrographs of an emulsion containing 2 wt% of Cy3-labeled PNIPAM in the aqueous phase at 18 °C and 45 °C (scale bars = 30 µm). B) Fluorescence radial profiles of the droplet indicated with a white arrow in the micrographs.

These results confirm that the hydrophilic-to-hydrophobic transition of the PLL-g-PNIPAM shell – initially formed by interfacial complexation – enables to drive the accumulation of polymer chains towards the interface upon gentle heating. This phenomenon can be viewed as a thermo-induced enrichment of the shell since it can involve free polymer chains that were initially dispersed in the core of the droplets. The example of thermo-accumulation of free and neutral PNIPAM chains (non-grafted on PLL) suggests that the massive polymer clustering at the interface is likely due to hydrophobic interactions and not to electrostatic complexation with Krytox. This phenomenon turned out to be reversible as the free PNIPAM chains were redispersed in the core of the droplets after cooling back the emulsion below the cloud point (see **Figure 3.29**).

3.6 Encapsulation of a model protein in the aqueous core

The possibility to encapsulate proteins in PLL-g-PNIPAM core-shell droplets was tested using eGFP (enhanced Green Fluorescent Protein) as a fluorescent model protein. The eGFP was kindly provided by a colleague (R. Chouket), who produced and purified it according to a protocol described in the literature.[257]

An aqueous solution containing 2 wt% of coumarin-labeled PLL-g-PNIPAM and 10 µM of eGFP was prepared in phosphate buffer (pH = 7.3) and emulsified in oil containing 0.03 wt% of Krytox. The polymer and protein distributions within droplets were determined by confocal imaging at 18 °C and 45 °C (see **Figure 3.31**).

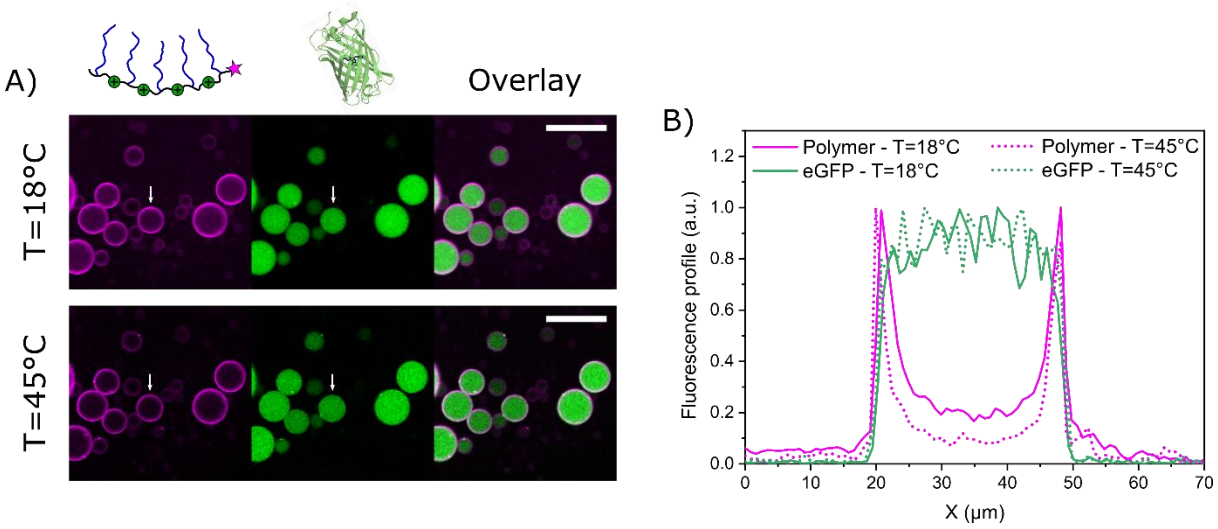

Figure 3.31. Encapsulation of eGFP in PLL-g-PNIPAM capsule precursors. A) Confocal micrographs of an emulsion containing 1 wt% of PLLcoum-g-PNIPAM and 10 µM of eGFP in the aqueous phase and 0.03 wt% of Krytox in the oil phase, at 18 °C and 45° C (scale bars = 50 µm). B) Fluorescence profiles of the representative droplet indicated by a white arrow in the micrographs.

The bright coumarin fluorescence signal at the droplet edge shows that PLL-g-PNIPAM was concentrated at the water/oil interface as expected, demonstrating that the presence of the protein in the aqueous phase did not affect the formation of the interfacial polymer layer induced by complexation with Krytox. The uniform distribution of eGFP within droplets showed that the protein had been efficiently encapsulated in the aqueous droplet cores. The overlay of confocal images clearly shows the "core-shell" distribution of the species, with the polymer at the droplet edge and the protein entrapped in the droplet core. The high fluorescence signal of the protein as well as the absence of visible protein aggregates suggest that the integrity of the protein has been preserved upon encapsulated and even after heating at 45 °C.

As a first approximation, the preservation of the protein integrity may be quantified by comparing the fluorescence level in the droplets with the fluorescence level of the initial protein

solution. For that, the normalized core concentration was calculated with the fluorescence calibration method described in section 3.4.2. Briefly, the fluorescence level of eGFP in the droplets was normalized by the fluorescence level of the bulk aqueous solution and corrected by the geometrical factor measured on Cy-3 labeled PNIPAM-Cy3 (accounting for size and curvature biases). Around 70-75 % of the eGFP initial fluorescence was detected in droplets bigger than 25 µm (see **Figure 3.32**), indicating that the protein had not been dramatically denatured during the encapsulation in water droplets. In droplets smaller than 25 µm, the higher loss of fluorescence intensity in water droplets may be reasonably attributed to optical distortion of the fluorescence signal (not compensated by the correction process) and to bleaching of eGFP, rather than to a significant alteration of eGFP.

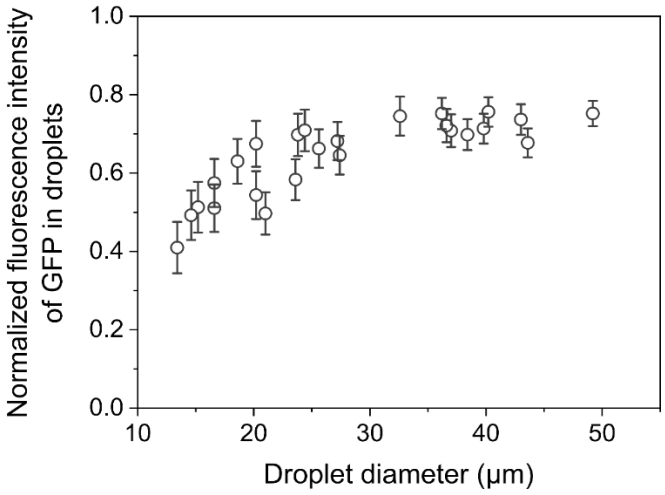

Figure 3.32. Normalized fluorescence level of eGFP in an emulsion containing 1 wt% of coumarin-labeled PLL-g-PNIPAM and 10 µM of eGFP in the aqueous phase and 0.03 wt% of Krytox in the oil phase.

3.7 Conclusion

In this chapter, we evidenced the ability of PLL derivatives to form concentrated polymer layers at the surface of water droplets by interfacial complexation with a surfactant (Krytox) across the water/oil interface of inverse emulsion in fluorocarbon oils. We showed that the tight PLL/Krytox interaction led to a strong decrease of the water/oil interfacial tension, allowing the formation of stable inverse emulsions.

We synthetized PLL-g-PNIPAM and PLL-g-PEG comb-like copolymers via the grafting of PNIPAM and PEG strands onto PLL. We showed that the interfacial complexation of these polymers with Krytox could lead to the formation of hollow polymer microcapsules – provided the optimization of the formulation – with a polymer shell thickness of ~1 µm and an aqueous core of controlled pH and ionic strength. In mild conditions of formulation, a model protein could be readily encapsulated in the core of the droplets without interfering with the formation of the polymer shell, demonstrating that our approach is promising for the storage of potentially fragile biomolecules.

In the case of PLL-g-PNIPAM, we showed that the thermoresponsive behavior of PNIPAM strands – switching from hydrophilic coils to hydrophobic globules at a cloud point of 34°C – was preserved in the interfacial complexation state, suggesting that thermo-responsiveness was successfully imparted in the polymer shells. In addition, the LCST transition of PNIPAM strands was used to thermo-induce an additional accumulation of polymer chains on the pre-formed interfacial layer of PLL-g-PNIPAM. Above the temperature of collapse transition, we observed a massive clustering of PLL-g-PNIPAM at the edge of the droplets, likely due to hydrophobic interactions between PNIPAM strands (**Figure 3.33**). This process contributed to enrich the interfacial polymer layer as demonstrated by the increase in polymer surface excess measured from fluorescence images. Interestingly, the persistence of high surface excesses when droplets were cooled back to room temperature suggests that the thermo-induced accumulation of polymer chains in the shell wall was irreversible.

This thermo-induced polymer accumulation was also successfully implemented on free PNIPAM chains that could not be involved in primary interfacial complexation (as non-grafted onto PLL cationic chains). Upon heating, a massive accretion of free PNIPAM chains was

observed onto the germinal interfacial PLL-g-PNIPAM layer. This process turned out to be reversible as the free PNIPAM chains turned out to redisperse in the core of the droplet after cooling the sample back to ambient temperature. These results suggest that materials can be easily captured and released from interfacial layers of PLL derivatives and thus open new perspectives in the design of more complex and functional polymer shells. These perspectives will be explored in Chapter 2 with the design of polymer shells that can incorporate nanoparticles.

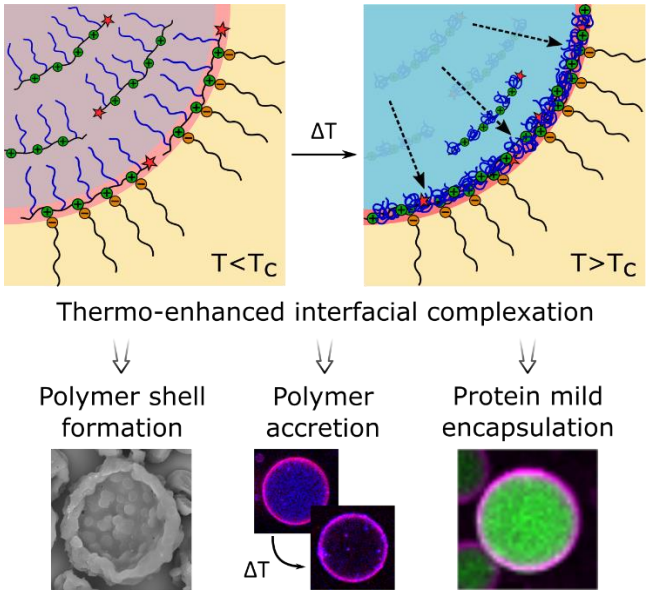

Figure 3.33. Phenomenon of "thermo-induced interfacial complexation" described in this Chapter.

Chapter 4

Formation of polymer-nanoparticles mixed capsules by interfacial complexation

4.1 Introduction

In Chapter 3, we showed that thermo-responsive polymer shells, made of PLL-g-PNIPAM, can be readily formed by interfacial complexation in water-in-oil emulsions and in mild conditions. We showed that the collapse transition of PNIPAM chains localized in the polymer shell can induce the interfacial accumulation of PNIPAM chains that are soluble in the core of the emulsion droplets, and named this phenomenon "thermo-enhanced interfacial complexation". In this Chapter, we will extend this phenomenon to the interfacial segregation of nanoparticles in order to design "composite" or "hybrid" polymer-particles shells.

The incorporation of nanoparticles (NPs) in the shell of polymer capsules or vesicles has been extensively explored in the literature. A first advantage provided by the presence of NPs is the improvement of the mechanical stability of the shell, due to the intrinsic mechanical properties of the NPs and/or their role of physical cross-links between polymer chains.[258] For delivery applications, the introduction of NPs can be advantageous to modulate the permeability of the carrier,[259] and to limit the undesired "burst release effect" in biological conditions.[260] The introduction of NPs also enables to impart new functionalities in the polymer container, especially additional stimuli-responsiveness. For instance, gold nanoparticles can be used as light-to-heat converters at the nanoscale and can be used to trigger thermal transition upon light irradiation (see Chapter 1). Magnetic nanoparticles (such as iron oxides) have also been introduced in polymer capsules to trigger on demand release upon application of an alternative magnetic field.[261]

The incorporation of NPs in polymer shells can be achieved via different strategies:

- Metal NPs can be grown within the polymer shell by reduction of soluble precursors that have impregnated the polymer scaffold. This strategy has been used to load polymer shells with silver or gold NPs for instance.[262,263] The reduction process can also be specifically directed at the outer surface of the capsules, which can be interesting for further catalysis applications.[264,265] This strategy of *in situ* reduction has also been implemented in the membrane of polymersomes[259] or in the core of microgels.[266]
- Pre-formed NPs can be adsorbed at the surface of the compartments, as it has been demonstrated on polymer capsules[267] and more importantly on microgels.[268,269]

- NPs can be embedded in the polymer shell during its formation. An important illustration of this approach is the formation of layer-by-layer capsules by alternative deposition of polymer chains and NPs.[270]
- NPs can be self-assembled at the surface of emulsion droplets prior to the formation a polymer shell via classical emulsion-based processes (especially interfacial polymerization). This strategy has been used to produce composite polymer capsules that incorporate TiO_2, gold, or silica nanoparticles.[271–273]

As an alternative to these conventional methods, we showed that our system based on interfacial complexation of PLL-g-PNIPAM offers a straightforward way to incorporate NPs in the polymer shell. We demonstrated that, upon adsorption of PLL derivatives on the surface of the NPs, the latter can participate to the thermo-induce accumulation of the polymer at the interface, resulting in the formation of a polymer-NPs mixed shells simply by heating.

In a first approach, fluorescent NPs were used to visualize the distribution of the particles in the droplets upon thermal response of the polymer. Then, gold NPs were used as a promising additive to trigger the phase transition of PLL-g-PNIPAM by thermoplasmonic excitation, extending the stimuli-responsiveness of the system. For this photo-thermal application, the issue of measuring temperature at low scales with high spatial resolution will be discussed before precisely focusing on a particular microscopy method enabling to retrieve the temperature increase generated by plasmonic systems. The power of this method will be demonstrated on experimental examples of temperature measurements *in situ* in emulsion containing both polymer and gold nanoparticles.

4.2 Interactions between PLL derivatives and nanoparticles

4.2.1 Gold nanoparticles (AuNPs)

We used two types of commercial gold NPs (AuNPs): bare AuNPs (the surface is actually occupied by residual citrate groups that are highly labile complexing agents) and AuNPs coated with poly(viny pyrrolidone) (PVP) that ensure steric stabilization of NPs.

The aggregation of AuNPs in presence of additives can be easily revealed by UV-Vis spectrophotometry. Indeed, non-aggregated spherical AuNPs exhibit a sharp absorbance peak at 532 nm, corresponding to the localized plasmon resonance. Upon aggregation, this peak in the green range progressively disappeared in favor of a red-shifted peak which is characteristic of plasmon resonance in elongated AuNPs.[274] UV-Vis spectra of AuNPs solutions in presence and absence of PLL were thus compared. This simple qualitative experiment was performed for both bare and PVP-coated NPs solutions, with PLL concentrations in the wt% range (typically used in the experiments of capsule formations).

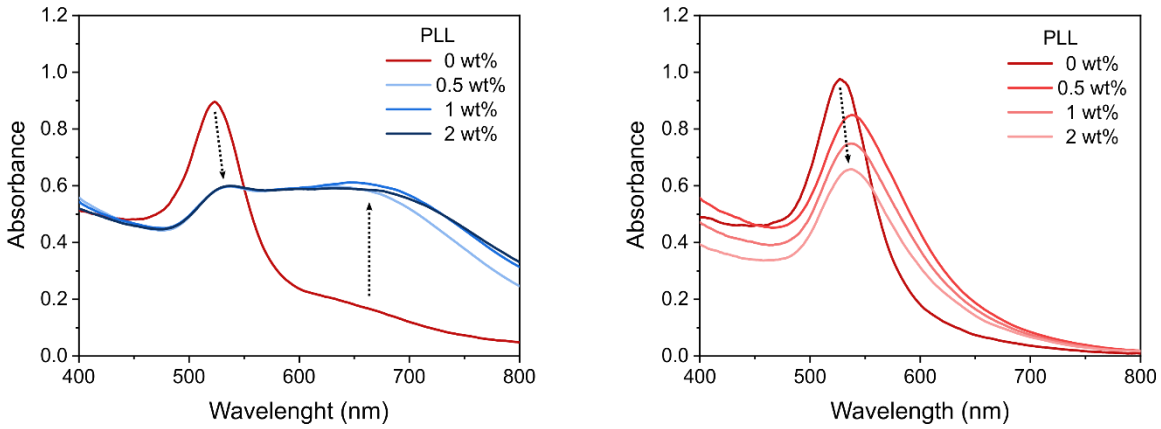

Figure 4.1. UV-Vis spectra of bare AuNPs (*left*) and PVP-coated AuNPs (*right*) solutions containing various concentrations in PLL.

For mother solutions of bare and PVP-coated NPs, the plasmon peak at 530 nm was well defined (in dark red, corresponding to the real color of the commercial AuNPs solutions). When PLL is

added – at any concentration – in the solution of bare AuNPs, the intensity of the 530-nm peak drastically decreased and a broad bump appeared at higher wavelengths. This red-shift is typical of anisotropic aggregates of AuNPs and was also evidenced by a color switch of the solution from dark red to blue. This phenomenon was expected since these bare AuNPs have a zeta potential of – 52 mV (according to the data sheet), favoring the adsorption of cationic PLL at their surface, eventually inducing their aggregation by inter-particle bridging.

For PVP-coated AuNPs, the addition of PLL did not change the shape of the initial spectrum, except that a slight shift of the peak to 538 nm and a slight decrease of its intensity can be noticed. The preservation of the plasmon resonance characteristic of spherical AuNPs suggests that the presence of PLL did not induce their aggregation. This high stability can be attributed to the presence of the PVP coating that probably hinders the adsorption of PLL at the surface of the AuNPs (despite their negative zeta potential of – 33 mV).

To confirm these results, the effective size of the aggregates was measured by dynamic light scattering (DLS) for both bare and PVP-coated AuNPs solutions containing various amount of PLL (see **Figure 4.2**).

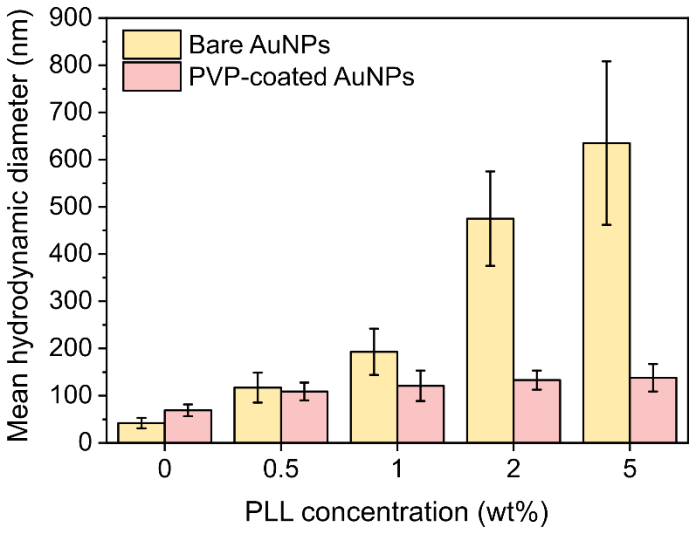

Figure 4.2. Effective hydrodynamic diameters of objects measured by DLS in solution of AuNPs containing various amount of PLL.

For initial solution of AuNPs (in absence of PLL), the hydrodynamic diameters measured by DLS were consistent with the data sheet: ~ 40 nm for bare AuNPs and ~ 70 nm for PVP-coated AuNPs (the Au core in itself has a diameter of 50 nm according to TEM data but the presence of the PVP coating increases the effective diameter which is measured by DLS). The addition of PLL induces a slight increase of the effective diameter for PVP-coated AuNPs up to 100-150 nm, suggesting a limited aggregation. For bare AuNPs solutions, the increase of PLL concentration induces a continuous increase of the effective mean diameter (up to ~ 650 nm for 5 wt% of PLL) and a concomitant broadening of the size distribution, indicating a massive clustering of the AuNPs in presence of PLL. These results are consistent with the UV-Vis measurements and tend to validate the propensity of PLL to adsorb on bare NPs and almost not on PVP-coated AuNPs.

Because the addition of PLL on bare AuNPs leads to a spontaneous and uncontrolled colloidal aggregation, the use of PVP-coated AuNPs will be privileged in the rest of the experiments involving AuNPs.

4.2.2 Surface-functionalized polystyrene nanoparticles

We also used two types of commercial fluorescent polystyrene NPs with different surface modifications: NeutrAvidin-modified polystyrene NPs (NeutravNPs) and carboxylate-modified polystyrene NPs (CarboxyNPs). At physiological pH, the surface of NeutravNPs is expected to be almost neutral (the pI of the NeutrAvidin protein being of 6.3) and the surface of CarboxyNPs is expected be highly anionic (the pKa of carboxylic acids being around 4). Contrary to gold nanoparticles, the absorbance of fluorescent commercial NPs (NeutravNPs and CarboxyNPs) is not sensitive to the aggregation state of the NPs (the fluorophore being buried in the core of the NPs). UV-Vis was thus inappropriate to probe the interaction between NeutravNPs or CarboxyNPs with PLL. As an alternative, zeta potential measurements were used to assess the modification of the surface charge of the NPs after incubation with PLL chains at pH = 7.3. For these experiments, NPs with a diameter of 200 nm were used in order to facilitate the removal of excess polymer chains by filtration on Amicon device after the incubation step (see Material and methods). The zeta potential distributions for the two types of nanoparticles before (commercial solutions) and after incubation with PLL (PLL-g-PNIPAM-coated NPs) are shown in **Figure 4.3**.

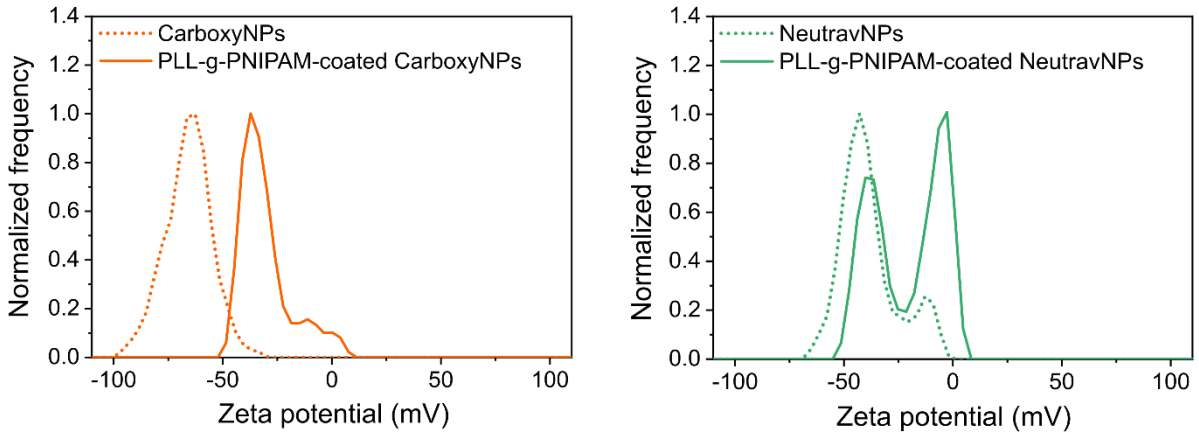

Figure 4.3. Zeta potential distributions of 200-µm CarboxyNPs (left) and NeutravNPs (right) from commercial solutions (dashed lines) and after incubation with PLL solutions (solid lines). The distributions are the average of three measurements by sample.

Both commercial NeutravNPs and CarboxyNPs are highly anionic with a distribution of the zeta potential centered around –42 mV and –64 mV respectively. This value is not surprising for CarboxyNPs since surface carboxylic acids are deprotonated at pH = 7.3. The anionic character of NeutravNPs is less pronounced since Neutravidin is only slightly negatively charged at pH = 7.3 (pI = 6.3). A fraction of the sample even exhibits near neutral surface charge as suggested by a small shoulder observed around –11 mV in the zeta potential distribution. After incubation of the NPs with PLL and filtration of the polymer excess, a shift of the zeta distribution towards "less negative" values was observed for both types of NPs. This effect can be attributed to a significant adsorption of cationic PLL chains at the surface of the NPs, hence increasing their surface charge by partial compensation of the initial anionic charges. For CarboxyNPs, the distribution has been shifted around –37 mV with a small shoulder reaching neutral values. For NeutravNPs, two populations of same magnitude have appeared, one still negatively charges around –38 mV and one near neutral around –5 mV. This partially efficient adsorption of PLL suggests that the NeutrAvidin surface coverage is non-uniform within the NPs sample. In any case, PLL apparently develops electrostatic interactions with negatively-charged surface-modified polystyrene nanoparticles, as it did with bare AuNPs. This ability of PLL to bind to anionic surface has already

been reported in the literature for various types of materials including silica, ceramics, plastics such as polystyrene, protein particles, etc.[275–278]

The adsorption of PLL on NPs is not necessarily prejudicial *per se* (as long as it does not destabilize the NPs solution). However, it implies that *functional* PLL derivatives such as PLL-g-PNIPAM may also coat anionic NPs. In that case, since PNIPAM chains become hydrophobic at high temperature, PLL-g-PNIPAM-coated NPs may undergo aggregation upon heating via inter-coating hydrophobic interactions, as already demonstrated in previous works.[278] This process has been assessed for "naked" and PLL-g-PNIPAM-coated NeutravNPs and CarboxyNPs by monitoring the evolution of their hydrodynamic diameter by DLS upon heating. To evidence any aggregation process occurring upon the LCST transition of PNIPAM, the mean hydrodynamic diameter measured at each temperature was normalized by the initial diameter value of ~ 200 µm obtained at 20 °C (see **Figure 4.4**).

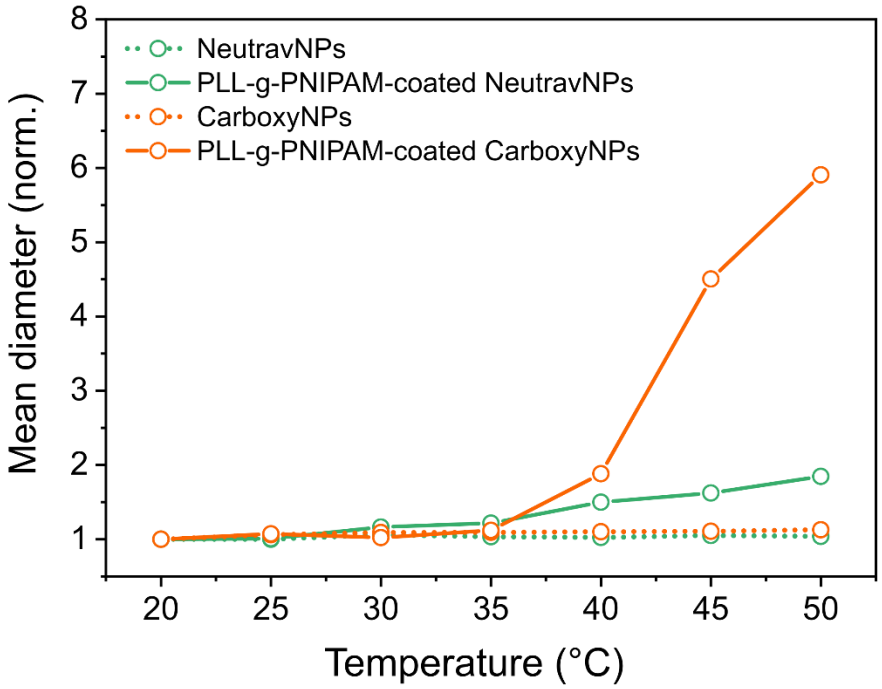

Figure 4.4. Evolution of the mean effective diameter measured by DLS in NPs solution upon heating. The effective diameter has been normalized by its initial value of 200 µm (at 20 °C) to evidence the progressive aggregation of PLL-g-PNIPAM-coated NPs compared to non-coated NPs.

For initial NPs solutions, the diameter was constant at each temperature between 20 °C and 50 °C, indicating that the initial colloidal solutions are stable upon heating. For PLL-g-PNIPAM-coated nanoparticles, the mean diameter measured in the samples is increasing continuously from 35 °C to 50 °C. As this trend starts at a temperature that corresponds to the cloud point of PLL-g-PNIPAM (see Chapter 1), this process can be reasonably attributed to a progressive agglomeration of NPs driven by hydrophobic interactions between the PLL-g-PNIPAM layers that decorate their surface. The amplitude of this phenomenon is markedly higher for CarboxyNPs than for NeutravNPs. Indeed the effective diameter of the aggregates at 50 °C is 6 times the diameter of the individual NPs in the case of CarboxyNPs, corresponding to an aggregation number of ~ 160 NPs/aggregate (calculated as $0.74 \times \left(\frac{d_{\mathrm{agg}}(T=50°C)}{d_{\mathrm{NP}}(T=20°C)}\right)^3$ in a model of compact stacking of hard spheres). Conversely, in the case of NeutravNPs, the effective diameter is only 2 times the initial one meaning that the aggregates contain roughly 6 NPs. These results confirm that (i) PLL-g-PNIPAM can adsorb at the surface of anionic nanoparticles without significant destabilization below the LCST of PNIPAM, (ii) the hydrophilic-to-hydrophobic transition of the PLL-g-PNIPAM coating induces the aggregation of the NPs above the LCST, and (iii) the adsorption of PLL-g-PNIPAM seems more efficient on CarboxyNPs than on NeutravNPs since the aggregation process is more pronounced. This last point is consistent with a partial adsorption of PLL on NeutravNPs as previously suggested by a double distribution of zeta potential.

Regarding the initial goal of incorporating NPs in polymer capsules formed by interfacial complexation, the possibility to coat NPs with PLL-g-PNIPAM can actually be advantageous. As shown in Chapter 1, hydrophobic PNIPAM can be accumulated in pre-formed PLL-g-PNIPAM shells upon heating. As PLL-g-PNIPAM-coated NPs tend to form hydrophobic aggregates, we could expect their accumulation in PLL-g-PNIPAM shells as well. This phenomenon will be investigated by confocal microscopy on fluorescent NPs in the next section.

4.3 Design of composite polymer shells by interfacial complexation

4.3.1 Incorporation of AuNPs in PLL-g-PNIPAM shells

Because AuNPs are not fluorescent, their precise localization in PLL-g-PNIPAM capsules formed by interfacial complexation could not be probed by fluorescence microcopy. However, as AuNPs are metallic, their incorporation in PLL-g-PNIPAM capsules may be evidenced on SEM images by contrast with the polymer matrix.

The capsules were formed and observed by SEM according following the protocols described in Chapter 1. Briefly, an aqueous solution was prepared by mixing 1 wt% of PLL-g-PNIPAM with 0.05 wt% of 50-nm PVP-coated AuNPs in phosphate buffer, and then emulsified in FC-70 oil phase containing 0.03 wt% of Krytox to form aqueous-core polymer capsules by interfacial complexation. SEM imaging of dried capsules are shown in **Figure 4.5**.

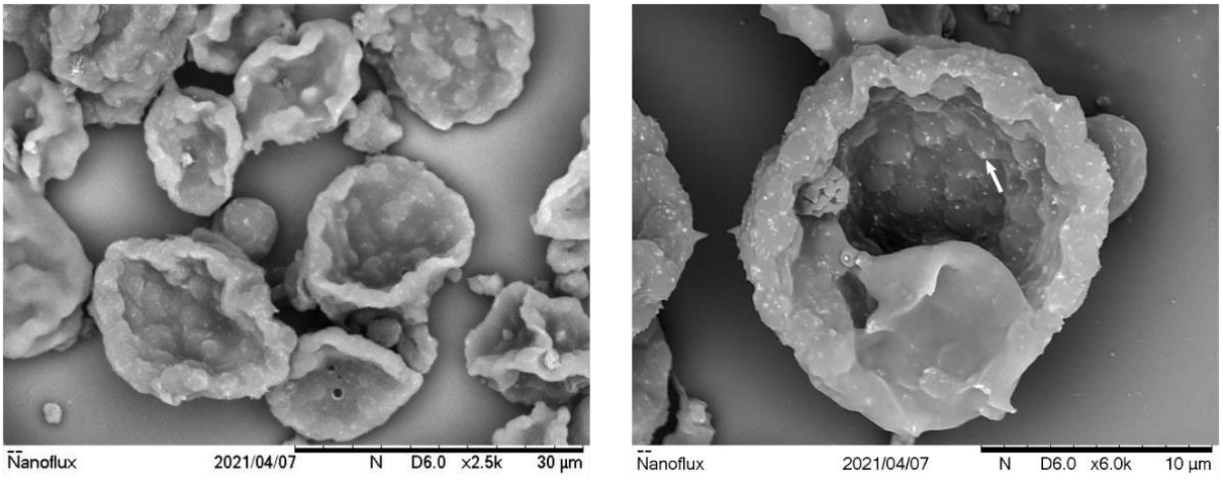

Figure 4.5. SEM micrographs of dried emulsion with 1 %wt of PLL-g-PNIPAM an 0.05% AuNPs in the aqueous phase and 0.05 wt% of Krytox in the oil phase. The small white dots correspond to AuNPs aggregated embedded in the polymer shell (as indicated by the white arrow on the second micrograph).

The presence of AuNPs in the formulation did not prevent the formation of PLL-g-PNIPAM capsules (showing the same structural features than the one presented in Chapter 1 in absence of NPs). In addition, a multitude of nanometric white spots were clearly visible at the surface of the capsule shells, whereas they were absent in pure PLL-g-PNIPAM capsules. The typical size and high SEM contrast of these spots undoubtedly indicate that they are AuNPs aggregates, hence confirming an effective incorporation of the AuNPs in the polymer shell walls.

However, AuNPs may have been embedded in the capsule envelope only upon drying. To better understand the interactions between NPs and PLL derivatives in emulsion droplets, AuNPs have been substituted by fluorescent NPs (NeutravNPs and CarboxyNPs) and the formation of polymer-NPs composite shells was investigated by confocal microscopy.

4.3.2 Proof of concept on NeutrAvidin-modified polystyrene NPs

For the proof of concept, the formation of polymer-NPs mixed shells was investigated in detail with fluorescent NeutravNPs. In these experiments, the PLL-g-PNIPAM used to form the capsules was not dye-labeled so that the fluorescence signal was only due to the NPs, enabling to directly visualize their distribution in the emulsion droplets.

Figure 4.6.A show confocal micrographs of an emulsion containing 2 wt% of PLL-g-PNIPAM and 0.025 wt% of NeutravNPs in the aqueous phase at 18 °C and 45 °C, below and above the LCST of PNIPAM respectively. At 18 °C, the NeutravNPs were homogeneously distributed within the droplets. At 45 °C, the NeutravNPs were essentially located at the droplet edge, indicating that they had been segregated at the water/oil interface concomitantly with the collapse transition of PNIPAM (occurring at 34 °C). This process of thermo-induced co-segregation of polymer chains and NeutravNPs at the interface is depicted in **Figure 4.6**.B (Krytox molecules and PLL positive charges have been removed for the sake of readability). It may be reasonably attributed to the combination of two results previously described: (i) the adsorption of PLL-g-PNIPAM chains at the surface of NeutravNPs (see section 4.2.2) and (ii) the thermo-induced accumulation of PNIPAM derivatives onto the PLL-g-PNIPAM shell at high temperature (see section 3.5.3 in Chapter 1). In other words, PLL-g-PNIPAM-coated NPs become hydrophobic and

sticky at high temperature and agglomerate onto the polymer shell which is hydrophobic and sticky as well.

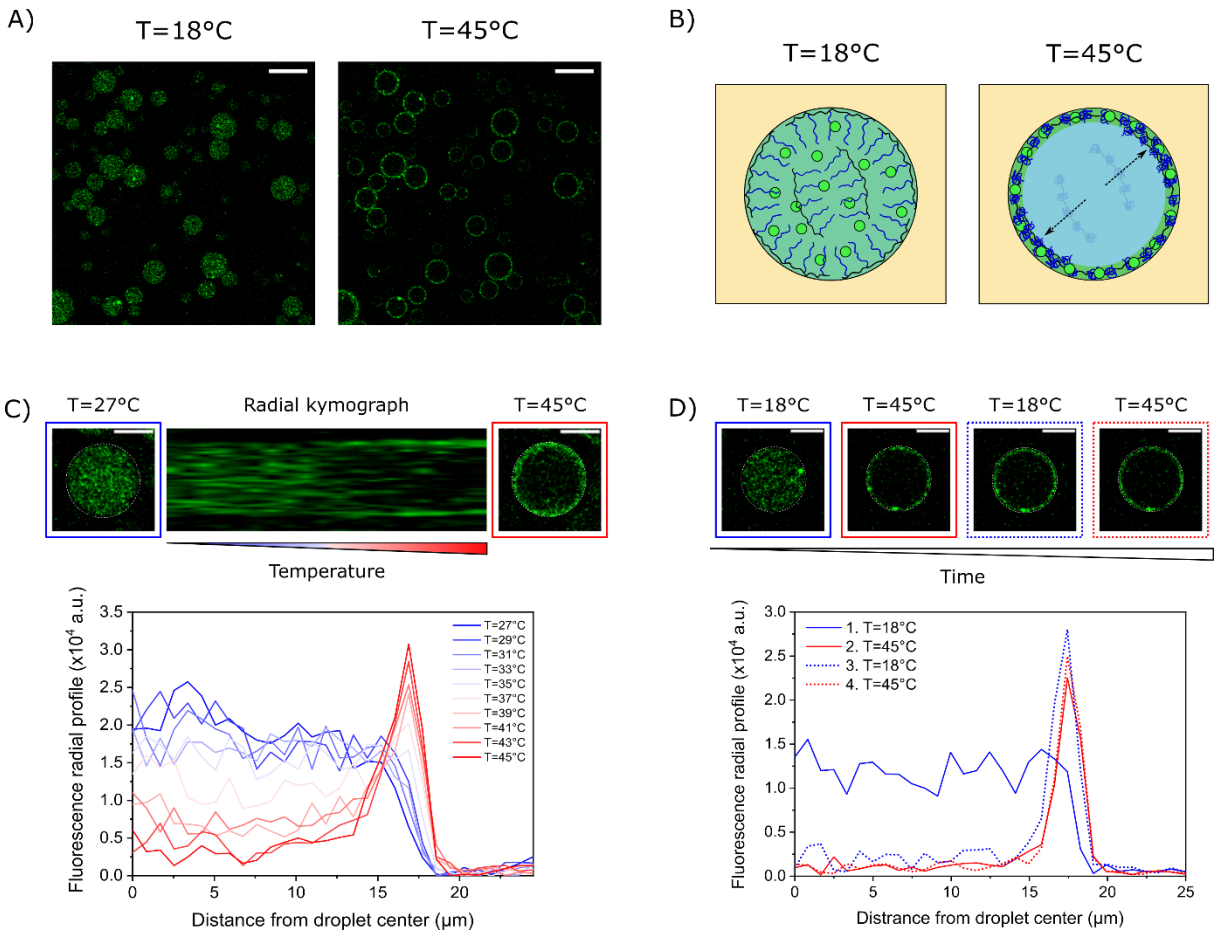

Figure 4.6. Thermo-induced capture of NeutravNPs in PLL-g-PNIPAM shell upon collapse transition of PLL-g-PNIPAM. A) Confocal micrographs of an emulsion containing 2 wt% of PLL-g-PNIPAM (non-fluorescent) and 0.025 wt% of 50-nm fluorescent NeutravNPs in the aqueous phase and 0.05 wt% of Krytox in the oil phase, at 18 °C and 45 °C (scale bars = 50 µm). B) Schematic representation of the thermo-induced co-segregation of PLL-g-PNIPAM and NeutravNPs at the interface upon heating. For the sake of readability, positive charges of PLL and Krytox molecules are not represented. C) Radial kymograph and fluorescence profiles of a representative droplet upon heating from 27 °C to 45 °C (scale bars in the micrographs = 10 µm). D) Confocal micrographs and fluorescence radial profiles of a representative droplet over temperature switches between 18 °C and 45 °C.

The evolution of the emulsion was recorded over time while temperature was increased (from 27 °C to 45 °C) to assess the dynamics of NeutravNPs more precisely within the droplets. For the representative droplet showed in **Figure 4.6**.C, the evolution of the radial profile and the

radial kymograph are represented along the temperature sweep. In the radial kymograph, the projections of the radial fluorescence image at increasing temperatures have been put side by side in a continuous image. It illustrates the progressive disappearance of fluorescence in the droplet core concomitantly with an accumulation of the fluorescence at the droplet edge. This process is also highlighted by the evolution of the radial profile as temperature rises: the uniform profile of fluorescence at low temperature (T < 34 °C) was progressively replaced by a sharp peak of fluorescence localized at the droplet edge (T > 34 °C).

The consistency of the so-formed polymer-NPs mixed layer was assessed by two qualitative observations: (i) micron-size aggregates of NeutravNPs that had reached the interface were totally immobilized at 45 °C as shown in **Figure 4.7**, (ii) the corona of NeutravNPs formed at 45 °C did not redisperse as the emulsion was cooled below 34 °C (see **Figure 4.6**.D), suggesting that the co-segregation of NeutravNPs and PLL-g-PNIPAM at the interface was irreversible. Together, these data suggest that the polymer-NPs mixed layers formed upon heating behave like highly viscous or gel-like shells, probably due to PLL-NPs interactions that play the role of physical cross-links.

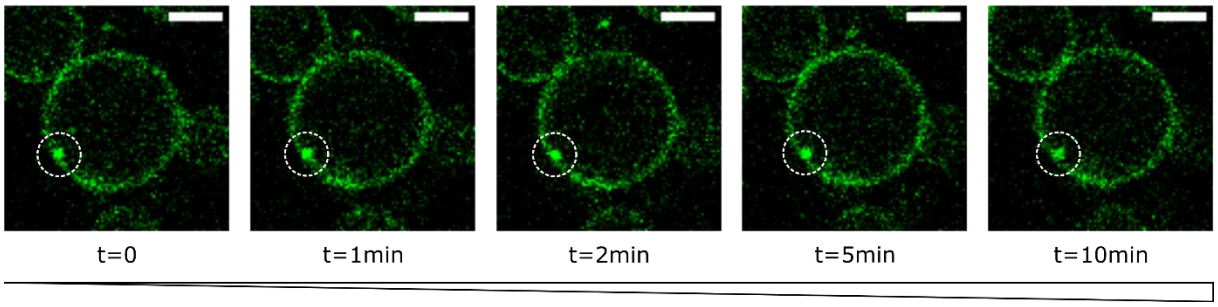

Figure 4.7. Temporal evolution at 45 °C of a representative water droplet containing 2 wt% of PLL-g-PNIPAM and 0.025 wt% of NeutravNPs, dispersed in oil phase containing 0.05 wt% of Krytox (scale bars = 10 µm). The white circle highlights the immobilization of a µm-size aggregate of NeutravNPs within the polymer shell.

To confirm the role of hydrophobic PNIPAM strands in the thermo-induced accumulation of NeutravNPs at the interface, a control emulsion was made with non-thermo-responsive PLL-g-PEG shells (PLL-g-PNIPAM was replaced by PLL-g-PEG in the formulation). The NeutravNPs distribution was uniform in the droplets at 18 °C and 45 °C (see **Figure 4.8**), without any noticeable aggregation at the interface upon heating. This result suggests that the interfacial capture of

NeutravNPs observed with PLL-g-PNIPAM was due to the thermo-responsiveness of PNIPAM strands and was not inherent to the nature of the NPs or to the very heating process.

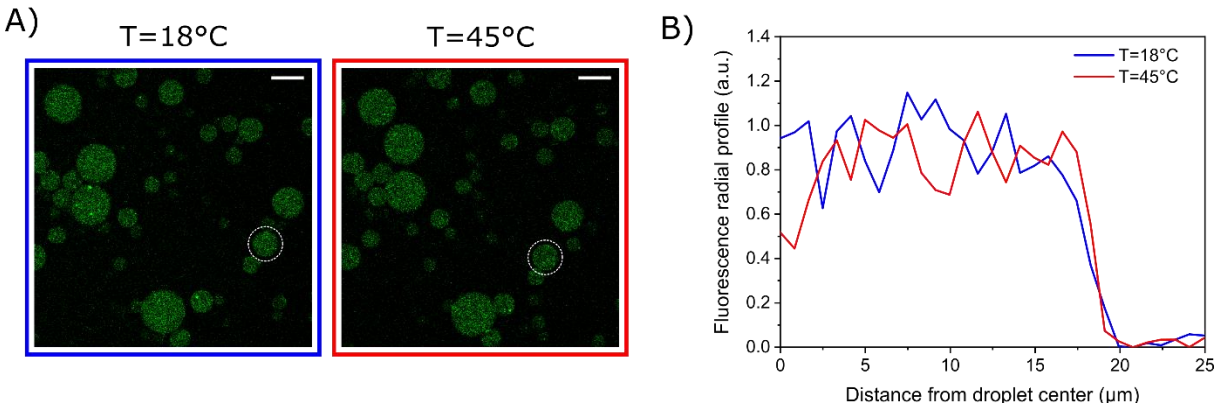

Figure 4.8. Control experiment with non-thermo-responsive PLL-g-PEG. A) Confocal micrographs of an emulsion containing 2 wt% of PLL-g-PEG (non-fluorescent) and 0.025 wt% of NeutravNPs in the aqueous phase and 0.05 wt% of Krytox in the oil phase, at 18 °C and 45 °C (scale bars = 50 µm). B) Radial fluorescence profile of the droplet encircled in white in the micrographs, at 18 °C and 45 °C.

4.3.3 Case of anionic carboxylate-modified polystyrene NPs

As a complement to the experiments on NeutravNPs, the thermally-induced capture of NPs in the polymer shell was also demonstrated with CarboxyNPs in identical conditions (see **Figure 4.9**).

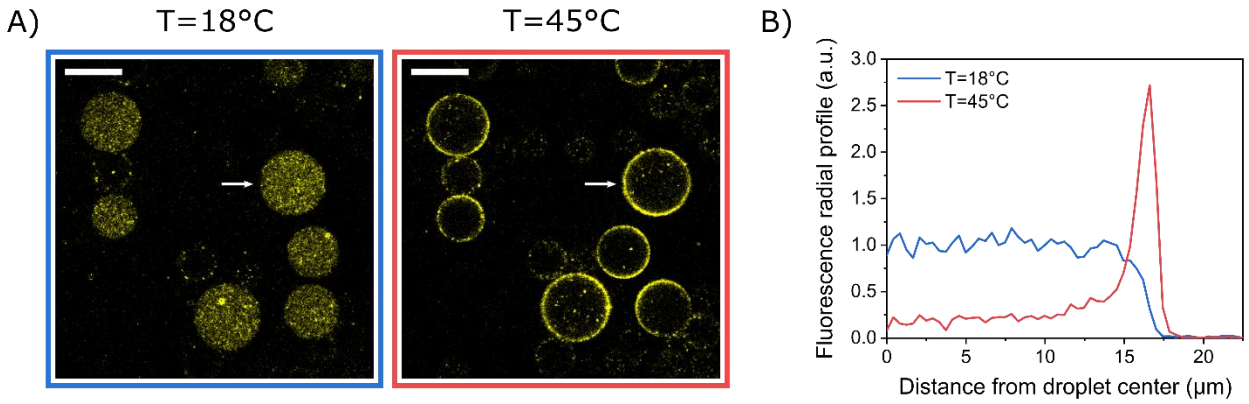

Figure 4.9. Thermo-induced capture of Carboxy-NPs in PLL-g-PNIPAM shells. A) Confocal micrographs of an emulsion containing 2 wt% of PLL-g-PNIPAM (non-fluorescent) and 0.025 wt% of 50-nm CarboxyNPs fluorescent nanoparticles in the aqueous phase and 0.05 wt% of Krytox in the oil phase, at T = 18°C and T = 45°C (scale bars = 30 µm). B) Fluorescence radial profiles of the droplet indicated with a white arrow in the micrographs.

This new approach of formation of polymer-NPs (or "composite") shells has the advantage to rely on a spontaneous self-assembly upon gentle heating and does not require any pre-modification of the NPs of interest or post-modification of the polymer capsules. The irreversible capture of NPs in PLL-g-PNIPAM shells has been demonstrated in the case of one type of NPs (NeutrAvidin-coated) but this approach is likely to be generic as PLL can interact with a great variety of materials (silica, oxides, plastics, gold).

4.4 Thermoplasmonic effect in AuNPs-loaded droplets

4.4.1 Photothermal transition of PLL-g-PNIPAM in emulsion: a qualitative approach

In section 4.3.1, we showed that AuNPs can be incorporated in the shell of PLL-g-PNIPAM capsules. As mentioned in Chapter 1 (section 2.3.4), AuNPs are interesting for their thermoplasmonic properties. The incorporation of AuNPs in PLL-g-PNIPAM capsules should in principle enable to trigger the thermal collapse transition of the polymer upon light irradiation in

individual droplets, instead of heating the whole sample. Qualitative experiments will be first presented as a proof of concept to show that photothermal effects can be generated in AuNPs-loaded emulsion droplets and to identify the main parameters that have an influence on the efficiency of the process. Then a quantitative approach will be presented to measure *in situ* the temperature variations that can be generated by light excitation of AuNPs.

4.4.1.1 Evidence for collapse transition of PLL-g-PNIPAM induced by light irradiation of AuNPs

The possibility to use thermoplasmonic effects of AuNPs to trigger the aggregation of PLL-g-PNIPAM was directly assessed in situ, i.e. in emulsion droplets. An aqueous solutions containing 10 wt% of PLL-g-PNIPAM and 0.05 wt% of AuNPs (PVP-coated) was prepared in phosphate buffer and emulsified in an oil phase containing 0.05 wt% of Krytox. The use of a high concentration in PLL-g-PNIPAM should saturate the interface and facilitate the visualization of its collapse transition upon heating, through the formation of a large amount of micrometric aggregates in the droplet cores.

A laser source emitting at 532 nm with a nominal power of 40 mW was used to excite the AuNPs. The laser beam was focalized on the sample through the side port of the LEICA microscope used to image the sample. At the level of the sample, the laser power was reduced up to 25 mW due to power losses within the microscope set-up. The diameter of the laser spot was typically 10 µm in the focal plane of the objective.

Figure 4.10 shows an irradiation experiment on an individual droplet with a diameter of 30 µm. The droplet was exposed to different light powers (5, 10, 15 mW) for a few seconds (**Figure 4.10**.A). At 5 mW, some granules appeared in small region of the droplet after 10 s of irradiation, suggesting that enough heat had been generated to locally reach 34 °C and trigger the collapse transition of PLL-g-PNIPAM. This phenomenon is better evidenced at 15 mW since the droplet core gets entirely filled with polymer granules after only 1 s of irradiation. At 25 mW, the collapse transition of PLL-g-PNIPAM is turning into a macro-phase separation of the polymer within the droplet core after 10 s of irradiation.

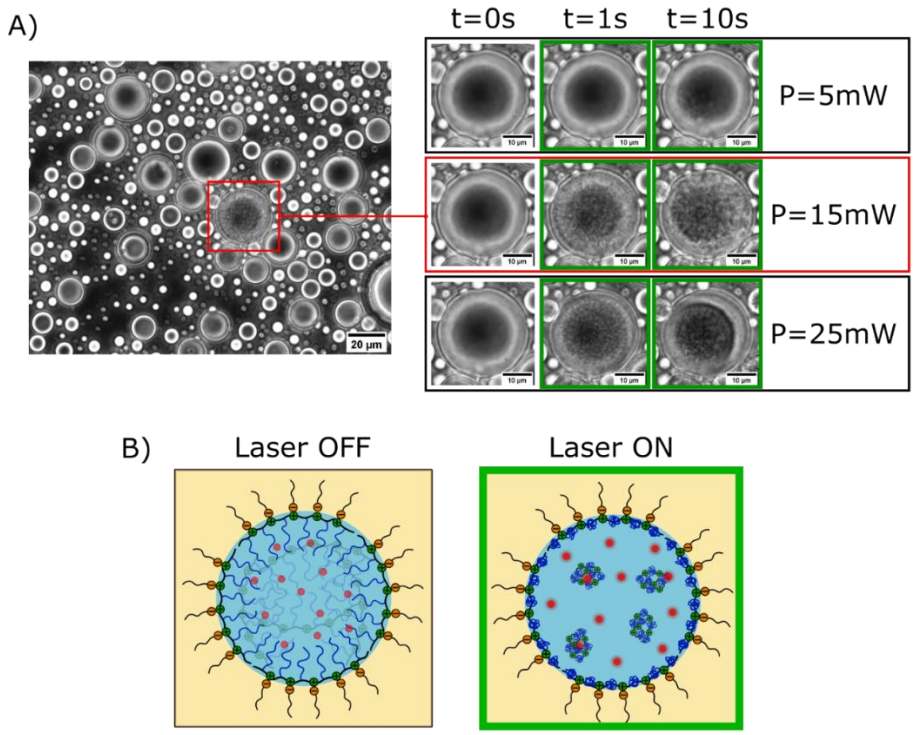

Figure 4.10. Collapse transition of PLL-g-PNIPAM triggered by AuNPs thermoplasmonic effect. A) Phase contrast micrograph of an emulsion containing 10 wt% of PLL-g-PNIPAM and 0.05 wt% of AuNPs in the aqueous phase and 0.05 wt% of Krytox in the oil phase. A 532-nm laser was focused on an individual 30-µm droplet to induce the collapse of PLL-g-PNIPAM in its core. The collapse transition of the polymer was clearly identified upon 1 s of irradiation with a light power P of 15 and 25 mW. B) Representation of the light-induced thermal collapse transition of PLL-g-PNIPAM occurring in the water droplet via thermoplasmonic effects of encapsulated AuNPs.

These preliminary results suggest that the presence of AuNPs in the water droplets allows to generate enough heat upon light irradiation to induce the collapse transition of PLL-g-PNIPAM.

4.4.1.2 Parameters influencing the efficiency of light-induced PLL-g-PNIPAM collapse

The possibility to induce the collapse of PLL-g-PNIPAM with light is intrinsically related to the maximum temperature increase that can be generated by AuNPs under irradiation. In a given

droplet, the temperature increase depends on two parameters: the number of encapsulated AuNPs (itself depending on the AuNPs concentration and the droplet size) and the laser power. The simple experiment presented in the previous section does not give access to a quantitative measurement of the temperature in the droplet. However, we can affirm that the temperature has exceeded the cloud point of PLL-g-PNIPAM (34 °C) as soon as the first polymer aggregates are visible in the droplet core. This qualitative approach can be used to perform a first screening of the crucial parameters that govern this process.

Concretely, we prepared different emulsions containing 10 wt% of PLL-g-PNIPAM and different AuNPs concentration (from 0.020 wt% to 0.100 wt%). The emulsions were successively thermalized at 20 °C, 24 °C and 28 °C, i.e. at temperatures progressively closer to the theoretical cloud point of 34 °C. Accordingly, a progressively smaller increase of temperature should be required to trigger the collapse transition of PLL-g-PNIPAM entrapped in the droplets. At each temperature, we focused the 532-nm laser on different droplets (with diameters ranging from 20 to 50 µm) and determined the light power which is required to observe the formation of polymer granules. The results are shown in **Figure 4.11**.

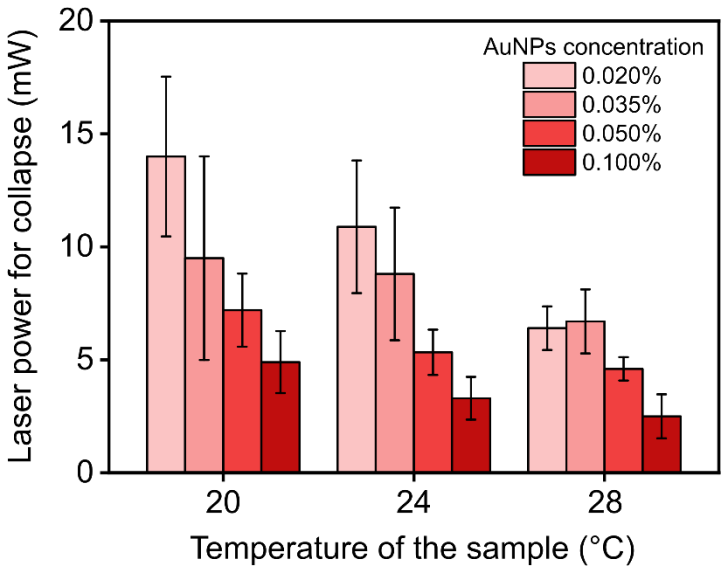

Figure 4.11. Laser power required to trigger the collapse transition of PLL-g-PNIPAM in emulsion droplets containing various concentrations in AuNPs and thermalized at different temperatures (error bars = standard deviation on 5-8 droplets).

The laser power which is required to trigger the collapse of PLL-g-PNIPAM decreases as the AuNPs concentration increases and/or the temperature of the sample increases. These results are consistent with the fact that (i) the highest AuNPs concentrations generate the highest temperature raises at a given laser power and (ii) decreasing the temperature gap that separates the actual temperature from the cloud point enables to decrease the laser power required to trigger the collapse.

The high dispersity that is observed for some experimental condition may be associated to an influence of the droplet size on the required laser power. However, we did not identify any consistent evolution of the laser power with the droplet size, probably because the droplets were not uniformly irradiated (the 10-µm laser spot was smaller than the droplets). At this stage, these experiments only provide qualitative arguments for choosing the suitable set of experimental parameters that may enable to trigger the collapse transition of PLL-g-PNIPAM with light. However, this method requires highly concentrated polymer solutions to visualize the collapse phenomenon, what is contradictory with the design of hollow capsules, and does not give access to quantitative values of temperature.

In the next section, we present an alternative microscopy approach that enables a quantitative measurement of the temperature in the droplet, independently of the presence of PLL-g-PNIPAM.

4.4.2 Quantitative analysis of thermoplasmonic effects in emulsion based on quantitative phase microscopy

4.4.2.1 The measurement of temperature at microscales

As demonstrated in the previous section, generating heat by thermoplasmonic effects is easy as it occurs as soon as AuNPs are irradiating with a sufficient laser power. The most challenging issue in any thermoplasmonic application is to be able to measure the temperature that is reached upon light excitation. Indeed, temperature gradients are generated at nano- and microscales that are obviously not accessible to standard thermometry techniques. The development of techniques for *in situ* measurement of temperature generated by thermoplasmonic systems is quite recent as it began in the last 2000s-early 2010s.[204] The first thermometry techniques implemented in thermoplasmonics were essentially based on fluorescence properties of extrinsic reporters dispersed in the vicinity of the plasmonic structures. Indeed, many fluorescence features such as intensity, life-time, spectrum or anisotropy are temperature-dependent.[279] Thus, measuring changes of these properties upon heating may enable to retrieve local temperature values, provided a suitable calibration. However, these approaches based on fluorescence may be limited in terms of spatial resolution, and may suffer from measurement biases related to photo- or thermo-bleaching of the fluorescent reporters.[204] As an alternative, label-free and non-invasive imaging techniques – that may have already been used for "conventional" microscopy – have been adapted for temperature mapping of thermoplasmonic nanostructures. It was the case of quantitative phase microscopy techniques. Before detailing how they can be used in the context of thermoplasmonics, these techniques will be presented in more detail.

4.4.2.2 Quantitative phase imaging

When a sample is subjected to a uniform light illumination, a distortion of the incident planar wavefront is observed as the light passes through refractive features (**Figure 4.12**). Quantitative Phase Microscopy (QPM) techniques are based on the detection of this wavefront distortion to retrieve structural information on the sample. More precisely, QPM measures the optical path difference (OPD), also termed optical thickness in the literature, imprinted to the light wavefront upon sample imaging.[280] The OPD, usually denoted δ, contains information on the geometrical profile and the refractive index of the distorting objects crossed by the illumination light. Since the OPD is directly proportional to the phase delay undergone by light during its propagation, the OPD image of the sample can be converted in a phase image, hence the term of quantitative *phase* microscopy.

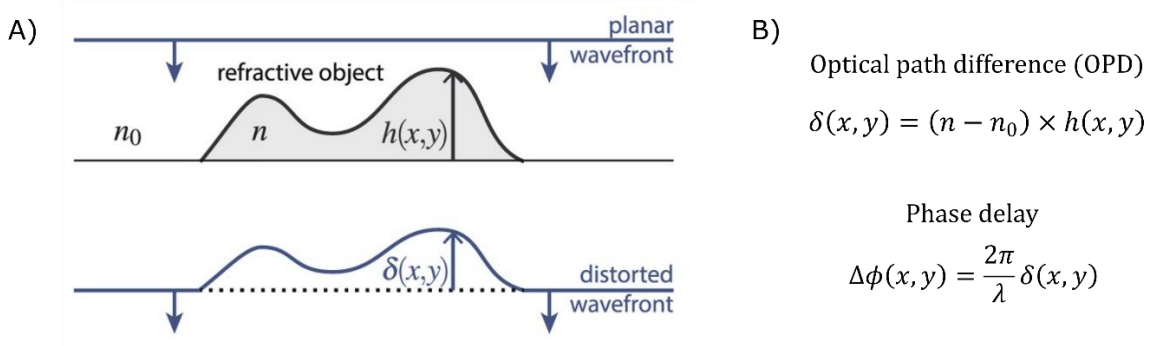

Figure 4.12. Physical values measured and imaged by Quantitative Phase Microscopy techniques. A) Distortion of a planar light wavefront passing through a refractive object characterized by a geometrical profile $h(x,y)$ and a refractive index n. B) The wavefront distortion can be equivalently quantified either by the optical phase difference $\delta(x,y)$ or by the phase delay which are both directly proportional to the geometrical profile of the illuminated object.[280]

Classical microscopy techniques are based on the measurement of light intensity. They are sensitive to diffusive or reflecting objects but are less suitable for imaging samples which are mostly transparent. QPM techniques have the advantage to be highly sensitive to very small variations of refractive index, enabling the imaging of multi-media transparent samples, such as living cells,[281] with a high spatial resolution. For this reason, QPM techniques have been

extensively used for the observation of biological samples, and so much so that QPM has been for long restricted to this application field.[282]

The extension of QPM to the fields of physics and material science is only a recent trend, that has been instigated by Guillaume Baffou at the Fresnel Institute in Marseille. In this context, QPM turned out to be particularly efficient for the characterization of thermoplasmonic systems and for the precise mapping of temperature at microscales. Indeed, upon excitation, plasmonic nanostructures generate temperature gradients in their vicinity that result in refractive index variations in the surrounding medium. These local variations of refractivity may induce the wavefront distortion of planar light used to image the sample (see **Figure 4.13**). By mapping the OPD upon plasmonic excitation, QPM techniques may thus enable to retrieve the temperature distribution around the plasmonic nanostructure.[283]

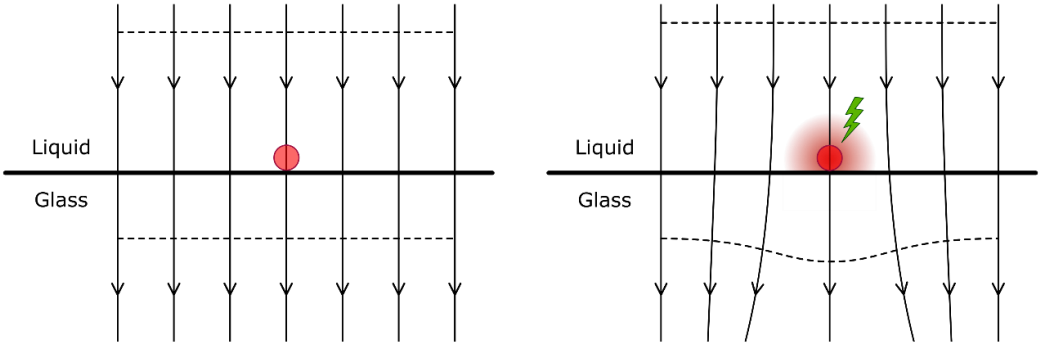

Figure 4.13. Distortion of a planar light wavefront passing through a temperature gradient locally generated by the photoexcitation of a plasmonic gold nanoparticle.

The most common QPM techniques are based on the generation of interferences as it is a simple way to convert (invisible) phase information in (visible) intensity modulations. These techniques, such as digital holographic microscopy, rely on the splitting of the source light along two paths, one passing through the sample the other not, to create an interference pattern that contains the phase information of the sample.[284] These techniques benefit from high spatial resolution but suffer from instability issues. Indeed, extended propagation paths are required for the interfering light beams. Thus, the interference-based optical set-ups are highly sensitive to environmental perturbations (vibrations, temperature variations), resulting in ersatz fringes or speckle features that deteriorate the quality of the final phase image.

Alternative QPM techniques, that do not involve extended set-up, can be used for phase imaging of thermoplasmonic systems. Grating-shadow phase microscopy is one of these technics and will be presented in the next section.

4.4.2.3 The technique of grating-shadow phase microscopy

Grating-Shadow Phase Microscopy (GSPM) is a QPM technique based on wavefront sensing as described in the previous section. This technique follows on from precursor works of Primot in the mid-90s and has been commonly termed Quadriwave Lateral Shearing Interferometry in the literature.[280] The name of Grating-Shadow Phase Microscopy has been recently proposed as a simpler and more relevant alternative to better understand and disseminate this microscopy technique.[280]

GSPM relies on an imaging system made of the association of a specific diffraction grating and a classic CCD camera. The grating is a bidimensional periodic arrangement of transmitting glass squares (windows) separated by opaque horizontal and vertical lines. A chessboard-like phase pattern is imprinted on the grating such that adjacent windows alternatively induce a phase delay of 0 or π to the transmitted light (see **Figure 4.14**).

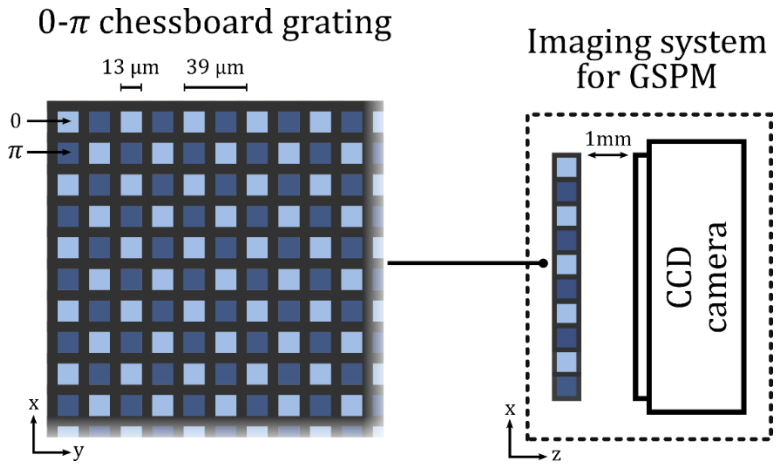

Figure 4.14. Grafting-Shadow Phase Microscopy imaging system composed of a bidimensional $0-\pi$ chessboard grating placed just in front of a CCD camera. The grating is typically made of 300×300 $\begin{vmatrix} 0 & \pi \\ \pi & 0 \end{vmatrix}$ unit cells.

The image formed on the camera sensor upon illumination of the grating is called interferogram. It is made of fringes resulting from the interference between the multiple diffracted beams coming out of the grating. Because of the $0 - \pi$ chessboard pattern, only symmetrical first diffraction orders along two orthogonal directions participate significantly to the interference phenomenon (**Figure 14.**A). In these conditions the interferogram generated by a planar irradiation is the exact shadow of the grating (i.e. a periodic bidimensional arrangement of bright squares separated by dark lines), as if light was passing in straight line through the windows without undergoing diffraction effects (**Figure 14.**B).[280] Interestingly, a local distortion of the incident wavefront results in a local deformation of the shadow pattern (**Figure 4.15**.B). As a consequence, the interferogram generated by the illumination of a complex sample is not a regular but a distorted grating shadow that "geometrically" contains the sample phase information. An OPD image of the sample can be retrieved from the distorted interferogram thanks to an algorithm based on image processing in the Fourier space (**Figure 4.16**).[285]

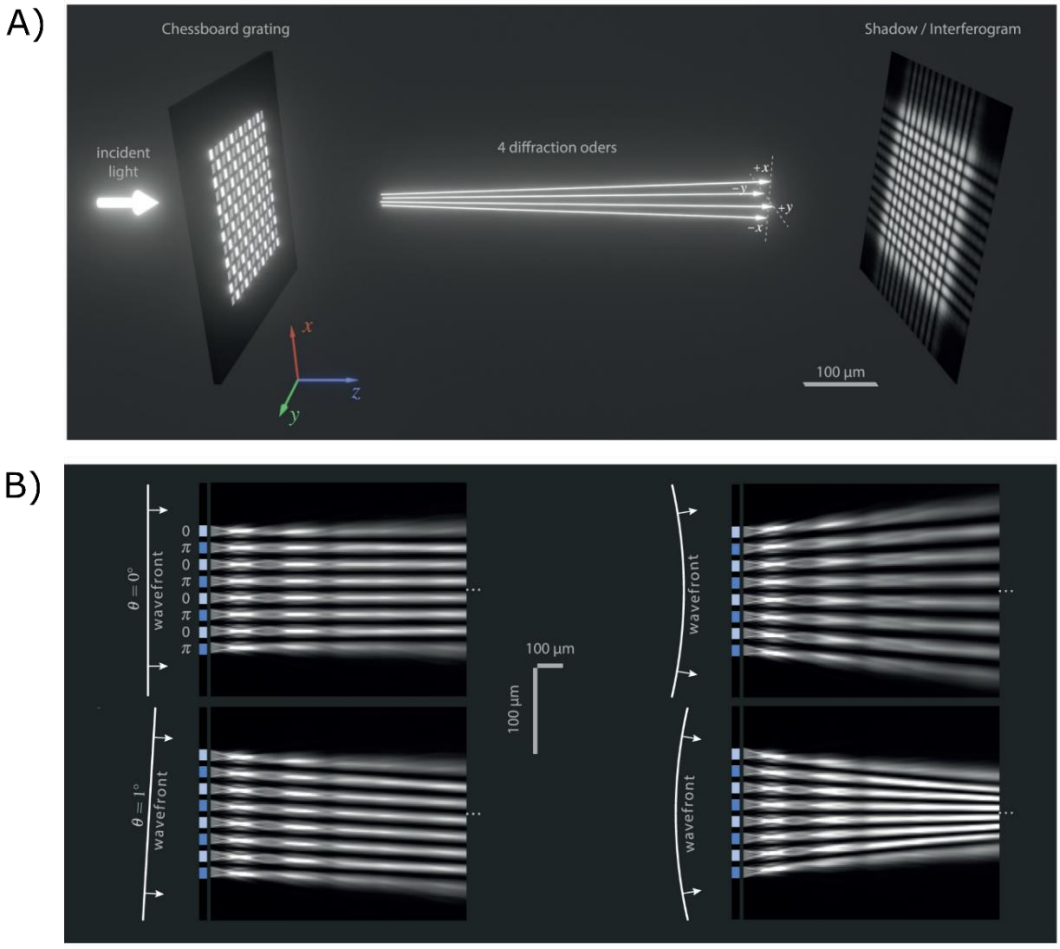

Figure 4.15. Wavefront sensing with Grating-Shadow Phase Microscopy. A) Formation of the chessboard grating's shadow by interference of 4 first diffraction orders along two orthogonal directions upon transmission of a planar incident light. B) Distortion of the shadow pattern upon distortion of the incident light wavefront: tilting or curving the wavefront may induce the translation or spreading/shrinking of the shadow, respectively.[280]

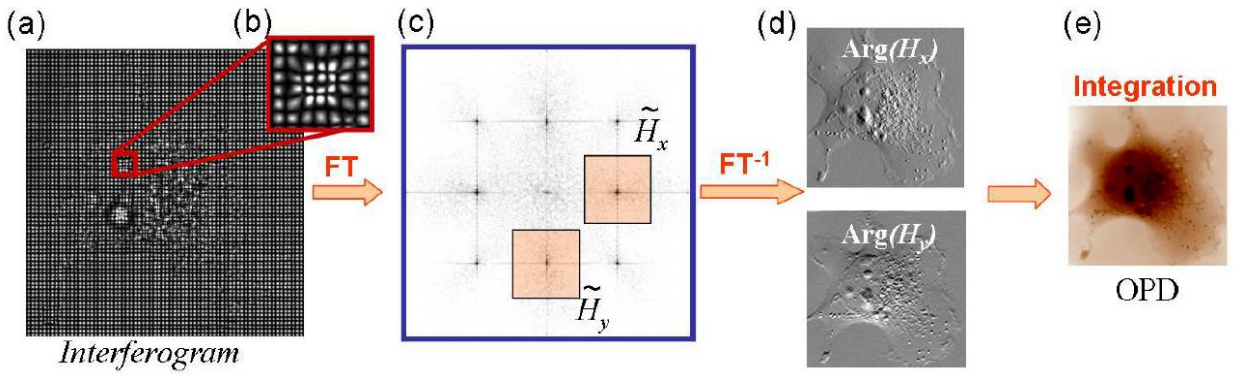

Figure 4.16. Main steps involved in the GSPM algorithm that enables to retrieve a phase (or OPD) map from the distortion of the interferogram fringes. The 2D Fourier transform (FT) of the interferogram reveals orthogonal first order diffraction spots ($\tilde{H}_x$ and $\tilde{H}_y$) that can be demodulated (isolated) in the Fourier space. The inverse Fourier transform (FT^{-1}) of these spots yields two complex images, whose arguments ($Arg(H_x)$ and $Arg(H_y)$) correspond to wavefront gradient maps along the two orthogonal directions. A 2D integration of these gradient maps eventually yields the phase image of the sample.[285]

GSPM has many advantages compared to other common QPM techniques. Thanks to the high pixel density on the grating, GSPM benefits from a high spatial resolution, which is basically limited by the optical resolution of the camera. It also benefits from a high sensitivity, the typical standard deviation of an OPD noise image being ~ 0.1 nm.[280] With these performances, GSPM turned out to be particularly appropriate for the imaging and characterization of nanoparticles (with sizes down to 60 nm diameter).[286] As previously mentioned, the light coming out of the grating behaves as if it has not been subjected to diffraction. A reliable image of the interferogram can thus be formed by placing the sensor of the camera only 1 mm behind the grating. The interference phenomenon occurring in a very short space, GSPM is not sensitive to environmental perturbations and is thus more stable and robust than other interference-based QPM techniques. In addition, GSPM does not require temporal coherence for the illumination, and is even more effective with a polychromatic source. A commercial GSPM device has been commercialized by the company PHASICS, and can be easily implemented on any optical set-ups, including on the side port of commercial microscopes.

4.4.2.4 Use of GSPM for imaging of thermoplasmonic systems

Based on wavefront sensing of refractive index variations as depicted in **Figure 4.13**, GSPM has been successfully implemented for the characterization of thermoplasmonic systems and the measurement of temperature gradients at the microscales. Baffou et al. developed a suitable algorithm to retrieve, from the OPD image obtained by GSPM, the distribution of heating power and temperature gradients generated by gold nanostructures upon plasmonic excitation.[283] Note that two contributions may be observed in raw OPD images of a plasmonic nanostructure: the OPD due to the nanostructure itself (highly refractive compared to its environment) and the OPD due to the local variations of refractive index induced by heating. This latter contribution can be isolated by simply subtracting the OPD image of the nanostructure from the OPD image during photo-excitation.

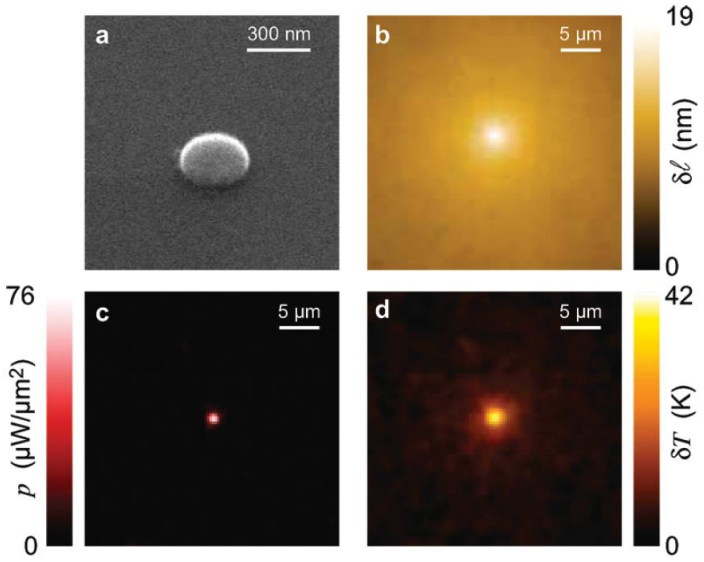

Figure 4.17. GSPM mapping of light-induced heat generation in a gold nanostructure excited at 808 nm and illuminated with a white source. a) SEM image of the targeted gold nanostructure. b) Map of OPD generated by the local heating of the nanostructure upon plasmonic excitation (the OPD due to the nanostructure itself was subtracted). c) Map of heating power density dissipated by the nanostructure, retrieved from image processing of the OPD map with a suitable algorithm. d) Temperature distribution around the nanostructure, also deduced from image processing of the OPD map.[283]

The image processing developed by Baffou et al. to retrieve temperature maps is restricted to the characterization of 0D, 1D or 2D heat sources, i.e. individual nanoparticles (nanospheres or nanowires) or arrays of such nanoparticles. This method is no longer suitable for 3D heat source

distributions (i.e. sources much larger than the illumination wavelength along the three spatial dimensions). Indeed, since the OPD maps correspond to a 2D projection of the sample phase, all the contributions gathered along the direction of light propagation are overlapping in the final image. Complex deconvolution processes may be required to retrieve such 3D source distributions, and have never been developed so far. For now, direct 3D temperature mapping from raw images of OPD has been restricted to the study of 2D heat sources (by reconstruction from stacked OPD images).[287] For more complex heat source distributions, simulation is required to correlate OPD imaging with temperature distributions.

Our system (AuNPs-loaded emulsion droplets) is a typical example of complex 3D heat source distribution for which the temperature field cannot be analytically retrieved from OPD maps provided by GSPM. COMSOL simulations of temperature distributions on an approximate model may be helpful to correlate the OPD images of the sample to actual *in situ* temperatures. The following sections will present and discuss this approach.

4.4.2.5 Experimental set-up and measurement of OPD profiles

The GSPM experiments were performed in Guillaume Baffou's lab at the Fresnel Institute in Marseille. The experimental set-up of is shown in **Figure 4.18**. It was used to image the OPD induced by AuNPs-loaded emulsion droplets upon thermoplasmonic irradiation. In the following, the sample will consist in a water-in-oil emulsions containing 1 wt% of PLL-g-PNIPAM and 0.025 wt% of PVP-coated AuNPs in the aqueous phase and 0.05 wt% of Krytox in the oil phase. The emulsion was injected in a capillary with an internal height of 100 µm.

The sample was illuminated from the top with a 625-nm planar illumination. The OPD image of the sample was recorded with the GSPM wavefront sensing device presented in **Figure 4.14**. The plasmonic excitation of AuNPs was performed by irradiated the sample from the bottom with a 532-nm laser. The diameter of the laser spot in the focal plane of the objective was set to 50 µm (a uniform irradiation was thus ensured for droplets smaller than 50 µm). The laser power

delivered to the sample was typically between 0 and ~ 40 mW, which correspond to an irradiance (i.e. a power per unit area) between 0 and ~ 20 µW/µm².

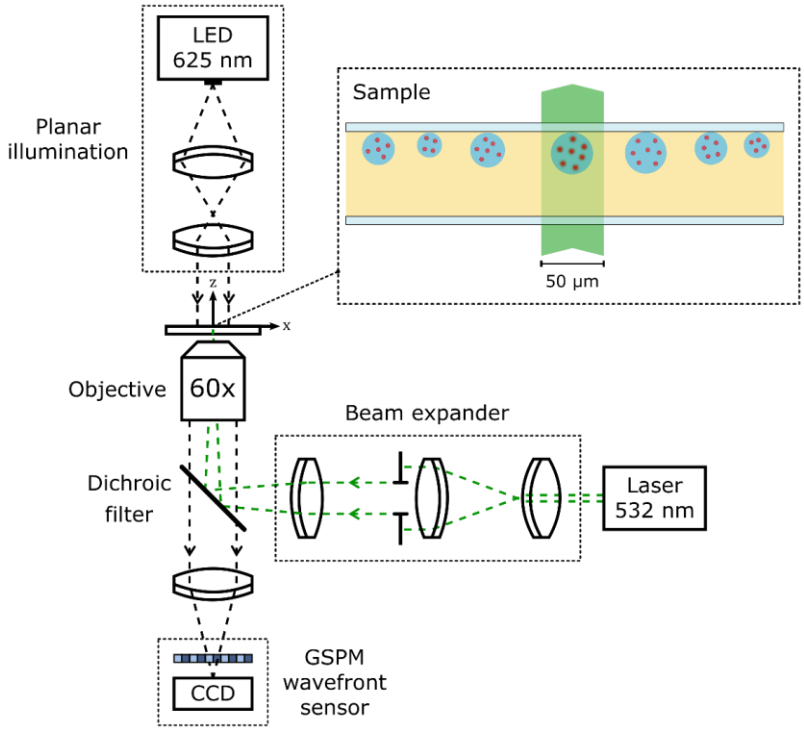

Figure 4.18. Experimental grating-shadow phase microscopy set up. The sample is a water-in-oil emulsion injected in a glass capillary. The water droplets (blue disks) are loaded with 1 wt% of PLL-g-PNIPAM (not showed) and 0.025 wt% AuNPs (red dots). The sample is illuminated by the top with a 625-nm red diode and excited by the bottom with a 532-nm laser (green). The OPD image of the sample is recorded with the GSPM device previously described.

In the following, the protocol for imaging and post-processing will be detailed for a droplet with a diameter of 30 µm. **Figure 4.19** shows the interferogram of the droplet provided by GSPM. A zoom on the edge of the droplet highlights the distortion of the grating shadow. From this interferogram, intensity and OPD images of the droplets are generated by the GSPM software. In the OPD image, the droplet appears as a bright white disk standing out of the dark background generated by the continuous oil phase. This sharp contrast suggests that the presence of the water droplet imprints a large OPD to the transmitting light, generated by the mismatch of refractive index between water and oil. A crucial point to have mind for the quantitative interpretation of such image is the fact that an OPD value measures a “difference”. In the sample image, OPD values can be retrieved by measuring differences of “grey level” between two regions of the

sample. As an alternative, the grey level can be arbitrarily and uniformly set to zero at a given time of acquisition or for a given image in order to directly measure OPD in the images recorded at further acquisition time.

From the raw OPD image showed in Figure 18, we could deduce the OPD generated by the water droplet using the oil background as a "zero" baseline. The profile of the droplet indicates a maximum OPD of $\delta = 900\ nm$ reached at the center (projection of the longest droplet portion crossed by light). This positive value confirm that the refractive index of water is higher than the oil's one. This latter can even be deduced from the formula presented in **Figure 4.12**: $n_O = n_W - \delta/d = 1.30$ with $d = 30$ µm the droplet diameter and $n_W = 1.33$ the refractive index of the water droplet assimilated to pure water (the presence of the polymer and the AuNPs is neglected). This experimental value of n_O fits exactly with the value indicated by the commercial data sheet of the oil.

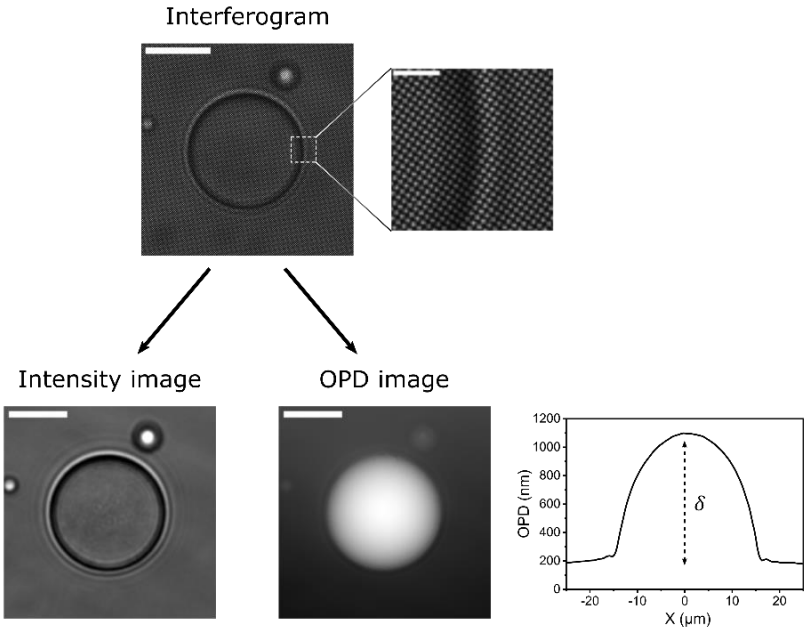

Figure 4.19. Interferogram, intensity image, and OPD image of a 30-µm droplet recorded by GSPM (scale bar = 15 µm). The zoom on the droplet edge in the interferogram reveals the distorted grating shadow (scale bar = 2 µm). The OPD profile of the droplet highlight the high contrast between the water droplet and the continuous oil phase ($\delta = 900\ nm$ at the center of the droplet $X = 0$).

The previous images were obtained in absence of plasmonic excitation. When the green laser was turned on, heat was generated by the AuNPs dispersed in the water droplet, inducing an additional contribution to the OPD signal. To isolate this thermoplasmonic contribution, a reference image of the droplet was taken before laser irradiation and was subtracted from the image recorded upon laser irradiation. Concretely, the OPD image of the sample was uniformly set to 0 just before irradiation (**Figure 4.20**). Upon laser irradiation, an OPD pattern appeared and was characterized by a dark and diffuse corona at the periphery of the droplet, surrounded by a bright oil background (**Figure 4.20**). This distribution of grey values suggests that OPD is negative in the droplet compared to the oil phase, which is consistent with a local decrease of the refractive index of the medium upon heating (the $\frac{dn}{dT}$ coefficient of liquids is negative). As the manipulation and graphical representation of negative values can be counterintuitive and confusing, the data treatment of GSPM images will be systematically done with *absolute* values of OPD. To retrieve quantitative values, a zero OPD reference should be taken in a region which has not been perturbed by temperature gradients generated by thermoplasmonic effects. The ideal choice would be to take this reference infinitely far from the droplet but, since the imaging field of view is limited, we are compelled to set the OPD reference arbitrarily as far as possible from the droplet, but we are aware that it does not correspond to a real "zero". Figure 4***.20*** shows the OPD radial profile of the droplet upon laser irradiation, plotted in *absolute* values with the OPD origin set *arbitrarily* far from the droplet center. This radial profile shows that a high OPD is generated in the droplet (with a maximum value reached at the periphery) and then diffuses in the oil phase with a characteristic spatial decay.

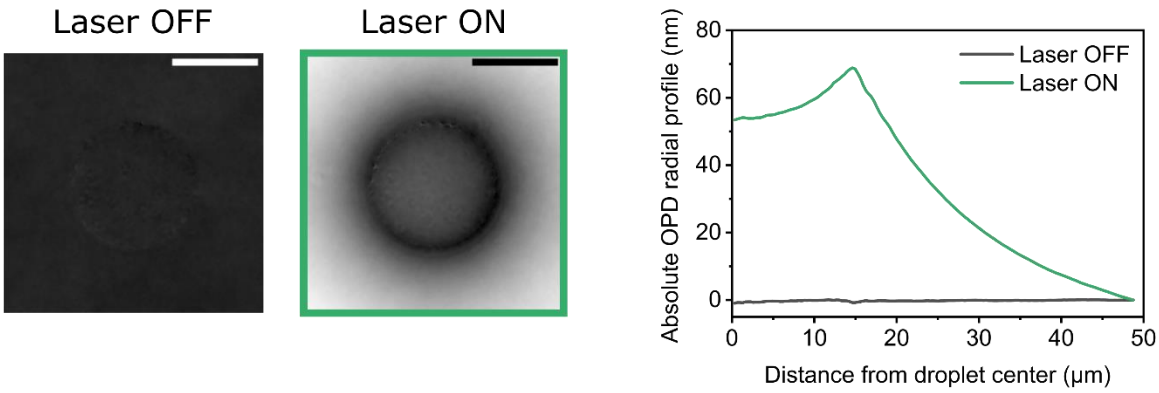

Figure 4.20. OPD images of the droplet before and during laser irradiation (λ = 532 nm, I = 12.7 µW/µm²) and the corresponding radial profiles (plotted in absolute value and arbitrarily set to 0 far from the droplet). The OPD was uniformly set to 0 before irradiation to specifically isolate the contribution of the thermoplasmonic effect on the wavefront distortion upon irradiation. Scale bars = 20 µm.

4.4.2.6 Mathematical modelling of the decay portion of the OPD radial profile

In theory, the OPD decay observed in the oil phase should asymptotically reach 0 infinitely far from the droplet but it was arbitrarily set to 0 at a finite distance due to the spatial limitations of the image. A theoretical fit of this decay should enable to properly rescale the OPD curve and to retrieve the actual values of OPD. A simple model is proposed to describe the system and predict the evolution of the OPD in the oil phase. Axisymmetric side-view representation of the droplet is shown in **Figure 4.21**. The z axis corresponds to the axis of light propagation (downwards for the illumination and upwards for the excitation laser) and its origin is set on the upper capillary side. Since the aqueous phase is less dense than the oil phase, the water droplet is in contact with the upper capillary side. According to the side view micrographs shown in Chapter 1 (**Figure 3.7**), the top of the droplet is slightly flattened by the contact with the glass slide, from a distance denoted e and which is typically ~ 1 µm. Accordingly, the center of the droplet is shifted in $z = -R + e$ where R is the droplet radius. The x axis goes along the upper capillary side and its origin is set vertically above the center of the droplet. Since the system show a rotational invariance around the z axis, the analysis of the system can be restricted to the (xz) plane to deduce radial properties.

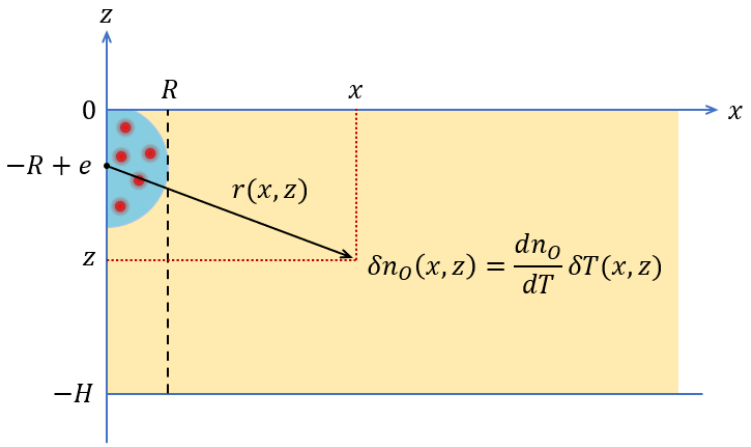

Figure 4.21. Axisymmetric side-view representation of the system. The water droplet of radius R (containing the AuNPs) is in contact with the upper capillary side (the droplet is flattened on a distance e). The center of the water droplet is set at the position ($x = 0; z = -R + e$). The heat generated by the droplet (assimilated to a uniform spherical heat source delivering a power Q) creates a local increase of temperature $\delta T(x,z)$ at each position $r(x,z)$ from the droplet center. This local temperature increase induces a local variation of refractive index in the oil phase $\delta n_0(x,z)$ that can be integrated along the z axis to retrieve the OPD radial profile.

Upon the plasmonic excitation of AuNPs, a certain amount of heat, denoted Q, is produced in the droplet and is supposed to be uniformly distributed such that the droplet can be seen as an isotropic spherical heat source (we neglect the droplet flattening in the model). Following the heat equation, the progressive diffusion of heat through the medium generates temperature gradients. Assuming that the steady state is rapidly reached, a simple expression of the temperature field in the oil phase can be derived:

$$T(r > R) = \frac{Q}{4\pi\kappa_o}\frac{1}{r} + T_\infty$$

In this expression, r designates the radial distance from the droplet center. By restricting this equation to the (*xz*) plane, the distance r is expressed in cartesian coordinates as follows:

$$r = \sqrt{x^2 + (z + R - e)^2}$$

(see schematic in **Figure 4.21**). $\kappa_o = 0.07\ W.m^{-1}.K^{-1}$ designates the thermal conductivity of the oil phase (commercial data sheet) and T_∞ corresponds to the temperature infinitely far from the heat source (for $x \to \infty$) and is equal to room temperature, i.e. $T_\infty = 273\ K$. This equation can be rewritten in terms of temperature increase $\Delta T = T(r) - T_\infty$ and in cartesian coordinates for $x > R$:

$$\Delta T(x,z) = \frac{Q}{4\pi\kappa_o}\frac{1}{\sqrt{x^2+(z+R-e)^2}}$$

From a physical point of view, an infinitesimal variation of temperature δT in the oil phase induces an infinitesimal variation of refractive index δn_O, which is given by $\delta n_O = \frac{dn_O}{dT}\delta T$ with $\frac{dn_O}{dT} = -3.16 \times 10^{-4}\ K^{-1}$ (this value has been measured with GSPM, see section 7.9.3 in **Appendix A**).

Local variations of refractive index are at the origin of the OPD signature observed upon laser irradiation. The OPD radial profile in the oil phase (along the x direction) can be calculated by integration of the infinitesimal variations of refractive index of the oil along the z direction (i.e. the direction of light transmission): $OPD(x>R) = \int_{-H}^{0}\delta n_O(x,z)dz = \int_{-H}^{0}\frac{dn_O}{dT}\delta T(x,z)dz$

Assuming that $\frac{dn_O}{dT}$ is a constant and that $\delta T(x,z)$ can be assimilated to $\Delta T(x,z)$, we obtain:

$$OPD(x>R) = \frac{dn_O}{dT}\frac{Q}{4\pi\kappa_o}\int_{-H}^{0}\frac{dz}{\sqrt{x^2+(z+R-e)^2}}$$

The calculation of the integral eventually yields an analytical expression for the OPD in the oil phase for $x > R$:

$$OPD(x>R) = \frac{dn_O}{dT}\frac{Q}{4\pi\kappa_o}ln\left[\frac{R-e+\sqrt{x^2+(R-e)^2}}{R-e-H+\sqrt{x^2+(R-e-H)^2}}\right] = A \times f(x)$$

where $A = \frac{dn_O}{dT}\frac{Q}{4\pi\kappa_o}$ is a constant depending on the heat source power and structural parameters of the oil phase, and $f(x) = ln\left[\frac{R-e+\sqrt{x^2+(R-e)^2}}{R-e-H+\sqrt{x^2+(R-e-H)^2}}\right]$ is a decreasing function depending on the structural parameters of the droplet (radius R, flattening distance e) and the thickness of the capillary H.

Since $\frac{dn_O}{dT} < 0$, the constant A as well as the final OPD are negative, what is consistent with the experimental observations. But as previously mentioned, the OPD data are treated in *absolute* values for the sake of convenience. With that in mind, the theoretical OPD is a decreasing function

that tends to 0 for $x \to \infty$. This asymptotical behavior was not observed in the experimental OPD profile (since the curve was artificially set to 0 at a finite distance from the droplet center), but can be retrieved by applying a suitable offset to the curve. The offset value can be introduced in the form of an additive constant B in the analytical expression of the OPD used for the fit, now reading: $OPD(x) = A \times f(x) - B$.

In the fitting procedure, the constants A and B were let free to optimization but the definition of the function f was fed with the experimental values of R, e and H. The value of B given by the fit was used to shift up the experimental curve and thus retrieve the asymptotical behavior of the OPD profile. The fitting procedure is demonstrated on a 30-µm droplet (R = 15 µm) for different laser irradiances (**Figure 4.22**). The values of e and H were fixed at 1 µm and 100 µm respectively. The fit was only applied to the tail of the decay portion as it gave less reliable results in the region near the droplet. This hiatus is likely due to an over-simplification of the model to derive the analytical expression of the radial OPD. In particular, we used an expression for the temperature field which is only valid for an isotropic source heat in a uniform medium. We did not take into account the presence of the capillary sides that (i) break the isotropy of heat diffusion and (ii) induces a local modification of the thermal conductivity (along the oil/glass interface, the effective conductivity is the mean of the conductivity of the two media). These effects are predominant near the droplet but can be neglected far from it.

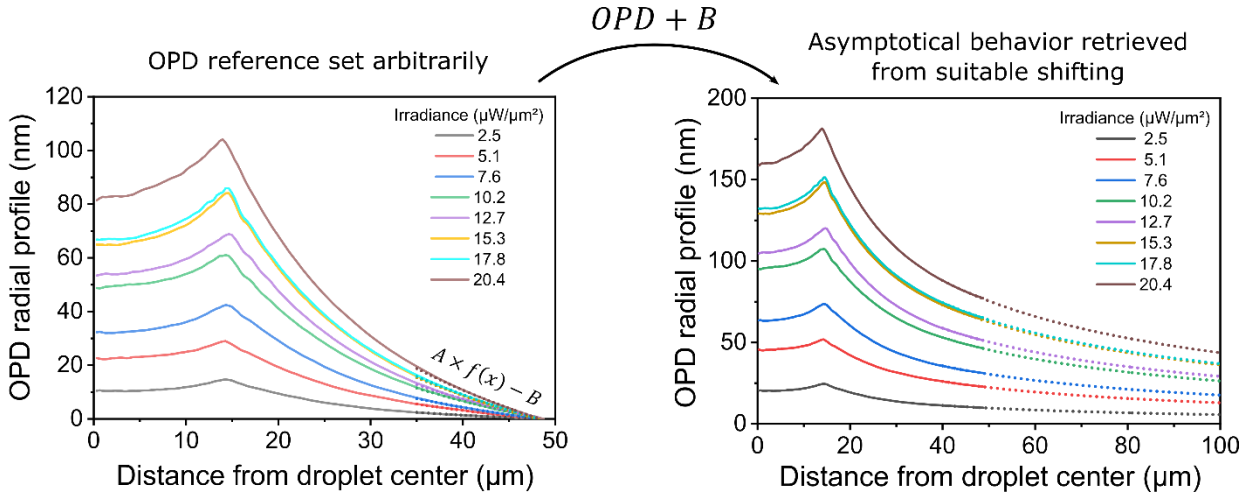

Figure 4.22. Rescaling of the experimental OPD radial profiles by an appropriate fit of the decay portion. *Left*: Experimental OPD radial profiles of the 30-µm droplet under study for different laser irradiances. All the curves were artificially set to 0 at a distance arbitrarily far from the droplet center. The tail of the decay portion of the profiles was fitted with the analytical function derived from the mathematical model: $A \times f(x) - B$ where A and B were unfixed parameters and $f(x) = ln\left[\frac{R-e+\sqrt{x^2+(R-e)^2}}{R-e-H+\sqrt{x^2+(R-e-H)^2}}\right]$ with R=15µm, e=1µm, H=100µm. *Right*: The curves were shifted up by addition of the offset parameter B deduced from the fit. Doing that, the OPD profiles retrieved the asymptotical behavior which is physically expected, i.e. OPD → 0 when $x \to \infty$.

After application of the suitable offset, the experimental OPD profiles exhibit the expected asymptotical behavior (**Figure 4.22**). The thermal signature of the droplet was quantified by the measurement of the OPD value at the center of the droplet, termed "core OPD". This parameter was plotted as a function of the irradiance for the 30-µm droplet under study in **Figure 4.23**.

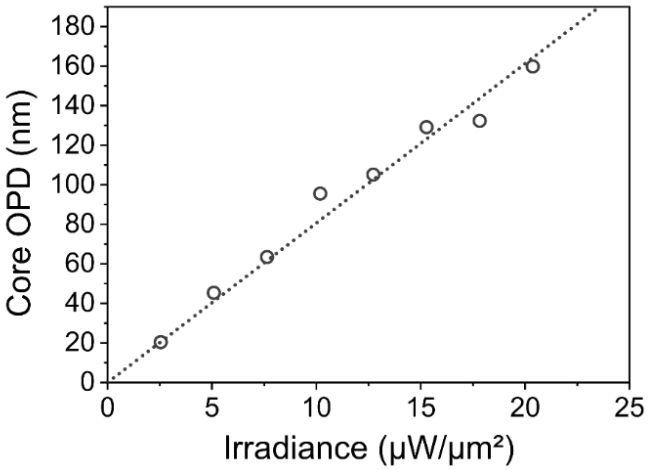

Figure 4.23. Evolution of the droplet core OPD value extracted from the rescaled experimental profiles as a function of the laser irradiance.

At this stage, GSPM only gives quantitative OPD values in the water droplet upon thermoplasmonic excitation. A quantitative value of temperature cannot be directly deduced from the raw OPD measurement. But reciprocally, an OPD radial profile can be easily calculated from a given temperature distribution, for example generated by simulation tools. This "retro-active" approach was used to correlate the core OPD values obtained experimentally to the temperature locally reached in the droplet.

4.4.2.7 Simulation of OPD profiles with COMSOL

COMSOL simulations were performed on the same 2D axisymmetric geometrical configuration than presented in the previous section to predict the temperature distribution in the droplet and the surrounding oil. To enable the direct comparison with the precedent experimental part, the simulation will be demonstrated on a droplet with 30 µm diameter. **Figure 4.24**.A shows the simulation domain, with the different media and the corresponding thermal diffusion coefficients. The water droplet (radius R, volume V) is defined as a uniform heat source that delivers a heating power Q (set as an input parameter in the simulation). The temperature field is obtained by solving the stationary heat equation in all the domain ($-\kappa_W \Delta T = Q/V$ in the droplet and $\Delta T = 0$ out of the droplet). For that COMSOL uses the finite element method on a triangular integration mesh

showed in **Figure 4.24**.B. The mesh size was refined at the droplet periphery to precisely assess the temperature distribution around the water/oil interface. **Figure 4.24**.C shows the temperature map resulting from the numerical simulation for $Q = 0.3\ mW$. The highest temperature is reached in the bottom half-portion of the droplet (here ~ 12 °C for $Q = 0.3\ mW$). Due to the presence of the capillary side on top of the droplet, a "pseudo-radial" temperature gradient is generated in the oil phase surrounding the side and bottom part of droplet. The range of this gradient is proportional to the heating power (here ~ 70 µm for $Q = 0.3\ mW$).

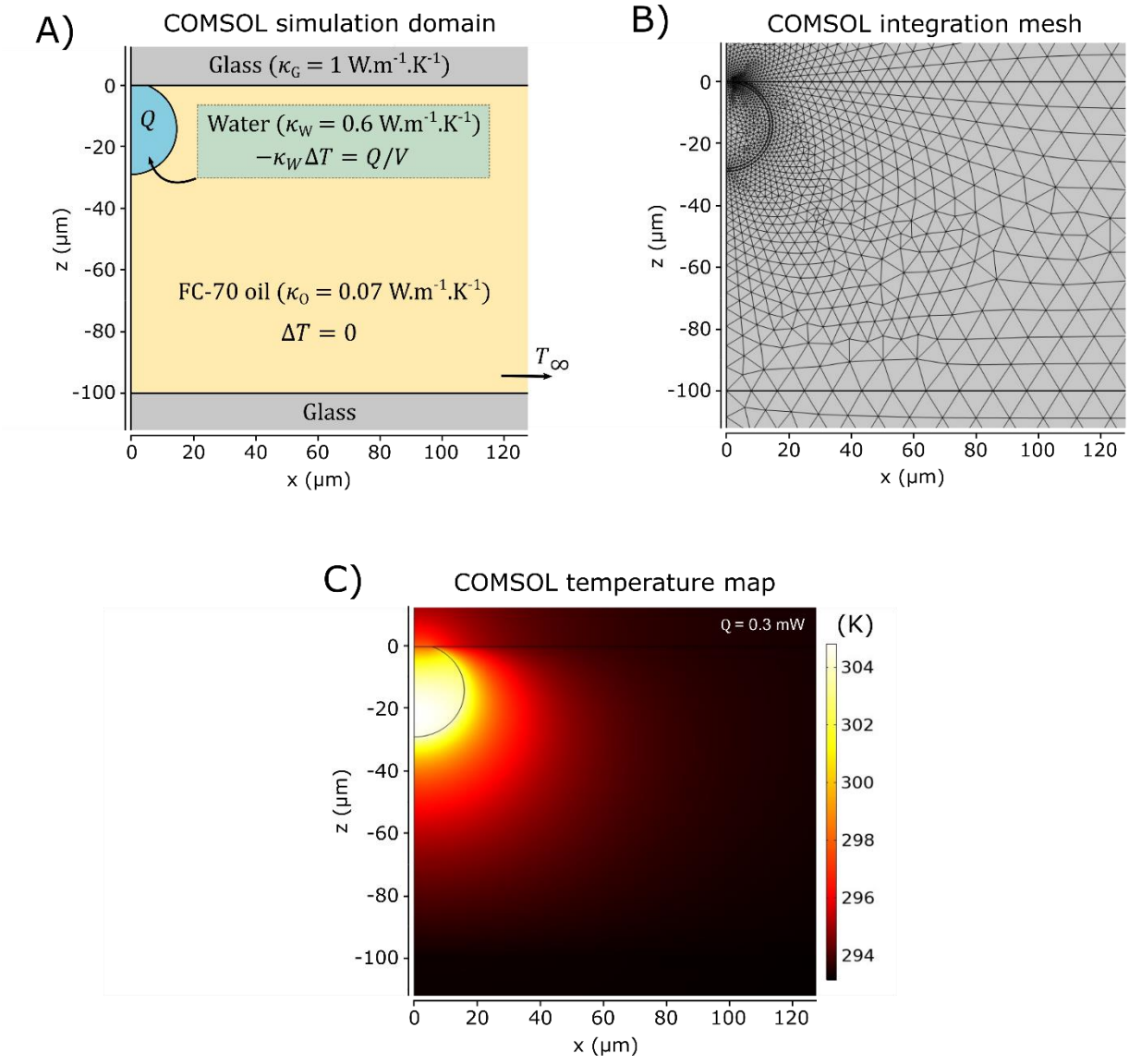

Figure 4.24. COMSOL simulation of the temperature field generated by a 30-µm droplet. A) Axisymmetric projection of the simulation domain (restricted to the direct vicinity of the droplet). The thermal diffusion coefficients κ and the

expression of the heat equation are indicated for each medium. The simulation domain was contained in a sphere which was 500 µm in radius (way larger than the droplet radius), used to fix the boundary condition $T_\infty = 273\ K$. B) Integration mesh used to solve the heat equation. C) Temperature map obtained for a heating power $Q = 0.3\ mW$ uniformly distributed in the water droplet.

The temperature map provided by COMSOL simulations can be post-processed to retrieve the local temperature increase ΔT and the corresponding variation of refractive index Δn in the droplet and the oil phase. The Δn map was calculated by multiplying each pixel of the ΔT map with the appropriate $\frac{dn}{dT}$ coefficient, namely $-0.90 \times 10^{-4}\ K^{-1}$ in the water droplet and $-3.16 \times 10^{-4}\ K^{-1}$ in the oil phase. **Figure 4.25**.A and B show the ΔT and Δn maps of a 30-µm droplet for $Q = 0.3\ mW$ (the domain has been restricted to the capillary interior on a length of 100 µm). The Δn map reveals that the largest variations of refractive index (in absolute values) are obtained in a thin oil layer surrounding the water droplet, and not in the droplet core where the highest temperatures are yet reached. This corona-like pattern is essentially due the highest thermal sensitivity of the oil phase compared to the water phase (the $\frac{dn}{dT}$ coefficient is 3.5 times higher for the oil compared to water).

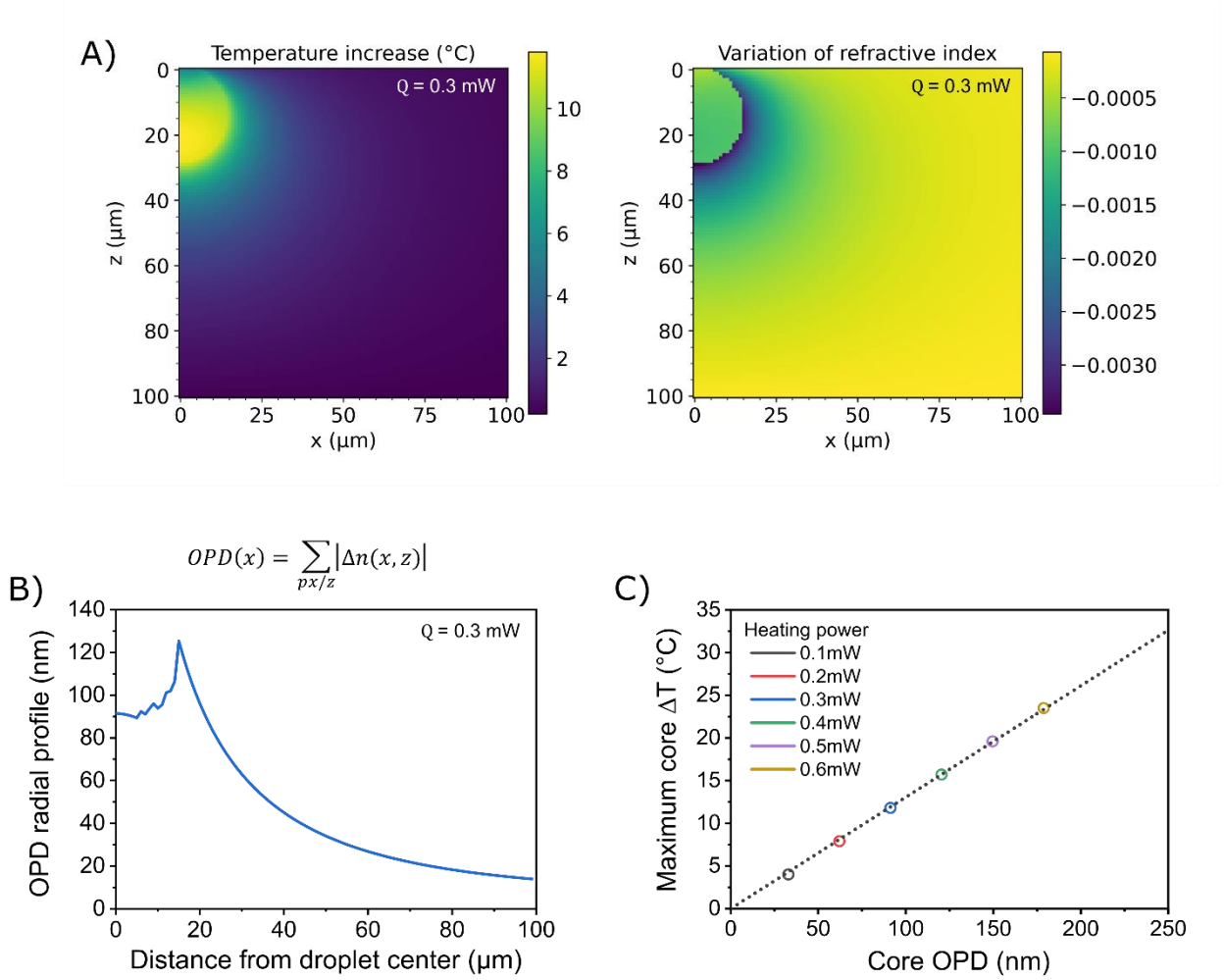

Figure 4.25. Image processing of the temperature map to retrieve numerical OPD profiles (demonstrated on a 30-µm droplet). A) Maps representing the variations of temperature and refractive index in the domain, deduced from the raw temperature map provided by COMSOL simulation (for a heating power of 30 mW). B) OPD radial profile calculated by numerical integration of the map of variations of refractive index along the z direction. C) Correlation between the OPD (measured on profile C) and the maximum temperature variation (measured on map A) in the core of the droplet. This process has been reproduced for different values of heating power used in the COMSOL simulation.

A numerical radial OPD profile can be deduced from the Δn image by summing the intensity of the pixels along the columns (which is the numerical equivalence of an integral along the z direction). This operation was made with absolute values of Δn to get positive OPD profiles (to be consistent with the analysis of the experimental data). **Figure 4.25**.C shows the OPD radial profile calculated from the Δn map showed in **Figure 4.25**.B (for $Q = 0.3\,mW$). This profile generated numerically shows the same qualitative features than the profiles obtained

experimentally (see **Figure 4.22**), suggesting that our system can be successfully simulated with COMSOL. In addition, the value of the core OPD measured on the numerical profile (at the center of the droplet) can be directly correlated to the maximum temperature increase in the droplet core (which was measured on the ΔT map). A linear relationship between these two parameters can be eventually obtained by running the simulation and numerical processing for different heating powers on the same droplet geometry. **Figure 4.25**.D shows this correlation curve for the model 30-µm droplet under study. For any droplet of radius R, a linear relationship reading $\Delta T_{max} = \alpha(R) \times OPD_{core}$ (with $\alpha(R)$ a coefficient depending on the droplet radius) can be deduced from simulation. This relationship will be applied to the experimental OPD profiles to retrieve the temperature increase reached in the droplet.

4.4.2.8 Conversion of experimental OPD in temperature increase

Thanks to the OPD-ΔT correlation obtained numerically with COMSOL simulations, we can convert the core OPD measured in the experimental profiles into a maximum temperature increase reached in the droplet core, as demonstrated in **Figure 4.26** for the droplet under study. The values of temperature increase (right axis) have been deduced from the core OPD values (left axis) via the linear relationship presented in **Figure 4.25**.

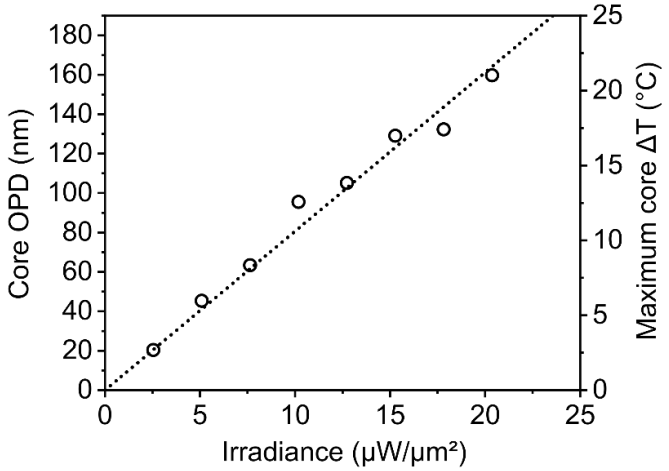

Figure 4.26. Determination of the temperature increase reached in the droplet core from the correlation between the experimental OPD value (left axis) and the simulated temperature map obtained with COMSOL (right axis, see **Figure 4.25**.C) in a 30-µm droplet for different laser irradiances.

This approach coupling experimental data and simulation enables to retrieve quantitative values of temperature increase in AuNPs-loaded droplets subjected to thermoplasmonic effects. For the 30-µm droplet under study, the temperature in the core of the droplet can reach 45 °C (increase by 20 °C) for the higher irradiance that was tested, i.e. temperature well above the LCST of PLL-g-PNIPAM.

This thermometry approach was used for droplets of different diameters: 20, 23, 27 and 30 µm (the latter being the droplet under study in the previous figures). For each droplet size, the evolution of the core OPD as a function of the laser irradiance was measured experimentally. Then the OPD-ΔT correlation was determined with COMSOL simulations and was used to retrieve the temperature increase in the droplet core as function of the laser irradiance (**Figure 4.27**).

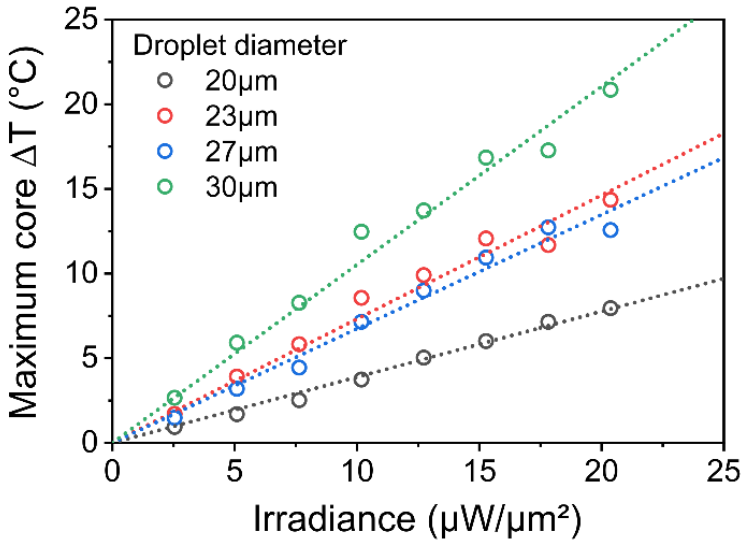

Figure 4.27. Evolution of the maximum temperature increase reached in the droplet core as a function of the laser irradiance for different droplet diameters.

A general trend appears from **Figure 4.27**: the largest the droplet, the highest the temperature increase in the droplet core. It may be explained by the fact that smaller droplets contain a lower amount of AuNPs, resulting in a lower production of heat upon irradiation. As an illustrative example, the temperature increases by less than 8 °C in a 20-µm droplet versus more than 20 °C in a 30-µm droplet for the same irradiance of 20 µW/µm². Moreover, the quasi-superimposition of the curves for the 23 and 27 µm droplet suggests that these two droplets contain a similar number of AuNPs, indicating concentration heterogeneities between the droplets in the same emulsion. To achieve a better control on the droplet size and AuNPs loading, an interesting way to explore would be the production of the emulsion by microfluidics. With this approach a proper calibration of the temperature increase as a function of the droplet size and the AuNPs concentration may be easier to implement.

These results demonstrate that GSPM can be used as a micro-thermometry technique to access the temperature generated in-situ by thermoplasmonic effects in individual droplets. However, this approach can face some experimental difficulties that need to be mentioned. First, the technique is highly sensitive to the movement of the droplet upon irradiation. Since a reference OPD image is taken *at a given droplet position* before irradiation, any translational movement of the droplet

during the measurements imprints a strong OPD signature on the image. This signal is associated to the high water-oil contrast that masks the contribution of thermoplasmonic effects and alters the associated OPD radial profiles (especially at the periphery of the droplet). Second, low concentrations of PLL-g-PNIPAM are required to avoid the formation of micron-size polymer aggregates in the core of the droplets at high temperature (i.e. at high irradiance). Indeed, these aggregates may also contribute to the wavefront distortion and may perturb the quantitative analysis of the heating-induced OPD. This effect was typically observed at 2 wt% and 5 wt% in PLL-g-PNIPAM. Therefore, we used a concentration of 1 wt% for which the formation of visible aggregates was not observed. Third, the droplets can undergo stability issues over prolongated periods of irradiation, that can lead to droplet burst or polymer leakage in the oil phase. These negative effects were particularly observed at high irradiance (> 15 µW/µm²) and/or high AuNPs. That is why the irradiance range was limited and the AuNPs concentration was restricted to 0.05 wt%.

4.4.3 Application: light-induced accumulation of nanoparticles in PLL-g-PNIPAM shells

In the previous sections, we demonstrated that the collapse transition of PLL-g-PNIPAM in emulsion droplets can be induced by the photoexcitation of AuNPs and that the temperature reached in the core of the droplets can be measured thanks to grating-shadow phase microscopy. We proposed to apply this light-responsiveness to trigger the thermo-induced accumulation of NPs in the polymer shell (described in section 4.3.2) with a better spatio-temporal control. The idea would be to mix fluorescent NeutravNPs and plasmonic AuNPs with PLL-g-PNIPAM in the emulsion droplets. As demonstrated in section 4.3.2, an accumulation of NeutravNPs can be observed at the droplet periphery upon heating, mediated by the collapse transition of PLL-g-PNIPAM. In absence of AuNPs, the heating process was performed at the scale of the whole sample within a few minutes. The addition of AuNPs in the aqueous phase may enable to trigger

the thermo-induced interfacial accumulation upon laser excitation at the level of an individual droplet and quasi-instantaneously.

As a proof of concept, an aqueous solution containing 1 wt% of PLL-g-PNIPAM, 0.01 wt% of NeutravNPs and 0.05 wt% of AuNPs was prepared and emulsified in an oil phase containing 0.05 wt% of Krytox. As in section 4.3.2, the distribution of NeutravNPs in the droplets was assessed with confocal imaging. The plasmonic excitation could not be directly implemented within the confocal microscope since it was not equipped with sufficiently powerful laser source in the green range. The plasmonic excitation was performed on the commercial microscope used for bright field imaging (see Chapter 1), supplemented with a 532-nm laser diode that can deliver a nominal power up of 25 mW at the level of the sample (see **Appendix A**). The diameter of the laser spot was set to 20 µm in focal plane.

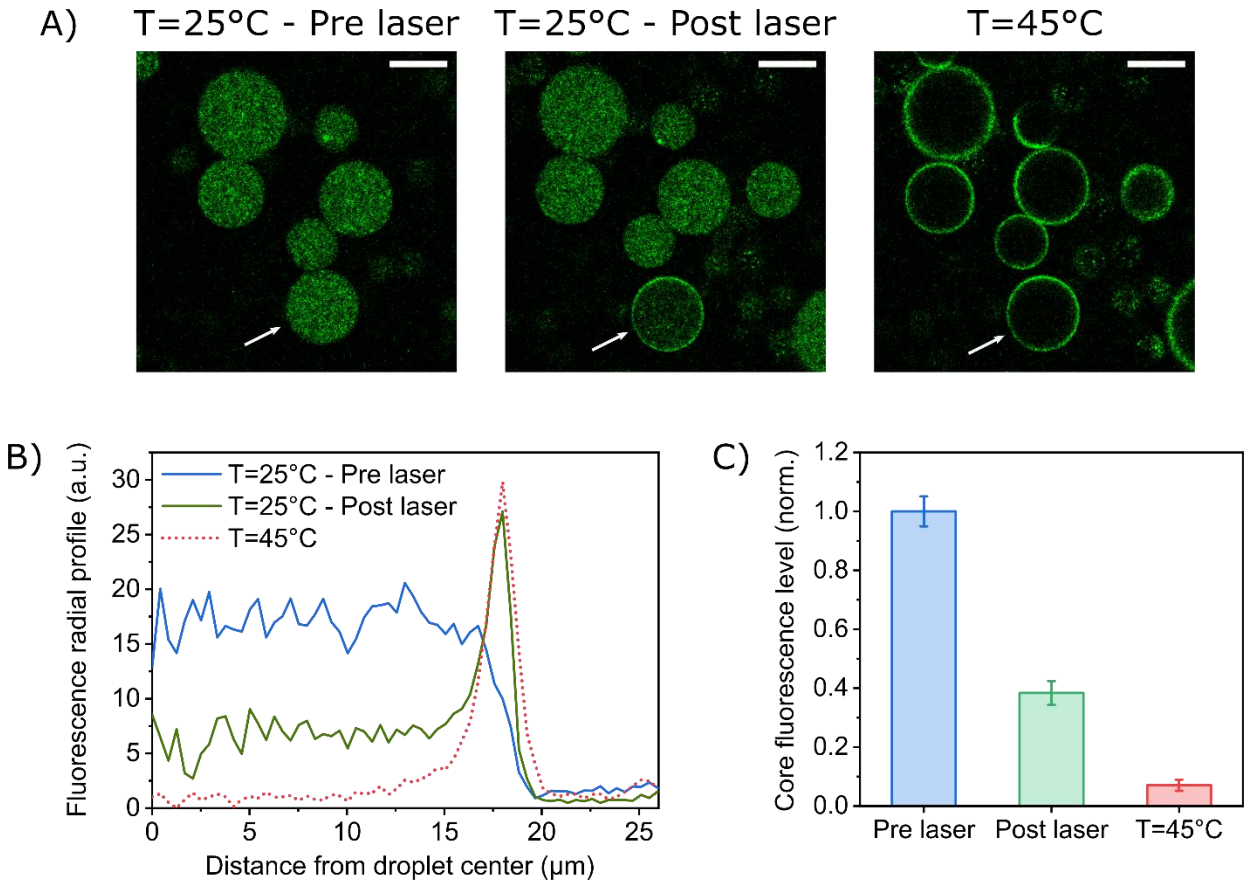

Figure 4.28. Light-induced accumulation of NeutravNPs in the PLL-g-PNIPAM shell via the thermoplasmonic excitation of AuNPs. A) Confocal micrographs of an emulsion containing 1 wt% PLL-g-PNIPAM, 0.01 wt% of

NeutravNPs and 0.05 wt% of AuNPs in the aqueous phase and 0.05 wt% of Krytox in the oil phase. The emulsion was imaged at 25 °C before and after 532-nm light irradiation of an individual droplet (indicated with a white arrow) for 30 s at 31.8 µW/µm², and then uniformly heated at 45 °C (scale bars = 30 µm). B) Fluorescence radial profiles of the droplet indicated with a white arrow. C) Core fluorescence level of the droplet indicated with a white arrow expressed as a fraction of the initial value at 25 °C (error bars = standard deviation of the mean).

Figure 4.28.A shows confocal micrographs of the emulsion at 25 °C before and after laser irradiation of an individual droplet (indicated by a white arrow) for 30 s with an irradiance of 31.8 µW/µm². The fluorescence signal detected in the micrographs is only due to NeutravNPs. Before irradiation, they were uniformly distributed in all the droplets of the emulsion, as expected at room temperature according to previous results (see section 4.3.2). After irradiation, a bright corona was observed at the periphery of the targeted droplet, in addition to a decrease of the fluorescence level in the core. This pattern, highlighted in the fluorescence radial profile in **Figure 4.28**.B, is characteristic of the thermal-induced accumulation of NeutravNPs in the PLL-g-PNIPAM shell which has been described in section 4.3.2. In comparison, a uniform volume distribution was still observed in the other droplets. This result demonstrates that the interfacial capture of NPs in the PLL-g-PNIPAM shell can be triggered with light in individual droplets. After the irradiation experiment, the whole emulsion was thermalized at 45 °C, i.e. above the LCST of PLL-g-PNIPAM. At this temperature, the thermo-induced accumulation of NeutravNPs at the interface was observed in all the droplets, as expected regarding the results of section 4.3.2. In the droplet previously targeted with the laser, this step of uniform heating induced a further decrease of the fluorescence level that almost fell to 0 (see the radial profile in **Figure 4.28**.B). This result suggests that the migration of NeutravNPs towards the interface was only partially achieved upon light irradiation and was less efficient than a global heating of the system. This result is quantitatively confirmed by the comparison of the fluorescence level in the droplet core after irradiation at 25 °C and after heating at 45 °C. **Figure 4.28**.C shows that 60 % of the fluorescence has disappeared after irradiation, compared to 95 % after heating.

This result suggests that the temperature has not reached 45 °C in the droplet upon irradiation of the AuNPs, at least non uniformly or not during enough time. However, considering the size of the droplet (34 µm diameter) and the irradiance used during the experiment (31.8 µW/µm²), the irradiation should generate at least 20 °C in the core of the droplet according to the

GSPM results (since 20 °C were reached with 20 µW/µm² in a 30-µm droplet, see **Figure 4.27**). The lower efficiency observed in the confocal experiments was probably due to the non-uniform irradiation of the droplet, as the diameter of the laser spot (20 µm) was smaller than the droplet diameter (34 µm). Accordingly, the temperature reached in the sample was not uniform, and likely lower along the equatorial periphery of the droplet, which could explain the partial migration of the NeutravNPs to the interface. This issue of non-uniform irradiation was not experienced in the GSPM experiments since the diameter of the laser spot in the focal plane was 50 µm, i.e. larger than the droplet size.

The same experiment was performed with higher irradiances on droplet of similar sizes and on smaller droplets, but the decrease of the fluorescence core level was always around 60 %. We demonstrated that the segregation of NPs in the polymer shell can be induced by light in presence of AuNPs but some additional experiments should be made to precisely assess the efficiency of this process. In particular, the optical set-up should be optimized to enable the plasmonic excitation and the confocal observation on the same device. This may enable to observe the evolution of the NPs distribution concomitantly to the laser excitation, especially to determine the influence of the irradiation time on the process.

4.5 Conclusion

In this Chapter we demonstrated that our system based on interfacial complexation of PLL derivatives enables the straightforward formation of “composite” shells associating polymer and NPs. We evidenced the propensity of PLL to adsorb at the surface of NPs of different nature such as gold NPs, or carboxylate- or protein-modified polystyrene NPs. In particular, we showed that PLL-g-PNIPAM can coat the NPs and induce their aggregation upon hydrophilic-to-hydrophobic transition of the PNIPAM strands. We transposed this phenomenon in emulsions, in conditions of interfacial complexation of PLL-g-PNIPAM. We demonstrated that NPs, that were initially dispersed in the core of the droplets at ambient temperature, spontaneously accumulated at the surface of the droplets upon heating above the cloud point of PLL-g-PNIPAM. We attributed this

process to a thermo-induced aggregation of the NPs and their progressive capture in the polymer shell, driven by hydrophobic interactions between PNIPAM chains localized both at the surface of the NPs and at the water/oil interface. Interestingly, the NPs remained segregated in the polymer shell when the emulsion was cooled back to ambient temperature. We thus evidenced a straightforward way to incorporate NPs in polymer shells without resorting to chemical reactions or capsule post-processing.

In the context of "composite" capsules, gold NPs (AuNPs) are particularly attractive due to their capability to convert light into heat at the microscale via thermoplasmonic effects. We demonstrated that, in presence of AuNPs, the thermal transition of PLL-g-PNIPAM can be achieved upon light irradiation. We applied this technique to successfully trigger the thermo-induced accumulation of NPs in the polymer shell upon light irradiation for a few seconds in individual droplets, showing the potential of the technique to achieve a better spatio-temporal control of the capsule stimulation.

We also developed a protocol based on quantitative phase imaging to measure the temperature that can be reached in AuNPs-loaded droplets upon thermoplasmonic excitation. This protocol relies on the measurement of optical path difference induced by local temperature gradients generated upon AuNPs excitation. Thanks to a calibration obtained by simulation, the optical path difference can be converted in a local measurement of the temperature increase. This technique revealed that the temperature can be increased by more than 20 °C in a few ms in sufficiently large droplets (typically 30 µm), which is promising for on-demand delivery upon photo-thermal stimulation.

Chapter 5

Polymer capsules with UCST behavior formed by interfacial complexation

5.1 Introduction

In Chapter 3, we evidenced the potential of PLL comb-like derivatives to form polymer shells by interfacial complexation. We made an exhaustive study on a LCST derivative, namely PLL-g-PNIPAM, to characterize physico-chemical changes of the shell upon temperature variations. In Chapter 4, we demonstrated that the thermal response of PLL-g-PNIPAM enables the capture NPs in the polymer shell when its state is switched to hydrophobic, i.e. at high temperature.

In this Chapter, we propose to extend our approach with the study of a UCST comb-like derivative of PLL, namely PLL-g-PAAMAN. We evidenced the formation of PLL-g-PAAMAN shells by interfacial complexation, switching from a hydrophobic state at ambient temperature to a hydrophilic state upon heating. This work constitutes, as far as we know, the first demonstration of the formation of aqueous-core polymer microcapsules exhibiting a UCST behavior. This system is particularly promising for delivery applications since it implies the solubilization of the capsule shell upon heating, and consequently the release of the encapsulated content.

We demonstrated that NPs can be incorporated in the PLL-g-PAAMAN shell during the preparation of the emulsion, resulting in “composite” capsules at ambient temperature. Upon heating, the NPs were redispersed in the droplet core, resulting from the solubilization and partial redispersion of the PLL-g-PAAMAN shell. In addition, we demonstrated that the phase transition of the polymer shell can be induced upon light irradiation in presence of AuNPs, paving the way to photo-thermal delivery from UCST polymer capsules.

5.2 Synthesis of PLL-g-PAAMAN polymer and formation of PLL-g-PAAMAN shells by interfacial complexation

5.2.1 PAAMAN polymers

The PAAMAN polymers used in this work were synthesized in the group of Prof. Yue Zhao (Sherbrooke University, Canada). Only two polymers, named P1 and P2, will be presented as potential candidates for the formation of UCST capsules (**Figure 5.1**). P1 and P2 were synthesized by RAFT from two different RAFT agents, with acrylamide/acrylonitrile ratios of 0.72/0.28 and 0.66/0.34 respectively (see **Appendix A** for experimental details). The molecular masses were 12 kDa and 15 kDa respectively.

The cloud point of each polymer was evaluated by turbidity measurements on solutions at 1 wt% in water (**Figure 5.1**). The cloud point was ~39 °C for P1 and ~45 °C for P2 (temperature corresponding to 50 % of transmittance). At this stage, P1 seems more appropriate for delivery applications since its cloud point is lower and easier to reach in biological contexts.

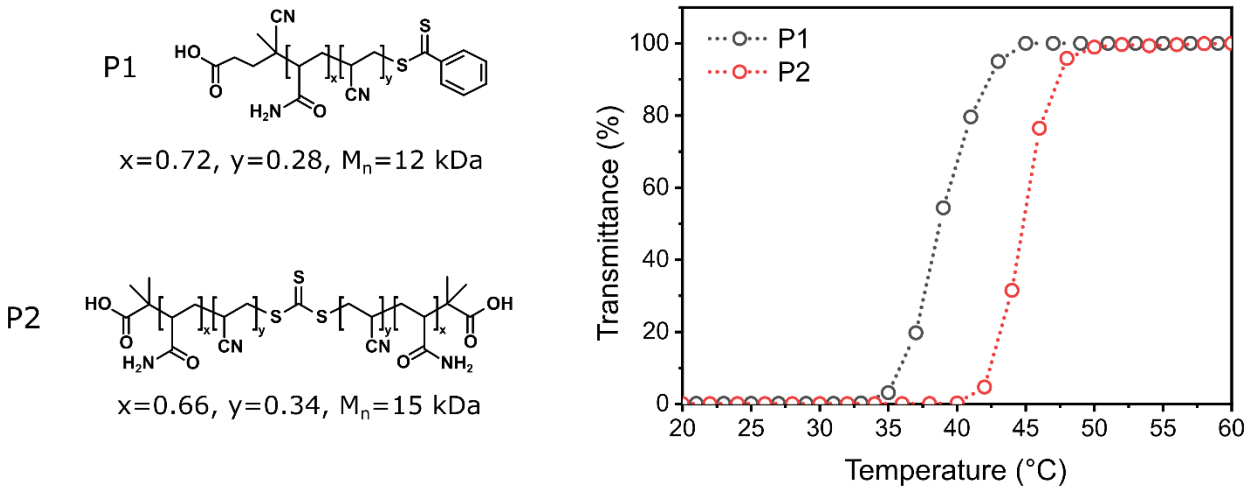

Figure 5.1. Structure of the two PAAMAN polymers considered as candidates for the formation of polymer capsules and the corresponding turbidimetry heating curves (at 1 wt% in pure water).

The physical behavior of the two PAAMAN polymers in solution was further analyzed by bright field confocal microscopy (**Figure 5.2**). Solutions at 10 wt% in pure water were heated at 48 °C (above their cloud point) and then cooled back to 18 °C to trigger the collapse transition of the polymer.

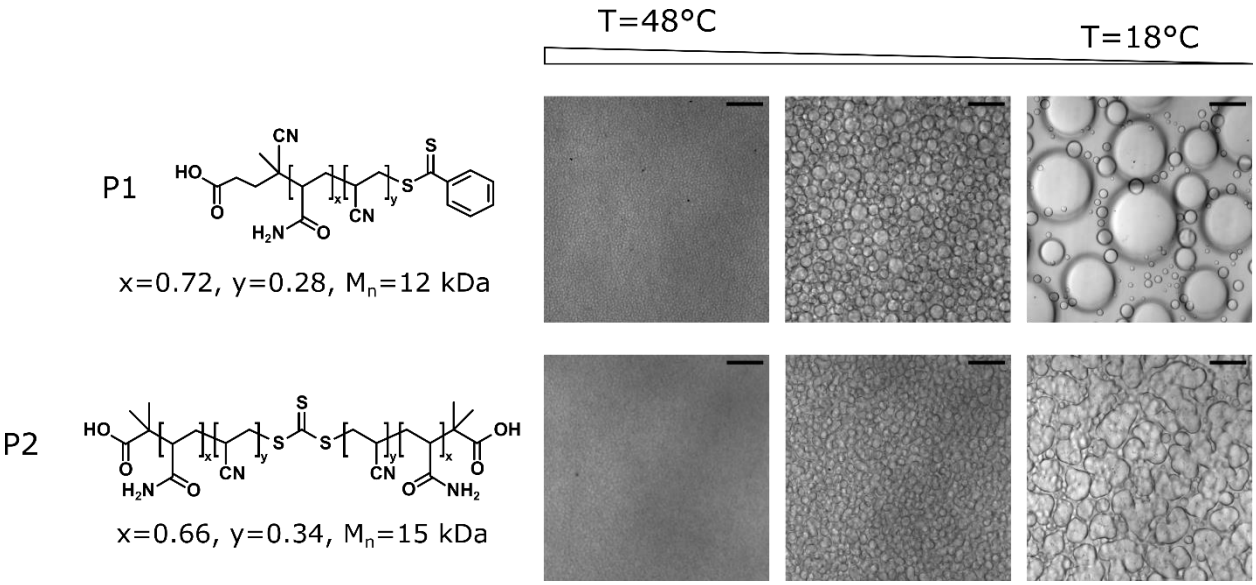

Figure 5.2. Confocal micrographs of solutions of the two PAAMAN polymers at 10 wt% in pure water upon cooling from 48 °C to 18 °C (scale bars = 50 µm).

Upon cooling, each polymer undergoes a liquid-liquid phase separation characteristic of a UCST-type behavior, but the dynamics of their polymer-enriched phase is drastically different. P1 forms liquid droplets that rapidly coalesce and relax whereas P2 forms gel-like irregular aggregates that partially and slowly merge. This difference of behavior can be due to several factors: the difference in chain composition (monomer ratio, end-groups, chain length), the potential presence of residual traces of solvent synthesis, or the degree of hydration of the initial polymer powder.

The gel-like behavior of P2 seems more appropriate for the formation of robust/rigid polymer shells at ambient temperature and was selected for the rest of the experiments (despite its higher cloud point). Accordingly, in the following the term of PAAMAN will refer to the polymer P2.

5.2.2 Synthesis of PLL-g-PAAMAN copolymer

As for PNIPAM in Chapter 1, non-ionic PAAMAN chains were grafted onto PLL to drive its interfacial complexation at the surface of emulsions droplets. However, the PAAMAN chains were terminated by carboxylic acid groups at both ends. A direct coupling on PLL (via esterification) would thus promote the formation of cross-links and not the formation of comb-like copolymers. As an alternative, the central trithiocarbonate unit of PAAMAN chains was cleaved by aminolysis to yield two shorter chains terminated by a thiol group at one end. Then the grafting of thiol-terminated PAAMAN strands onto PLL was mediated by an intermediary short PEG linker terminated with an NHS-ester group at one end (for the anchoring on PLL) and a maleimide group at the other (for thiol-ene click reaction). The synthesis of PLL-g-PAAMAN was achieved in one-pot according to a two-step procedure described in **Appendix A** and schematized in **Figure 5.3**. In this synthesis, a slight excess of PEG linkers was used compared to aminolyzed PAAMAN moieties to achieve the complete incorporation of the PAAMAN chains introduced in the reactive bath (typically 7 mol% of the side amino groups of PLL were functionalized with the linker, for 2-4 wt% of thiol-terminated PAAMAN strands produced *in situ*).

Fluorescent derivatives of PLL-g-PAAMAN were obtained by addition of a reactive fluorophore that can be grafted on PLL (rhodamine-NHS or coumarin-NHS) during the first step of the synthesis.

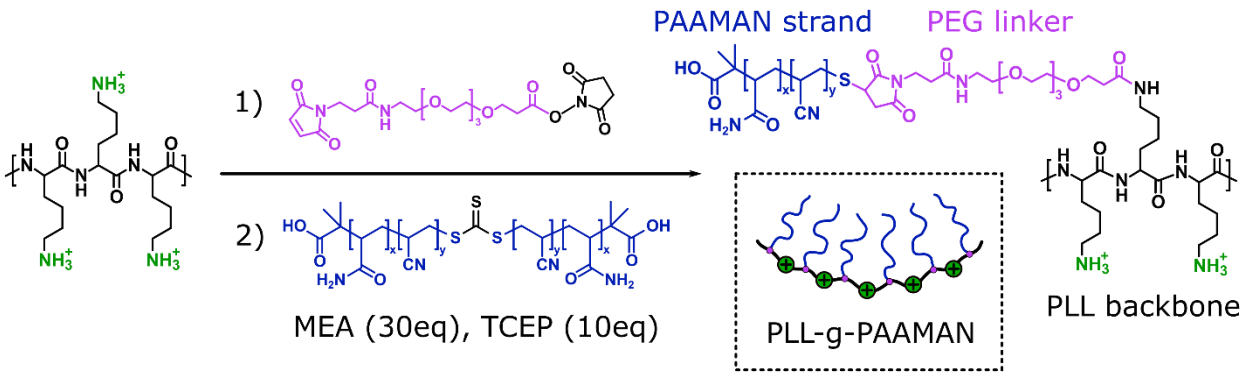

Figure 5.3. Synthesis procedure for the grafting of PAAMAN strands on a PLL backbone using an intermediary poly(ethylene glycol) difunctional linker. MEA = monoethanolamine, TCEP = tris(2-carboxyethyl)phosphine.

The composition of the PLL-g-PAAMAN copolymer can be tuned by adjusting the PLL/PAAMAN weight ratio during the synthesis. In the following, most of the results are related to two copolymers with different PLL/PAAMAN weight ratio :

- $PLL_{0.53}$-g-$PAAMAN_{0.47}$ with a PLL/PAAMAN weight ratio of 53/47 wt%, obtained by grafting 6 PAAMAN strands on a 52 kDa PLL.
- $PLL_{0.42}$-g-$PAAMAN_{0.58}$ with a lower PLL/PAAMAN ratio of 42/58 wt%, obtained by grafting 4 PAAMAN strands grafted on a 22 kDa PLL.

The thermoresponsiveness of PLL-g-PAAMAN in solution will be illustrated in the case of $PLL_{0.53}$-g-$PAAMAN_{0.47}$. The cloud point of this copolymer (at 1 wt% in pure water) was measured at ~ 49 °C, i.e. 4 °C above the cloud point of non-grafted PAAMAN (dashed lines in **Figure 5.4)**, indicating that the grafting on PLL slightly shifted the UCST of PAAMAN chains towards higher temperature. This behavior can be attributed to the participation of PLL in the inter-PAAMAN hydrogen-bond network, hence favoring the aggregative state of the polymer on a broader temperature range.

For practical reasons related to microscopy observations, we needed to decrease the cloud point of PLL-g-PAAMAN solutions, typically below 45 °C. For that, we supplemented the polymer solutions with 20 mM of the chaotropic salt KSCN.[1] In these conditions, a "salting out" effect was observed for non-grafted PAAMAN for which the cloud point was shifted from 45 °C to 40 °C (**Figure 5.4**). Interestingly, this effect was more important for PLL-g-PAAMAN with a decrease of the cloud point from 49 °C to 37 °C and a significant broadening of the temperature range of the UCST transition (now ranging from 30 °C to 48 °C). Thanks to this cloud point adjustment, the thermo-responsive behavior of PLL-g-PAAMAN could be observed in a temperature window which was (i) more accessible in the confocal microscopy set-up and (ii) more appropriate for biological applications.

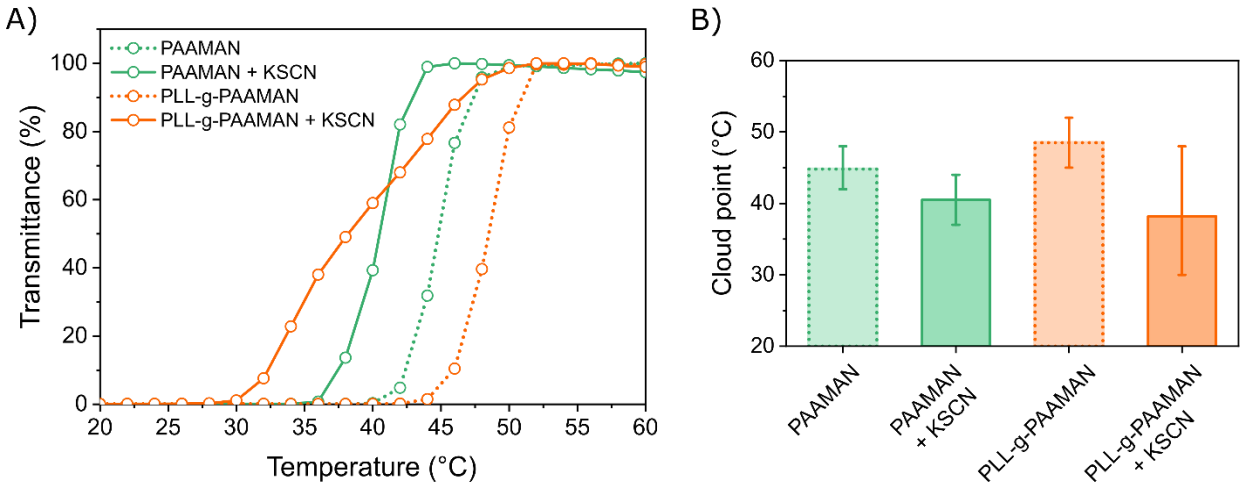

Figure 5.4. Adjustment of the cloud point of PLL-g-PAAMAN solutions with thiocyanate salt. A) Turbidimetry heating curves of pristine PAAMAN and $PLL_{0.53}$-g-$PAAMAN_{0.47}$ solutions at 1 wt% in either pure water or 20 mM KSCN solution. B) Cloud points extracted from the turbidimetry curves at 50 % transmittance (the bars indicate the initial and final temperatures of the UCST transition).

5.2.3 Formation of PLL-g-PAAMAN capsules

The formation of PLL-g-PAAMAN shells was achieved by interfacial complexation in water-in-oil emulsions as presented in Chapter 1, except that the emulsification was not performed at room temperature but well above the cloud point of PLL-g-PAAMAN. Briefly, an aqueous phase containing PLL-g-PAAMAN (typically in the wt% range) and 20 mM KSCN was emulsified at 60 °C in a continuous oil phase made of FC-70 oil containing Krytox surfactant (typically at 0.05-0.1 wt%).

The distribution of the polymer in the emulsion droplets after cooling down to 18 °C was assessed by confocal microscopy using rhodamine-labeled PLL-g-PAAMAN. **Figure 5.5.**A and B shows the results for $PLL_{0.53}$-g-$PAAMAN_{0.47}$ and $PLL_{0.42}$-g-$PAAMAN_{0.58}$, respectively.

For $PLL_{0.53}$-g-$PAAMAN_{0.47}$, the bright fluorescent corona observed at the periphery of the droplets was indicative of the formation of a polymer shell (**Figure 5.5.**A). For $PLL_{0.42}$-g-$PAAMAN_{0.58}$, micrometric globular aggregates punctuating both the core and the periphery of the droplets were observed (**Figure 5.5.**B). These results suggest that the ability of PLL-g-PAAMAN to adsorb at the water/oil interface is highly dependent on the composition of the polymer, and

seems to require a relatively high PLL/PAAMAN weight fraction (or at least a sufficiently long PLL chain length). The predominance of PAAMAN in the polymer (in terms of weight fraction) may favor phase separation under the form of globules below the cloud point – as do non-grafted PAAMAN chains, hence promoting clustering in solution instead of complexation at the water/oil interface.

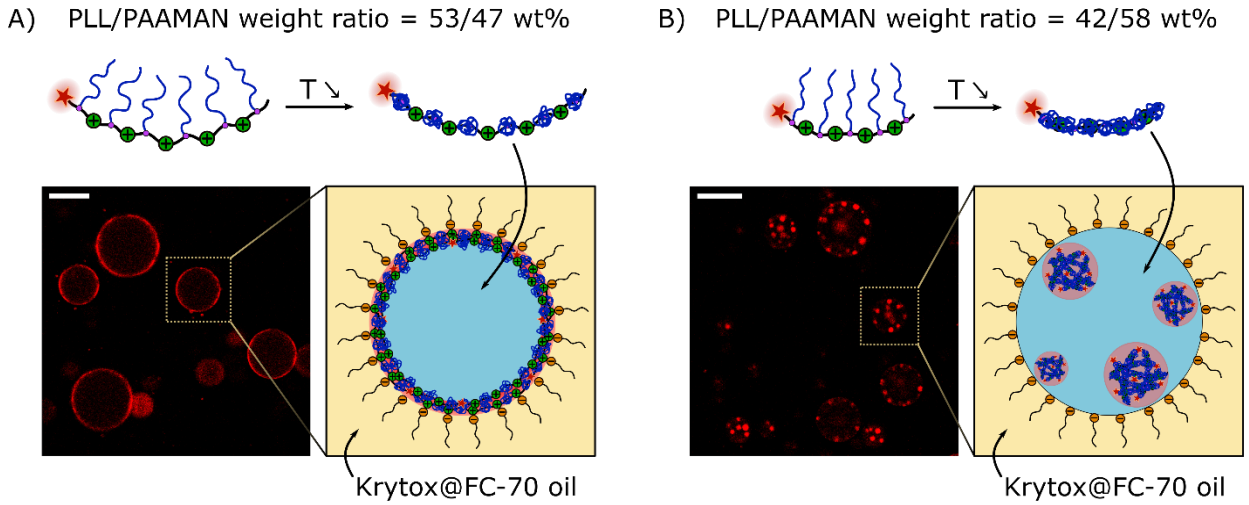

Figure 5.5. Influence of the composition of PLL-g-PAAMAN on the ability to form polymer shells by interfacial complexation. Water-in-oil emulsions were prepared at 60 °C with 1 wt% of rhodamine-labeled PLL-g-PAAMAN and 20 mM of KSCN in the aqueous phase and 0.05 %wt of Krytox in the oil phase. A) Polymer shells were effectively formed at the periphery of the water droplets in the case of $PLL_{0.53}$-g-$PAAMAN_{0.47}$, after cooling the emulsion down to 18 °C. B) In the case of $PLL_{0.42}$-g-$PAAMAN_{0.58}$, the flat deposition of the polymer at the interface was supplanted by a globular association of the polymer within the droplet core. Scale bar in the confocal micrographs = 30 µm.

The impact of chain length and grafting ratio on the behavior of PLL-g-PAAMAN in emulsion would deserve further studies to rationalize the synthesis of the copolymer and optimize the formation of uniform capsule shells. In this study however, $PLL_{0.53}$-g-$PAAMAN_{0.47}$ has been used for the proof of concept. In the following, this polymer will be simply referred to as PLL-g-PAAMAN for the sake of readability.

5.3 Thermoresponsive behavior of PLL-g-PAAMAN shells

5.3.1 Thermal transition assessed with ANS fluorescence

As for PLL-g-PNIPAM in Chapter 2, the fluorescence of ANS was used as an extrinsic polarity/hydrophobicity probe. **Figure 5.6** shows confocal micrographs of a representative droplet containing PLL-g-PAAMAN (non-fluorescent) and ANS below and above the cloud point. High fluorescence intensity at the surface of the droplets at 18 °C validates the hydrophobic nature of the polymer shell below the cloud point. In contrast, a low and homogeneous fluorescence was observed in the droplet at 48 °C, suggesting a highly hydrophilic environment both in the core and near the interface. When the temperature was brought back below the cloud point, the high fluorescence level was recovered at the surface of the droplet interface. These results confirm the existence of a reversible hydrophobic-to-hydrophilic transition of the PLL-g-PAAMAN upon heating.

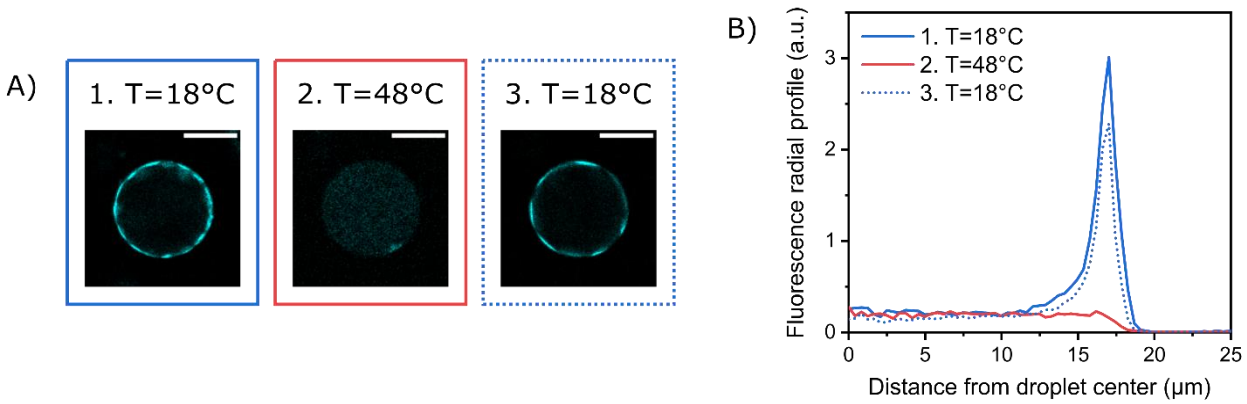

Figure 5.6. Visualization of the UCST-type transition of PLL-g-PAAMAN shell using ANS as extrinsic fluorescent probe. A) Confocal micrographs of a representative droplet containing 1 wt% PLL-g-PAAMAN and 100 µM ANS in 20 mM KSCN, dispersed in oil containing 0.05 wt% Krytox. The emulsion was thermalized at 18 °C, 48 °C and 18 °C successively. B) Fluorescence radial profiles of the droplet.

5.3.2 Measurement of polymer surface excess with intrinsic fluorescence measurements

The thermo-responsiveness of the shell was quantitatively assessed in-situ by measuring the surface excess while increasing the temperature above the cloud point (from 18 °C to 48 °C). Upon heating, a decrease of the fluorescence level was observed in the interfacial layer concomitantly with an increase of the fluorescence level in the core of the droplets, as illustrated by the fluorescence radial profiles obtained by confocal imaging (see **Figure 5.7.**A and B). This qualitative evolution was attributed to the hydrophobic-to-hydrophilic transition of the PAAMAN strands that may induce the solubilization of the interfacial polymer layer and its partial redispersion in the core, as depicted in **Figure 5.7.**A. The quantitative measurement of the polymer surface excess previously introduced in Chapter 1 was implemented here in the case of PLL-g-PAAMAN. The evolution of the surface excess as a function of the droplet diameter or the residual core concentration at 18 °C and 48 °C are shown in **Figure 5.7.**C and D, respectively. These data confirm that the raise of temperature induces (i) a decrease of the surface excess for any droplet size (of 45 % in average) and (ii) an increase of the polymer concentration in the core of the droplets (of 130 % in average). These results are consistent with a partial solubilization of the hydrophilic PLL-g-PAAMAN shell upon heating.

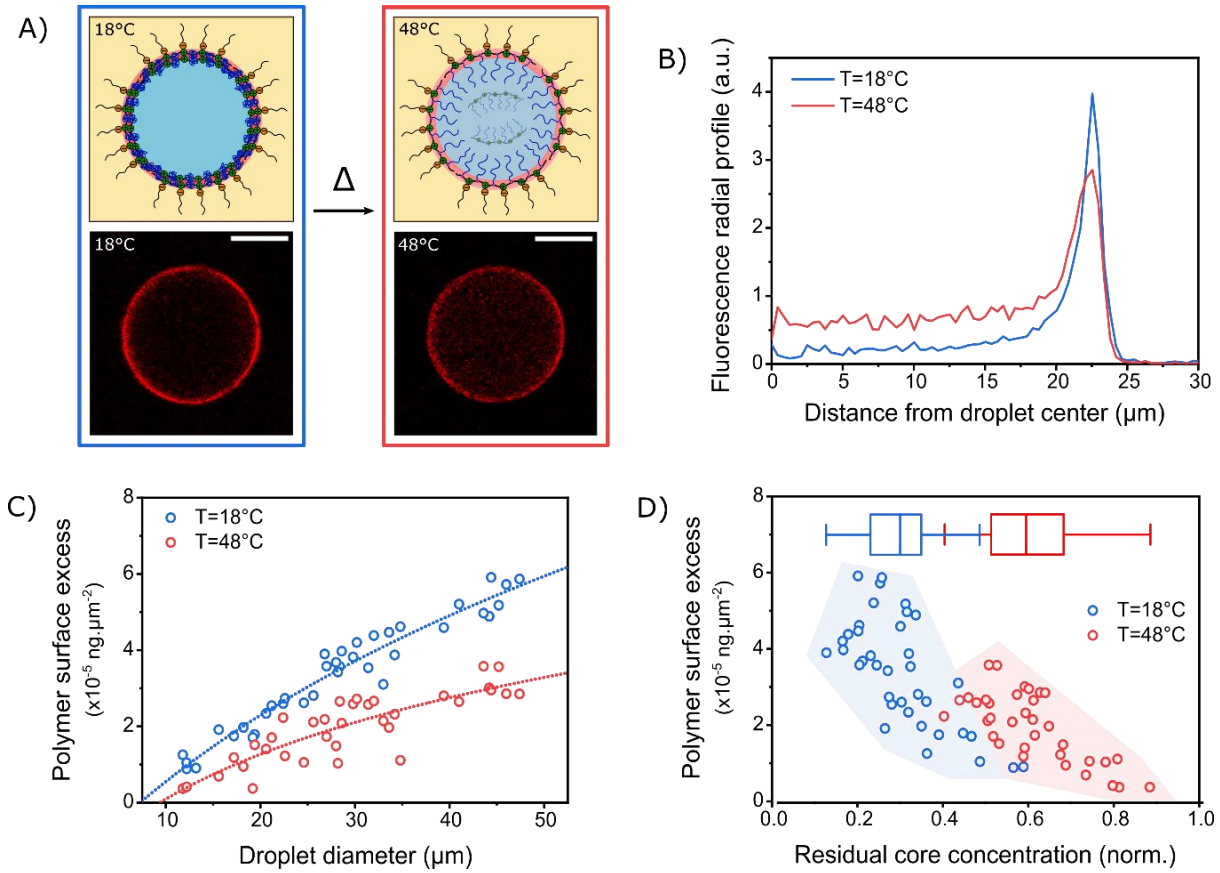

Figure 5.7. Quantification of the polymer surface excess by intrinsic fluorescence measurements. A) Confocal micrographs of a representative water droplet containing 1 wt% of rhodamine-labeled PLL-g-PAAMAN (in 20 mM KSCN) dispersed in FC-70 oil containing 0.05 wt% of Krytox at 18 °C and 48°C (scale bars = 20 µm). B) Fluorescence radial profiles of the droplets. C) Evolution of the surface excess of PLL-g-PAAMAN as a function of the droplet diameter at 18 °C and 48 °C, calculated from fluorescence measurements. D) Evolution of the surface excess of PLL-g-PAAMAN as a function of the residual polymer concentration in the droplet core at 18°C and 48°C (colored domains are guides for the eye). Box plots give the min/Q1/median/Q3/max values of the distribution of the residual core concentration.

5.3.3 Evaluation of the fluidity of the polymer shell by fluorescence recovery after photobleaching

Changes in fluidity/dynamics of the polymer shell with temperature was assessed by Fluorescence Recovery After Photobleaching (FRAP). FRAP experiments were performed on coumarin-labeled

PLL-g-PAAMAN shells (prepared in the same concentration and temperature conditions as described above) at 18 °C and 48 °C (**Figure 5.8**.A). The fraction of mobile chains within the polymer shell, denoted M_f, was deduced from the following equation:

$$M_f = \frac{I_\infty - I_0}{I_i - I_0}$$

where I_i was the fluorescence intensity before bleaching (fixed at 1 by normalization), I_0 the intensity just after bleaching and I_∞ the intensity at t = 2 min (assuming that a steady state was approximately reached at this time). Representative curves are shown in **Figure 5.8**.B. At 18 °C, almost no fluorescence recovery was observed in the photobleached area, indicating that mobile chain fraction was below 10 %. In these conditions, the diffusion of polymer chains within the shell below the cloud point is likely frozen. In contrast at 48 °C, a partial recovery was observed at t = 2 min. suggesting a diffusion of the chains in the polymer shell (an estimate of the mobile fraction being here slightly above 50%). These results are consistent with a thermo-induced transition of the polymer shell from a solid-like (or frozen) state to a fluid-like state upon heating.

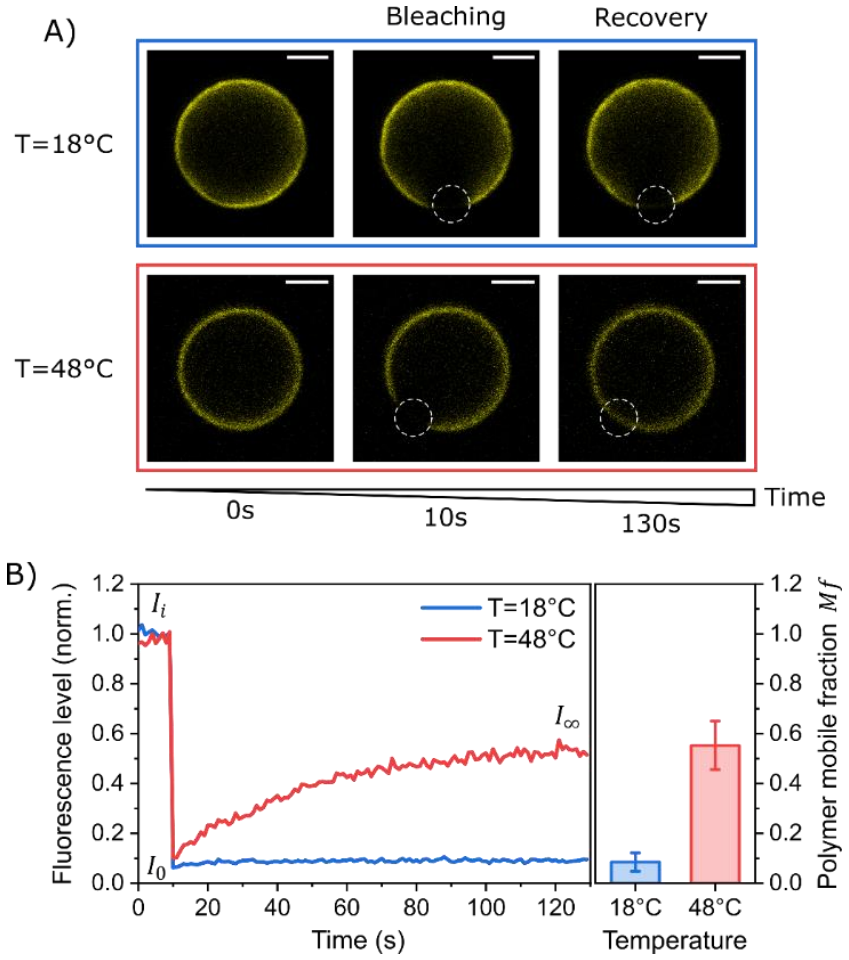

Figure 5.8. Fluorescence Recovery After Photobleaching (FRAP) experiments on thermoresponsive PLL-g-PAAMAN shells. A) Confocal micrographs of representative droplets containing 1 wt% of coumarin-labeled PLL-g-PNIPAM (in 20 mM KSCN) during FRAP experiments at 18 °C and 48 °C (scale bars = 5 µm). B) Left: FRAP curves from the top experiments. Right: polymer mobile fraction $M_f = \frac{I_\infty - I_0}{I_i - I_0}$ calculated from the fluorescence intensity levels measured in the FRAP curves at 18 °C and 48 °C (error bars = standard deviation on 5 and 8 droplets respectively).

As a comparison, FRAP experiments were conducted in the same conditions on a non-thermoresponsive coumarin-labeled PLL-g-PEG (**Figure 5.9**). Compared to PAAMAN strands, PEG strands do not develop inter-chain hydrogen bonds that may affect the dynamics of the chains within the shell. At 18 °C the mobile fraction of PLL-g-PEG reaches ~45 %, which is far above the mobile fraction obtained for PLL-g-PAAMAN (< 10 %). This difference in dynamics at low temperature confirms the frozen nature of the PLL-g-PAAMAN shell, associated to a robust inter-polymer hydrogen-bond network. At 48 °C, the mobile fraction of PLL-g-PEG increases up to ~70 %. This fluidification is due to the temperature-dependent nature of the diffusion process (the

diffusion coefficient increases with temperature). This evolution was also observed in the case of PLL-g-PAAMAN but at a lower level (up to ~50 % of mobile chains), suggesting that the PLL-g-PAAMAN shell becomes more fluid above the cloud point but is still less fluid than a "model" polymer exhibiting no specific polymer interactions.

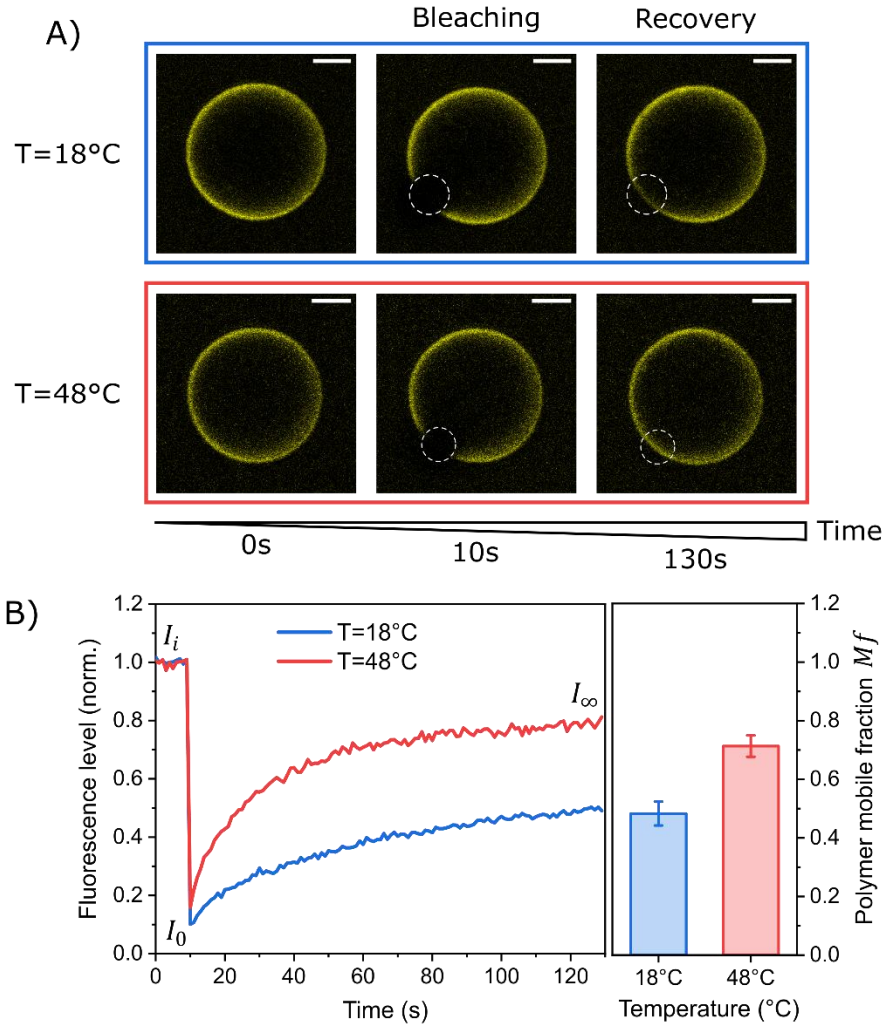

Figure 5.9. Fluorescence Recovery After Photobleaching (FRAP) experiments on non-thermoresponsive PLL-g-PEG shells. A) Confocal micrographs of representative droplets containing 1 wt% of coumarin-labeled PLL-g-PEG (in 20 mM KSCN) during FRAP experiments at 18 °C and 48 °C (scale bars = 5 µm). B) *Left*: FRAP curves from the top experiments. *Right*: polymer mobile fraction $M_f = \frac{I_\infty - I_0}{I_i - I_0}$ calculated from the fluorescence intensity levels measured in the FRAP curves at 18 °C and 48 °C (error bars = standard deviation on 6 droplets).

5.4 Towards the formation of UCST-type composite capsules

5.4.1 Incorporation of NeutravNPs in PLL-g-PAAMAN shells

We assessed the capacity of PLL-g-PAAMAN to drive the co-precipitation of nanoparticles and accordingly the straightforward formation of polymer-particles mixed shells. We used NeutravNPs as a proof of concept, as we did for PLL-g-PNIPAM shells in Chapter 2.

NeutravNPs were added in the aqueous phase containing PLL-g-PAAMAN prior to emulsification at 60 °C. Cooling down the emulsion to ambient temperature led to the segregation of the NeutravNPs in the PLL-g-PAAMAN shell, ascribed to a hydrophobic co-aggregation of polymers chains and NPs at the interface (see **Figure 5.10.**A). Heating the system up to 48 °C enabled to recover soluble NeutravNPs uniformly distributed in the droplet cores (see **Figure 5.10.**B). Interestingly, when the sample was cooled back below the cloud point, NeutravNPs were mostly recaptured in the shell. This reversible process associated to the reversible transition of PLL-g-PAAMAN is schematized in Figure 5.10.A and highlighted in the radial profiles of a representative droplet shown in Figure 5.10.B.

These results show that NPs can be spontaneously embedded in the polymer shell upon its formation. This approach is promising for the straightforward design of UCST-type composite capsules.

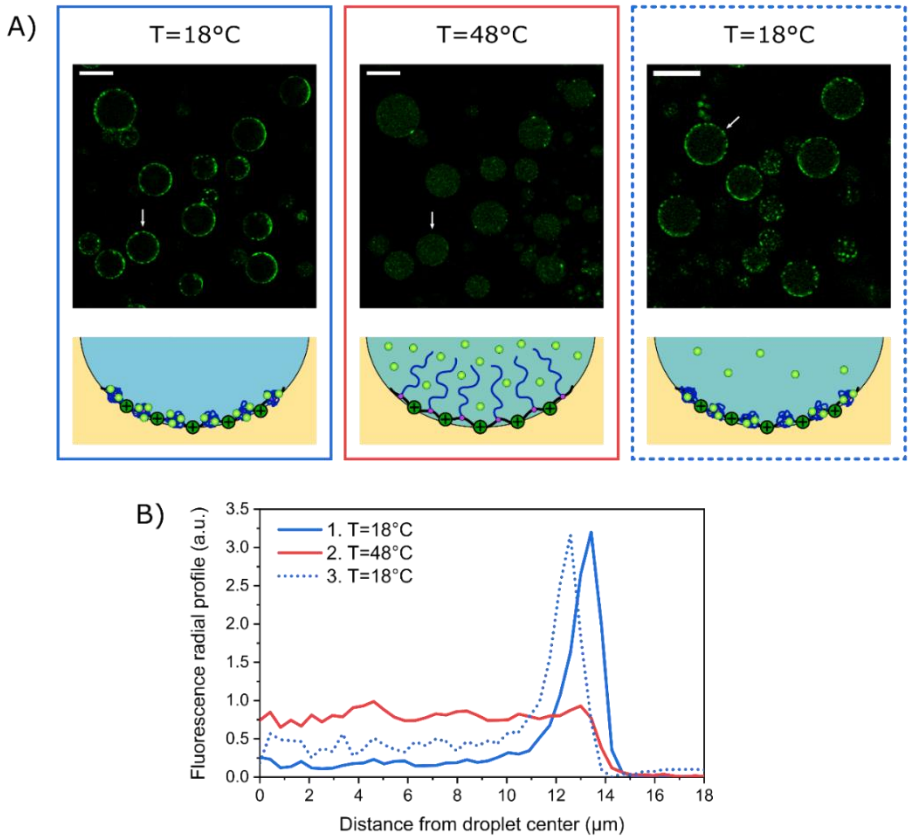

Figure 5.10. Reversibility of the capture of NeutrAvidin-coated fluorescent nanoparticles (NeutravNPs) upon UCST-type transition of PLL-g-PAAMAN. A) Top: Confocal micrographs of droplets containing 1 %wt of PLL-g-PAAMAN and 0.025 wt% of NeutravNPs at 18 °C, 48 °C and 18 °C successively (scale bars = 30 µm). Bottom: Partial schematics representing the state of PLL-g-PAAMAN and the distribution of the NeutravNPs in the droplets as observed in the top micrographs (Krytox molecules are not represented for the sake of readability and the scale was not respected). B) Fluorescence radial profiles of the droplets indicated with a white arrow in the top micrographs (the droplet at step 3 is different from the one at steps 1 and 2).

5.4.2 Encapsulation of AuNPs and photothermal stimulation

The possibility to incorporate NPs in PLL-g-PAAMAN adlayers was extended to the formation of polymer shells doped with AuNPs to impart light-responsiveness to the capsules. As AuNPs were not fluorescent, their presence in the polymer shell at low temperature was assessed by comparison of SEM pictures of droplets subjected to (i) homogenization at 60°C with or without AuNPs present in the aqueous phase, (ii) cooling down to room temperature, and (iii) drying at ambient

air (**Figure 5.11**). In absence of AuNPs, the surface of PLL-g-PAAMAN is smooth, except the presence of cracks and folds that probably appeared during the drying step. In presence of AuNPs, white dots and aggregates at clearly visible at the surface of the PLL-g-PAAMAN capsules and are ascribed to the AuNPs. The presence of AuNPs at the outer surface of the capsules suggests that they can be (at least partially) embedded in the PLL-g-PAAMAN shell upon formation below the cloud point.

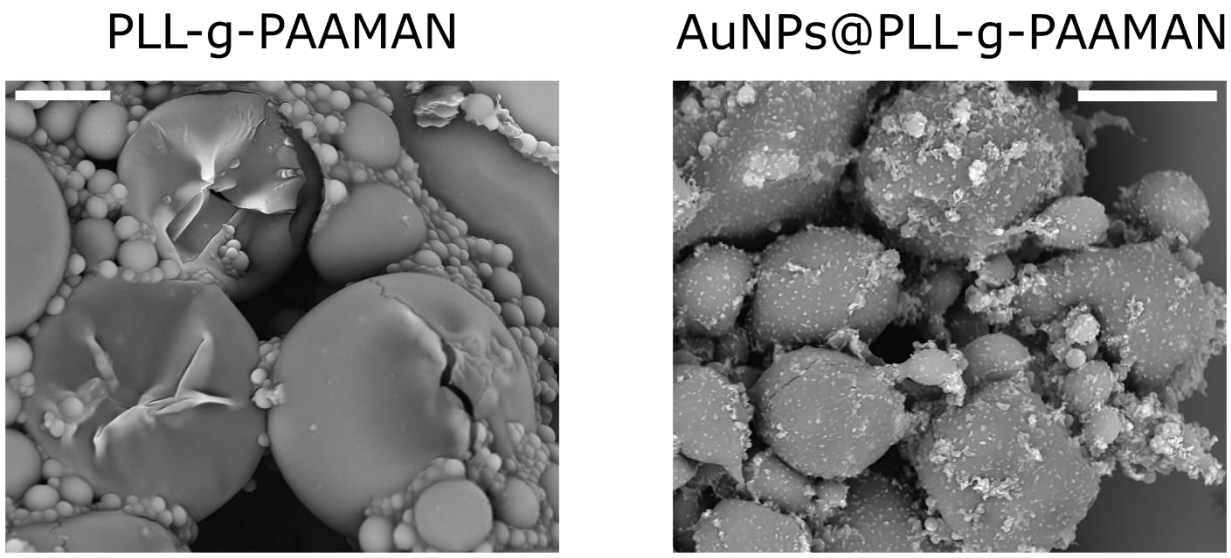

Figure 5.11. SEM micrographs of dried PLL-g-PAAMAN capsules prepared from aqueous phases with or without PVP-coated AuNPs (scale bars = 10 µm). The original emulsions contained 1 wt% PLL-g-PAAMAN with/without 0.05 wt% AuNPs and 20 mM KSCN in the aqueous phase and 0.1 wt% Krytox in the oil phase.

We assessed the possibility to trigger the dissolution of the PLL-g-PAAMAN shell via light irradiation of encapsulated AuNPs. An emulsion was prepared with 2 wt% of PLL-g-PAAMAN and 0.05 wt% of AuNPs in the aqueous phase (20 mM KSCN) and 0.1 wt% of Krytox in the oil phase. The emulsion was observed at 25 °C under phase contrast microscopy (**Figure 5.12**). At this temperature, no polymer globules were visible in the core of the droplets and the periphery was slightly irregular, suggesting the presence of PLL-g-PAAMAN shells. When a 532-nm laser beam was focused on a given droplet, we should expect an increase of temperature via thermoplasmonic effect of AuNPs, that may eventually trigger the solubilization transition of the PLL-g-PAAMAN shell. This light-induced process was not clearly visible in phase contrast

microscopy, except through a slight shrinkage of the droplet. When the laser was turned off, polymer granules instantaneously appeared in the droplet core Then the granules progressively migrated from the core to the periphery of the droplet and merged to retrieve the initial shell configuration. This suggests that (i) the temperature was raised above the cloud point upon light irradiation and (ii) polymer chains have been detached from the interface upon heating and have been redispersed in the core (iii) upon cooling they precipitate first under the form of aggregates that eventually migrate to the interface. The entire process is depicted below the micrographs in **Figure 5.12**.

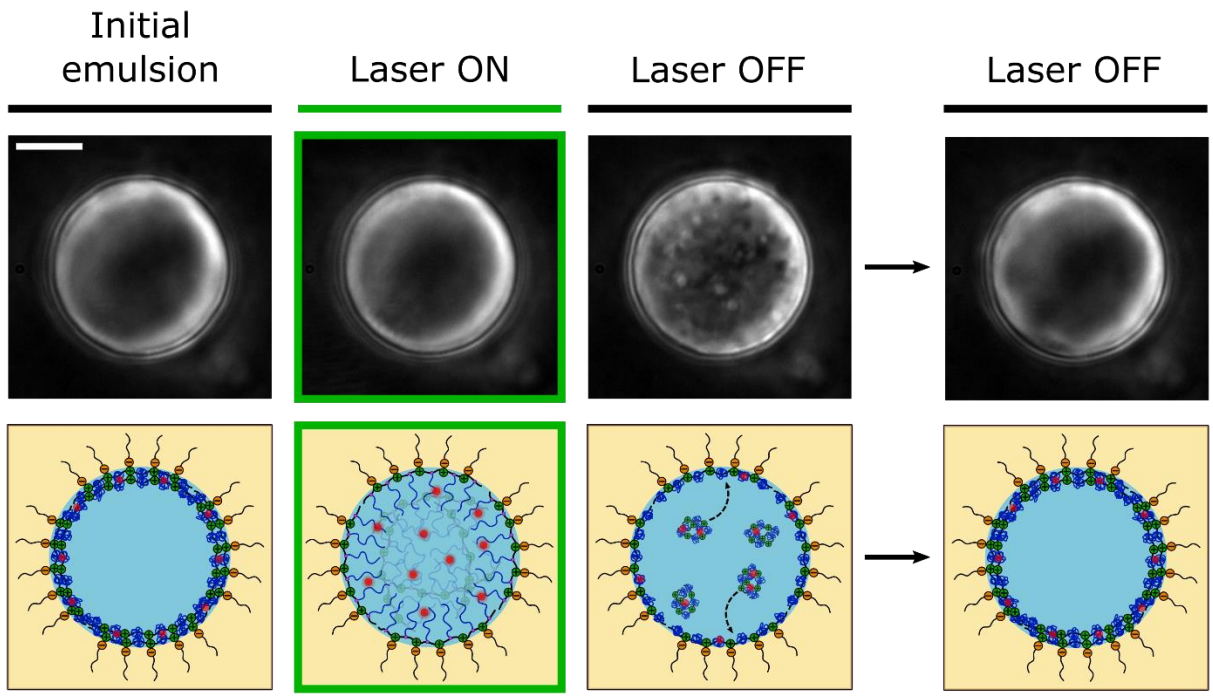

Figure 5.12. Light-triggered dissolution of PLL-g-PAAMAN shell induced by thermoplasmonic effects of co-encapsulated AuNPs. The phase contrast micrographs represent a water droplet containing 2 wt% of PLL-g-PAAMAN and 0.05 wt% of AuNPs (in 20 mM KSCN) dispersed in oil phase containing 0.1 wt% of Krytox, and thermalized at 25 °C (scale bar = 10 µm). The droplet was irradiated with a 532-nm laser at 15 mW for a few seconds. After turning off the laser, polymer granules spontaneously formed in the droplet core and progressively migrate towards the interface in a few minutes.

5.5 Encapsulation of a model protein

The compatibility of the PLL-g-PAAMAN shells with the presence of a protein encapsulated in the core of the droplets was tested on the model eGFP, as it was done in Chapter 2 for PLL-g-PNIPAM shells.

Figure 5.13 shows confocal micrographs of an emulsion containing 1 wt% of rhodamine-labeled PLL-g-PAAMAN and 50 µM of eGFP in the aqueous phase, at 18 °C and 48 °C. At 18 °C, PLL-g-PAAMAN was not localized at the periphery of the droplet under the form of a flat shell but formed globules in the droplet core. These globules also contained a fraction of eGFP as revealed in the protein fluorescence channel. This observation suggests that, unfortunately, protein-polymer interactions drive the co-precipitation of PLL-g-PAAMAN and eGFP in the droplet core and prevents the deposition of the polymer at the interface via interfacial complexation. At 48 °C, the polymer-protein-enriched globules have been dissolved upon the hydrophobic-to-hydrophilic transition of the polymer. GFP was uniformly distributed within in the droplet core and PLL-g-PAAMAN formed irregular spots at the interface.

These results suggest that the presence of eGFP strongly interferes with the formation of a polymer shell by interfacial complexation. Further optimization should be done to improve the guarantee the formation of a polymer shell in presence of a protein of interest for delivery applications.

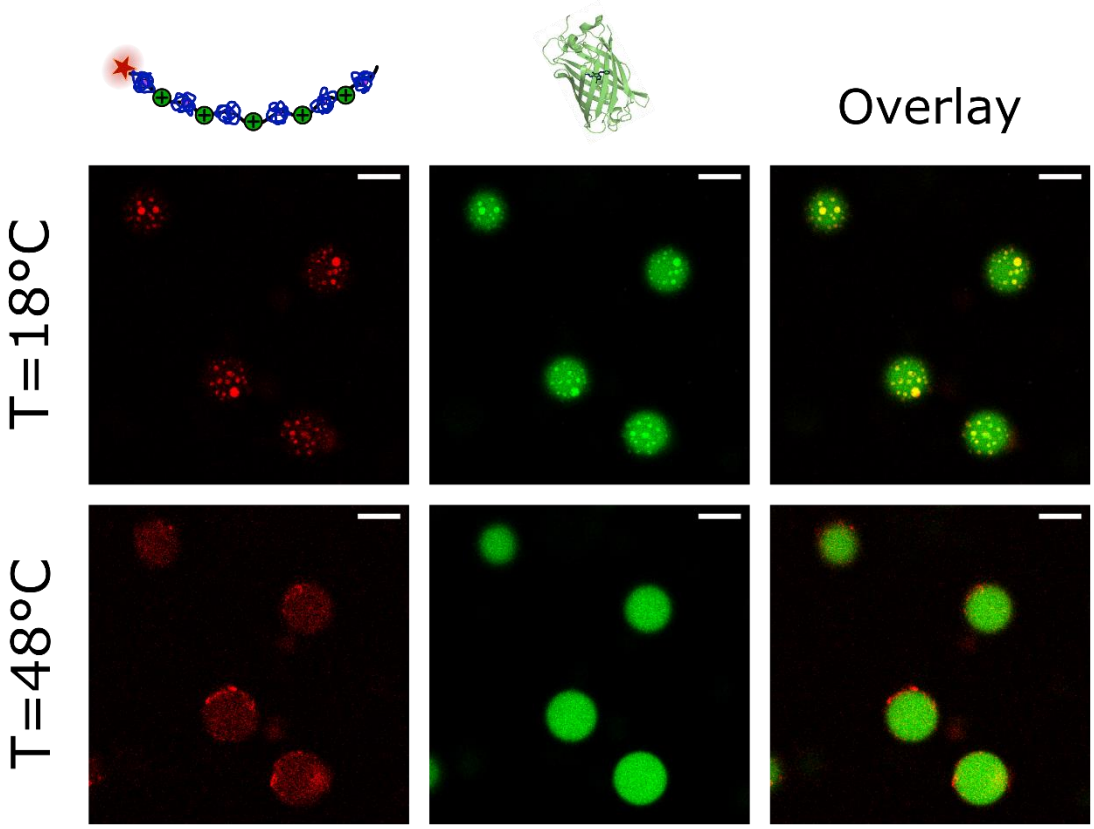

Figure 5.13. Encapsulation of eGFP in PLL-g-PAAMAN capsule precursors. Confocal micrographs of an emulsion containing 1 wt% of rhodamine-labeled PLL-g-PAAMAN (left channel) and 50 µM of eGFP (middle channel) in the aqueous phase (20 mM KSCN) and 0.05 wt% of Krytox in the oil phase, at T = 18 °C and T = 48° C (scale bars = 50 µm). The focal plane was set below the equatorial place of the droplets to show the formation and sedimentation of PLL-g-PAAMAN globules at 18 °C.

5.6 Conclusion

In this Chapter, we reported the formation by interfacial complexation in water-in-oil emulsion of aqueous-core PLL-g-PAAMAN microcapsules exhibiting a UCST-type behavior (**Figure 5.14**). After emulsification above the cloud point of the polymer and cooling down to room temperature, a hydrophobic and gel-like polymer shell was readily formed by complexation of PLL-g-PAAMAN chains with an oil-soluble surfactant at the surface of water droplets. We showed that this process enabled the straightforward incorporation of nanoparticles previously dispersed in the

aqueous phase in the polymer shell upon temperature switch. The hydrophobic-to-hydrophilic transition of PAAMAN chains upon heating triggered a partial redispersion of the polymer shell and a drastic change in its fluidity, switching from a gel-like state to liquid-like state. These thermoresponsive properties combined with the ability to readily encapsulate nanoparticles show the high potential of our approach for advanced delivery applications, such as photothermal delivery with gold nanoparticles, or magnetic hyperthermia with SPIONs.

However, the encapsulation of eGFP as a model protein has not been achieved yet since the protein interferes with the formation of PLL-g-PAAMAN shell. Polymer-protein interactions seem to favor the co-precipitation of PLL-g-PAAMAN and eGFP into globular aggregates in the droplet core, at the expense of interfacial complexation of PLL-g-PAAMAN at the droplet surface.

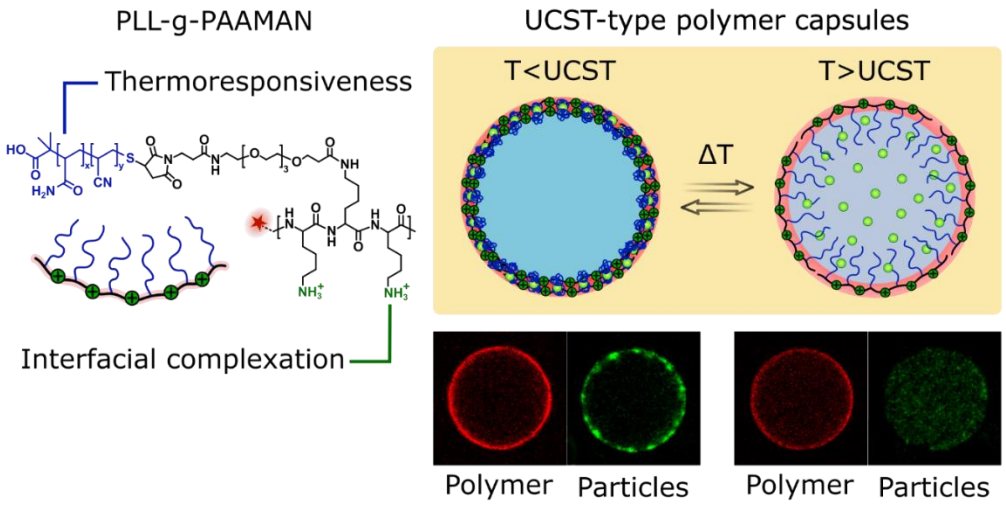

Figure 5.14. Formation of UCST-type polymer shells made of PLL-g-PAAMAN chains by interfacial complexation in water-in-oil emulsion.

Chapter 6

Conclusion and outlooks

6.1 Conclusion

Many bio-applications require the encapsulation and the controlled release of hydrophilic payloads, such as localized drug delivery, tissue regeneration or exploration of cell signaling for instance. An ideal encapsulation system is designed to (i) preserve the integrity and bioactivity of the encapsulation content during all the steps of formulation, (ii) enable the on-demand release of the payload upon application of an external stimulus, (iii) be versatile, i.e. appropriate for the encapsulation of a large range of hydrophilic payloads (including fragile biomacromolecules such as proteins or DNA). In this context, hollow capsules composed of an aqueous core surrounded by a polymer shell are promising encapsulation systems. An ideal polymer capsule could be described as the combination of a polymer shell that plays the dual role of protecting envelop upon encapsulation/storage and stimuli-responsive gate for on demand release of the payload, and a liquid core that enables to maintain mild aqueous conditions in the capsule. The objective of the present work was to elaborate a versatile approach for the design of stimuli-responsive aqueous-core polymer capsules that meet the specifications enumerated above.

For that, aqueous-core capsules were here formed by structuration of a polymer shell around water droplets via interfacial complexation in water-in-fluorocarbon oil emulsions. The complexation process involved two oppositely charges species that were initially solubilized in their own phase: a cationic comb-like copolymer in the water phase and an anionic surfactant called Krytox in the oil phase. Upon emulsification of the water phase into the oil phase, the anionic surfactant and the cationic polymer interact at the surface of the water droplets via electrostatic interactions. In appropriate conditions of formulation, these interactions resulted in the formation of a surfactant-polymer mixed shell with a thickness of typically 0.5-1 µm. Interfacial complexation has the advantage to be a spontaneous self-assembly process that does not require in-situ chemical reactions (potentially prejudicial for the stability of co-encapsulated payloads).

We demonstrated via interfacial tension measurements that the cationic poly(L-lysine) (PLL) is an interesting building block for the design of functional shells as it can be effectively adsorbed at the water/oil interface via complexation with Krytox. We thus used this strategy to generate thermo-responsive polymer shells by interfacial complexation of comb-like copolymers

composed of a PLL backbone and thermo-responsive comb strands: the LCST-type poly(N-isopropylacrylamide) (PNIPAM) which is hydrophilic and soluble in water at ambient temperature and becomes hydrophobic and insoluble upon heating, and the UCST-type poly(acrylamide-co-acrylonitrile) (PAAMAN) which has the inverse behavior.

A detailed study has been performed on PLL-g-PNIPAM to evidence the formation of thermo-responsive polymer shells by interfacial complexation. After grafting on the PLL, the comb like copolymer exhibited a LSCT behavior similar to the thermoresponsive strands. We showed that PLL-g-PNIPAM shells could be formed at the surface of water droplets by interfacial complexation, provided a balanced concentration ratio between polymer and surfactant. Furthermore, we confirmed by fluorescence measurements that hydrophilic-to-hydrophobic transition of the polymer shell occurs upon heating above 34 °C. Interestingly, this transition was able to drive the accumulation of materials towards the polymer shell via hydrophobic interactions. This led to an increase of the surface excess of PLL-g-PNIPAM upon heating. More interestingly, we observed the coprecipitation at the interface of non-grafted PNIPAM chains that were initially soluble in the droplet core at ambient temperature. We also demonstrated that nanoparticles (NPs) initially dispersed in the droplet core at ambient temperature could be irreversibly sequestered in the polymer shell upon heating. This process was ascribed to the propensity of PLL to adsorb at the surface of the NPs, leading to the capture of the NPs in the hydrophobic polymer shell at high temperature. Through this process, we evidenced a straightforward mean to access polymer-particle "composite" shells with no other treatment than a gentle heating.

In a parallel study, we demonstrated that PLL-g-PAAMAN can also form polymer shells by interfacial complexation, provided an appropriate chemical structure of the copolymer. We evidenced a UCST behavior of PLL-g-PAAMAN shells, characterized by a reversible transition from a hydrophobic gel-like state at ambient temperature to a hydrophilic liquid-like state at high temperature (typically 45 °C). This transition led to a partial redispersion of the shell upon heating. In addition, we demonstrated that NPs can be embedded in the PLL-g-PAAMAN shells during its formation and could be redispersed in the droplet core upon heating. These capsules are promising for the design of composite capsules that are robust at low temperature and can be solubilized at high temperature, i.e. appropriate for a controlled release upon heating.

The thermo-responsiveness of PLL-g-PNIPAM and PLL-g-PAAMAN was initially triggered by a global heating of the sample. To achieve a better spatio-temporal control, we

proposed to use light as an external trigger. Since the PLL derivatives were not intrinsically light-sensitive but only thermo-sensitive, we supplemented the aqueous solutions with gold nanoparticles (AuNPs) which played the role of light-to-heat converters via thermoplasmonic effects. We qualitatively showed that, in presence of AuNPs in the droplet core, the thermal transition of PLL-g-PNIPAM of PLL-g-PAAMAN could be triggered in individual droplets upon light irradiation at 532 nm. In the case of PLL-g-PNIPAM, light irradiation was able to both trigger the aggregation of PLL-g-PNIPAM chains and induce the segregation of NPs at the interface similarly to a global heating of the sample. In the case of PLL-g-PAAMAN, polymer granules appeared in the core of irradiated droplets just after stopping the irradiation, revealing that a fraction of the polymer shell has been solubilized and detached from the interface upon light irradiation. In the experimental conditions tested in this work, the light excitation was slightly less efficient than a global heating to induce physical changes in the polymer shells. However, the light triggering benefits from a high degree of tunability since the irradiation power, the irradiation time, and the amount of AuNPs can be adjusted to optimize the response of the system.

In addition to the qualitative results obtained upon light irradiation, we developed a protocol to measure *in situ* the temperature that can be reached in AuNPs-loaded droplets upon light excitation. This protocol was based on quantitative phase imaging of droplets upon irradiation with a technique called grating-shadow phase microscopy. This technique enabled to map the optical path difference induced by local heating in the vicinity of an irradiated droplet. The pattern of optical path difference was correlated to the increase of temperature reached in the droplet core thanks to simulations. This approach showed that the highest temperature increases are observed in the largest droplets. Typically, a temperature increase of 20 °C can be reached in 30-µm droplets with an irradiance of 20 µW/µm² (easily accessible with commercial laser sources).

The possibility to encapsulate fragile biomacromolecules such as proteins was an initial motivation of this work. The formation of PLL-based polymer capsules by interfacial complexation does not require strong physical or chemical treatments that could damage the encapsulated payloads (no sonication, no chemical reactions) and enable to keep a mild aqueous environment in the droplets which are capsule precursors. We used eGFP as a model protein to assess the compatibility of our protocol with the presence of proteins. eGFP was successfully encapsulated in PLL-g-PNIPAM capsule precursors as evidenced by the presence of the protein in the droplet core and the effective formation of a polymer shell, with no signs of polymer-protein

interactions. In the case of PLL-g-PAAMAN, the presence of the protein hindered the formation of a polymer shell by interfacial complexation. Instead, globules containing both the polymer and the protein were formed in the droplet core, suggesting that strong polymer-protein interactions interfered with the deposition of the polymer at the surface of the droplets. These results suggest that the nature of the polymer used to form the capsule shell is crucial regarding the encapsulation of a protein of interest.

6.2 Outlooks

6.2.1 Possible improvements

PLL-g-PNIPAM was used to demonstrate the feasibility of our approach, namely the formation of functional polymer shells by interfacial complexation of PLL derivatives. In terms of applications however, the LCST behavior of PLL-g-PNIPAM shells is not ideal for on-demand release since the shell becomes hydrophobic upon heating. The efforts should focus on UCST-type shells, such as PLL-g-PAAMAN, that are gel-like at ambient temperature and undergo solubilization upon heating.

Regarding the formation of UCST-type polymer capsules, a first way of improvement would consist in the optimization of the composition of the PLL derivatives. As demonstrated in the case of PLL-g-PAAMAN, the size of the PLL backbone, as well as the grafting ratio of functional strands, have a drastic effect on the propensity of PLL to adsorb at curved water/oil interfaces upon interfacial complexation. A rationalization of the influence of these structural parameters on the amount of polymer adsorbed at the interface should enable to maximize the uniformity and the thickness of the polymer shell. The intrinsic thermal properties of UCST-type polymers are also key parameters that dictate the behavior of the shell. As demonstrated in the beginning of Chapter 4, the cloud point of PAAMAN and the dynamics of the polymer-enriched phase upon phase separation can be tuned by changing the polymer composition. The synthesis protocol of PAAMAN chains should be optimized to get a cloud point closer to practical temperatures

(typically 35 °C) without need of additional salts, and a gel-like dynamics in the polymer-enriched phase to improve the mechanical properties of the resulting shell.

Regarding the experiments of light triggering, two ways of improvement can be mentioned:

- In this work, the plasmonic excitation and the confocal imaging of emulsion droplets loaded with AuNPs were performed in separated set-ups. The laser sources of the confocal microscope were not sufficiently powerful to trigger significant thermoplasmonic effects, and the apparatus was not appropriate for the addition of an external laser source. Therefore, the plasmonic excitation was performed on a commercial microscope which did not work in confocal mode, but which can be supplemented with an external laser source. This set up suffered from two limitations: 1) the irradiation laser beam was passing through the internal optical system of the microscope, resulting in losses of power and optical deformations of the laser spot due to multiple reflections, 2) the impact of thermoplasmonic effects on the properties of the polymer shells were not easy to visualize since it was restricted to bright field imaging (the fluorescence imaging was forbidden by the presence of the irradiation laser). A home-made optical set-up combining confocal detection and orthogonal laser irradiation should enable to both properly control the shape and size of the laser spot in the focal plane and generate thermoplasmonic effects and simultaneously follow the distribution of polymer and NPs species within the droplets.
- Regarding the thermometry protocol developed with grating-shadow phase microscopy, further studies are required to precisely quantify the influence of the droplet size and the AuNPs concentration on the temperature reached upon irradiation. For that, monodisperse emulsions with a uniform distribution of AuNPs in the droplet core are required to assess the repeatability and the reliability of the measurements. The production of droplets by microfluidics is an interesting outlook for that purpose.

6.2.2 Transfer of the polymer capsules in aqueous environment

At this stage of the work, the polymer shells formed by interfacial complexation are only "capsule precursors" since they are still surrounded by an oil phase. To envisage biological applications, the polymer shells should be transferred into an aqueous environment without falling apart. This extraction step is challenging since the mechanical stability of the polymer shell is difficult to evaluate in emulsion and even more difficult to extrapolate in all-aqueous environment. Two approaches have been tested to recover the capsules in water : the first one consisted in removing the oil phase from the original emulsion and redispersing the residual aqueous content in water, the second was based on the "cushion method" developed by He et al.[288] In the following, we will briefly describe how we tried to adapt these strategies to our system and the experimental difficulties that have been faced.

The first approach of capsule extraction that has been tested relied on the removal of the continuous oil phase by simple evaporation. The FC-70 oil phase used so far was not appropriate for that purpose since its boiling point was of 215 °C. This oil was thus substituted with another fluorocarbon oil, called Novec^{TM} 7100 (Sigma-Aldrich), characterized by a low boiling point of 61 °C. The extraction was first tested on PLL-g-PNIPAM shells. The emulsion was exposed to ambient air to let the oil phase evaporate. Then, addition of a large amount of water on the aqueous pellet should enable to recover the capsules, eventually dispersed in water. The ideal protocol is schematized in **Figure 6.1**.A. To assess the efficiency of the capsule recovery by microscopy imaging, we supplemented the inner aqueous phase with 5 % of Cy3-labeled PNIPAM that plays the role of fluorescent payload. The experimental results are schematized in **Figure 6.1.**B. The original emulsion was characterized by stable micrometric water droplets. The presence of PNIPAM in the droplets was evidenced by a high fluorescence level in the droplet core and the formation of polymer aggregates at 45 °C (**Figure 6.1**.C). Upon oil evaporation, the water droplets were subjected to destabilization and coalescence, resulting in the disruption of the polymer shells. This process was confirmed by the absence of polymer capsules in the final aqueous phase. Instead, the "outer" aqueous phase was composed of dispersed polymer residues (highlighted in fluorescence images) and small droplets that are probably oil droplets resulting from the emulsification of residual traces of oil contained in the pellet (**Figure 6.1**.D).

This preliminary result suggested that the PLL-g-PNIPAM shells have a poor mechanical stability. We tried to strengthen the polymer shells by introducing polymerizable groups along the PLL backbone of the copolymer. As an example, we synthesized a copolymer by co-grafting PNIPAM strands and acrylate-terminated PEG strands onto PLL. After formation of a polymer shell at the surface of water droplets, the copolymer chains were cross-linked via photopolymerization of the acrylate groups. Upon application of the extraction protocol described in **Figure 6.1**.A, the capsules shells were however subjected to the same destabilization issues than PLL-g-PNIPAM shells and were not successfully recovered in the aqueous phase.

As an alternative to the evaporation step that probably induces mechanical stress that disrupt the polymer shells, we tried to adapt the "cushion method" developed by He et al.[288] This method consists in mixing the original emulsion containing the capsule precursors with a metastable emulsion that triggers the macroscopic phase separation of the mixture. During this demixing process, the fusion of the "metastable" aqueous droplets with the capsule precursors leads to the recovery of the capsules in the water phase. The addition of a "cushion agent" (typically citrate) in the aqueous phase of the metastable emulsion enables to stabilize the polymer capsules upon transfer from oil into water. This method has been originally implemented for the recovery of mechanically robust polymer capsules prepared by interfacial polymerization in water-in-toluene emulsions. Since toluene is less dense than water, the polymer capsules can be easily collected from the bottom phase after the transfer process. In addition, due to the mechanical stability of their polymerized shell, the capsules could be subjected to washing and centrifugation steps without major degradation.

We tried to adapt this "cushion method" approach on our system. Briefly, PLL-g-PNIPAM shells were formed by interfacial complexation in an original water-in-oil emulsion (with FC-70 as the oil). Then, a metastable water-in-oil emulsion was prepared with (i) citrate in the aqueous phase, used as "cushion agent" and (ii) perfluorooctanol in the oil phase, used as a destabilizing additive. The metastable emulsion was injected in the initial emulsion to trigger the macroscopic phase separation of the water and oil phases. The polymer capsules were expected to be recovered at the bottom of the aqueous phase. Because the aqueous phase was lying onto the oil phase, the collection of the capsules – if they were intact – was particularly difficult. At the end of the process, microscopy imaging of an aqueous fraction picked up at the water/oil interface only showed

residual traces of oil and no rigid capsules. This protocol may require further optimization to be able to properly recover polymer capsules in the water phase.

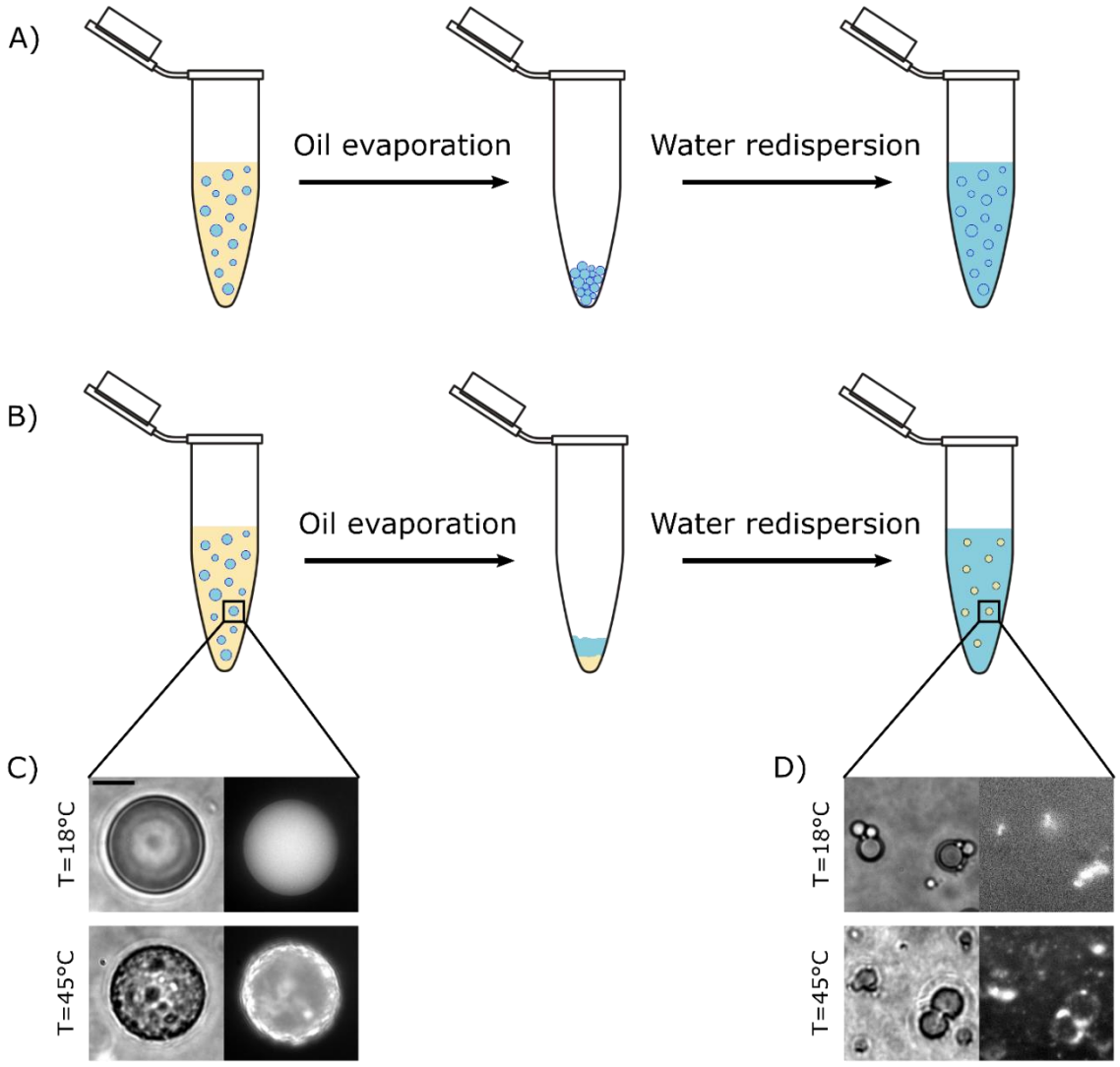

Figure 6.1. Attempt of capsule extraction based on the evaporation of the continuous oil phase and the redispersion of the capsule precursors in water. A) Representation of the ideal protocol. Polymer capsule shells are formed in water-in-oil emulsion as described in the previous Chapters, but with the fluorocarbon oil Novec 7100 characterized by a lower boiling point (61 °C). The evaporation of the oil phase and the addition of a large amount of water should enable to redisperse the capsules precursors in an aqueous environment. B) Representation of the actual result. The evaporation of the oil phase leads to the destabilization and coalescence of the water droplets. The presence of residual traces of oil results in the formation of an undesired direct emulsion upon redispersion of the pellet in water. C)

Micrographs of the initial emulsion containing 1 wt% of PLL-g-PNIPAM and 5 wt% of Cy3-labeled PNIPAM (used as a fluorescent payload) in the aqueous phase and 0.05 wt% of Krytox in the Novec 7100 oil phase. D) Micrographs of the aqueous medium after redispersion of the pellet in water. The scale bar in C corresponds to 10 µm and is valid for all the micrographs.

6.2.3 Production of capsules in microfluidics

As an alternative to the transfer of polymer capsules from the oil phase to an aqueous environment, we envisage to produce polymer shells in a microfluidics device in order to facilitate the recovery of the capsules. A promising approach is depicted in **Figure 6.2** and consists in the microfluidic generation of a water-in-oil-in-water (W/O/W) double emulsion in which the capsule shell is formed at the inner W/O interface and is recovered in the continuous water phase by evaporation of the thin intermediary oil layer.

Figure 6.2.A shows a potential microfluidic device and the composition of the phases that could be used to generate W/O/W emulsions. An aqueous solution containing the polymer of interest (here PLL-g-PNIPAM) is injected in the device and pinched at a first flow-focusing junction by an orthogonal flow of oil phase containing Krytox, resulting in the formation of a W/O emulsion where interfacial complexation can take place. In a second flow-focusing junction, an aqueous solution containing a surfactant that can stabilize oil-in-water emulsions (here the semi-fluorinated surfactant called F_8-TAC_{13}) is used to pinch the W/O emulsion, resulting in the formation of a W/O/W emulsion in which the inner aqueous droplet is surrounded by an intermediary oil layer. If the oil used in this process has a low boiling point, the intermediary oil layer can be removed by evaporation upon heating, resulting in the dispersion of the polymer shell in an aqueous environment. This process is depicted in **Figure 6.2**.B in the case of PLL-g-PNIPAM shells. In this case the heating step is also expecting to trigger the collapse and accumulation of PLL-g-PNIPAM in the shell, which could enhance the mechanical properties of the capsule upon oil removal.

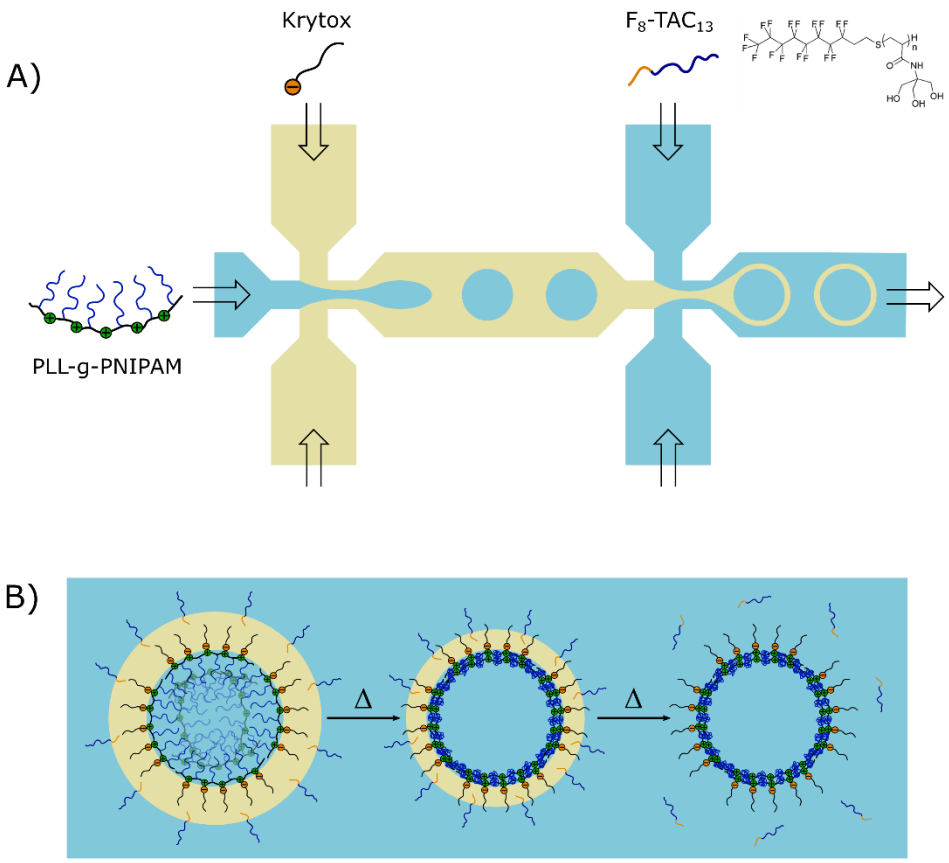

Figure 6.2. Microfluidic approach for the production of polymer capsules by interfacial complexation in W/O/W double emulsion. A) Representation of the microfluidic device used to produce W/O/W double emulsion. A primary aqueous phase containing the polymer of interest (here PLL-g-PNIPAM) flows through the main channel of the device. In a first flow-focusing junction, an oil phase (with low boiling point) containing Krytox is injected orthogonally to pinch the aqueous flow, resulting in the formation of a W/O emulsion in which the interfacial complexation takes place. In a second flow-focusing junction, a second aqueous phase containing a semi-fluorinated surfactant called F_8-TAC_{13} is injected to pinch the oil flow, resulting in the formation of a W/O/W double emulsion with a polymer shell formed at the inner W/O interface. B) Ideal illustration of the composition of the W/O/W emulsion coming out the microfluidic device. Heating the emulsion Heating the system would enable to (i) collapse and accumulate PLL-g-PNIPAM at the inner water/oil interface and (ii) evaporate the intermediary oil phase, eventually yielding a polymer capsule dispersed in an aqueous environment.

For the moment, this approach has not been tested yet but is envisaged through a collaboration with physicist colleagues (W. Urbach at the Physics Department of ENS and N. Taulier at the LIB lab of Sorbonne University). However, a first collaborative work has been

recently started with them on a delivery system which derives from the W/O/W emulsion presented above.

Actually, in absence of interfacial polymer layer, W/O/W emulsions can be seen as a core-shell system with an aqueous core surrounded by a protective oil shell. In this configuration, the evaporation of the oil phase would correspond to the shell disruption and would trigger the release of payloads pre-encapsulated in the aqueous core.

As a preliminary proof of concept, we demonstrated that the evaporation of the oil layer in W/O/W emulsions can be triggered by thermoplasmonic excitation of AuNPs encapsulated in the aqueous core. This experiment was performed on a "multi-core" double emulsion generated by microfluidics, i.e. an aqueous dispersion of micrometric oils droplets punctuated by a multitude of smaller water droplets. This double emulsion was produced in two steps: 1) an aqueous phase containing 0.05 wt% of AuNPs was emulsified in perfluorohexane (fluorinated oil with a boiling point of 57 °C) containing 5 wt% of Krytox, to yield a nanometric W/O emulsion. The volume ratio of this W/O emulsion was 40/60 and the size of the water droplets was typically 500 nm. 2) This emulsion was injected in a microfluidic flow-focusing junction to be pinched by an aqueous phase containing 0.1 wt% of F_8TAC_{13}, resulting in the multi-core W/O/W double emulsion showed in **Figure 6.3**.

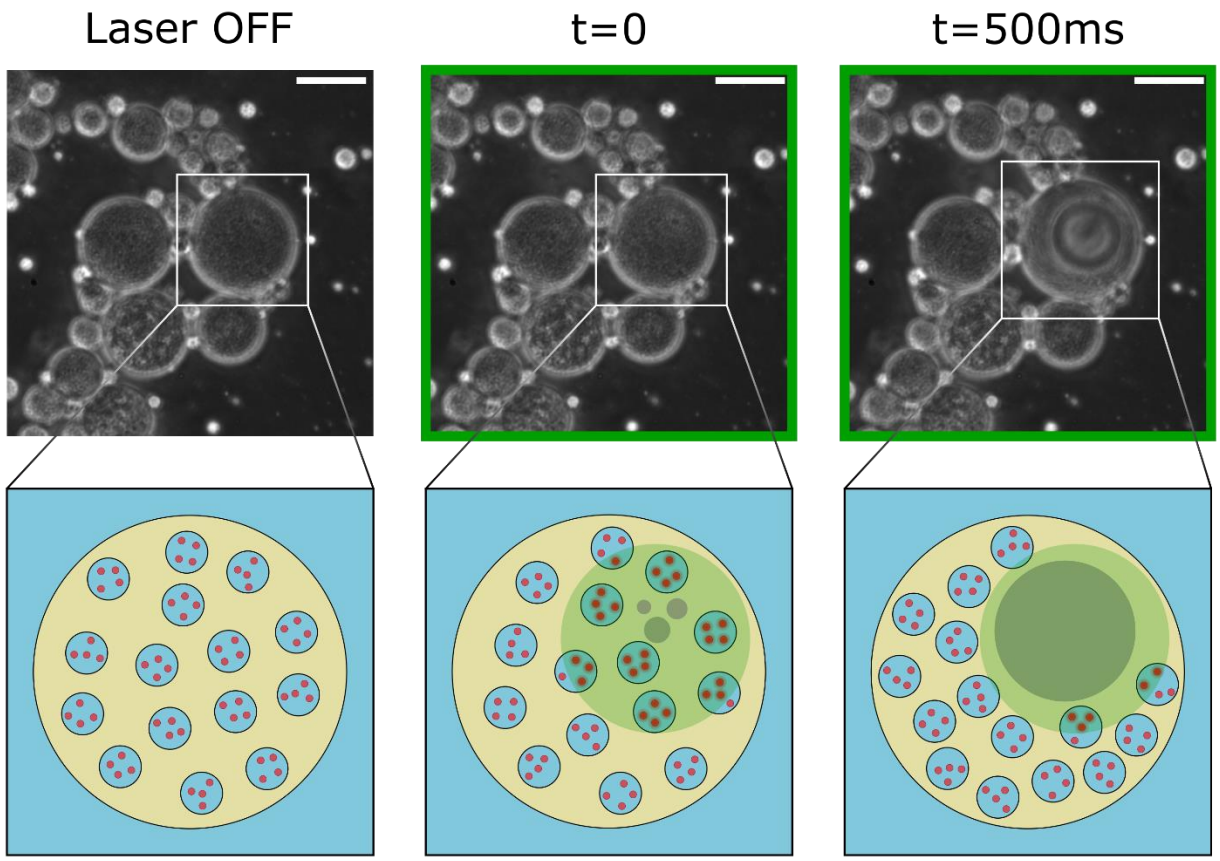

Figure 6.3. Light-triggered destabilization of a multi-core W/O/W double emulsion, consisting in AuNPs-loaded nanometric water droplets dispersed in micrometric oil droplets exhibiting a low boiling point (57 °C). The focalization of a 532-nm laser beam (green disk) on a multi-core droplet induces a raise of temperature that locally triggers the evaporation of the oil phase. A gas bubble (grey disk) rapidly grows within the droplet, resulting in its disruption in a few seconds.

The emulsion was dispersed in a polymer gel (poloxamer 407 at 30 wt%) to immobilize the oil droplets and was thermalized at 30 °C. When a 532-nm laser beam (15 mW) was focused on an individual oil droplet, a gas bubble appeared in less than 500 ms in the droplet core, suggesting that the raise of temperature induced by thermoplasmonic excitation of encapsulated AuNPs has triggered the local evaporation of the oil phase. After a few seconds of laser irradiation, the droplet was totally disrupted.

This illustrative experiment is a first step towards the formation of light-responsive delivery systems based on the combination of AuNPs and liquid shells made of volatile fluorinated

oils. This system will be explored in parallel of the systems based on polymer shells that may be produced by microfluidics.

Appendix A

Materials, instrumentation, and experimental protocols

7.1 Materials

7.1.1 Polymers and organic compounds

Polymers: Poly(L-lysine) hydrobromide (**PLL**) was purchased from Sigma-Aldrich (M_W = 15-30 kDa) and Alamanda Polymers (M_W = 6 kDa, 52 kDa). (N-hydroxysuccinimidyl ester)-terminated poly(N-isopropylacrylamide) (**PNIPAM-NHS**, M_W = 2 kDa), azide-terminated poly(N-isopropylacrylamide) (**PNIPAM-N_3**, M_W = 5 kDa), O-[N-(3-Maleimidopropionyl)aminoethyl]-O′-[3-(N-succinimidyloxy)-3-oxopropyl]triethylene glycol (**Mal-PEG4-NHS**) were purchased from Sigma-Aldrich. (N-hydroxysuccinimidyl ester)-terminated poly(ethylene glycol) (**PEG-NHS**, M_W = 2 kDa) was purchased from Rapp Polymere.

Fluorophores: 5(6)-carboxy-X-rhodamine N-hydroxysuccinimidyl ester (**rho-NHS**), 7-(diethylamino)coumarin-3-carboxylic acid N-succinimidyl ester (**coum-NHS**), dibenzocyclooctyne-Cy3 (**DBCO-Cy3**) and 8-anilino-1-naphthalenesulfonic acid (**ANS**) were purchased from Sigma-Aldrich.

Protein: Enhanced Green Fluorescent Protein (**eGFP**) has been produced and purified by colleagues (R. Chouket) according to a protocol described in the literature.[257]

Other compounds: Tris(2-carboxyethyl)phosphine (**TCEP**), monoethanolamine (**MEA**) and the different buffer ingredients (NaH_2PO_4, Na_2HPO_4, CHES, KSCN) were purchased from Sigma-Aldrich.

7.1.2 Fluorinated species

Three types of Fluorinert™ fluorocarbon oil were purchased from Sigma-Aldrich: **FC-40** (mixture of perfluoro-N-methyldibutylamine and perfluoro-tributylamine, density = 1.885), **FC-70** (perfluoro-tripentylamine, density = 1.940), and **Novec 7100** (methoxy-nonafluorobutane, density = 1.5). FC-40 was only used in surface tension experiments. FC-70 was used for the preparation of all the water-in-oil emulsions described in Chapter 2, 3 and 4. Novec 7100 was only used for preliminary experiments on capsule extraction presented in Chapter 6.

Krytox 157 FSL surfactant (M_W = 2.5 kDa) was purchased from Samaro.

7.1.3 Nanoparticles

Two types of fluorescent polystyrene nanoparticles were purchased from ThermoFisher Scientific (FluoSpheres™ range): NeutrAvidin™-coated nanoparticles (**NeutravNPs**) and carboxylate-modified nanoparticles (**CarboxyNPs**) purchased at 1 wt% in water. For both types, 200-nm NPs were used for zeta potential and DLS measurements, and 50-nm NPs were used for emulsion formulations and microscopy experiments. Both types of nanoparticles were displaying yellow-green fluorescence (505/515 nm).

Two types of gold nanoparticles (**AuNPs**) were purchased from NanoComposix: BioPure™ bare AuNPs (40-nm diameter, 1 mg/mL in water) and Econix™ AuNPs coated with 40 kDa poly(vinyl pyrrolidone) (50-nm diameter, 5 mg/mL in water).

Prior to use, NPs solutions were sonicated with a Sonics Vibra-Cell VCX 750 equipped with a 3 mm microtip for 2 min at 225 W.

7.1.4 Aqueous buffers

If not otherwise specified, aqueous solutions were systematically prepared in a home-made 7.7 mM phosphate buffer, prepared by dissolving 360 mg of NaH_2PO_4 (3 mmol) and 670 mg of Na_2HPO_4 (4.7 mmol) in 1 L of deionized water ([phosphate] = 7.7 mM, pH = 7.3, ionic strength = 17 mM, Debye length = 2.3 nm).

For the specific experiments about the pH-dependance of interfacial complexation (Chapter 2, section XX), we used a 30 mM Britton-Robinson (BR) buffer – made of 10 mM NaH_2PO_4/10 mM NaOAc/10 mM CHES – allowing for a buffering effect on a large range of pH. This buffer was prepared by dissolving 480 mg of NaH_2PO_4 (4 mmol), 328 mg of NaOAc (4 mmol) and 828 mg of CHES (4 mmol) in 0.4 L of deionized water (pH = 5.7, ionic strength = 30 mM, Debye length = 1.7 nm). The pH was adjusted at 4.3 (resp. 9.4) by addition of 150 µL of 1 M H_3PO_4 (resp. 500 µL of 1 M NaOH) in 30 mL of initial BR buffer. Aqueous phases containing the polymer were prepared in BR buffer at either acidic or alkaline pH, namely at pH = 4.3 or pH = 9.4.

7.2 Synthesis of polymers

7.2.1 Synthesis of PLL-g-PNIPAM and PLL-g-PEG

PLL-g-PNIPAM and PLL-g-PEG polymers were obtained by grafting NHS-terminated strands (PNIPAM or PEG) onto PLL. The number of NHS-terminated strands was adjusted as a molar fraction of the total number of lysine units (H·Br lysine, M = 209 g/mol) to reach the targeted theoretical grafting ratio τ (number of functionalized lysine units/total number of lysine units). Fluorescence properties were provided by the labeling of the PLL backbone with NHS-terminated fluorophores (rhodamine or coumarin). The synthesis protocol will be detailed for the preparation of PLL-g-PNIPAM. PLL-g-PEG was prepared by adjusting this protocol with reactive PEG chains instead of reactive PNIPAM chains).

PLL hydrobromide (M_W = 15-30 kDa, 15 mg) and NHS-terminated PNIPAM (M_W = 2 kDa, 48 mg for τ = 0.33) were dissolved in sodium tetraborate alkaline buffer (5 mL, pH = 8.5) under stirring at 4 °C to facilitate the dissolution of PNIPAM. Then the reaction was completed under stirring for 4h at room temperature. The resulting solution was dialyzed against deionized water (regularly renewed) for 3 days in a Thermo Scientific Slide-A-Lyzer cassette (3-12 mL, M_W cutoff = 3.5 kDa) and finally freeze-dried for 2 days in a Labconco Freezone Plus 2.5 apparatus, yielding a white fluffy powder (144 mg, yield = 83%).

For the synthesis of fluorescent derivatives, the appropriate reactive dye (rho-NHS or coum-NHS) was added in the reaction batch at the same time than the reactive PNIPAM chains. The dye was prepared in solution at 1 g/L in DMSO and the appropriate volume was added in the reaction batch to target ~1 graft/PLL chain.

A representative ^{1}H NMR spectrum of PLL-g-PNIPAM is showed in **Figure 7.1**. Peak identification (chemical shift in ppm, proton identification, integration): 1.16, PNIPAM [CH_2-CH-CO-NH-CH-($C\mathbf{H}_3$)$_2$], 55.2H; 1.4-2.2, lysine [β,γ,δ-$C\mathbf{H}_2$] + PNIPAM [$C\mathbf{H}_2$-CH-CO-NH-CH-(CH_3)$_2$], 35.7H; 2.45-2.52, lysine-CO-$C\mathbf{H}_2$-CH_2-S-PNIPAM + PNIPAM [CH_2-$C\mathbf{H}$-CO-NH-CH-(CH_3)$_2$, 1.3H; 2.70-2.75, lysine-CO-CH_2-$C\mathbf{H}_2$-S-PNIPAM + PNIPAM [CH_2-$C\mathbf{H}$-CO-NH-CH-(CH_3)$_2$], 2.1H; 2.98, lysine [non-grafted α-$C\mathbf{H}_2$], 1.7H; 3.18, lysine [grafted α-$C\mathbf{H}_2$], 0.4H; 3.92, PNIPAM [CH_2-CH-CO-NH-$C\mathbf{H}$-(CH_3)$_2$], 9.2H; 4.32, lysine backbone [CONH-$C\mathbf{H}$R-CONH], 1H (*reference for integration*).

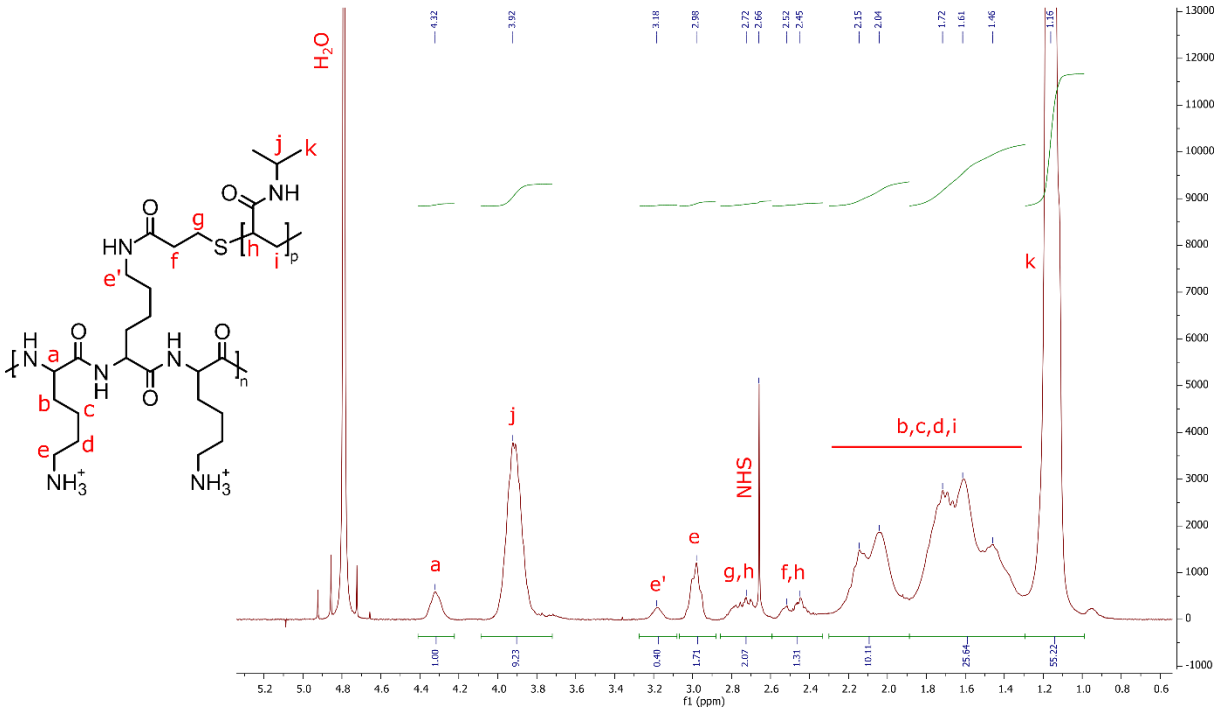

Figure 7.1. ^{1}H NMR spectrum of PLL-g-PNIPAM at 400 MHz in D_2O.

The experimental grafting ratio τ_{exp} of the PLL backbone by PNIPAM was determined by the signal integration value of the protons characterizing the grafted lysine units (protons **e'**) with the proton of the PLL backbone (proton **a**) as a reference (2 protons **e'** for 1 proton **a**): τ_{exp} = 0.40/2 = 0.20. This result means that 1/5 of the lysine units have been grafted with a PNIPAM strands. For a PLL chain with a mean molar mass of 22 kDa (105 lysine units), it means that 21 PNIPAM chains have been grafted in average. In total, the PLL-g-PNIPAM copolymer has a molar mass of around 64 kDa, the PLL backbone representing 34 wt% and the PNIPAM strands representing 66 wt%.

7.2.2 Fluorescent labeling of "free" PNIPAM

Controlled experiments required the use of fluorescent PNIPAM chains non grafted on PLL. Azide-terminated PNIPAM (M_W = 5 kDa, 100 mg) was dissolved in deionized water (5 mL). DBCO-Cy3 (23 µL at 1 g/L in PBS buffer) was added and the solution was stirred for 5h at room temperature. The resulting solution was dialyzed against deionized water (regularly renewed) for 3 days (Slide-A-Lyzer cassette, M_W cutoff = 3.5 kDa) and finally freeze-dried for 2 days, yielding a pink fluffy powder.

7.2.3 Synthesis of PLL-g-PAAMAN

Synthesis of PAAMAN chains

The UCST poly(acrylamide-co-acrylonitrile) (PAAMAN) used in Chapter 5 were synthesized in the group of Prof. Yue Zhao at Sherbrooke University (Canada). A typical synthesis protocol for PAAMAN named P2 is reported below:

Acrylamide (1.40g, 1eq), acrylonitrile (667µL, 0.51eq), AIBN (3.3mg, 0.001eq) and (2,2′-[carbonothioylbis(thio)]bis[2-methylpropanoic acid]) CTA agent‡ (12.1mg, 0.002) were dissolved in 20 mL DMSO in a 50 mL round-bottom flask. The mixture was degassed by three "freeze-pump-thaw" cycles. The mixture was then placed in an oil bath at 70 °C and polymerization was

‡ Prepared according to Lai et al.[291]

allowed to proceed for 24 h under stirring. The final product was purified by two precipitation-redispersion cycles in a suitable solvent. The resulting product was dissolved in a minimum of DI water and dialyzed against DI water at a temperature slightly above its cloud point for 2 days. Freeze-drying of the purified solution yielded the copolymer as a white fluffy solid.

The ^{1}H NMR spectrum of PAAMAN P2 in d_6-DMSO is represented in **Figure 7.2**.

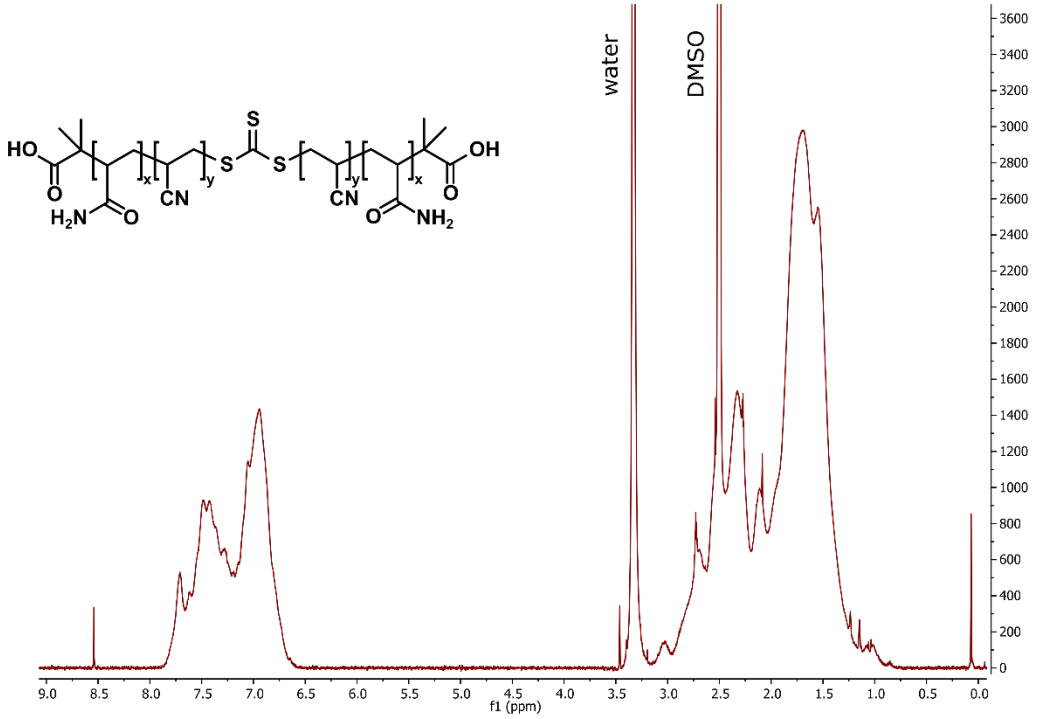

Figure 7.2. ^{1}H NMR spectrum of PAAMAN P2 with x=0.66 and y=0.34 at 400 MHz in d_6-DMSO.

Aminolysis of PAAMAN chains

For the synthesis of PLL-g-PAMAAN, we performed the *in situ* aminolysis reaction of the trithiocarbonate unit present in the middle of the PAAMAN chains. The efficiency of this reaction was previously controlled with UV-Vis spectrophotometry. The spectrum of PAAMAN chains at 0.1 wt% in DMSO was measured before and after addition of an excess of monoethanolamine (MEA, 30eq) and tris(2-carboxyethyl)phosphine (TCEP, 10eq) (**Figure 7.3**.A). The absorbance

peak characteristic of the trithiocarbonate unit at 280 nm disappeared after addition of MEA and TCEP, suggesting that it was readily cleaved by aminolysis to yield two thiol-terminated PAAMAN strands.

This reaction was then conducted in water retrieve the aminolyzed polymer after purification and lyophilization (according to the precipitation-washing protocol presented above for PLL-g-PAAMAN). The cloud point of the aminolyzed polymer was measured in water by turbidimetry and was rigorously equal to the cloud point of the original polymer (**Figure 7.3**.B), suggesting that the UCST-type behavior of PAAMAN chains was not affected by the aminolysis reaction.

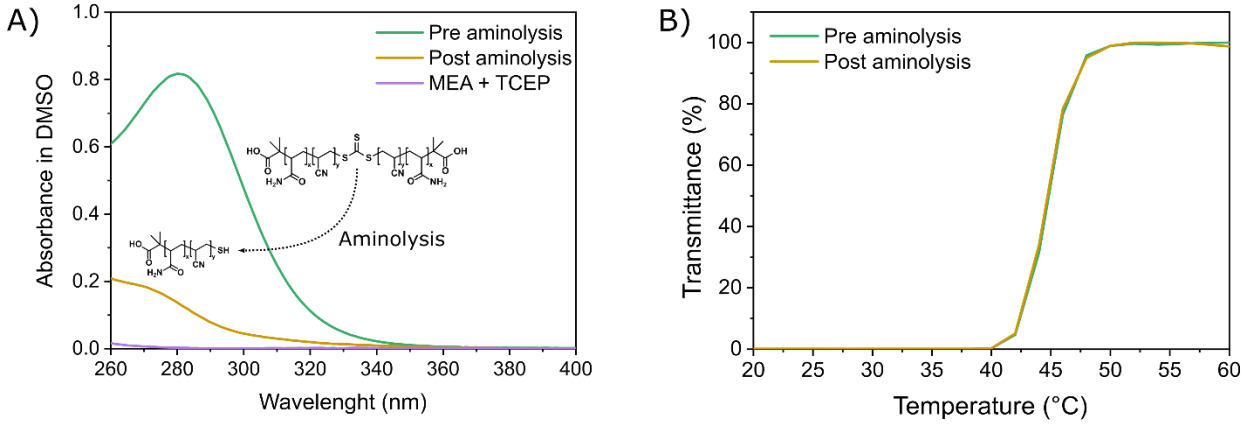

Figure 7.3. A) Absorbance spectrum of the PAAMAN polymer P2 used in Chapter 3, before and after aminolysis with monoethanolamine (MEA) and tris(2-carboxyethyl)phosphine (TCEP) in DMSO. B) Turbidimetry heating curves of the polymer before and after aminolysis.

Synthesis of poly(L-lysine)-g-poly(acrylamide-co-acrylonitrile) (PLL-g-PAAMAN)

A typical synthesis of $PLL_{0.53}$-g-$PAAMAN_{0.47}$ (PLL/PAAMAN weight ratio of 53/47 %) is reported below:

52 kDa PLL (20 mg, 250eq lysine) and Mal-PEG4-NHS (2.0 mg, 10eq) were dissolved in 3 mL D_2O in a 10 mL round-bottom flask. The solution was stirred for 4 h at room temperature. 300 µL of solution were taken and mixed with 300 µL of D_2O for NMR analysis of the intermediary PLL-g-(PEG4-Mal). After heating the solution at 60 °C, PAAMAN (17.2 mg, 3eq), MEA (4 µL, 175eq) and TCEP (2.9 mg, 30eq) were introduced, and the solution was stirred at 60 °C for 4 h. After

cooling back to room temperature, the solution was purified by 3 centrifugation/redispersion cycles. The centrifugation was performed at 4 °C for 10 min at 15 000 rcf. After removing the supernatant, the pellet was redispersed in DI water by sonication using a Sonics Vibra-Cell VCX 750 equipped with a 3-mm microtip. The final solution was lyophilized overnight using a Labconco Freezone Plus 2.5 apparatus, yielding a white powder.

A similar protocol was used for the synthesis of $PLL_{0.42}$-g-$PAAMAN_{0.58}$ with a 22 kDa PLL instead of 52 kDa and with adapted polymer ratio.
For the synthesis of fluorescent derivatives, the appropriate reactive dye (rho-NHS or coum-NHS) was added in the reaction batch at the same time than the PEG linker. The dye was prepared in solution at 1 g/L in DMSO and the appropriate volume was added in the reaction batch to target ~2 grafts/PLL chain.

Figure 7.4 shows a typical ^{1}H NMR spectrum of the maleimide-grafted PLL intermediary in D_2O (chemical shift in ppm, proton identification, integration): 1.5-1.7 (lysine [β,γ,δ-C**H**$_2$], 6.22H), 2.5 (linker [C**H**$_2$-CONH], 0.23H), 2.8 (released NHS units, 0.33H), 3.0 (lysine [non-grafted α-C**H**$_2$], 1.94H), 3.2 (lysine [grafted α-C**H**$_2$], 0.15H), 3.3 (linker [CONH-C**H**$_2$], 0.16H), 3.6-3.8 (PEG backbone, 1.5H), 4.3 (lysine backbone, 1H), 6.9 (maleimide double-bond, 0.14H).

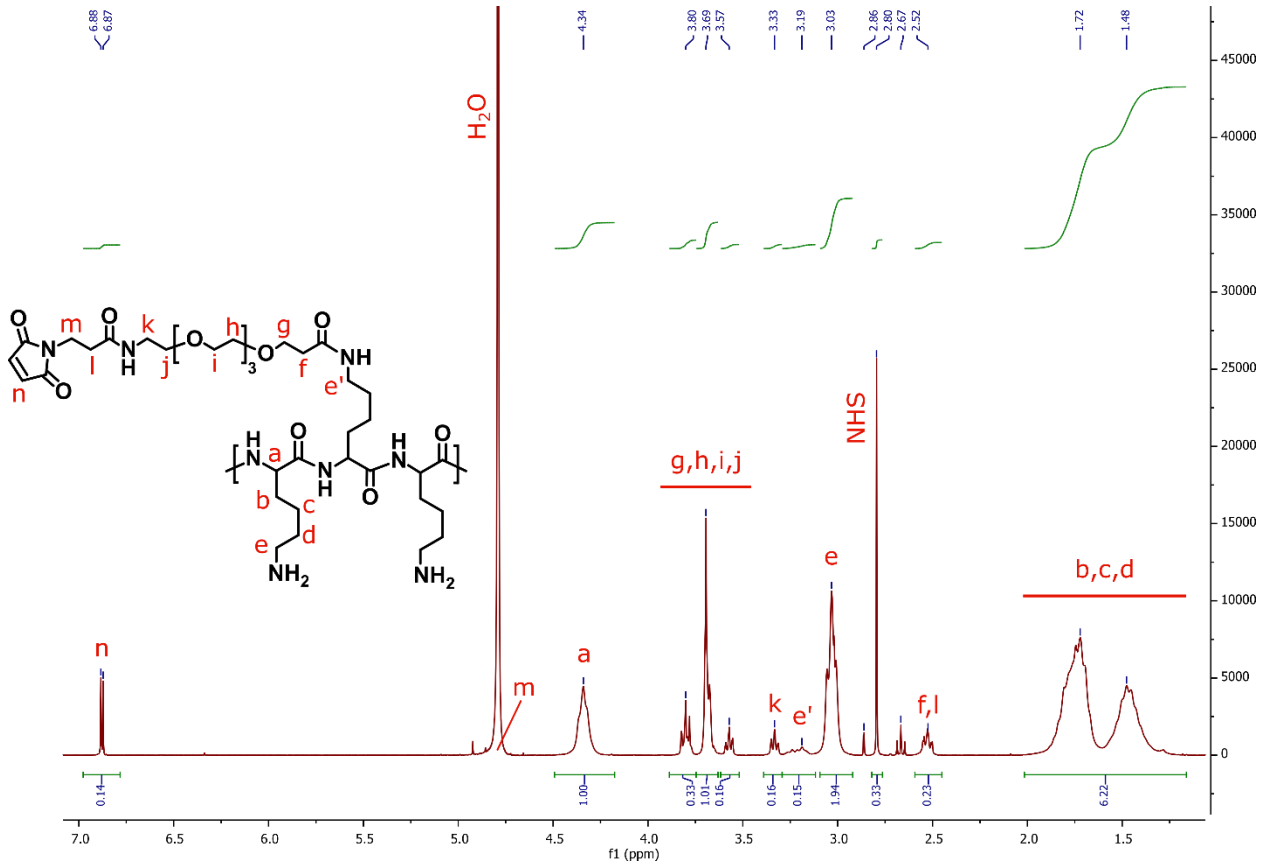

Figure 7.4. ^{1}H NMR spectrum of PLL-g-(PEG4-Mal) at 400 MHz in D_2O.

The experimental grafting ratio τ_{exp} of PLL by Mal-PEG4-NHS linkers was determined by comparing ^{1}H NMR integration values of protons characterizing grafted and non-grafted lysine units (e' and e respectively), with protons of PLL backbone (a) as reference protons: $\tau_{exp} = 0.15/2 \sim 0.07$.

A typical ^{1}H NMR spectrum of $PLL_{0.53}$-g-$PAAMAN_{0.47}$ in d_6-DMSO is represented in **Figure 7.5**.

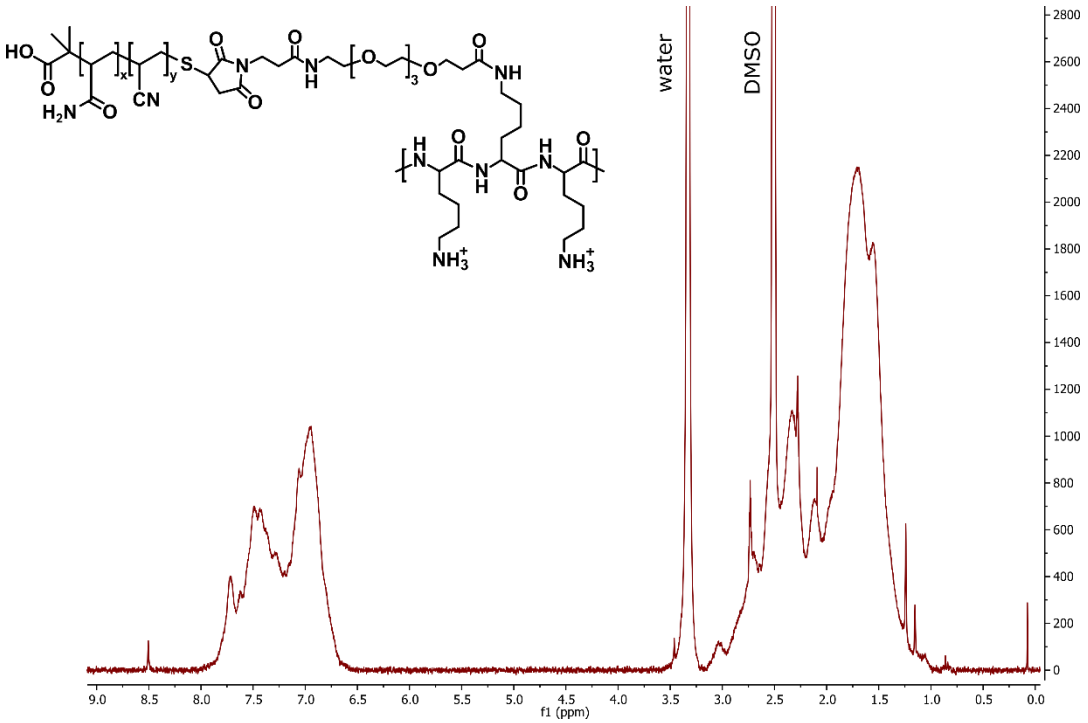

Figure 7.5. ^{1}H NMR spectrum of $PLL_{0.53}$-g-$PAAMAN_{0.47}$ at 400 MHz in d_6-DMSO.

The UCST behavior of PLL-g-PAAMAN (0.53/0.47 wt%) was compared to the one of non-grafted PAAMAN chains in presence of PLL (**Figure 7.6**).

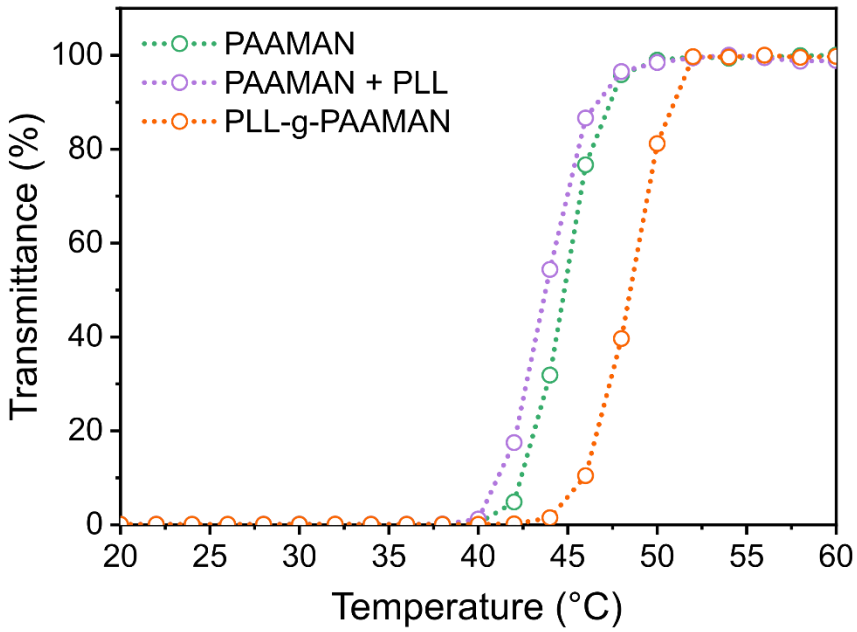

Figure 7.6. Turbidity heating curve of solutions of PAAMAN (1 wt%), PAAMAN + PLL (1 wt% + 1 wt%) and PLL-g-PAAMAN (1 wt%) in water.

Compared to pure PAAMAN and PAAMAN in presence of PLL (but non grafted), the cloud point of PLL-g-PAAMAN is shifted from 4-5 °C towards higher temperatures.

7.3 Preparation of emulsions

Water-in-oil emulsions were obtained by manually emulsifying 5 µL of aqueous phase (containing polymers, NPs, and other water-soluble compounds) in 95 µL of oil phase (containing Krytox) in a 0.5 mL Eppendorf tube.

For microscopy experiments, the emulsions were observed in hollow rectangle glass capillaries (CMScientific) with the following dimensions: inner height = 100 µm, width = 1 mm, length = ~1 cm (adjusted manually). Prior to emulsion injection, the internal sides of the capillary were coated with PLL-g-PEG to prevent the breakage of water droplets at the contact with bare glass side (see Chapter 2). Briefly the capillary was filled with an aqueous solution of PLL-g-PEG (M_W = 2 kDa, 1 g/L in 7.7 mM phosphate buffer) and incubated for 30 min before evaporation on a heating plate at 60 °C. Then, deionized water was injected and evaporated at 60 °C. The microscopy samples were prepared by injecting a few µL of emulsion in a PLL-g-PEG-coated capillary. After injection, the capillary was sealed at its extremities with Vitrex putty.

7.4 Coating of NPs with PLL derivatives

200-µm NeutravNPs and CarboxNPs were coated with PLL-g-PNIPAM for dynamic light scattering and zeta potential measurements. The coating protocol was the following: a 250-µL solution containing 0.5 wt% of PLL-g-PNIPAM and 0.02 wt% of NPs in phosphate buffer (~ 10^{16} polymer chains for ~ 10^{10} NPs) was gently sonicated for 5 min prior to 1h incubation at room temperature. The excess of polymer was then removed by filtration on Amicon® Ultra 0.5 mL centrifugal filters (cut-off 100 kDa), following the sequential procedure of centrifugation (10 min at 14 000 rcf), removal of the filtrate and redispersion of the NPs (retained in the filter) in the device by addition of 250 µL of fresh phosphate buffer. After three cycles of this filtration

procedure, the solution was retrieved from the filter device and was diluted in 250 µL of buffer + 500 µL of pure water to yield 1 mL of solution useable in DLS and Zeta potential measurements. Control solutions of pristine NPs at 0.02 wt% were obtained by simple dilution and sonication of the commercial solutions in 500 µL phosphate buffer + 500 µL pure water.

7.5 Interfacial tension measurements

The interfacial tension measurements were performed at room temperature using a TRACKER^{TM} automatic drop tensiometer (Teclis Scientific). The oil phase was made of FC-40 containing Krytox surfactant. The aqueous phase was made of 6 kDa PLL in phosphate buffer. Pure (deionized) water was also used as a reference aqueous medium. Rising aqueous droplets were formed at the tip of a J-shaped curved needle submerged in 2-mL bath of oil phase. The droplet shape was imaged with a camera and processed with the TRACKER apparatus software. A value of the interfacial tension was obtained from an automatic fit of the droplet profile using the Young-Laplace model.[289]

The reliability of the profile fit depends on the shape and the stability of the droplet. First, the Young-Laplace model remains valid as long as gravity and capillarity effects are balancing each other. When the droplet starts to grow out of the needle, its shape is quasi-spherical because essentially dictated by capillarity. The action of gravity starts to be visible as soon as the droplet elongates at the tip of the needle, what requires a minimum injected volume.[290] Thus, the interfacial tension can be accurately measured provided a droplet shape which is significantly different from the spherical shape. Then, the droplet surface needs to be at equilibrium to properly fit its profile and to extract a reliable value of interfacial tension.[290]

In our case, due to the high difference of density between the two phases, the water droplets tend to quickly detach from the needle and to flow up in the oil phase. The optimal shape and the interfacial equilibrium are probably not reached before the droplet is released. As a consequence, the raw values of interfacial tension measured with this approach could be skewed. Nevertheless, droplets were imaged after the maximum stabilization time before release and approximate values of the interfacial tension were extracted from the fit of the droplet profile in this condition. For the

interpretation, the focus was put on the qualitative evolution of the interfacial tension rather than on the quantitative data.

7.6 UV-Vis spectrophotometry

Absorbance and transmittance spectra were recorded on a single cell Thermo Scientific Evolution Array UV-Vis spectrophotometer equipped with a Peltier temperature-controlled cell holder (+/- 0.1 °C). The sample solutions were injected in a 150 µL quart micro-cuvette with an optical path length of 1 cm.

UV-Vis spectrophotometry of AuNPs

Absorbance spectra of AuNPs were recorded at 25 °C on solutions containing 0.005 wt% of AuNPs and a variable concentration of 6 kDa PLL in the 0-5 wt% range.

Turbidity measurements of thermoresponsive polymer solutions

Thermoresponsive polymers (PNIPAM, PAAMAN and their PLL comb-like derivatives) were dissolved at 1 wt% in the appropriate buffer (pure water, phosphate buffer or KSCN buffer). The solutions were submitted to a sweep of temperature between 20 °C and 60 °C by steps of 2 °C. A spectrum was recorded at each step temperature after 3 min thermalization. The mean transmittance between 650 and 750 nm was used to plot the turbidimetry curves.

7.7 Zeta potential measurements

Zeta potential measurements were performed on solutions of 200-nm NeutravNPs or CarboxyNPs (pristine or PLL-g-PNIPAM-coated) prepared according to the protocol described in section 7.4 and injected in DTS 1060C Zeta cells. The measurements were performed at 25 °C using a

Zetasizer Nano-ZS (Malvern Instruments). For each sample, the average zeta distribution was obtained from the average of three measurements (22 runs each), separated by 2 min stabilization.

7.8 Dynamic light scattering (DLS) measurements

DLS experiments were performed at 90° angle and at room temperature on a BI-200SM Goniometer System (Brookhaven Instruments Corp.) equipped with a 30 mW LED laser operating at 637 nm and a BI-CROSS CORR dual photomultiplier as the detector. The scattered light intensity and the correlation function were monitored using BIC Dynamic Light Scattering software. The mean hydrodynamic diameter was automatically extracted from the correlogram using the cumulant expansion analysis.

Characterization of water-in-oil emulsions

DLS was used to determine the influence of polymer and Krytox concentrations on the stability of water-in-oil emulsions, following a suitable design of experiments. The results are given in Appendix B. For these experiments, DLS samples were prepared as follows: 5 %vol water-in-oil emulsions were prepared by mixing 5 µL of aqueous phase (PLL-g-PNIPAM in phosphate buffer) and 95 µL of oil phase (Krytox in FC-70 oil) in a 0.5 mL Eppendorf tube. The two phases were emulsified by tip sonication using a Sonics Vibra-Cell VCX 750 for 3 min at 300 W (the sample was placed in an ice bath to limit undesired heating). The resulting emulsions were diluted 20 times in pure FC-70 oil prior to DLS measurements. The mean hydrodynamic diameter of emulsion droplets and the associated standard deviation were measured at 25 °C.

Characterization of nanoparticles

DLS measurements were performed on solutions of 200-nm NeutravNPs or CarboxyNPs (pristine or PLL-g-PNIPAM-coated) prepared according to the protocol described in section 7.4. The hydrodynamic diameter of the samples was measured at intervals of 5 °C between 20 °C and 50 °C (after 5 min thermalization at teach temperature step).

7.9 Microscopy techniques

7.9.1 Bright field and phase-contrast microscopy

Bright field and phase contrast imaging were performed with a LEICA DM IRE2 microscope equipped with a long-focal ×63 air objective. Images were acquired with a Retina 6000 Q-imaging camera and processed with Micro-Manager 1.4 software (Image J).

The plasmonic excitation of AuNPs was achieved with a 532-nm diode laser with 40 mW nominal power (DJ532-40 DPSS model from Thorlabs) that was mounted on the side port of the microscope. The laser was controlled with a TED200C Thermoelectric Temperature Controller and a LDC210C Laser Diode Controller (from Thorlabs).

7.9.2 Confocal Laser Scanning Microscopy

Confocal microscope

Confocal images were acquired on a Zeiss LSM 710 META Laser Scanning Microscope equipped with a Plan Apochromat x20 (0.8 NA) objective and a temperature-controlled heating stage (25-50 °C). To ensure emulsion thermalization, capillaries filled with the emulsion were placed on a pierced supporting copper slide that was fixed on the heating stage of the confocal microscope. Low temperatures (16-20 °C) were achieved by placing a glass petri dish full of ice on top of the supporting copper slide close to the capillary. The actual temperature of the supporting copper slide was measured with a REED ST-640B thermocouple. The 405 nm excitation of ANS or coumarin was performed using a 30 mW CW/pulsed diode laser. The 458 nm excitation of eGFP or FluoSpheres™ NeutrAvidin™-Labeled Microspheres, and the 514 nm excitation of rhodamine or Cy3 were performed using a 25 mW argon laser. Images were acquired using LSM ZEN 2009 software and processed with Fiji software (ImageJ).

Fluorescence recovery after photobleaching (FRAP) experiments

FRAP experiments were performed on shells made of coumarin-labeled polymers (PLL-g-PAAMAN, PLL-g-PEG) at 18 °C and 48 °C on the Zeiss LSM 710 confocal microscope presented above. The sample was imaged upon 405-nm excitation at 0.15 mW (0.5 % of the maximum intensity) with a scanning speed of 0.39 µs/px. The photobleaching was performed in a circular region of interest (ROI) upon 405-nm excitation at 30 mW (100 % of the maximum intensity) with a scanning speed of 6.30 µs/px. The acquisition rate was set at 1 image/second and the mean fluorescence level in the ROI was monitored for 10 s before bleaching and 120 s after.

7.9.3 Grating-shadow phase microscopy (GSPM)

Microscopy set up

GSPM experiments were performed in the lab of Guillaume Baffou at the Fresnel Institute (Marseille). The OPD images were recorded on a home-made optical set up including : a 700 mW LED illumination at 625 nm (M625L3, Thorlabs), a x60 objective (LUC Plan FLN, NA 0.7, Olympus), a and a SID4-sC8 wavefront sensor and imaging device (Phasics). The plasmonic excitation of the sample was achieved with a MGL-FN-532 DPSS laser operating at 532 nm with a nominal power up to 1500 mW (CNI Optoelectronics Tech). The power at the sample level was limited to 40 mW with a laser spot of 50 µm in diameter.

The entire optical set-up is represented in **Chapter 4** (section 4.4.2.5).

Measurement of the $\frac{dn_O}{dT}$ coefficient of FC-70 oil

The measurement of the $\frac{dn_O}{dT}$ coefficient of FC-70 was performed using GSPM. A 12 µm-deep crater etched in a glass slide was filled with FC-70 oil. An OPD image of the crater was taken at different temperature upon heating. **Figure 7.7**.A shows the OPD image at 90 °C. At each temperature, the refractive index of the oil n_O was deduced from the measurement of the OPD (δ) between the bottom of the crater and the surface of the glass slide, according to the formula: $n_O = n_{air} + \delta/h$ with $n_{air} = 1.00$ and $h = 12\ \mu m$. The evolution of n_O with the temperature is shown

in **Figure 7.7**.B. The slope of this curve gives $\frac{dn_O}{dT} = -3.16 \times 10^{-4}\ K^{-1}$. This experiment was performed by Sadman Shakib, PhD student in the team of Guillaume Baffou.

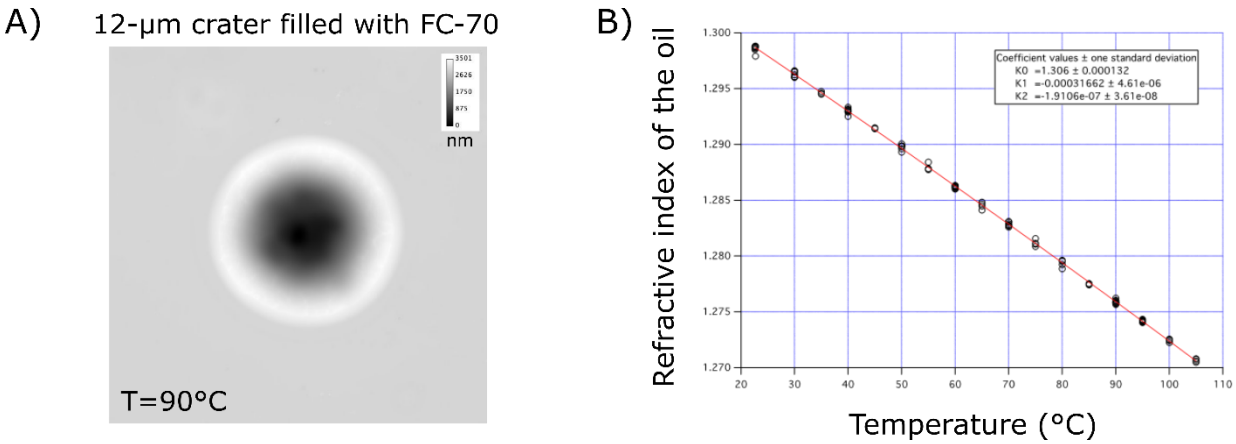

Figure 7.7. GSPM measurement of the $\frac{dn_O}{dT}$ coefficient of FC-70. A) OPD image of a 12-µm crater filled with FC-70 oil at 90 °C. The refractive index of the oil is deduced from the measurement of the OPD generated by the crater. B) Evolution of the refractive index of the oil with temperature (triplicate) and corresponding linear regression.

7.10 Scanning electron microcopy (SEM) imaging

SEM imaging was performed on isolated capsules resulting from the drying of water-in-oil emulsions (5 µL deposited on a glass coverslide) for three days at ambient air. To prevent the degradation of dried capsules during SEM imaging to enhance their contrast, the samples were metalized by deposition of a 30 nm-thin layer of Ag using an Emitech K675X Sputter Coater (Ag sputtering for 60 s at 120 mA). SEM images were recorded with a Hitachi TM3030 Tabletop Microscope either at 15 kV or in EDX mode.

Appendix B

Influence of the formulation of water-in-oil emulsions on the size and stability of emulsion droplets

As a complement to the surface tension measurements and the qualitative observation of the emulsions made in Chapter 1 (sections 3.2.1 and 3.2.3), the influence of the Krytox and PLL-g-PNIPAM concentrations on the water/oil interface stability was investigated by measuring the droplet size for different emulsion formulations by Dynamic Light Scattering (DLS). This quantitative data will be analyzed using the statistical approach of fractional design of experiment (DOE).

The Krytox and PLL-g-PNIPAM concentrations were studied as two factors (factors A and B respectively) in a 2^2 factorial DOE. Two levels – one low denoted "−1" and one high denoted "+1" – were assigned to both factors, leading to 4 different formulations for which the mean droplet size was measured by DLS. The levels of the two factors were chose to cover an experimental range of concentration that seemed relevant for the formulation of the emulsions. The detailed formulations of the DOE are summarized in **Table 8.1**.

	Factor A Krytox concentration (wt%)	Factor B Polymer concentration (wt%)
Low level (−1)	0.01	0.5
High level (+1)	0.05	5.0

Table 8.1. Composition of the 2^2 factorial design of experiment implemented to determine the effect of Krytox and PLL-g-PNIPAM on the droplet size of water-in-oil emulsions.

For each emulsion formulation, the *mean* water droplet diameter was measured on 3 different samples to determine an *average* diameter and an experimental variance (accounting for the experimental residual error). Note the difference between the terms "mean" and "average" in this case: the *mean* diameter refers to the mean diameter *within a given size distribution* (resulting from the measurement of a given polydisperse sample); and the *average* diameter results from the calculation of the *arithmetic* mean of the (mean) diameters measured for the 3 samples. For a given formulation i, the mean diameter measured by DLS on the sample j will be denoted $d_{i,j}$ and the average diameter calculated from the 3 samples will be denoted $\bar{d}_i$.

The experimental results of the DOE are gathered in the **Table 8.2**. The average diameters are also graphically reported below in **Figure 8.1**.A.

Formulation i	Factor A	Factor B	Crossed factor AB	Mean diameter Sample 1 $d_{i,1}$ (nm)	Mean diameter Sample 2 $d_{i,2}$ (nm)	Mean diameter Sample 3 $d_{i,3}$ (nm)	Average diameter $\bar{d}_i$ (nm)	Experimental variance $\hat{\sigma}_i^2$ (nm²)	Std Dev $\hat{\sigma}_i$ (nm²)
1	−1	−1	+1	657	276	428	454	36826	192
2	+1	−1	−1	100	96	140	112	597	24
3	−1	+1	−1	227	347	166	358	8494	92
4	+1	+1	+1	80	70	73	74	29	5

Table 8.2. DLS measurements of the water droplet diameter for all the samples prepared in the DOE.

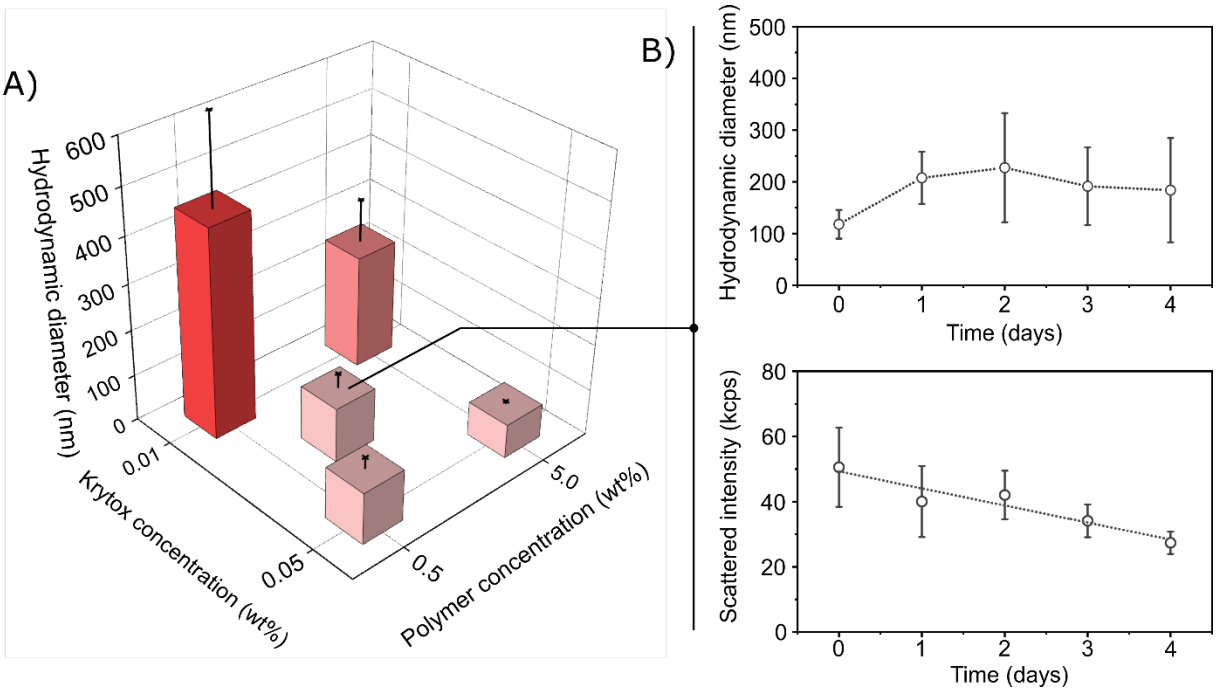

Figure 8.1. DLS analysis of water-in-oil emulsions. A) Evolution of the hydrodynamic diameter of water droplets as a function of the PLL-g-PNIPAM concentration in the aqueous phase and the Krytox concentration in the oil phase (error bars = standard deviation on 3 samples). B) Evolution over time of the droplet diameter and the scattered intensity for the emulsion with 2 wt% PLL-g-PNIPAM and 0.03 wt% Krytox.

The results of the formulations of interest are located at the corners of the experimental domain showed in **Figure 8.1.**A. In presence of the lowest Krytox concentration (0.01 wt%), relatively big droplets and high standard deviations were observed, suggesting that the emulsions were highly polydisperse and barely repeatable, which are signs of poor stability. On the other hand, in presence of the highest Krytox concentration (0.05 wt%), significantly smallest droplet sizes were reached (around 100 nm) with low standard deviations, indicating an efficient dispersion of the water phase in the oil phase. At first sight, the effect of PLL seems not to be significative compared to the effect of Krytox, what is consistent with the results of interfacial tension reported in **Figure 3.3** in Chapter 3 (the same decrease of the interfacial tension with Krytox concentration was observed independently of the PLL concentration).

To validate these observations, a statistical analysis of the effects of Krytox and PLL-g-PNIPAM concentrations was developed as reported in the following.

As 3 independent samples were tested for each formulation i, the experimental variance $\hat{\sigma}_i^2$ for each formulation was determined with 2 degrees of freedom (dof). In total, the DOE involves 8 dof (4 formulations with 2 dof per formulation). Assuming that the hypothesis of homoscedasticity is verified (all the $\hat{\sigma}_i^2$ estimate the same residual variance), the intraclass variance $\hat{\sigma}^2$ can be used as an optimal estimation of the residual variance. It is calculated as the arithmetic mean of the variances, weighted by their respective number of dof:

$$\hat{\sigma}^2 = \frac{\sum_i 2\hat{\sigma}_i^2}{8} = 11487 \text{ nm}^2$$

The average effect $\bar{E}$ of each factor was deduced from the results by calculating the arithmetic mean of the diameter measured for each formulation but weighted with the suitable ± 1 factor indicated in **Table 8.2**. As an example: $\bar{E}(A) = \frac{-\bar{d}_1+\bar{d}_2-\bar{d}_3+\bar{d}_4}{4} = -128.6$ nm. The effects were calculated for A, B and the cross-factor AB (accounting for the interaction between A and B) and are reported in **Table 8.3**. Given that the homoscedasticity is assumed for the 12 experiments, the variance on the effects $\hat{\sigma}_E^2$ is equal to $\hat{\sigma}^2/12 = 957$ nm^2. From that, we can deduce an estimation for the standard deviation on the effects which is $\hat{\sigma}_E = 31$ nm.

To evaluate the significativity of the effects, we assumed that the effect of a given factor X is not significant, i.e. $E(X) = 0$ (null hypothesis) and we proceeded to a Student test to verify it from a statistical point of view. Under this condition, the experimental ratio $\bar{E}(X)/\hat{\sigma}_E$ follows a Student law with 8 dof ($\bar{E}(X)/\hat{\sigma}_E \rightsquigarrow t_8$). We calculated the experimental Student parameter $t_{exp} = \bar{E}(X)/\hat{\sigma}_E$ for each factor X and compared it to the corresponding tabulated value t_8 (which depends itself on a confidence parameter p). If $|t_{exp}| > t_8(p)$ for a given p, the null hypothesis can be rejected with a level of confidence of $1 - p$, indicating that the factor X has a *significant* effect on the droplet diameter (with a certain level of confidence).

The experimental Student parameters t_{exp} for the factors A, B and AB are reported in **Table 8.3**. The tabulated values of the Student parameters with 8 dof t_8 for a given confidence parameter p are given in **Table 8.4**.

Factor $\boldsymbol{X}$	Effect Sample 1	Effect Sample 2	Effect Sample 3	Average effect $\bar{\boldsymbol{E}}$ (nm)	Experimental Student parameter (with 8 dof) $\boldsymbol{t_{exp} = \bar{E}/\hat{\sigma}_E}$
A	−176,05	−114,45	−95,25	**−128.6**	**−4.1**
B	−112,55	11,25	−82,35	**−61.2**	**−2.0**
AB	102,5	−24,25	48,7	**+42.3**	**+1.4**

Table 8.3. Average effect and experimental Student parameters calculated for all the factors of the DOE.

Confidence parameter $\boldsymbol{p}$	Student parameter with 8 dof $\boldsymbol{t_8}$
0.01	**3.355**
0.02	2.896
0.05	2.306
0.10	1.860
0.20	1.387

Table 8.4. Tabulated values of Student parameters with 8 degrees of freedom as a function of the confidence parameter.

The data will be analyzed taking $p = 0.01$, so that the results of the Student test can be guaranteed with a confidence of 99 % (see **Table 8.4**). According to the results given in **Table 8.3**, the condition $|t_{exp}| > t_8(0.01) = 3.355$ is verified for the factor A ($t_{exp} = -4.1$ in green) but not for the factors B ($t_{exp} = -2.0$ in red) and AB ($t_{exp} = +1.4$ in red). Consequently, the null hypothesis can be rejected for the factor A with a confidence of 99 % but not for the factors B and AB. In other words, the factor A has a *significant* effect (from a statistical point of view) on the water droplet diameter, what is not the case for the factor B or the crossed-factor AB. Coming back to the physics of the system, these results indicate that the Krytox concentration has a significant influence on the water droplet size and that this size decreases when the Krytox concentration increases ($E(A) < 0$). In contrast, the PLL-g-PNIPAM concentration does not have a major

influence on the water droplet size and there is no interaction between the effects of Krytox and PLL-g-PNIPAM concentrations.

In Section 3.2.1, we reported that, in presence of PLL as complexation partner, an increase in Krytox concentration led to a sharp decrease in water/oil interfacial tension. Considering the process of droplet formation upon emulsification, we will show that the interfacial tension is a key parameter that dictates the size of the emulsified droplets. The driving force of droplet formation upon emulsification is the shearing stress produced by the sonication, which stands as $\eta\dot{\gamma}$ with η the viscosity of the continuous oil phase and $\dot{\gamma}$ the shear rate. In opposition, the droplet formation is hindered by the energetic cost related to the creation of water/oil interfaces, which is nothing else than the interfacial stress Γ/R with Γ the water/oil interfacial tension and R the radius of the droplets. The competition between shearing and interfacial stresses can be described by a dimensionless number, called the capillary number Ca, which reads:

$$Ca = \frac{\text{shearing stress}}{\text{interfacial stress}} = \frac{\eta\dot{\gamma}R}{\Gamma}$$

The regime of droplet formation is set when the shearing stress balances the interfacial stress, i.e. for $Ca \sim 1$. Given that η and $\dot{\gamma}$ are fixed in the experimental conditions (the oil viscosity is a constant and the same sonication power was used for all the emulsions), the droplet radius R would thus be proportional to the interfacial tension Γ. Then an increase in Krytox concentration leads to a decrease in interfacial tension, and consequently a decrease in the droplet size formed upon emulsification. This result makes the connection between the interfacial tension measurements reported in **Section XX** and the droplet size measurements reported in this section.

In addition to the 4 formulations used in the DOE, a formulation with "intermediate" concentrations in additives (2 wt% PLL-g-PNIPAM and 0.03 wt% Krytox) was characterized and added to the data as an example of a "central" point in the experimental domain defined by the DOE (see **Figure 8.1.A**). The mean droplet diameter of this formulation was measured for consecutive days to follow the stability of the emulsion over time (see **Figure 8.1.B**). Starting from a value of 100 nm just after emulsification, the average droplet diameter increases to 200 nm after one day and seems to stabilize at this value afterwards. Note that a standard deviation of around

100 nm was determined, suggesting a high degree of polydispersity (what was confirmed by a relatively high polydispersity index around 0.2 in the size distribution of a given sample) and probably a partial destabilization of the emulsion over time. This process can also be pointed out regarding the progressive decrease of the scattering intensity of the samples over time (see **Figure 8.1.B**). This result can be attributed to a less efficient redispersion of the water droplets in the oil over time, suggesting a progressive – but not drastic – destabilization of the emulsion.

References

(1) Khurana, A.; Allawadhi, P.; Khurana, I.; Allwadhi, S.; Weiskirchen, R.; Banothu, A. K.; Chhabra, D.; Joshi, K.; Bharani, K. K. Role of Nanotechnology behind the Success of MRNA Vaccines for COVID-19. *Nano Today* **2021**, *38*, 101142. https://doi.org/10.1016/j.nantod.2021.101142.

(2) Kim, S. B.; Ito, Y.; Torimura, M. Bioluminescent Capsules for Live-Cell Imaging. *Bioconjug. Chem.* **2012**, *23* (11), 2221–2228. https://doi.org/10.1021/bc300323x.

(3) Liang, K.; Gunawan, S. T.; Richardson, J. J.; Such, G. K.; Cui, J.; Caruso, F. Endocytic Capsule Sensors for Probing Cellular Internalization. *Adv. Healthc. Mater.* **2014**, *3* (10), 1551–1554. https://doi.org/10.1002/adhm.201400139.

(4) Jeyaraman, J.; Shukla, A.; Sivakumar, S. Targeted Stealth Polymer Capsules Encapsulating Ln3+-Doped LaVO4 Nanoparticles for Bioimaging Applications. *ACS Biomater. Sci. Eng.* **2016**, *2* (8), 1330–1340. https://doi.org/10.1021/acsbiomaterials.6b00252.

(5) Martina, M. S.; Fortin, J. P.; Ménager, C.; Clément, O.; Barratt, G.; Grabielle-Madelmont, C.; Gazeau, F.; Cabuil, V.; Lesieur, S. Generation of Superparamagnetic Liposomes Revealed as Highly Efficient MRI Contrast Agents for in Vivo Imaging. *J. Am. Chem. Soc.* **2005**, *127* (30), 10676–10685. https://doi.org/10.1021/ja0516460.

(6) Jagielski, N.; Sharma, S.; Hombach, V.; Mailänder, V.; Rasche, V.; Landfester, K. Nanocapsules Synthesized by Miniemulsion Technique for Application as New Contrast Agent Materials. *Macromol. Chem. Phys.* **2007**, *208* (19–20), 2229–2241. https://doi.org/10.1002/macp.200700254.

(7) Pisani, E.; Tsapis, N.; Galaz, B.; Santin, M.; Berti, R.; Taulier, N.; Kurtisovski, E.; Lucidarme, O.; Ourevitch, M.; Doan, B. T.; Beloeil, J. C.; Gillet, B.; Urbach, W.; Bridal, S. L.; Fattal, E. Perfluorooctyl Bromide Polymeric Capsules as Dual Contrast Agents for Ultrasonography and Magnetic Resonance Imaging. *Adv. Funct. Mater.* **2008**, *18* (19), 2963–2971. https://doi.org/10.1002/adfm.200800454.

(8) Cheng, Z.; Al Zaki, A.; Jones, I. W.; Hall, H. K.; Aspinwall, C. A.; Tsourkas, A. Stabilized Porous Liposomes with Encapsulated Gd-Labeled Dextran as a Highly Efficient MRI

Contrast Agent. *Chem. Commun.* **2014**, *50* (19), 2502–2504. https://doi.org/10.1039/c3cc48939f.

(9) De Cock, L. J.; De Koker, S.; De Geest, B. G.; Grooten, J.; Vervaet, C.; Remon, J. P.; Sukhorukov, G. B.; Antipina, M. N. Polymeric Multilayer Capsules in Drug Delivery. *Angew. Chemie - Int. Ed.* **2010**, *49* (39), 6954–6973. https://doi.org/10.1002/anie.200906266.

(10) Hu, X.; Zhang, Y.; Xie, Z.; Jing, X.; Bellotti, A.; Gu, Z. Stimuli-Responsive Polymersomes for Biomedical Applications. *Biomacromolecules* **2017**, *18* (3), 649–673. https://doi.org/10.1021/acs.biomac.6b01704.

(11) Bordat, A.; Boissenot, T.; Nicolas, J.; Tsapis, N. Thermoresponsive Polymer Nanocarriers for Biomedical Applications. *Adv. Drug Deliv. Rev.* **2019**, *138*, 167–192. https://doi.org/10.1016/j.addr.2018.10.005.

(12) Sun, T.; Zhang, Y. S.; Pang, B.; Hyun, D. C.; Yang, M.; Xia, Y. Engineered Nanoparticles for Drug Delivery in Cancer Therapy. *Angew. Chemie - Int. Ed.* **2014**, *53* (46), 12320–12364. https://doi.org/10.1002/anie.201403036.

(13) Senapati, S.; Mahanta, A. K.; Kumar, S.; Maiti, P. Controlled Drug Delivery Vehicles for Cancer Treatment and Their Performance. *Signal Transduct. Target. Ther.* **2018**, *3* (1), 1–19. https://doi.org/10.1038/s41392-017-0004-3.

(14) Ke, W.; Li, J.; Mohammed, F.; Wang, Y.; Tou, K.; Liu, X.; Wen, P.; Kinoh, H.; Anraku, Y.; Chen, H.; Kataoka, K.; Ge, Z. Therapeutic Polymersome Nanoreactors with Tumor-Specific Activable Cascade Reactions for Cooperative Cancer Therapy. *ACS Nano* **2019**, *13* (2), 2357–2369. https://doi.org/10.1021/acsnano.8b09082.

(15) Saunders, B. R.; Fraylich, M.; Alexander, C.; Wang, W.; Liang, H.; Cheikh Al Ghanami, R.; Hamilton, L.; Shakesheff, K. M. Biodegradable Thermoresponsive Microparticle Dispersions for Injectable Cell Delivery Prepared Using a Single-Step Process. *Adv. Mater.* **2009**, *21* (18), 1809–1813. https://doi.org/10.1002/adma.200800382.

(16) Facca, S.; Cortez, C.; Mendoza-palomares, C.; Messadeq, N.; Dierich, A.; Johnston, A. P. R.; Mainard, D. Active Multilayered Capsules for in Vivo Bone Formation. **2009**. https://doi.org/10.1073/pnas.0908531107.

(17) Zheng, Z.; Wang, H.; Li, J.; Shi, Q.; Cui, J.; Sun, T.; Huang, Q.; Fukuda, T. 3D Construction of Shape-Controllable Tissues through Self-Bonding of Multicellular Microcapsules. *ACS*

Appl. Mater. Interfaces **2019**, *11* (26), 22950–22961. https://doi.org/10.1021/acsami.9b05108.

(18) Wang, F.; Xiao, J.; Chen, S.; Sun, H.; Yang, B.; Jiang, J.; Zhou, X.; Du, J. Polymer Vesicles: Modular Platforms for Cancer Theranostics. *Adv. Mater.* **2018**, *30* (17). https://doi.org/10.1002/adma.201705674.

(19) Delcassian, D.; Luzhansky, I.; Spanoudaki, V.; Bochenek, M.; McGladrigan, C.; Nguyen, A.; Norcross, S.; Zhu, Y.; Shan, C. S.; Hausser, R.; Shakesheff, K. M.; Langer, R.; Anderson, D. G. Magnetic Retrieval of Encapsulated Beta Cell Transplants from Diabetic Mice Using Dual-Function MRI Visible and Retrievable Microcapsules. *Adv. Mater.* **2020**, *32* (16). https://doi.org/10.1002/adma.201904502.

(20) Shakeri, S.; Ashrafizadeh, M.; Zarrabi, A.; Roghanian, R.; Afshar, E. G.; Pardakhty, A.; Mohammadinejad, R.; Kumar, A.; Thakur, V. K. Multifunctional Polymeric Nanoplatforms for Brain Diseases Diagnosis, Therapy and Theranostics. *Biomedicines* **2020**, *8* (1). https://doi.org/10.3390/biomedicines8010013.

(21) Chiang, W. H.; Huang, W. C.; Chang, C. W.; Shen, M. Y.; Shih, Z. F.; Huang, Y. F.; Lin, S. C.; Chiu, H. C. Functionalized Polymersomes with Outlayered Polyelectrolyte Gels for Potential Tumor-Targeted Delivery of Multimodal Therapies and MR Imaging. *J. Control. Release* **2013**, *168* (3), 280–288. https://doi.org/10.1016/j.jconrel.2013.03.029.

(22) Schoebitz, M.; López, M. D.; Roldán, A. Bioencapsulation of Microbial Inoculants for Better Soil-Plant Fertilization. A Review. *Agron. Sustain. Dev.* **2013**, *33* (4), 751–765. https://doi.org/10.1007/s13593-013-0142-0.

(23) Camara, M. C.; Campos, E. V. R.; Monteiro, R. A.; Do Espirito Santo Pereira, A.; De Freitas Proença, P. L.; Fraceto, L. F. Development of Stimuli-Responsive Nano-Based Pesticides: Emerging Opportunities for Agriculture. *J. Nanobiotechnology* **2019**, *17* (1), 1–19. https://doi.org/10.1186/s12951-019-0533-8.

(24) Blanco-Padilla, A.; Soto, K. M.; Hernández Iturriaga, M.; Mendoza, S. Food Antimicrobials Nanocarriers. *Sci. World J.* **2014**, *2014*. https://doi.org/10.1155/2014/837215.

(25) Ezhilarasi, P. N.; Karthik, P.; Chhanwal, N.; Anandharamakrishnan, C. Nanoencapsulation Techniques for Food Bioactive Components: A Review. *Food Bioprocess Technol.* **2013**, *6* (3), 628–647. https://doi.org/10.1007/s11947-012-0944-0.

(26) Lohani, A.; Verma, A.; Joshi, H.; Yadav, N.; Karki, N. Nanotechnology-Based

Cosmeceuticals. **2018**, *2014*.

(27) He, L.; Hu, J.; Deng, W. Preparation and Application of Flavor and Fragrance Capsules. *Polym. Chem.* **2018**, *9* (40), 4926–4946. https://doi.org/10.1039/c8py00863a.

(28) Vimalanandan, A.; Lv, L. P.; Tran, T. H.; Landfester, K.; Crespy, D.; Rohwerder, M. Redox-Responsive Self-Healing for Corrosion Protection. *Adv. Mater.* **2013**, *25* (48), 6980–6984. https://doi.org/10.1002/adma.201302989.

(29) Zhu, D. Y.; Rong, M. Z.; Zhang, M. Q. Self-Healing Polymeric Materials Based on Microencapsulated Healing Agents: From Design to Preparation. *Prog. Polym. Sci.* **2015**, *49–50*, 175–220. https://doi.org/10.1016/j.progpolymsci.2015.07.002.

(30) Salunkhe, P. B.; Shembekar, P. S. A Review on Effect of Phase Change Material Encapsulation on the Thermal Performance of a System. *Renew. Sustain. Energy Rev.* **2012**, *16* (8), 5603–5616. https://doi.org/10.1016/j.rser.2012.05.037.

(31) Shchukin, D. G.; Möhwald, H. Urea Photosynthesis inside Polyelectrolyte Capsules: Effect of Confined Media. *Langmuir* **2005**, *21* (12), 5582–5587. https://doi.org/10.1021/la050429+.

(32) Küchler, A.; Yoshimoto, M.; Luginbühl, S.; Mavelli, F.; Walde, P. Enzymatic Reactions in Confined Environments. *Nat. Nanotechnol.* **2016**, *11* (5), 409–420. https://doi.org/10.1038/nnano.2016.54.

(33) Musyanovych, A.; Mailänder, V.; Landfester, K. Miniemulsion Droplets as Single Molecule Nanoreactors for Polymerase Chain Reaction. *Biomacromolecules* **2005**, *6* (4), 1824–1828. https://doi.org/10.1021/bm050084+.

(34) Comellas-Aragonès, M.; Engelkamp, H.; Claessen, V. I.; Sommerdijk, N. A. J. M.; Rowan, A. E.; Christianen, P. C. M.; Maan, J. C.; Verduin, B. J. M.; Cornelissen, J. J. L. M.; Nolte, R. J. M. A Virus-Based Single-Enzyme Nanoreactor. *Nat. Nanotechnol.* **2007**, *2* (10), 635–639. https://doi.org/10.1038/nnano.2007.299.

(35) Dong, R.; Liu, W.; Hao, J. Soft Vesicles in the Synthesis of Hard Materials. *Acc. Chem. Res.* **2012**, *45* (4), 504–513. https://doi.org/10.1021/ar200124g.

(36) Cacace, D. N.; Rowland, A. T.; Stapleton, J. J.; Dewey, D. C.; Keating, C. D. Aqueous Emulsion Droplets Stabilized by Lipid Vesicles as Microcompartments for Biomimetic Mineralization. *Langmuir* **2015**, *31* (41), 11329–11338. https://doi.org/10.1021/acs.langmuir.5b02754.

(37) Tian, H.; Liang, J.; Liu, J. Nanoengineering Carbon Spheres as Nanoreactors for Sustainable Energy Applications. *Adv. Mater.* **2019**, *31* (50). https://doi.org/10.1002/adma.201903886.

(38) De Martino, M. T.; Abdelmohsen, L. K. E. A.; Rutjes, F. P. J. T.; Van Hest, J. C. M. Nanoreactors for Green Catalysis. *Beilstein J. Org. Chem.* **2018**, *14* (2), 716–733. https://doi.org/10.3762/bjoc.14.61.

(39) Marguet, M.; Bonduelle, C.; Lecommandoux, S. Multicompartmentalized Polymeric Systems: Towards Biomimetic Cellular Structure and Function. *Chem. Soc. Rev.* **2013**, *42* (2), 512–529. https://doi.org/10.1039/c2cs35312a.

(40) Peters, R. J. R. W.; Marguet, M.; Marais, S.; Fraaije, M. W.; van Hest, J. C. M.; Lecommandoux, S. Cascade Reactions in Multicompartmentalized Polymersomes. *Angew. Chemie* **2014**, *126* (1), 150–154. https://doi.org/10.1002/ange.201308141.

(41) Schoonen, L.; Van Hest, J. C. M. Compartmentalization Approaches in Soft Matter Science: From Nanoreactor Development to Organelle Mimics. *Adv. Mater.* **2016**, *28* (6), 1109–1128. https://doi.org/10.1002/adma.201502389.

(42) Kurihara, K.; Tamura, M.; Shohda, K. I.; Toyota, T.; Suzuki, K.; Sugawara, T. Self-Reproduction of Supramolecular Giant Vesicles Combined with the Amplification of Encapsulated DNA. *Nat. Chem.* **2011**, *3* (10), 775–781. https://doi.org/10.1038/nchem.1127.

(43) Tian, L.; Li, M.; Patil, A. J.; Drinkwater, B. W.; Mann, S. Artificial Morphogen-Mediated Differentiation in Synthetic Protocells. *Nat. Commun.* **2019**, *10* (1), 1–13. https://doi.org/10.1038/s41467-019-11316-4.

(44) Berhanu, S.; Ueda, T.; Kuruma, Y. Artificial Photosynthetic Cell Producing Energy for Protein Synthesis. *Nat. Commun.* **2019**, *10* (1). https://doi.org/10.1038/s41467-019-09147-4.

(45) Rodríguez-Arco, L.; Kumar, B. V. V. S. P.; Li, M.; Patil, A. J.; Mann, S. Modulation of Higher-Order Behaviour in Model Protocell Communities by Artificial Phagocytosis. *Angew. Chemie - Int. Ed.* **2019**, *58* (19), 6333–6337. https://doi.org/10.1002/anie.201901469.

(46) Hindley, J. W.; Zheleva, D. G.; Elani, Y.; Charalambous, K.; Barter, L. M. C.; Booth, P. J.; Bevan, C. L.; Law, R. V.; Ces, O. Building a Synthetic Mechanosensitive Signaling Pathway in Compartmentalized Artificial Cells. *Proc. Natl. Acad. Sci. U. S. A.* **2019**, *116*

(34), 16711–16716. https://doi.org/10.1073/pnas.1903500116.

(47) Wang, X.; Tian, L.; Du, H.; Li, M.; Mu, W.; Drinkwater, B. W.; Han, X.; Mann, S. Chemical Communication in Spatially Organized Protocell Colonies and Protocell/Living Cell Micro-Arrays. *Chem. Sci.* **2019**, *10* (41), 9446–9453. https://doi.org/10.1039/c9sc04522h.

(48) Qiao, Y.; Li, M.; Qiu, D.; Mann, S. Response-Retaliation Behavior in Synthetic Protocell Communities. *Angew. Chemie* **2019**, *131* (49), 17922–17927. https://doi.org/10.1002/ange.201909313.

(49) Villringer, S.; Madl, J.; Sych, T.; Manner, C.; Imberty, A.; Römer, W. Lectin-Mediated Protocell Crosslinking to Mimic Cell-Cell Junctions and Adhesion. *Sci. Rep.* **2018**, *8* (1), 1–11. https://doi.org/10.1038/s41598-018-20230-6.

(50) Bekir, M.; Jelken, J.; Jung, S. H.; Pich, A.; Pacholski, C.; Kopyshev, A.; Santer, S. Dual Responsiveness of Microgels Induced by Single Light Stimulus. *Appl. Phys. Lett.* **2021**, *118* (9). https://doi.org/10.1063/5.0036376.

(51) Nijemeisland, M.; Abdelmohsen, L. K. E. A.; Huck, W. T. S.; Wilson, D. A.; Van Hest, J. C. M. A Compartmentalized Out-of-Equilibrium Enzymatic Reaction Network for Sustained Autonomous Movement. *ACS Cent. Sci.* **2016**, *2* (11), 843–849. https://doi.org/10.1021/acscentsci.6b00254.

(52) Xu, Z.; Hueckel, T.; Irvine, W. T. M.; Sacanna, S. Transmembrane Transport in Inorganic Colloidal Cell-Mimics. *Nature* **2021**, *597* (7875), 220–224. https://doi.org/10.1038/s41586-021-03774-y.

(53) Reis, C. P.; Ribeiro, A. J.; Houng, S.; Veiga, F.; Neufeld, R. J. Nanoparticulate Delivery System for Insulin: Design, Characterization and in Vitro/in Vivo Bioactivity. *Eur. J. Pharm. Sci.* **2007**, *30* (5), 392–397. https://doi.org/10.1016/j.ejps.2006.12.007.

(54) Tayalia, P.; Mooney, D. J. Controlled Growth Factor Delivery for Tissue Engineering. *Adv. Mater.* **2009**, *21* (32–33), 3269–3285. https://doi.org/10.1002/adma.200900241.

(55) Slastnikova, T. A.; Ulasov, A. V.; Rosenkranz, A. A.; Sobolev, A. S. Targeted Intracellular Delivery of Antibodies: The State of the Art. *Front. Pharmacol.* **2018**, *9* (OCT), 1–21. https://doi.org/10.3389/fphar.2018.01208.

(56) Frézard, F.; Silva-Barcellos, N. M.; dos Santos, R. A. S. A Novel Approach Based on Nanotechnology for Investigating the Chronic Actions of Short-Lived Peptides in Specific Sites of the Brain. *Regul. Pept.* **2007**, *138* (2–3), 59–65.

https://doi.org/10.1016/j.regpep.2006.11.021.

(57) Wang, W. Instability, Stabilization, and Formulation of Liquid Protein Pharamceuticals. *Int. J. Pharm.* **1999**, *185*, 129–188.

(58) Bilati, U.; Allémann, E.; Doelker, E. Strategic Approaches for Overcoming Peptide and Protein Instability within Biodegradable Nano- and Microparticles. *Eur. J. Pharm. Biopharm.* **2005**, *59* (3), 375–388. https://doi.org/10.1016/j.ejpb.2004.10.006.

(59) Blocher McTigue, W. C.; Perry, S. L. Protein Encapsulation Using Complex Coacervates: What Nature Has to Teach Us. *Small* **2020**, *16* (27), 1–17. https://doi.org/10.1002/smll.201907671.

(60) Feng, A.; Yuan, J. Smart Nanocontainers: Progress on Novel Stimuli-Responsive Polymer Vesicles. *Macromol. Rapid Commun.* **2014**, *35* (8), 767–779. https://doi.org/10.1002/marc.201300866.

(61) Rideau, E.; Dimova, R.; Schwille, P.; Wurm, F. R.; Landfester, K. Liposomes and Polymersomes: A Comparative Review towards Cell Mimicking. *Chem. Soc. Rev.* **2018**, *47* (23), 8572–8610. https://doi.org/10.1039/c8cs00162f.

(62) Wang, G.; Hoornweg, A.; Wolterbeek, H. T.; Franken, L. E.; Mendes, E.; Denkova, A. G. Enhanced Retention of Encapsulated Ions in Cross-Linked Polymersomes. *J. Phys. Chem. B* **2015**, *119* (11), 4300–4308. https://doi.org/10.1021/jp5125316.

(63) Lai, M. H.; Lee, S.; Smith, C. E.; Kim, K.; Kong, H. Tailoring Polymersome Bilayer Permeability Improves Enhanced Permeability and Retention Effect for Bioimaging. *ACS Appl. Mater. Interfaces* **2014**, *6* (13), 10821–10829. https://doi.org/10.1021/am502822n.

(64) Wang, X.; Liu, G.; Hu, J.; Zhang, G.; Liu, S. Concurrent Block Copolymer Polymersome Stabilization and Bilayer Permeabilization by Stimuli-Regulated "Traceless" Crosslinking. *Angew. Chemie - Int. Ed.* **2014**, *53* (12), 3138–3142. https://doi.org/10.1002/anie.201310589.

(65) Terreau, O.; Bartels, C.; Eisenberg, A. Effect of Poly(Acrylic Acid) Block Length Distribution on Polystyrene-b-Poly(Acrylic Acid) Block Copolymer Aggregates in Solution. 2. A Partial Phase Diagram. *Langmuir* **2004**, *20* (3), 637–645. https://doi.org/10.1021/la035557h.

(66) Lasic, D. D. Les Liposomes. *Recherche* **1989**, *20* (212), 904–913.

(67) Colletier, J. P.; Chaize, B.; Winterhalter, M.; Fournier, D. Protein Encapsulation in

Liposomes: Efficiency Depends on Interactions between Protein and Phospholipid Bilayer. *BMC Biotechnol.* **2002**, *2*, 1–8. https://doi.org/10.1186/1472-6750-2-9.

(68) Walde, P.; Cosentino, K.; Engel, H.; Stano, P. Giant Vesicles: Preparations and Applications. *ChemBioChem* **2010**, *11* (7), 848–865. https://doi.org/10.1002/cbic.201000010.

(69) Hwang, S. Y.; Kim, H. K.; Choo, J.; Seong, G. H.; Hien, T. B. D.; Lee, E. K. Effects of Operating Parameters on the Efficiency of Liposomal Encapsulation of Enzymes. *Colloids Surfaces B Biointerfaces* **2012**, *94*, 296–303. https://doi.org/10.1016/j.colsurfb.2012.02.008.

(70) Dominak, L. M.; Keating, C. D. Macromolecular Crowding Improves Polymer Encapsulation within Giant Lipid Vesicles. *Langmuir* **2008**, *24* (23), 13565–13571. https://doi.org/10.1021/la8028403.

(71) Zhu, Y.; Yang, B.; Chen, S.; Du, J. Polymer Vesicles: Mechanism, Preparation, Application, and Responsive Behavior. *Prog. Polym. Sci.* **2017**, *64*, 1–22. https://doi.org/10.1016/j.progpolymsci.2015.05.001.

(72) Carugo, D.; Bottaro, E.; Owen, J.; Stride, E.; Nastruzzi, C. Liposome Production by Microfluidics: Potential and Limiting Factors. *Sci. Rep.* **2016**, *6*, 1–15. https://doi.org/10.1038/srep25876.

(73) Kim, S. H.; Shum, H. C.; Kim, J. W.; Cho, J. C.; Weitz, D. A. Multiple Polymersomes for Programmed Release of Multiple Components. *J. Am. Chem. Soc.* **2011**, *133* (38), 15165–15171. https://doi.org/10.1021/ja205687k.

(74) Weiss, M.; Frohnmayer, J. P.; Benk, L. T.; Haller, B.; Janiesch, J. W.; Heitkamp, T.; Börsch, M.; Lira, R. B.; Dimova, R.; Lipowsky, R.; Bodenschatz, E.; Baret, J. C.; Vidakovic-Koch, T.; Sundmacher, K.; Platzman, I.; Spatz, J. P. Sequential Bottom-up Assembly of Mechanically Stabilized Synthetic Cells by Microfluidics. *Nat. Mater.* **2018**, *17* (1), 89–95. https://doi.org/10.1038/NMAT5005.

(75) Deshpande, S.; Caspi, Y.; Meijering, A. E. C.; Dekker, C. Octanol-Assisted Liposome Assembly on Chip. *Nat. Commun.* **2016**, *7*, 1–9. https://doi.org/10.1038/ncomms10447.

(76) Szoka, F.; Papahadjopoulos, D. Procedure for Preparation of Liposomes with Large Internal Aqueous Space and High Capture by Reverse-Phase Evaporation. *Proc. Natl. Acad. Sci. U. S. A.* **1978**, *75* (9), 4194–4198. https://doi.org/10.1073/pnas.75.9.4194.

(77) Sah, H. Stabilization of Proteins against Methylene Chloride/Water Interface-Induced Denaturation and Aggregation. *J. Control. Release* **1999**, *58* (2), 143–151. https://doi.org/10.1016/S0168-3659(98)00148-5.

(78) Van De Weert, M.; Hoechstetter, J.; Hennink, W. E.; Crommelin, D. J. A. The Effect of a Water/Organic Solvent Interface on the Structural Stability of Lysozyme. *J. Control. Release* **2000**, *68* (3), 351–359. https://doi.org/10.1016/S0168-3659(00)00277-7.

(79) Kwon, Y. M.; Baudys, M.; Knutson, K.; Kim, S. K. In Situ Study of Insulin Aggregation Induced by Water-Organic Solvent Interface. *Pharm. Res.* **2001**, *18* (12), 1754–1759. https://doi.org/10.1023/A:1013334916162.

(80) Yoo, H. S.; Choi, H. K.; Park, T. G. Protein-Fatty Acid Complex for Enhanced Loading and Stability within Biodegradable Nanoparticles. *J. Pharm. Sci.* **2001**, *90* (2), 194–201. https://doi.org/10.1002/1520-6017(200102)90:2<194::AID-JPS10>3.0.CO;2-Q.

(81) Panganiban, B.; Qiao, B.; Jiang, T.; Delre, C.; Obadia, M. M.; Nguyen, T. D.; Smith, A. A. A.; Hall, A.; Sit, I.; Crosby, M. G.; Dennis, P. B.; Drockenmuller, E.; Olvera, M.; Cruz, D.; Xu, T. Random Heteropolymers Preserve Protein Function in Foreign Environments. *Science (80-.).* **2018**, *1243*, 1239–1243. https://doi.org/10.1126/science.aao0335.

(82) Penfold, N. J. W.; Yeow, J.; Boyer, C.; Armes, S. P. Emerging Trends in Polymerization-Induced Self-Assembly. *ACS Macro Lett.* **2019**, *8* (8), 1029–1054. https://doi.org/10.1021/acsmacrolett.9b00464.

(83) Zhang, W. J.; Hong, C. Y.; Pan, C. Y. Efficient Fabrication of Photosensitive Polymeric Nano-Objects via an Ingenious Formulation of RAFT Dispersion Polymerization and Their Application for Drug Delivery. *Biomacromolecules* **2017**, *18* (4), 1210–1217. https://doi.org/10.1021/acs.biomac.6b01887.

(84) Charleux, B.; Delaittre, G.; Rieger, J.; D'Agosto, F. Polymerization-Induced Self-Assembly: From Soluble Macromolecules to Block Copolymer Nano-Objects in One Step. *Macromolecules* **2012**, *45* (17), 6753–6765. https://doi.org/10.1021/ma300713f.

(85) D'Agosto, F.; Rieger, J.; Lansalot, M. RAFT-Mediated Polymerization-Induced Self-Assembly. *Angew. Chemie - Int. Ed.* **2020**, *59* (22), 8368–8392. https://doi.org/10.1002/anie.201911758.

(86) Warren, N. J.; Armes, S. P. Polymerization-Induced Self-Assembly of Block Copolymer Nano-Objects via RAFT Aqueous Dispersion Polymerization. *J. Am. Chem. Soc.* **2014**, *136*

(29), 10174–10185. https://doi.org/10.1021/ja502843f.

(87) Albertsen, A. N.; Szymaski, J. K.; Pérez-Mercader, J. Emergent Properties of Giant Vesicles Formed by a Polymerization-Induced Self-Assembly (PISA) Reaction. *Sci. Rep.* **2017**, *7*, 41534. https://doi.org/10.1038/srep41534.

(88) Blackman, L. D.; Varlas, S.; Arno, M. C.; Fayter, A.; Gibson, M. I.; O'Reilly, R. K. Permeable Protein-Loaded Polymersome Cascade Nanoreactors by Polymerization-Induced Self-Assembly. *ACS Macro Lett.* **2017**, *6* (11), 1263–1267. https://doi.org/10.1021/acsmacrolett.7b00725.

(89) Varlas, S.; Blackman, L. D.; Findlay, H. E.; Reading, E.; Booth, P. J.; Gibson, M. I.; O'Reilly, R. K. Photoinitiated Polymerization-Induced Self-Assembly in the Presence of Surfactants Enables Membrane Protein Incorporation into Vesicles. *Macromolecules* **2018**, *51* (16), 6190–6201. https://doi.org/10.1021/acs.macromol.8b00994.

(90) Kabanov, A. V.; Vinogradov, S. V. Nanogels as Pharmaceutical Carriers: Finite Networks of Infinite Capabilities. *Angew. Chemie - Int. Ed.* **2009**, *48* (30), 5418–5429. https://doi.org/10.1002/anie.200900441.

(91) Mauri, E.; Giannitelli, S. M.; Trombetta, M.; Rainer, A. Synthesis of Nanogels: Current Trends and Future Outlook. *Gels* **2021**, *7* (2), 1–23. https://doi.org/10.3390/gels7020036.

(92) Chan, M.; Almutairi, A. Nanogels as Imaging Agents for Modalities Spanning the Electromagnetic Spectrum. *Mater. Horizons* **2016**, *3* (1), 21–40. https://doi.org/10.1039/c5mh00161g.

(93) Sanson, N.; Rieger, J. Synthesis of Nanogels/Microgels by Conventional and Controlled Radical Crosslinking Copolymerization. *Polym. Chem.* **2010**, *1* (7), 965–977. https://doi.org/10.1039/c0py00010h.

(94) Taton, D.; Baussard, J. F.; Dupayage, L.; Poly, J.; Gnanou, Y.; Ponsinet, V.; Destarac, M.; Mignaud, C.; Pitois, C. Water Soluble Polymeric Nanogels by Xanthate-Mediated Radical Crosslinking Copolymerisation. *Chem. Commun.* **2006**, No. 18, 1953–1955. https://doi.org/10.1039/b601456a.

(95) Es Sayed, J.; Lorthioir, C.; Perrin, P.; Sanson, N. PEGylated NiPAM Microgels: Synthesis, Characterization and Colloidal Stability. *Soft Matter* **2019**, *15* (5), 963–972. https://doi.org/10.1039/c8sm02156b.

(96) Ryu, J.-H.; Chacko, R. T.; Jiwpanich, S.; Bickerton, S.; Babu, R. P.; Thayumanavan, S.

Self-Cross-Linked Polymer Nanogels: A Versatile Nanoscopic Drug Delivery Platform. *J. Am. Chem. Soc.* **2010**, *132* (48), 17227–17235. https://doi.org/10.1021/ja1069932.

(97) Mueller, E.; Alsop, R. J.; Scotti, A.; Bleuel, M.; Rheinstädter, M. C.; Richtering, W.; Hoare, T. Dynamically Cross-Linked Self-Assembled Thermoresponsive Microgels with Homogeneous Internal Structures. *Langmuir* **2018**, *34* (4), 1601–1612. https://doi.org/10.1021/acs.langmuir.7b03664.

(98) Chen, X.; Chen, L.; Yao, X.; Zhang, Z.; He, C.; Zhang, J.; Chen, X. Dual Responsive Supramolecular Nanogels for Intracellular Drug Delivery. *Chem. Commun.* **2014**, *50* (29), 3789–3791. https://doi.org/10.1039/c4cc00016a.

(99) Gao, L.; Zabihi, F.; Ehrmann, S.; Hedtrich, S.; Haag, R. Supramolecular Nanogels Fabricated via Host–Guest Molecular Recognition as Penetration Enhancer for Dermal Drug Delivery. *J. Control. Release* **2019**, *300* (February), 64–72. https://doi.org/10.1016/j.jconrel.2019.02.011.

(100) Es Sayed, J.; Lorthioir, C.; Banet, P.; Perrin, P.; Sanson, N. Reversible Assembly of Microgels by Metallo-Supramolecular Chemistry. *Angew. Chemie - Int. Ed.* **2020**, *59* (18), 7042–7048. https://doi.org/10.1002/anie.201915737.

(101) Chattopadhyay, S.; Heine, E.; Mourran, A.; Richtering, W.; Keul, H.; Möller, M. Waterborne Physically Crosslinked Antimicrobial Nanogels. *Polym. Chem.* **2016**, *7* (2), 364–369. https://doi.org/10.1039/c5py01566a.

(102) Black, K. A.; Priftis, D.; Perry, S. L.; Yip, J.; Byun, W. Y.; Tirrell, M. Protein Encapsulation via Polypeptide Complex Coacervation. *ACS Macro Lett.* **2014**, *3* (10), 1088–1091. https://doi.org/10.1021/mz500529v.

(103) Perro, A.; Giraud, L.; Coudon, N.; Shanmugathasan, S.; Lapeyre, V.; Goudeau, B.; Douliez, J. P.; Ravaine, V. Self-Coacervation of Ampholyte Polymer Chains as an Efficient Encapsulation Strategy. *J. Colloid Interface Sci.* **2019**, *548*, 275–283. https://doi.org/10.1016/j.jcis.2019.04.033.

(104) Bewersdorff, T.; Gruber, A.; Eravci, M.; Dumbani, M.; Klinger, D.; Haase, A. Amphiphilic Nanogels: Influence of Surface Hydrophobicity on Protein Corona, Biocompatibility and Cellular Uptake. *Int. J. Nanomedicine* **2019**, *14*, 7861–7878. https://doi.org/10.2147/IJN.S215935.

(105) Gruber, A.; Işik, D.; Fontanezi, B. B.; Böttcher, C.; Schäfer-Korting, M.; Klinger, D. A

Versatile Synthetic Platform for Amphiphilic Nanogels with Tunable Hydrophobicity. *Polym. Chem.* **2018**, *9* (47), 5572–5584. https://doi.org/10.1039/c8py01123k.

(106) Akagi, T.; Shima, F.; Akashi, M. Intracellular Degradation and Distribution of Protein-Encapsulated Amphiphilic Poly(Amino Acid) Nanoparticles. *Biomaterials* **2011**, *32* (21), 4959–4967. https://doi.org/10.1016/j.biomaterials.2011.03.049.

(107) Krisch, E.; Messager, L.; Gyarmati, B.; Ravaine, V.; Szilágyi, A. Redox- and PH-Responsive Nanogels Based on Thiolated Poly(Aspartic Acid). *Macromol. Mater. Eng.* **2016**, *301* (3), 260–266. https://doi.org/10.1002/mame.201500119.

(108) Simonson, A. W.; Lawanprasert, A.; Goralski, T. D. P.; Keiler, K. C.; Medina, S. H. Bioresponsive Peptide-Polysaccharide Nanogels — A Versatile Delivery System to Augment the Utility of Bioactive Cargo. *Nanomedicine Nanotechnology, Biol. Med.* **2019**, *17*, 391–400. https://doi.org/10.1016/j.nano.2018.10.008.

(109) Plucinski, A.; Lyu, Z.; Schmidt, B. V. K. J. Polysaccharide Nanoparticles: From Fabrication to Applications. *J. Mater. Chem. B* **2021**, *9* (35), 7030–7062. https://doi.org/10.1039/d1tb00628b.

(110) Labie, H.; Perro, A.; Lapeyre, V.; Goudeau, B.; Catargi, B.; Auzély, R.; Ravaine, V. Sealing Hyaluronic Acid Microgels with Oppositely-Charged Polypeptides: A Simple Strategy for Packaging Hydrophilic Drugs with on-Demand Release. *J. Colloid Interface Sci.* **2019**, *535*, 16–27. https://doi.org/10.1016/j.jcis.2018.09.048.

(111) Azagarsamy, M. A.; Alge, D. L.; Radhakrishnan, S. J.; Tibbitt, M. W.; Anseth, K. S. Photocontrolled Nanoparticles for On-Demand Release of Proteins. *Biomacromolecules* **2012**, *13* (8), 2219–2224. https://doi.org/10.1021/bm300646q.

(112) Koppolu, B. prasanth; Smith, S. G.; Ravindranathan, S.; Jayanthi, S.; Suresh Kumar, T. K.; Zaharoff, D. A. Controlling Chitosan-Based Encapsulation for Protein and Vaccine Delivery. *Biomaterials* **2014**, *35* (14), 4382–4389. https://doi.org/10.1016/j.biomaterials.2014.01.078.

(113) Zhang, Y.; Zhu, W.; Wang, B.; Ding, J. A Novel Microgel and Associated Post-Fabrication Encapsulation Technique of Proteins. *J. Control. Release* **2005**, *105* (3), 260–268. https://doi.org/10.1016/j.jconrel.2005.04.001.

(114) Johansson, C.; Hansson, P.; Malmsten, M. Interaction between Lysozyme and Poly(Acrylic Acid) Microgels. *J. Colloid Interface Sci.* **2007**, *316* (2), 350–359.

https://doi.org/10.1016/j.jcis.2007.07.052.

(115) Bysell, H.; Malmsten, M. Interactions between Homopolypeptides and Lightly Cross-Linked Microgels. *Langmuir* **2009**, *25* (1), 522–528. https://doi.org/10.1021/la8029984.

(116) Coppi, G.; Iannuccelli, V.; Leo, E.; Bernabei, M. T.; Cameroni, R. Protein Immobilization in Crosslinked Alginate Microparticles. *J. Microencapsul.* **2002**, *19* (1), 37–44. https://doi.org/10.1080/02652040110055621.

(117) Li, Y.; Kleijn, M.; Slaghek, T.; Timmermans, J.; Stuart, M. C.; Norde, W. Lysozyme Uptake and Release by Oxidized Starch Polymer Microgels. *J. Control. Release* **2010**, *148* (1), 1754–1762. https://doi.org/10.1016/j.jconrel.2010.07.052.

(118) Welsch, N.; Wittemann, A.; Ballauff, M. Enhanced Activity of Enzymes Immobilized in Thermoresponsive Core-Shell Microgels. *J. Phys. Chem. B* **2009**, *113* (49), 16039–16045. https://doi.org/10.1021/jp907508w.

(119) Shao, P. G.; Bailey, L. C. Stabilization of PH-Induced Degradation of Porcine Insulin in Biodegradable Polyester Microspheres. *Pharm. Dev. Technol.* **1999**, *4* (4), 633–642. https://doi.org/10.1081/PDT-100101402.

(120) Esser-Kahn, A. P.; Odom, S. A.; Sottos, N. R.; White, S. R.; Moore, J. S. Triggered Release from Polymer Capsules. *Macromolecules* **2011**, *44* (14), 5539–5553. https://doi.org/10.1021/ma201014n.

(121) Peyratout, C. S.; Dähne, L. Tailor-Made Polyelectrolyte Microcapsules: From Multilayers to Smart Containers. *Angew. Chemie - Int. Ed.* **2004**, *43* (29), 3762–3783. https://doi.org/10.1002/anie.200300568.

(122) Gupta, N.; Kozlovskaya, V.; Dolmat, M.; Kharlampieva, E. Shape Recovery of Spherical Hydrogen-Bonded Multilayer Capsules after Osmotically Induced Deformation. *Langmuir* **2019**, *35* (33), 10910–10919. https://doi.org/10.1021/acs.langmuir.9b01795.

(123) Wang, Z.; Feng, Z.; Gao, C. Stepwise Assembly of the Same Poly Electrolytes Using Host-Guest Interaction to Obtain Microcapsules with Multiresponsive Properties. *Chem. Mater.* **2008**, *20* (13), 4194–4199. https://doi.org/10.1021/cm8003358.

(124) Städler, B.; Price, A. D.; Zelikin, A. N. A Critical Look at Multilayered Polymer Capsules in Biomedicine: Drug Carriers, Artificial Organelles, and Cell Mimics. *Adv. Funct. Mater.* **2011**, *21* (1), 14–28. https://doi.org/10.1002/adfm.201001676.

(125) De Temmerman, M. L.; Demeester, J.; De Vos, F.; De Smedt, S. C. Encapsulation

Performance of Layer-by-Layer Microcapsules for Proteins. *Biomacromolecules* **2011**, *12* (4), 1283–1289. https://doi.org/10.1021/bm101559w.

(126) Grigoriev, D. O.; Bukreeva, T.; Möhwald, H.; Shchukin, D. G. New Method for Fabrication of Loaded Micro- and Nanocontainers: Emulsion Encapsulation by Polyelectrolyte Layer-by-Layer Deposition on the Liquid Core. *Langmuir* **2008**, *24* (3), 999–1004. https://doi.org/10.1021/la702873f.

(127) Szczepanowicz, K.; Bazylińska, U.; Pietkiewicz, J.; Szyk-Warszyńska, L.; Wilk, K. A.; Warszyński, P. Biocompatible Long-Sustained Release Oil-Core Polyelectrolyte Nanocarriers: From Controlling Physical State and Stability to Biological Impact. *Adv. Colloid Interface Sci.* **2015**, *222*, 678–691. https://doi.org/10.1016/j.cis.2014.10.005.

(128) Atkin, R.; Davies, P.; Hardy, J.; Vincent, B. Preparation of Aqueous Core/Polymer Shell Microcapsules by Internal Phase Separation. *Macromolecules* **2004**, *37* (21), 7979–7985. https://doi.org/10.1021/ma048902y.

(129) Yu, X.; Zhao, Z.; Nie, W.; Deng, R.; Liu, S.; Liang, R.; Zhu, J.; Ji, X. Biodegradable Polymer Microcapsules Fabrication through a Template-Free Approach. *Langmuir* **2011**, *27* (16), 10265–10273. https://doi.org/10.1021/la201944s.

(130) Roux, R.; Sallet, L.; Alcouffe, P.; Chambert, S. P.; Sintes-Zydowicz, N.; Fleury, E.; Bernard, J. Facile and Rapid Access to Glyconanocapsules by CuAAC Interfacial Polyaddition in Miniemulsion Conditions. *ACS Macro Lett.* **2012**, *1* (8), 1074–1078. https://doi.org/10.1021/mz300281.

(131) Siebert, J. M.; Baier, G.; Musyanovych, A.; Landfester, K. Towards Copper-Free Nanocapsules Obtained by Orthogonal Interfacial "Click" Polymerization in Miniemulsion. *Chem. Commun.* **2012**, *48* (44), 5470–5472. https://doi.org/10.1039/c2cc30253e.

(132) Zhang, S.; Qin, B.; Huang, Z.; Xu, J. F.; Zhang, X. Supramolecular Emulsion Interfacial Polymerization. *ACS Macro Lett.* **2019**, *8* (2), 177–182. https://doi.org/10.1021/acsmacrolett.8b01003.

(133) Malzahn, K.; Marsico, F.; Koynov, K.; Landfester, K.; Weiss, C. K.; Wurm, F. R. Selective Interfacial Olefin Cross Metathesis for the Preparation of Hollow Nanocapsules. *ACS Macro Lett.* **2014**, *3* (1), 40–43. https://doi.org/10.1021/mz400578e.

(134) Breitenkamp, K.; Emrick, T. Novel Polymer Capsules from Amphiphilic Graft Copolymers and Cross-Metathesis. *J. Am. Chem. Soc.* **2003**, *125* (40), 12070–12071.

https://doi.org/10.1021/ja036561i.

(135) Scott, C.; Wu, D.; Ho, C. C.; Co, C. C. Liquid-Core Capsules via Interfacial Polymerization: A Free-Radical Analogy of the Nylon Rope Trick. *J. Am. Chem. Soc.* **2005**, *127* (12), 4160–4161. https://doi.org/10.1021/ja044532h.

(136) Sarkar, D.; El-Khoury, J.; Lopina, S. T.; Hu, J. An Effective Method for Preparing Polymer Nanocapsules with Hydrophobic Acrylic Shell and Hydrophilic Interior by Inverse Emulsion Radical Polymerization. *Macromolecules* **2005**, *38* (20), 8603–8605. https://doi.org/10.1021/ma050661m.

(137) Luo, Y.; Gu, H. A General Strategy for Nano-Encapsulation via Interfacially Confined Living/Controlled Radical Miniemulsion Polymerization. *Macromol. Rapid Commun.* **2006**, *27* (1), 21–25. https://doi.org/10.1002/marc.200500649.

(138) Sun, Q.; Deng, Y. In Situ Synthesis of Temperature-Sensitive Hollow Microspheres via Interfacial Polymerization. *J. Am. Chem. Soc.* **2005**, *127* (23), 8274–8275. https://doi.org/10.1021/ja051487k.

(139) Crespy, D.; Stark, M.; Hoffmann-Richter, C.; Ziener, U.; Landfester, K. Polymeric Nanoreactors for Hydrophilic Reagents Synthesized by Interfacial Polycondensation on Miniemulsion Droplets. *Macromolecules* **2007**, *40* (9), 3122–3135. https://doi.org/10.1021/ma0621932.

(140) Yiamsawas, D.; Baier, G.; Thines, E.; Landfester, K.; Wurm, F. R. Biodegradable Lignin Nanocontainers. *RSC Adv.* **2014**, *4* (23), 11661–11663. https://doi.org/10.1039/c3ra47971d.

(141) Jo, S. M.; Jiang, S.; Graf, R.; Wurm, F. R.; Landfester, K. Aqueous Core and Hollow Silica Nanocapsules for Confined Enzyme Modules. *Nanoscale* **2020**, *12* (47), 24266–24272. https://doi.org/10.1039/d0nr07148j.

(142) Monteillet, H.; Hagemans, F.; Sprakel, J. Charge-Driven Co-Assembly of Polyelectrolytes across Oil-Water Interfaces. *Soft Matter* **2013**, *9* (47), 11270–11275. https://doi.org/10.1039/c3sm52241e.

(143) Kaufman, G.; Boltyanskiy, R.; Nejati, S.; Thiam, A. R.; Loewenberg, M.; Dufresne, E. R.; Osuji, C. O. Single-Step Microfluidic Fabrication of Soft Monodisperse Polyelectrolyte Microcapsules by Interfacial Complexation. *Lab Chip* **2014**, *14* (18), 3494–3497. https://doi.org/10.1039/c4lc00482e.

(144) Ma, Q.; Song, Y.; Kim, J. W.; Choi, H. S.; Shum, H. C. Affinity Partitioning-Induced Self-

Assembly in Aqueous Two-Phase Systems: Templating for Polyelectrolyte Microcapsules. *ACS Macro Lett.* **2016**, *5* (6), 666–670. https://doi.org/10.1021/acsmacrolett.6b00228.

(145) Hann, S. D.; Niepa, T. H. R.; Stebe, K. J.; Lee, D. One-Step Generation of Cell-Encapsulating Compartments via Polyelectrolyte Complexation in an Aqueous Two Phase System. *ACS Appl. Mater. Interfaces* **2016**, *8* (38), 25603–25611. https://doi.org/10.1021/acsami.6b07939.

(146) Ma, Q.; Yuan, H.; Song, Y.; Chao, Y.; Mak, S. Y.; Shum, H. C. Partitioning-Dependent Conversion of Polyelectrolyte Assemblies in an Aqueous Two-Phase System. *Soft Matter* **2018**, *14* (9), 1552–1558. https://doi.org/10.1039/c7sm02275a.

(147) Huang, X.; Tian, L.; Wang, Z.; Zhang, J.; Chan, Y. S.; Cheng, S. H.; Yao, X. Bioinspired Robust All-Aqueous Droplet via Diffusion-Controlled Interfacial Coacervation. *Adv. Funct. Mater.* **2020**, *30* (49), 1–9. https://doi.org/10.1002/adfm.202004166.

(148) Chao, Y.; Shum, H. C. Emerging Aqueous Two-Phase Systems: From Fundamentals of Interfaces to Biomedical Applications. *Chem. Soc. Rev.* **2020**, *49* (1), 114–142. https://doi.org/10.1039/c9cs00466a.

(149) Zhang, L.; Cai, L. H.; Lienemann, P. S.; Rossow, T.; Polenz, I.; Vallmajo-Martin, Q.; Ehrbar, M.; Na, H.; Mooney, D. J.; Weitz, D. A. One-Step Microfluidic Fabrication of Polyelectrolyte Microcapsules in Aqueous Conditions for Protein Release. *Angew. Chemie - Int. Ed.* **2016**, *55* (43), 13470–13474. https://doi.org/10.1002/anie.201606960.

(150) Hann, S. D.; Stebe, K. J.; Lee, D. All-Aqueous Assemblies via Interfacial Complexation: Toward Artificial Cell and Microniche Development. *Langmuir* **2017**, *33* (39), 10107–10117. https://doi.org/10.1021/acs.langmuir.7b02237.

(151) Kim, M.; Doh, J.; Lee, D. PH-Induced Softening of Polyelectrolyte Microcapsules without Apparent Swelling. *ACS Macro Lett.* **2016**, *5* (4), 487–492. https://doi.org/10.1021/acsmacrolett.6b00124.

(152) Duan, G.; Haase, M. F.; Stebe, K. J.; Lee, D. One-Step Generation of Salt-Responsive Polyelectrolyte Microcapsules via Surfactant-Organized Nanoscale Interfacial Complexation in Emulsions (SO NICE). *Langmuir* **2018**, *34* (3), 847–853. https://doi.org/10.1021/acs.langmuir.7b01526.

(153) Zou, Y.; Song, J.; You, X.; Yao, J.; Xie, S.; Jin, M.; Wang, X.; Yan, Z.; Zhou, G.; Shui, L. Interfacial Complexation Induced Controllable Fabrication of Stable Polyelectrolyte

Microcapsules Using All-Aqueous Droplet Microfluidics for Enzyme Release. *ACS Appl. Mater. Interfaces* **2019**, *11* (23), 21227–21238. https://doi.org/10.1021/acsami.9b02788.

(154) Kim, B. J.; Han, S.; Lee, K. B.; Choi, I. S. Biphasic Supramolecular Self-Assembly of Ferric Ions and Tannic Acid across Interfaces for Nanofilm Formation. *Adv. Mater.* **2017**, *29* (28), 1–7. https://doi.org/10.1002/adma.201700784.

(155) Dupré De Baubigny, J.; Trégouët, C.; Salez, T.; Pantoustier, N.; Perrin, P.; Reyssat, M.; Monteux, C. One-Step Fabrication of PH-Responsive Membranes and Microcapsules through Interfacial H-Bond Polymer Complexation. *Sci. Rep.* **2017**, *7* (1), 1–7. https://doi.org/10.1038/s41598-017-01374-3.

(156) Wang, Y.; Chou, T.; Sukhishvili, S. A. Spontaneous, One-Pot Assembly of PH-Responsive Hydrogen-Bonded Polymer Capsules. *ACS Macro Lett.* **2016**, *5* (1), 35–39. https://doi.org/10.1021/acsmacrolett.5b00716.

(157) Trongsatitkul, T.; Budhlall, B. M. Microgels or Microcapsules? Role of Morphology on the Release Kinetics of Thermoresponsive PNIPAm-Co-PEGMa Hydrogels. *Polym. Chem.* **2013**, *4* (5), 1502–1516. https://doi.org/10.1039/c2py20889j.

(158) Gan, D.; Lyon, L. A. Tunable Swelling Kinetics in Core - Shell Hydrogel Nanoparticles. *J. Am. Chem. Soc.* **2001**, *123* (31), 7511–7517. https://doi.org/10.1021/ja010609f.

(159) Manuela Gaspar, M.; Blanco, D.; Cruz, M. E. M.; José Alonso, M. Formulation of L-Asparaginase-Loaded Poly(Lactide-Co-Glycolide) Nanoparticles: Influence of Polymer Properties on Enzyme Loading, Activity and in Vitro Release. *J. Control. Release* **1998**, *52* (1–2), 53–62. https://doi.org/10.1016/S0168-3659(97)00196-X.

(160) Pasparakis, G.; Tsitsilianis, C. LCST Polymers: Thermoresponsive Nanostructured Assemblies towards Bioapplications. *Polymer (Guildf).* **2020**, *211*, 123146. https://doi.org/10.1016/j.polymer.2020.123146.

(161) Seuring, J.; Agarwal, S. Polymers with Upper Critical Solution Temperature in Aqueous Solution. *Macromol. Rapid Commun.* **2012**, *33* (22), 1898–1920. https://doi.org/10.1002/marc.201200433.

(162) Halperin, A.; Kröger, M.; Winnik, F. M. Poly(N-Isopropylacrylamide) Phase Diagrams: Fifty Years of Research. *Angew. Chem. Int. Ed.* **2015**, *54* (51), 15342–15367. https://doi.org/10.1002/anie.201506663.

(163) Ma, Z.; Jia, X.; Hu, J.; Zhang, G.; Zhou, F.; Liu, Z.; Wang, H. Dual-Responsive Capsules

with Tunable Low Critical Solution Temperatures and Their Loading and Release Behavior. *Langmuir* **2013**, *29* (19), 5631–5637. https://doi.org/10.1021/la400025j.

(164) Hoogenboom, R.; Schlaad, H. Thermoresponsive Poly(2-Oxazoline)s, Polypeptoids, and Polypeptides. *Polym. Chem.* **2017**, *8* (1), 24–40. https://doi.org/10.1039/c6py01320a.

(165) Cortez-Lemus, N. A.; Licea-Claverie, A. Poly(N-Vinylcaprolactam), a Comprehensive Review on a Thermoresponsive Polymer Becoming Popular. *Prog. Polym. Sci.* **2016**, *53*, 1–51. https://doi.org/10.1016/j.progpolymsci.2015.08.001.

(166) Nolan, C. M.; Gelbaum, L. T.; Lyon, L. A. 1H NMR Investigation of Thermally Triggered Insulin Release from Poly(N-Isopropylacrylamide) Microgels. *Biomacromolecules* **2006**, *7* (10), 2918–2922. https://doi.org/10.1021/bm060718s.

(167) Qin, S.; Geng, Y.; Discher, D. E.; Yang, S. Temperature-Controlled Assembly and Release from Polymer Vesicles of Poly(Ethylene Oxide)-Block-Poly(N-Isopropylacrylamide). *Adv. Mater.* **2006**, *18* (21), 2905–2909. https://doi.org/10.1002/adma.200601019.

(168) Gao, H.; Yang, W.; Min, K.; Zha, L.; Wang, C.; Fu, S. Thermosensitive Poly(N-Isopropylacrylamide) Nanocapsules with Controlled Permeability. *Polymer (Guildf).* **2005**, *46*, 1087–1093. https://doi.org/10.1016/j.polymer.2004.11.078.

(169) Liu, F.; Kozlovskaya, V.; Medipelli, S.; Xue, B.; Ahmad, F.; Saeed, M.; Cropek, D.; Kharlampieva, E. Temperature-Sensitive Polymersomes for Controlled Delivery of Anticancer Drugs. *Chem. Mater.* **2015**, *27* (23), 7945–7956. https://doi.org/10.1021/acs.chemmater.5b03048.

(170) Amstad, E.; Kim, S. H.; Weitz, D. A. Photo- and Thermoresponsive Polymersomes for Triggered Release. *Angew. Chemie - Int. Ed.* **2012**, *51* (50), 12499–12503. https://doi.org/10.1002/anie.201206531.

(171) Yu, Y. L.; Zhang, M. J.; Xie, R.; Ju, X. J.; Wang, J. Y.; Pi, S. W.; Chu, L. Y. Thermo-Responsive Monodisperse Core-Shell Microspheres with PNIPAM Core and Biocompatible Porous Ethyl Cellulose Shell Embedded with PNIPAM Gates. *J. Colloid Interface Sci.* **2012**, *376* (1), 97–106. https://doi.org/10.1016/j.jcis.2012.03.028.

(172) Seuring, J.; Agarwal, S. Polymers with Upper Critical Solution Temperature in Aqueous Solution: Unexpected Properties from Known Building Blocks. *ACS Macro Lett.* **2013**, *2* (7), 597–600. https://doi.org/10.1021/mz400227y.

(173) Fu, W.; Luo, C.; Morin, E. A.; He, W.; Li, Z.; Zhao, B. UCST-Type Thermosensitive Hairy

Nanogels Synthesized by RAFT Polymerization-Induced Self-Assembly. *ACS Macro Lett.* **2017**, *6* (2), 127–133. https://doi.org/10.1021/acsmacrolett.6b00888.

(174) Wang, Y.; Hu, L.; Yin, Q.; Du, K.; Zhang, T.; Yin, Q. Multi-Responsive Hollow Nanospheres Self-Assembly by Amphiphilic Random Copolymer and Azobenzene. *Polymer (Guildf).* **2019**, *175* (April), 235–242. https://doi.org/10.1016/j.polymer.2019.04.071.

(175) Morimoto, N.; Oishi, Y.; Yamamoto, M. The Design of Sulfobetaine Polymers with Thermoresponsiveness under Physiological Salt Conditions. *Macromol. Chem. Phys.* **2020**, *221* (5), 1–7. https://doi.org/10.1002/macp.201900429.

(176) Niskanen, J.; Tenhu, H. How to Manipulate the Upper Critical Solution Temperature (UCST)? *Polym. Chem.* **2017**, *8* (1), 220–232. https://doi.org/10.1039/c6py01612j.

(177) Seuring, J.; Bayer, F. M.; Huber, K.; Agarwal, S. Upper Critical Solution Temperature of Poly(N-Acryloyl Glycinamide) in Water: A Concealed Property. *Macromolecules* **2012**, *45* (1), 374–384. https://doi.org/10.1021/ma202059t.

(178) Yu, X.; Liu, J.; Xin, Y.; Zhan, M.; Xiao, J.; Lu, L.; Peng, S. Temperature and Salt Responsive Zwitterionic Polysulfamide-Based Nanogels with Surface Regeneration Ability and Controlled Drug Release. *Polym. Chem.* **2019**, *10* (47), 6423–6431. https://doi.org/10.1039/c9py01548e.

(179) Maji, T.; Banerjee, S.; Biswas, Y.; Mandal, T. K. Dual-Stimuli-Responsive L-Serine-Based Zwitterionic UCST-Type Polymer with Tunable Thermosensitivity. *Macromolecules* **2015**, *48* (14), 4957–4966. https://doi.org/10.1021/acs.macromol.5b01099.

(180) Seuring, J.; Agarwal, S. First Example of a Universal and Cost-Effective Approach: Polymers with Tunable Upper Critical Solution Temperature in Water and Electrolyte Solution. *Macromolecules* **2012**, *45* (9), 3910–3918. https://doi.org/10.1021/ma300355k.

(181) Asadujjaman, A.; Kent, B.; Bertin, A. Phase Transition and Aggregation Behaviour of an UCST-Type Copolymer Poly(Acrylamide-Co-Acrylonitrile) in Water: Effect of Acrylonitrile Content, Concentration in Solution, Copolymer Chain Length and Presence of Electrolyte. *Soft Matter* **2017**, *13* (3), 658–669. https://doi.org/10.1039/c6sm02262f.

(182) Bordat, A.; Soliman, N.; Ben Chraït, I.; Manerlax, K.; Yagoubi, N.; Boissenot, T.; Nicolas, J.; Tsapis, N. The Crucial Role of Macromolecular Engineering, Drug Encapsulation and Dilution on the Thermoresponsiveness of UCST Diblock Copolymer Nanoparticles Used

for Hyperthermia. *Eur. J. Pharm. Biopharm.* **2019**, *142* (June), 281–290. https://doi.org/10.1016/j.ejpb.2019.07.001.

(183) Augé, A.; Fortin, D.; Tong, X.; Zhao, Y. Nanogel-like UCST Triblock Copolymer Micelles Showing Large Volume Expansion before Abrupt Dissolution. *Polym. Chem.* **2018**, *9* (37), 4660–4673. https://doi.org/10.1039/c8py00960k.

(184) Echeverria, C.; López, D.; Mijangos, C. UCST Responsive Microgels of Poly(Acrylamide-Acrylic Acid) Copolymers: Structure and Viscoelastic Properties. *Macromolecules* **2009**, *42* (22), 9118–9123. https://doi.org/10.1021/ma901316k.

(185) Wolf, T.; Rheinberger, T.; Simon, J.; Wurm, F. R. Reversible Self-Assembly of Degradable Polymersomes with Upper Critical Solution Temperature in Water. **2017**. https://doi.org/10.1021/jacs.7b02723.

(186) Huang, X.; Mutlu, H.; Lin, S.; Theato, P. Oxygen-Switchable Thermo-Responsive Polymers with Unprecedented UCST in Water. *Eur. Polym. J.* **2021**, *142* (August 2020), 110156. https://doi.org/10.1016/j.eurpolymj.2020.110156.

(187) Bertrand, O.; Gohy, J. F. Photo-Responsive Polymers: Synthesis and Applications. *Polym. Chem.* **2017**, *8* (1), 52–73. https://doi.org/10.1039/c6py01082b.

(188) Patnaik, S.; Sharma, A. K.; Garg, B. S.; Gandhi, R. P.; Gupta, K. C. Photoregulation of Drug Release in Azo-Dextran Nanogels. *Int. J. Pharm.* **2007**, *342* (1–2), 184–193. https://doi.org/10.1016/j.ijpharm.2007.04.038.

(189) Lin, H.; Xiao, W.; Qin, S. Y.; Cheng, S. X.; Zhang, X. Z. Switch on/off Microcapsules for Controllable Photosensitive Drug Release in a “release-Cease-Recommence” Mode. *Polym. Chem.* **2014**, *5* (15), 4437–4440. https://doi.org/10.1039/c4py00564c.

(190) Wang, X.; Hu, J.; Liu, G.; Tian, J.; Wang, H.; Gong, M.; Liu, S. Reversibly Switching Bilayer Permeability and Release Modules of Photochromic Polymersomes Stabilized by Cooperative Noncovalent Interactions. *J. Am. Chem. Soc.* **2015**, *137* (48), 15262–15275. https://doi.org/10.1021/jacs.5b10127.

(191) Rifaie-Graham, O.; Ulrich, S.; Galensowske, N. F. B.; Balog, S.; Chami, M.; Rentsch, D.; Hemmer, J. R.; Read De Alaniz, J.; Boesel, L. F.; Bruns, N. Wavelength-Selective Light-Responsive DASA-Functionalized Polymersome Nanoreactors. *J. Am. Chem. Soc.* **2018**, *140* (25), 8027–8036. https://doi.org/10.1021/jacs.8b04511.

(192) Lin, L.; Yan, Z.; Gu, J.; Zhang, Y.; Feng, Z.; Yu, Y. UV-Responsive Behavior of

Azopyridine-Containing Diblock Copolymeric Vesicles: Photoinduced Fusion, Disintegration and Rearrangement. *Macromol. Rapid Commun.* **2009**, *30* (13), 1089–1093. https://doi.org/10.1002/marc.200900105.

(193) Mabrouk, E.; Cuvelier, D.; Brochard-Wyart, F.; Nassoy, P.; Li, M. H. Bursting of Sensitive Polymersomes Induced by Curling. *Proc. Natl. Acad. Sci. U. S. A.* **2009**, *106* (18), 7294–7298. https://doi.org/10.1073/pnas.0813157106.

(194) Han, D.; Tong, X.; Zhao, Y. Fast Photodegradable Block Copolymer Micelles for Burst Release. *Macromolecules* **2011**, *44* (3), 437–439. https://doi.org/10.1021/ma102778d.

(195) Cabane, E.; Malinova, V.; Meier, W. Synthesis of Photocleavable Amphiphilic Block Copolymers: Toward the Design of Photosensitive Nanocarriers. *Macromol. Chem. Phys.* **2010**, *211* (17), 1847–1856. https://doi.org/10.1002/macp.201000151.

(196) Lee, J. S.; Deng, X.; Han, P.; Cheng, J. Dual Stimuli-Responsive Poly(β-Amino Ester) Nanoparticles for On-Demand Burst Release. *Macromol. Biosci.* **2015**, *15* (9), 1314–1322. https://doi.org/10.1002/mabi.201500111.

(197) Cao, Z.; Li, Q.; Wang, G. Photodegradable Polymer Nanocapsules Fabricated from Dimethyldiethoxysilane Emulsion Templates for Controlled Release. *Polym. Chem.* **2017**, *8* (44), 6817–6823. https://doi.org/10.1039/c7py01153a.

(198) Zhu, K.; Liu, G.; Zhang, G.; Hu, J.; Liu, S. Engineering Cross-Linkable Plasmonic Vesicles for Synergistic Chemo-Photothermal Therapy Using Orthogonal Light Irradiation. *Macromolecules* **2018**, *51* (21), 8530–8538. https://doi.org/10.1021/acs.macromol.8b01653.

(199) Fomina, N.; McFearin, C.; Sermsakdi, M.; Edigin, O.; Almutairi, A. UV and Near-IR Triggered Release from Polymeric Nanoparticles. *J. Am. Chem. Soc.* **2010**, *132* (28), 9540–9542. https://doi.org/10.1021/ja102595j.

(200) Liu, G.; Wang, X.; Hu, J.; Zhang, G.; Liu, S. Self-Immolative Polymersomes for High-Efficiency Triggered Release and Programmed Enzymatic Reactions. *J. Am. Chem. Soc.* **2014**, *136* (20), 7492–7497. https://doi.org/10.1021/ja5030832.

(201) Peyret, A.; Ibarboure, E.; Tron, A.; Beauté, L.; Rust, R.; Sandre, O.; McClenaghan, N. D.; Lecommandoux, S. Polymersome Popping by Light-Induced Osmotic Shock under Temporal, Spatial, and Spectral Control. *Angew. Chemie - Int. Ed.* **2017**, *56* (6), 1566–1570. https://doi.org/10.1002/anie.201609231.

(202) Paret, N.; Trachsel, A.; Berthier, D. L.; Herrmann, A. Controlled Release of Encapsulated Bioactive Volatiles by Rupture of the Capsule Wall through the Light-Induced Generation of a Gas. *Angew. Chemie - Int. Ed.* **2015**, *54* (7), 2275–2279. https://doi.org/10.1002/anie.201410778.

(203) Brongersma, M. L.; Halas, N. J.; Nordlander, P. Plasmon-Induced Hot Carrier Science and Technology. *Nat. Nanotechnol.* **2015**, *10* (1), 25–34. https://doi.org/10.1038/nnano.2014.311.

(204) Baffou, G. *Thermoplasmonics: Heating Metal Nanoparticles Using Light*; Cambridge University Press, 2017. https://doi.org/10.1017/9781108289801.

(205) Liz-Marzan, L. M. Tailoring Surface Plasmons through the Morphology and Assembly of Metal Nanoparticles. *Langmuir* **2006**, *22* (1), 32–41.

(206) Baffou, G.; Quidant, R.; Girard, C. Heat Generation in Plasmonic Nanostructures: Influence of Morphology. *Appl. Phys. Lett.* **2009**, *94* (15). https://doi.org/10.1063/1.3116645.

(207) Jacques, S. L. Optical Properties of Biological Tissues: A Review. *Phys. Med. Biol.* **2013**, *58* (14), 5007–5008. https://doi.org/10.1088/0031-9155/58/14/5007.

(208) Mathiyazhakan, M.; Wiraja, C.; Xu, C. A Concise Review of Gold Nanoparticles-Based Photo-Responsive Liposomes for Controlled Drug Delivery. *Nano-Micro Lett.* **2018**, *10* (1), 1–10. https://doi.org/10.1007/s40820-017-0166-0.

(209) Disalvo, G. M.; Robinson, A. R.; Aly, M. S.; Hoglund, E. R.; O'malley, S. M.; Griepenburg, J. C. Polymersome Poration and Rupture Mediated by Plasmonic Nanoparticles in Response to Single-Pulse Irradiation. *Polymers (Basel).* **2020**, *12* (10), 1–14. https://doi.org/10.3390/polym12102381.

(210) Radt, B.; Smith, T. A.; Caruso, F. Optically Addressable Nanostructured Capsules. *Adv. Mater.* **2004**, *16* (23–24), 2184–2189. https://doi.org/10.1002/adma.200400920.

(211) Shao, J.; Xuan, M.; Si, T.; Dai, L.; He, Q. Biointerfacing Polymeric Microcapsules for in Vivo Near-Infrared Light-Triggered Drug Release. *Nanoscale* **2015**, *7* (45), 19092–19098. https://doi.org/10.1039/c5nr06350g.

(212) Lee, M. H.; Hribar, K. C.; Brugarolas, T.; Kamat, N. P.; Burdick, J. A.; Lee, D. Harnessing Interfacial Phenomena to Program the Release Properties of Hollow Microcapsules. *Adv. Funct. Mater.* **2012**, *22* (1), 131–138. https://doi.org/10.1002/adfm.201101303.

(213) Sershen, S. R.; Westcott, S. L.; Halas, N. J.; West, J. L. Temperature-Sensitive Polymer-

Nanoshell Composites for Photothermally Modulated Drug Delivery. *J. Biomed. Mater. Res.* **2000**, *51* (3), 293–298. https://doi.org/10.1002/1097-4636(20000905)51:3<293::AID-JBM1>3.0.CO;2-T.

(214) Kang, H.; Trondoli, A. C.; Zhu, G.; Chen, Y.; Chang, Y. J.; Liu, H.; Huang, Y. F.; Zhang, X.; Tan, W. Near-Infrared Light-Responsive Core-Shell Nanogels for Targeted Drug Delivery. *ACS Nano* **2011**, *5* (6), 5094–5099. https://doi.org/10.1021/nn201171r.

(215) Jeong, W. C.; Kim, S. H.; Yang, S. M. Photothermal Control of Membrane Permeability of Microcapsules for On-Demand Release. *ACS Appl. Mater. Interfaces* **2014**, *6* (2), 826–832. https://doi.org/10.1021/am4037993.

(216) Hui, L.; Qin, S.; Yang, L. Upper Critical Solution Temperature Polymer, Photothermal Agent, and Erythrocyte Membrane Coating: An Unexplored Recipe for Making Drug Carriers with Spatiotemporally Controlled Cargo Release. *ACS Biomater. Sci. Eng.* **2016**, *2* (12), 2127–2132. https://doi.org/10.1021/acsbiomaterials.6b00459.

(217) Lin, Y. C.; Fang, T. Y.; Kao, H. Y.; Tseng, W. C. Nanoassembly of UCST Polypeptide for NIR-Modulated Drug Release. *Biochem. Eng. J.* **2021**, *176*, 108194. https://doi.org/10.1016/j.bej.2021.108194.

(218) Huang, X.; Brazel, C. S. On the Importance and Mechanisms of Burst Release in Matrix-Controlled Drug Delivery Systems. *J. Control. Release* **2001**, *73* (2–3), 121–136. https://doi.org/10.1016/S0168-3659(01)00248-6.

(219) Mai, X.; Chang, Y.; You, Y.; He, L.; Chen, T. Designing Intelligent Nano-Bomb with on-Demand Site-Specific Drug Burst Release to Synergize with High-Intensity Focused Ultrasound Cancer Ablation. *J. Control. Release* **2021**, *331* (September 2020), 270–281. https://doi.org/10.1016/j.jconrel.2020.09.051.

(220) Zhu, T. F.; Szostak, J. W. Exploding Vesicles. *J. Syst. Chem.* **2011**, *2* (1), 2–7. https://doi.org/10.1186/1759-2208-2-4.

(221) Zhang, W.; Qu, L.; Pei, H.; Qin, Z.; Didier, J.; Wu, Z.; Bobe, F.; Ingber, D. E.; Weitz, D. A. Controllable Fabrication of Inhomogeneous Microcapsules for Triggered Release by Osmotic Pressure. *Small* **2019**, *15* (42), 1–7. https://doi.org/10.1002/smll.201903087.

(222) Liu, L.; Wang, W.; Ju, X. J.; Xie, R.; Chu, L. Y. Smart Thermo-Triggered Squirting Capsules for Nanoparticle Delivery. *Soft Matter* **2010**, *6* (16), 3759–3763. https://doi.org/10.1039/c002231d.

(223) Sankaranarayanan, J.; Mahmoud, E. a; Kim, G.; Morachis, M.; Almutairi, A. Multiresponse Strategies To Modulate Nanoparticles. *ACS Nano* **2010**, *4* (10), 5930–5936.

(224) Scott, R. L. The Solubility of Fluorocarbons. *J. Am. Chem. Soc.* **1948**, *70* (12), 4090–4093. https://doi.org/10.1021/ja01192a036.

(225) Bai, Y.; He, X.; Liu, D.; Patil, S. N.; Bratton, D.; Huebner, A.; Hollfelder, F.; Abell, C.; Huck, W. T. S. A Double Droplet Trap System for Studying Mass Transport across a Droplet-Droplet Interface. *Lab Chip* **2010**, *10* (10), 1281–1285. https://doi.org/10.1039/b925133b.

(226) Gruner, P.; Riechers, B.; Chacòn Orellana, L. A.; Brosseau, Q.; Maes, F.; Beneyton, T.; Pekin, D.; Baret, J. C. Stabilisers for Water-in-Fluorinated-Oil Dispersions: Key Properties for Microfluidic Applications. *Curr. Opin. Colloid Interface Sci.* **2015**, *20* (3), 183–191. https://doi.org/10.1016/j.cocis.2015.07.005.

(227) Lowe, K. C.; Davey, M. R.; Power, J. B. Perfluorochemicals: Their Applications and Benefits to Cell Culture. *Trends Biotechnol.* **1998**, *16* (6), 272–277. https://doi.org/10.1016/S0167-7799(98)01205-0.

(228) Giaever, I.; Keese, C. R. Behavior of Cells at Fluid Interfaces. *Proc. Natl. Acad. Sci. U. S. A.* **1983**, *80* (1 I), 219–222. https://doi.org/10.1073/pnas.80.1.219.

(229) Lowe, K. C. Fluorinated Blood Substitutes and Oxygen Carriers. *J. Fluor. Chem.* **2001**, *109* (1), 59–65. https://doi.org/10.1016/S0022-1139(01)00374-8.

(230) Roach, L. S.; Song, H.; Ismagilov, R. F. Controlling Nonspecific Protein Adsorption in a Plug-Based Microfluidic System by Controlling Interfacial Chemistry Using Fluorous-Phase Surfactants. *Anal. Chem.* **2005**, *77* (3), 785–796. https://doi.org/10.1021/ac049061w.

(231) Holtze, C.; Rowat, A. C.; Agresti, J. J.; Hutchison, J. B.; Angilè, F. E.; Schmitz, C. H. J.; Köster, S.; Duan, H.; Humphry, K. J.; Scanga, R. A.; Johnson, J. S.; Pisignano, D.; Weitz, D. A. Biocompatible Surfactants for Water-in-Fluorocarbon Emulsions. *Lab Chip* **2008**, *8* (10), 1632–1639. https://doi.org/10.1039/b806706f.

(232) Wagner, O.; Thiele, J.; Weinhart, M.; Mazutis, L.; Weitz, D. A.; Huck, W. T. S.; Haag, R. Biocompatible Fluorinated Polyglycerols for Droplet Microfluidics as an Alternative to PEG-Based Copolymer Surfactants. *Lab Chip* **2016**, *16* (1), 65–69. https://doi.org/10.1039/c5lc00823a.

(233) Dejournette, C. J.; Kim, J.; Medlen, H.; Li, X.; Vincent, L. J.; Easley, C. J. Creating

Biocompatible Oil-Water Interfaces without Synthesis: Direct Interactions between Primary Amines and Carboxylated Perfluorocarbon Surfactants. *Anal. Chem.* **2013**, *85* (21), 10556–10564. https://doi.org/10.1021/ac4026048.

(234) O'Neal, K. L.; Geib, S.; Weber, S. G. Extraction of Pyridines into Fluorous Solvents Based on Hydrogen Bond Complex Formation with Carboxylic Acid Receptors. *Anal. Chem.* **2007**, *79* (8), 3117–3125. https://doi.org/10.1021/ac062287+.

(235) O'Neal, K. L.; Weber, S. G. Molecular and Ionic Hydrogen Bond Formation in Fluorous Solvents. *J. Phys. Chem. B* **2009**, *113* (1), 149–158. https://doi.org/10.1021/jp8084155.

(236) Parker, R. M.; Zhang, J.; Zheng, Y.; Coulston, R. J.; Smith, C. A.; Salmon, A. R.; Yu, Z.; Scherman, O. A.; Abell, C. Electrostatically Directed Self-Assembly of Ultrathin Supramolecular Polymer Microcapsules. *Adv. Funct. Mater.* **2015**, *25* (26), 4091–4100. https://doi.org/10.1002/adfm.201501079.

(237) Yu, Z.; Zhang, J.; Coulston, R. J.; Parker, R. M.; Biedermann, F.; Liu, X.; Scherman, O. A.; Abell, C. Supramolecular Hydrogel Microcapsules via Cucurbit[8]Uril Host-Guest Interactions with Triggered and UV-Controlled Molecular Permeability. *Chem. Sci.* **2015**, *6* (8), 4929–4933. https://doi.org/10.1039/c5sc01440a.

(238) Dalier, F.; Eghiaian, F.; Scheuring, S.; Marie, E.; Tribet, C. Temperature-Switchable Control of Ligand Display on Adlayers of Mixed Poly(Lysine)-g-(PEO) and Poly(Lysine)-g-(Ligand-Modified Poly-N-Isopropylacrylamide). *Biomacromolecules* **2016**, *17* (5), 1727–1736. https://doi.org/10.1021/acs.biomac.6b00136.

(239) Doan, V.; Köppe, R.; Kasai, P. H. Dimerization of Carboxylic Acids and Salts: An IR Study in Perfluoropolyether Media. *J. Am. Chem. Soc.* **1997**, *119* (41), 9810–9815. https://doi.org/10.1021/ja970304u.

(240) Boswell, P. G.; Lugert, E. C.; Rábai, J.; Amin, E. A.; Bühlmann, P. Coordinative Properties of Highly Fluorinated Solvents with Amino and Ether Groups. *J. Am. Chem. Soc.* **2005**, *127* (48), 16976–16984. https://doi.org/10.1021/ja055816k.

(241) Riechers, B. Dynamics of Surfactants at Soft Interfaces Using Droplet-Based Microfluidics Dissertation Birte Riechers. *PhD thesis* **2015**.

(242) Riechers, B.; Maes, F.; Akoury, E.; Semin, B.; Gruner, P.; Baret, J. C. Surfactant Adsorption Kinetics in Microfluidics. *Proc. Natl. Acad. Sci. U. S. A.* **2016**, *113* (41), 11465–11470. https://doi.org/10.1073/pnas.1604307113.

(243) Csucs, G.; Michel, R.; Lussi, J. W.; Textor, M.; Danuser, G. Microcontact Printing of Novel Co-Polymers in Combination with Proteins for Cell-Biological Applications. *Biomaterials* **2003**, *24* (10), 1713–1720. https://doi.org/10.1016/S0142-9612(02)00568-9.

(244) Van Dongen, S. F. M.; Maiuri, P.; Marie, E.; Tribet, C.; Piel, M. Triggering Cell Adhesion, Migration or Shape Change with a Dynamic Surface Coating. *Adv. Mater.* **2013**, *25* (12), 1687–1691. https://doi.org/10.1002/adma.201204474.

(245) Gruner, P.; Riechers, B.; Semin, B.; Lim, J.; Johnston, A.; Short, K.; Baret, J. C. Controlling Molecular Transport in Minimal Emulsions. *Nat. Commun.* **2016**, *7*. https://doi.org/10.1038/ncomms10392.

(246) Etienne, G.; Vian, A.; Biočanin, M.; Deplancke, B.; Amstad, E. Cross-Talk between Emulsion Drops: How Are Hydrophilic Reagents Transported across Oil Phases? *Lab Chip* **2018**, *18* (24), 3903–3912. https://doi.org/10.1039/c8lc01000e.

(247) Ali, S.; Prabhu, V. Relaxation Behavior by Time-Salt and Time-Temperature Superpositions of Polyelectrolyte Complexes from Coacervate to Precipitate. *Gels* **2018**, *4* (1), 11. https://doi.org/10.3390/gels4010011.

(248) Sing, C. E.; Perry, S. L. Recent Progress in the Science of Complex Coacervation. *Soft Matter* **2020**, *16* (12), 2885–2914. https://doi.org/10.1039/d0sm00001a.

(249) Chen, Y.; Yang, M.; Schlenoff, J. B. Glass Transitions in Hydrated Polyelectrolyte Complexes. *Macromolecules* **2021**, *54* (8), 3822–3831. https://doi.org/10.1021/acs.macromol.0c02682.

(250) Hawe, A.; Sutter, M.; Jiskoot, W. Extrinsic Fluorescent Dyes as Tools for Protein Characterization. *Pharm. Res.* **2008**, *25* (7), 1487–1499. https://doi.org/10.1007/s11095-007-9516-9.

(251) Gasymov, O. K.; Glasgow, B. J. ANS Fluorescence: Potential to Augment the Identification of the External Binding Sites of Proteins. *Biochim. Biophys. Acta - Proteins Proteomics* **2007**, *1774* (3), 403–411. https://doi.org/10.1016/j.bbapap.2007.01.002.

(252) Winnik, F. M.; Regismond, S. T. A. Fluorescence Methods in the Study of the Interactions of Surfactants with Polymers. *Colloids Surfaces A Physicochem. Eng. Asp.* **1996**, *118* (1–2), 1–39. https://doi.org/10.1016/0927-7757(96)03733-8.

(253) Hirokawa, Y.; Jinnai, H.; Nishikawa, Y.; Okamoto, T.; Hashimoto, T. Direct Observation of Internal Structures in Poly(N-Isopropylacrylamide) Chemical Gels. *Macromolecules*

1999, *32* (21), 7093–7099. https://doi.org/10.1021/ma990437v.

(254) Liu, X.; Gao, H.; Huang, F.; Pei, X.; An, Y.; Zhang, Z.; Shi, L. Structure Change of Mixed Shell Polymeric Micelles and Its Interaction with Bio-Targets as Probed by the 1-Anilino-8-Naphthalene Sulfonate (ANS) Fluorescence. *Polymer (Guildf).* **2013**, *54* (14), 3633–3640. https://doi.org/10.1016/j.polymer.2013.05.001.

(255) Pramanik, P.; Ghosh, S. Thermoresponsive Polymersome from a Double Hydrophilic Block Copolymer. *J. Polym. Sci. Part A Polym. Chem.* **2015**, *53* (21), 2444–2451. https://doi.org/10.1002/pola.27735.

(256) Longmire, M. R.; Ogawa, M.; Hama, Y.; Kosaka, N.; Regino, C. A. S.; Choyke, P. L.; Kobayashi, H. Determination of Optimal Rhodamine Fiuorophore for in Vivo Optical Imaging. *Bioconjug. Chem.* **2008**, *19* (8), 1735–1742. https://doi.org/10.1021/bc800140c.

(257) Quérard, J.; Zhang, R.; Kelemen, Z.; Plamont, M. A.; Xie, X.; Chouket, R.; Roemgens, I.; Korepina, Y.; Albright, S.; Ipendey, E.; Volovitch, M.; Sladitschek, H. L.; Neveu, P.; Gissot, L.; Gautier, A.; Faure, J. D.; Croquette, V.; Le Saux, T.; Jullien, L. Resonant Out-of-Phase Fluorescence Microscopy and Remote Imaging Overcome Spectral Limitations. *Nat. Commun.* **2017**, *8* (1), 1–8. https://doi.org/10.1038/s41467-017-00847-3.

(258) Bédard, M. F.; Munoz-Javier, A.; Mueller, R.; Del Pino, P.; Fery, A.; Parak, W. J.; Skirtach, A. G.; Sukhorukov, G. B. On the Mechanical Stability of Polymeric Microcontainers Functionalized with Nanoparticles. *Soft Matter* **2009**, *5* (1), 148–155. https://doi.org/10.1039/b812553h.

(259) Fu, J.; Liang, L.; Qiu, L. In Situ Generated Gold Nanoparticle Hybrid Polymersomes for Water-Soluble Chemotherapeutics: Inhibited Leakage and PH-Responsive Intracellular Release. *Adv. Funct. Mater.* **2017**, *27* (18). https://doi.org/10.1002/adfm.201604981.

(260) Hasan, A. S.; Socha, M.; Lamprecht, A.; Ghazouani, F. El; Sapin, A.; Hoffman, M.; Maincent, P.; Ubrich, N. Effect of the Microencapsulation of Nanoparticles on the Reduction of Burst Release. *Int. J. Pharm.* **2007**, *344* (1–2), 53–61. https://doi.org/10.1016/j.ijpharm.2007.05.066.

(261) Katagiri, K.; Imai, Y.; Koumoto, K. Variable On-Demand Release Function of Magnetoresponsive Hybrid Capsules. *J. Colloid Interface Sci.* **2011**, *361* (1), 109–114. https://doi.org/10.1016/j.jcis.2011.05.035.

(262) Wu, T.; Ge, Z.; Liu, S. Fabrication of Thermoresponsive Cross-Linked Poly(N-

Isopropylacrylamide) Nanocapsules and Silver Nanoparticle-Embedded Hybrid Capsules with Controlled Shell Thickness. *Chem. Mater.* **2011**, *23* (9), 2370–2380. https://doi.org/10.1021/cm200102g.

(263) Shi, S.; Chang, C.; Wang, T.; Ren, S.; Gao, Y.; Wang, N. A Novel Route to the Preparation of Polymer Hollow Particles Decorated with Gold Nanoparticles in the Shell. *J. Polym. Res.* **2015**, *22* (1). https://doi.org/10.1007/s10965-014-0632-z.

(264) Yun, G.; Hassan, Z.; Lee, J.; Kim, J.; Lee, N. S.; Kim, N. H.; Baek, K.; Hwang, I.; Park, C. G.; Kim, K. Highly Stable, Water-Dispersible Metal-Nanoparticle-Decorated Polymer Nanocapsules and Their Catalytic Applications. *Angew. Chemie - Int. Ed.* **2014**, *53* (25), 6414–6418. https://doi.org/10.1002/anie.201403438.

(265) Liu, D.; Jiang, X.; Yin, J. One-Step Interfacial Thiol-Ene Photopolymerization for Metal Nanoparticle-Decorated Microcapsules (MNP@MCs). *Langmuir* **2014**, *30* (24), 7213–7220.

(266) Shi, S.; Wang, Q.; Wang, T.; Ren, S.; Gao, Y.; Wang, N. Thermo-, PH-, and Light-Responsive Poly(N -Isopropylacrylamide- Co -Methacrylic Acid)-Au Hybrid Microgels Prepared by the in Situ Reduction Method Based on Au-Thiol Chemistry. *J. Phys. Chem. B* **2014**, *118* (25), 7177–7186. https://doi.org/10.1021/jp5027477.

(267) Hitchcock, J. P.; Tasker, A. L.; Stark, K.; Leeson, A.; Baxter, E. A.; Biggs, S.; Cayre, O. J. Adsorption of Catalytic Nanoparticles onto Polymer Substrates for Controlled Deposition of Microcapsule Metal Shells. *Langmuir* **2018**, *34* (4), 1473–1480. https://doi.org/10.1021/acs.langmuir.7b02874.

(268) Gorelikov, I.; Field, L. M.; Kumacheva, E. Hybrid Microgels Photoresponsive in the Near-Infrared Spectral Range. *J. Am. Chem. Soc.* **2004**, *126* (49), 15938–15939. https://doi.org/10.1021/ja0448869.

(269) Das, M.; Mordoukhovski, L.; Kumacheva, E. Sequestering Gold Nanorods by Polymer Microgels. *Adv. Mater.* **2008**, *20* (12), 2371–2375. https://doi.org/10.1002/adma.200702860.

(270) De Geest, B. G.; Skirtach, A. G.; De Beer, T. R. M.; Sukhorukov, G. B.; Bracke, L.; Baeyens, W. R. G.; Demeester, J.; De Smedt, S. C. Stimuli-Responsive Multilayered Hybrid Nanoparticle/Polyelectrolyte Capsules. *Macromol. Rapid Commun.* **2007**, *28* (1), 88–95. https://doi.org/10.1002/marc.200600631.

(271) Chen, T.; Colver, P. J.; Bon, S. A. F. Organic-Inorganic Hybrid Hollow Spheres Prepared from TiO 2-Stabilized Pickering Emulsion Polymerization. *Adv. Mater.* **2007**, *19* (17), 2286–2289. https://doi.org/10.1002/adma.200602447.

(272) Tian, J.; Yuan, L.; Zhang, M.; Zheng, F.; Xiong, Q.; Zhao, H. Interface-Directed Self-Assembly of Gold Nanoparticles and Fabrication of Hybrid Hollow Capsules by Interfacial Cross-Linking Polymerization. *Langmuir* **2012**, *28* (25), 9365–9371. https://doi.org/10.1021/la301453n.

(273) Wu, Y.; Shen, J.; Larcinese-Hafner, V.; Erni, P.; Ouali, L. Hybrid Microcapsules with Tunable Properties: Via Pickering Emulsion Templates for the Encapsulation of Bioactive Volatiles. *RSC Adv.* **2016**, *6* (104), 102595–102602. https://doi.org/10.1039/c6ra21338c.

(274) Doyen, M.; Goole, J.; Bartik, K.; Bruylants, G. Amino Acid Induced Fractal Aggregation of Gold Nanoparticles: Why and How. *J. Colloid Interface Sci.* **2016**, *464*, 160–166. https://doi.org/10.1016/j.jcis.2015.11.017.

(275) Kenausis, G. L.; Vörös, J.; Elbert, D. L.; Huang, N.; Hofer, R.; Ruiz-Taylor, L.; Textor, M.; Hubbell, J. A.; Spencer, N. D. Poly(L-Lysine)-g-Poly(Ethylene Glycol) Layers on Metal Oxide Surfaces: Attachment Mechanism and Effects of Polymer Architecture on Resistance to Protein Adsorption. *J. Phys. Chem. B* **2000**, *104* (14), 3298–3309. https://doi.org/10.1021/jp993359m.

(276) Singh, H. D.; Wang, G.; Uludağ, H.; Unsworth, L. D. Poly-L-Lysine-Coated Albumin Nanoparticles: Stability, Mechanism for Increasing in Vitro Enzymatic Resilience, and SiRNA Release Characteristics. *Acta Biomater.* **2010**, *6* (11), 4277–4284. https://doi.org/10.1016/j.actbio.2010.06.017.

(277) Louguet, S.; Kumar, A. C.; Sigaud, G.; Duguet, E.; Lecommandoux, S.; Schatz, C. A Physico-Chemical Investigation of Poly(Ethylene Oxide)-Block-Poly(l-Lysine) Copolymer Adsorption onto Silica Nanoparticles. *J. Colloid Interface Sci.* **2011**, *359* (2), 413–422. https://doi.org/10.1016/j.jcis.2011.03.093.

(278) Malinge, J.; Mousseau, F.; Zanchi, D.; Brun, G.; Tribet, C.; Marie, E. Tailored Stimuli-Responsive Interaction between Particles Adjusted by Straightforward Adsorption of Mixed Layers of Poly(Lysine)-g-PEG and Poly(Lysine)-g-PNIPAM on Anionic Beads. *J. Colloid Interface Sci.* **2016**, *461*, 50–55. https://doi.org/10.1016/j.jcis.2015.09.016.

(279) Wang, X. D.; Wolfbeis, O. S.; Meier, R. J. Luminescent Probes and Sensors for

Temperature. *Chem. Soc. Rev.* **2013**, *42* (19), 7834–7869. https://doi.org/10.1039/c3cs60102a.

(280) Baffou, G. Quantitative Phase Microscopy Using Quadriwave Lateral Shearing Interferometry (QLSI): Principle, Terminology, Algorithm and Grating Shadow Description. *J. Phys. D. Appl. Phys.* **2021**, *54* (29). https://doi.org/10.1088/1361-6463/abfbf9.

(281) Bon, P.; Lécart, S.; Fort, E.; Lévêque-Fort, S. Fast Label-Free Cytoskeletal Network Imaging in Living Mammalian Cells. *Biophys. J.* **2014**, *106* (8), 1588–1595. https://doi.org/10.1016/j.bpj.2014.02.023.

(282) Park, Y. K.; Depeursinge, C.; Popescu, G. Quantitative Phase Imaging in Biomedicine. *Nat. Photonics* **2018**, *12* (10), 578–589. https://doi.org/10.1038/s41566-018-0253-x.

(283) Baffou, G.; Bon, P.; Savatier, J.; Polleux, J.; Zhu, M.; Merlin, M.; Rigneault, H.; Monneret, S. Thermal Imaging of Nanostructures by Quantitative Optical Phase Analysis. *ACS Nano* **2012**, *6* (3), 2452–2458. https://doi.org/10.1021/nn2047586.

(284) Mann, C. J.; Yu, L.; Lo, C.-M.; Kim, M. K. High-Resolution Quantitative Phase-Contrast Microscopy by Digital Holography. *Opt. Express* **2005**, *13* (22), 8693. https://doi.org/10.1364/opex.13.008693.

(285) Bon, P.; Maucort, G.; Wattellier, B.; Monneret, S. Quadriwave Lateral Shearing Interferometry for Quantitative Phase Microscopy of Living Cells. *Opt. Express* **2009**, *17* (15), 13080. https://doi.org/10.1364/oe.17.013080.

(286) Khadir, S.; Andrén, D.; Chaumet, P. C.; Monneret, S.; Bonod, N.; Käll, M.; Sentenac, A.; Baffou, G. Full Optical Characterization of Single Nanoparticles Using Quantitative Phase Imaging. *Optica* **2020**, *7* (3), 243. https://doi.org/10.1364/optica.381729.

(287) Bon, P.; Belaid, N.; Lagrange, D.; Bergaud, C.; Rigneault, H.; Monneret, S.; Baffou, G. Three-Dimensional Temperature Imaging around a Gold Microwire. *Appl. Phys. Lett.* **2013**, *102* (24), 1–5. https://doi.org/10.1063/1.4811557.

(288) He, W.; Graf, R.; Vieth, S.; Ziener, U.; Landfester, K.; Crespy, D. The Cushion Method: A New Technique for the Recovery of Hydrophilic Nanocarriers. *Langmuir* **2016**, *32* (51), 13669–13674. https://doi.org/10.1021/acs.langmuir.6b02880.

(289) Andreas, J. M.; Hauser, E. A.; Tucker, W. B. Boundary Tension by Pendant Drops. *J. Phys. Chem.* **1938**, *42* (7), 1001–1019. https://doi.org/10.1021/j100903a002.

(290) Berry, J. D.; Neeson, M. J.; Dagastine, R. R.; Chan, D. Y. C.; Tabor, R. F. Measurement of Surface and Interfacial Tension Using Pendant Drop Tensiometry. *J. Colloid Interface Sci.* **2015**, *454*, 226–237. https://doi.org/10.1016/j.jcis.2015.05.012.

(291) Lai, J. T.; Filla, D.; Shea, R. Functional Polymers from Novel Carboxyl-Terminated Trithiocarbonates as Highly Efficient RAFT Agents. *Am. Chem. Soc. Polym. Prepr. Div. Polym. Chem.* **2002**, *43* (2), 122–123.